

${}^7\text{Li}(\text{p},\text{n}){}^7\text{Be}$ neutron fields and
their application for astrophysics

Dissertation

zur Erlangung des Doktorgrades
der Naturwissenschaften

vorgelegt am Fachbereich Physik
der Johann Wolfgang Goethe-Universität
in Frankfurt am Main

von
Benjamin Sebastian Brückner
aus Frankfurt am Main

Frankfurt am Main 2022
(D30)

Vom Fachbereich Physik der
Johann Wolfgang Goethe-Universität
als Dissertation angenommen.

Dekan:

Prof. Dr. Harald Appelshäuser

Gutachter:

Prof. Dr. René Reifarth

Prof. Dr. Christoph Langer

Datum der Disputation:

30.05.2022

Not everything that can be counted counts,
and not everything that counts can be counted.

Albert Einstein

One of the basic rules of the universe is that nothing is perfect.
Perfection simply doesn't exist.

Stephen Hawking

Abstract

Most elements heavier than iron are synthesized in stars during neutron capture reactions in the r- and s-process. The s-process nucleosynthesis is composed of the main and weak component. While the s-process is considered to be well understood, further investigations using nucleosynthesis simulations rely on measured neutron capture cross sections as crucial input parameters. Neutron capture cross sections relevant for the s-process can be measured using various experimental methods. A prominent example is the activation method relying on the ${}^7\text{Li}(\text{p},\text{n}){}^7\text{Be}$ reaction as a neutron source, which has the advantage of high neutron intensities and is able to create a quasi-stellar neutron spectrum at $k_{\text{B}}T = 25\text{ keV}$. Other neutron sources able to provide quasi-stellar spectra at different energies suffer from lower neutron intensities. Simulations using the PINO tool suggest the neutron activation of samples with different neutron spectra, provided by the ${}^7\text{Li}(\text{p},\text{n}){}^7\text{Be}$ reaction, and a subsequent linear combination of the obtained spectrum-averaged cross sections to determine the Maxwellian-averaged cross section (MACS) at various energies of astrophysical relevance. To investigate the accuracy of the PINO tool at proton energies between the neutron emission threshold at $E_{\text{p}} = 1880.4\text{ keV}$ and 2800 keV , measurements of the ${}^7\text{Li}(\text{p},\text{n}){}^7\text{Be}$ neutron fields are presented, which were carried out at the PTB Ion Accelerator Facility at the Physikalisch-Technische Bundesanstalt in Braunschweig. The neutron fields of ten different proton energies were measured. The presented neutron fields show a good agreement at proton energies $E_{\text{p}} = 1887, 1897, 1907, 1912$ and 2100 keV . For the other proton energies, $E_{\text{p}} = 2000, 2200, 2300, 2500$, and 2800 keV , differences between measurement and simulation were found and discussed. The obtained results can be used to benchmark and adapt the PINO tool and provide crucial information for further improvement of the neutron activation method for astrophysics.

An application for the ${}^7\text{Li}(\text{p},\text{n}){}^7\text{Be}$ neutron fields is presented as an activation experiment campaign of gallium, an element that is mostly produced during the weak s-process in massive stars. The available cross section data for the ${}^{69,71}\text{Ga}(\text{n},\gamma)$ reactions, mostly determined by activation measurements, show differences up to

a factor of three. To improve the data situation, activation measurements were carried out using the ${}^7\text{Li}(\text{p},\text{n}){}^7\text{Be}$ reaction. The neutron capture cross sections for a quasi-stellar neutron spectrum at $k_{\text{B}}T = 25\text{ keV}$ were determined for ${}^{69}\text{Ga}$ and ${}^{71}\text{Ga}$.

Kurzübersicht

Die meisten Elemente schwerer als Eisen werden durch Neutroneneinfangreaktionen während des r- und s-Prozesses erzeugt. Die s-Prozess Nukleosynthese wird unterteilt in die schwache Komponente und die Hauptkomponente. Der s-Prozess gilt als gut verstanden, und durch verschiedene Simulationen kann die Nukleosynthese nachgebildet werden. Wichtige Eingangsparameter für solche Simulationen sind gemessene Neutroneneinfangsquerschnitte. Um diese zu bestimmen, gibt es verschiedene experimentelle Techniken. Eine davon ist die Aktivierungsmethode in Kombination mit der ${}^7\text{Li}(\text{p},\text{n}){}^7\text{Be}$ Reaktion als Neutronenquelle. Diese hat den Vorteil von besonders hohen Neutronenintensitäten, und erzeugt bei einer Protonenenergie von $E_p = 1912\text{ keV}$ ein quasi-stellares Neutronenspektrum bei $k_B T = 25\text{ keV}$. Andere Neutronenquellen, welche auch stellare Neutronenspektren nachbilden können, haben den großen Nachteil einer vergleichsweise niedrigeren Neutronenausbeute. Eine Möglichkeit, Wirkungsquerschnitte für verschiedene astrophysikalisch relevante Energiebereiche zu bestimmen, ist die Aktivierung von Proben bei verschiedenen Energien mit der ${}^7\text{Li}(\text{p},\text{n}){}^7\text{Be}$ Reaktion als Neutronenquelle. Durch eine Linearkombination der verschiedenen Spektrum gemittelten Wirkungsquerschnitte kann der Maxwell gemittelte Wirkungsquerschnitt (MACS) bestimmt werden. Da diese Überlegungen auf Simulationen des PINO Tools beruhen, ist es nötig, die Genauigkeit dieses Tools zu überprüfen und zu verbessern. Dafür waren die Neutronenfelder der ${}^7\text{Li}(\text{p},\text{n}){}^7\text{Be}$ Reaktion bei Protonenenergien zwischen $E_p = 1880.4\text{ keV}$ und 2800 keV von Interesse. Diese wurden bei zehn verschiedenen Protonenenergien an der PTB Ion Accelerator Facility der Physikalisch-Technischen Bundesanstalt in Braunschweig untersucht. Die Messungen, welche in dieser Arbeit präsentiert werden, zeigen gute Übereinstimmungen für Protonenenergien von $E_p = 1887, 1897, 1907, 1912$ und 2100 keV . Für $E_p = 2000, 2200, 2300, 2500$ und 2800 keV zeigen sich teils deutliche Abweichungen.

Eine Anwendung für die Neutronenfelder der ${}^7\text{Li}(\text{p},\text{n}){}^7\text{Be}$ Reaktion ist die Aktivierung des Elements Gallium, welches hauptsächlich während des schwachen s-Prozesses in massiven Sternen gebildet wird. Die Datenlage, welche von Messungen mittels

der Aktivierungsmethode dominiert wird, beinhaltet Werte mit einer Abweichung von bis zu einem Faktor drei. In dieser Arbeit werden die Ergebnisse einer Aktivierungskampagne zur Bestimmung der Maxwell gemittelten Wirkungsquerschnitte bei $k_{\text{B}}T = 25 \text{ keV}$ der Reaktionen $^{69,71}\text{Ga}(\text{n},\gamma)$ präsentiert.

Contents

Abstract

Kurzübersicht

1. Introduction	1
1.1. The nucleosynthesis of the elements	1
1.1.1. From hydrogen to iron	1
1.1.2. From iron to lead	2
1.2. Determination of neutron capture cross sections relevant for the s- process nucleosynthesis	5
1.3. The case of gallium	6
1.4. Aim of the thesis	8
2. General principles	9
2.1. Cross section and astrophysical rate	9
2.2. Radiation interaction with matter	11
2.2.1. Charged particles interactions	11
2.2.2. Photon interactions	12
2.2.3. Neutron interactions	15
2.3. Detector technologies	15
2.3.1. Scintillation detectors	15
2.3.2. Semiconductor detectors	17
2.4. Data acquisition systems	18
2.4.1. Analog data acquisition systems	18
2.4.2. Digital data acquisition systems	19
2.5. Neutron sources and experimental techniques	20
2.5.1. The ${}^7\text{Li}(\text{p},\text{n}){}^7\text{Be}$ reaction	20
2.5.2. The neutron activation method	22
2.5.3. The neutron time-of-flight technique	24

3. Investigation of the ${}^7\text{Li}(\text{p},\text{n}){}^7\text{Be}$ neutron fields	25
3.1. Experimental preparations	26
3.1.1. ${}^6\text{Li}$ -Glass detectors	28
3.1.2. Detector mounting	30
3.1.3. Data acquisition	31
3.2. ${}^7\text{Li}(\text{p},\text{n}){}^7\text{Be}$ neutron fields - Experiment	35
3.2.1. Accelerator time resolution	38
3.2.2. Total time resolution	38
3.2.3. Neutron yield	40
3.3. Time-of-flight analysis	43
3.3.1. Time of flight to energy conversion	50
3.4. Neutron fields	53
3.5. Comparison with the PINO tool	58
3.5.1. Time resolution	60
3.5.2. Detector efficiency	60
3.5.3. Proton beam energy	63
3.5.4. Comparison of the ${}^7\text{Li}(\text{p},\text{n}){}^7\text{Be}$ neutron fields	69
4. Neutron activation of Gallium	91
4.1. Activation analysis	92
4.1.1. Ga analysis	94
4.2. Experimental preparations	95
4.2.1. Detector energy calibration	95
4.2.2. Detector energy resolution	96
4.2.3. Detector efficiency	96
4.3. Activation I	98
4.4. Activation II	105
4.5. Non-destructive material analysis	110
4.6. Activation III	112
4.7. Activation IV	115
5. Conclusion and outlook	119
6. Zusammenfassung	123
A. Appendix	129
B. Appendix - Investigation of the ${}^7\text{Li}(\text{p},\text{n}){}^7\text{Be}$ neutron fields	131

C. Appendix - Neutron activation of Gallium	146
List of figures	168
List of tables	172
List of literature	178

1. Introduction

Ever since the dawn of mankind and the formation of tribes and civilizations, objects in the sky have been seen as something unexplainable, yet mystical. Ancient civilizations, like the Egyptians, even regarded the Sun as a form of a god. Over the centuries the celestial objects have always been a region of interest for philosophers and scholars. One of the biggest questions was not solved until the 20th century, when H. Bethe, working together with C. Critchfield [9] and C. F. v. Weizäcker [70], found an explanation for the energy production in stars, and therefore, the synthesis of light elements. The origin of the elements heavier than iron remained a mystery up until the 1950s, when Burbidge, Burbidge, Fowler and Hoyle [19] and Cameron [22, 21] presented their ideas of the synthesis of elements heavier than iron. The field of nuclear astrophysics was born. With the foundation laid in the 1950s, the knowledge of the synthesis of the elements has been improving very well. However, questions remain.

1.1. The nucleosynthesis of the elements

In order to explain the abundance and creation of elements in our solar system, nuclear astrophysics made it possible to bring stars into the laboratory. The creation of the elements can be divided into two groups, the light elements, which are the elements up to a mass number of $A < 56$ and the heavy elements with $A > 56$.

1.1.1. From hydrogen to iron

The light elements starting with hydrogen and helium as well as traces of beryllium and lithium were created during and shortly after the Big Bang. This nucleosynthesis mechanism is therefore called the primordial or Big Bang nucleosynthesis, which lasted until twenty minutes after the Big Bang [46].

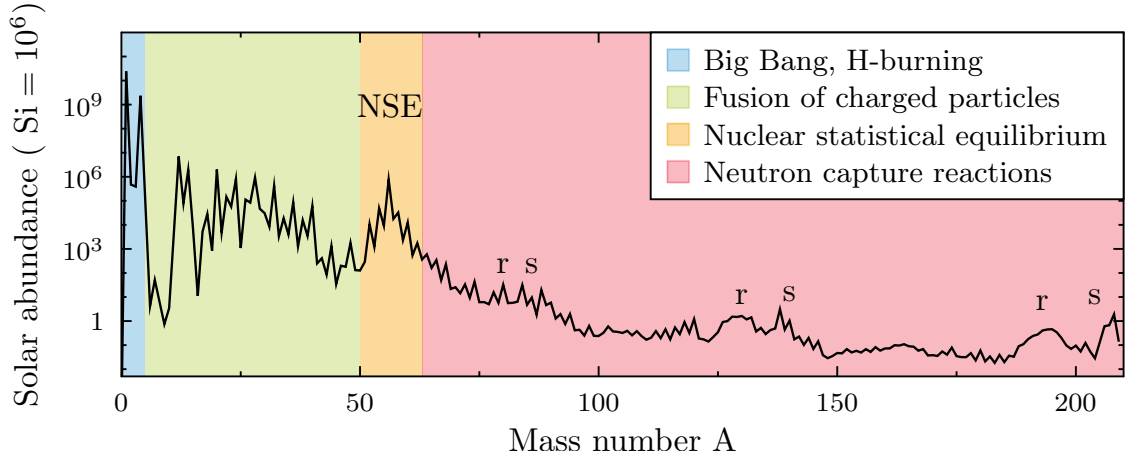


Figure 1.1.: Solar abundance distribution taken from Lodders *et al.* [48]. The given values are normalized to the silicon abundance. Most prominent are the peaks of H and He from the Big Bang nucleosynthesis, C and O from stellar nucleosynthesis, the iron peak and the r- and s-process peaks.

To create elements heavier than the ones synthesized in the primordial nucleosynthesis, stars had to form first. In stars the elements up to iron are synthesized by charged-particle fusion reactions. During the lifetime of a star, different burning phases are undergone depending on the mass of the star. Nuclear fusion reactions generate energy causing the thermal pressure to rise and stabilize the star against the gravitational contraction. If the nuclear fuel of the respective burning phase is exhausted, the thermal pressure declines leading to a contraction in the star. The temperature in the core rises significantly, allowing the next burning phase to ignite and the hydrostatic equilibrium is restored. With higher mass numbers, the Coulomb barrier becomes an obstacle for charged-particle fusion reactions. In heavy stars the fusion process ceases reaching the element region of Fe-Ni [60]. Due to the largest binding energy per nucleon, no energy is emitted during fusion reactions [55].

1.1.2. From iron to lead

Most of the elements heavier than iron are formed via neutron capture reactions [19, 22, 21]. These reactions take place in stars at different stages in their lifetime. Depending on the neutron density, the neutron capture process can be categorized as the slow neutron capture process (s) and the rapid neutron capture process (r).

The r-process

About half of the elements heavier than iron are produced during the r-process, where the neutron densities are above 10^{20} cm^{-3} and temperatures higher than 10^9 K . In this scenario neutron-capture times are shorter than the β^- -decay of the produced nuclei. Because of the rapid captures, elements up to the neutron drip line are synthesized. The high neutron flux and temperature cannot be maintained for a long period of time, hence, the origin of the r-process was long believed to be only possible in explosive scenarios such as supernovae [19]. As presented in Figure 1.1, the broad r-process peaks at $A = 80, 130$ and 195 are a result of accumulated matter at closed neutron shells ($N = 50, 82$ and 126) on the neutron rich side, far away from the stable nuclei, the so called valley of stability. The positions of the peaks indicate conditions realized in explosive environments with high neutron densities and high temperatures. More recent studies show another possible site for the r-process, neutron star mergers [32]. This theory was supported by the analysis of the neutron star merger GW170817, when in addition to the detection of gravitational wave signals, decay signatures from nuclei synthesized during the r-process were detected [65]. However, many other scenarios such as neutrino-driven winds are also possible candidates [6].

The s-process

The s-process is thought to be responsible for the synthesis of nuclei between $56 < A < 210$ [19]. The reaction path remains close to the valley of stability, starting at a seed nucleus, due to the rather long timescale of neutron captures compared to the typical half-lives of the created unstable nuclei. However, while models could successfully explain the measured abundances of elements with mass number larger 90, for lighter nuclei this was not successful [63]. This gave rise to the hypothesis that the s-process has to be divided into two different components, which take place in different stellar scenarios. The main component synthesizing elements between $90 < A < 210$ and the weak component responsible for the elements lighter than $A = 90$ [71]. The differences between the two components lie in neutron density, time-integrated neutron flux and temperature.

1. Introduction

The main s-process

The main s-process takes place in stars with masses between $1 - 5 M_{\odot}$. After the hydrogen in the stars core is spent, the star leaves the main sequence and continues to go through various stages of stellar development. Once the star has formed a carbon/oxygen core (C/O core), helium and hydrogen shell burning alternates. After about 10^4 years enough helium has been formed. It ignites creating a He-flash, which results in a thermal pulse. Since the shell is surrounded by a fully convective envelope, hydrogen is mixed into the helium intershell as sketched in Figure 1.2. This allows the creation of ^{13}C via proton capture on the abundant ^{12}C : $^{12}\text{C}(p, \gamma)^{13}\text{N}(\beta^+ \nu)^{13}\text{C}$ [33]. Neutrons can then be produced between two thermal pulses via the reaction



The neutron densities reach $\rho_n \approx 10^7 \text{ n/cm}^3$ and the temperature approximately 10^8 K or $k_B T = 8.6 \text{ keV}$ [20, 37]. In addition to the first neutron production mechanism, a second mechanism contributes via the reaction



This source becomes available during the maximum of the thermal pulse. Temperatures at the base of the convective zone need to be in the range of $2.5 \times 10^8 \text{ K}$ and $3 \times 10^8 \text{ K}$ ($k_B T \approx 21.5 - 25.8 \text{ keV}$). Even though the neutron densities reach up to 10^{10} cm^{-3} , it only contributes about 5% to the total neutron fluence, because of to the short duration of this phase [58].

The weak s-process

The weak s-process takes place in stars with masses $M_{\text{star}} \geq 8 M_{\odot}$, which explode as supernovae of type II. The name weak s-process originates in the rather modest integrated neutron flux compared to the main component. The neutrons are created during convective helium core burning by the $^{22}\text{Ne}(\alpha, n)^{25}\text{Mg}$ reaction at a temperature of $3 \times 10^8 \text{ K}$ or ($k_B T \approx 25.8 \text{ keV}$), where neutron densities reach $\rho_n \approx 10^6 \text{ cm}^{-3}$ [58, 54]. The necessary ^{22}Ne is synthesized in a series of α -capture reactions on ^{14}N , which is a product of the CNO-cycle in the previous hydrogen burning phase. During carbon shell burning at temperatures of 10^9 K ($k_B T \approx 90 \text{ keV}$) the neutron production mechanism is activated again. The neutron density during this phase can reach between $\rho_n \approx 10^{11}$ and $\rho_n \approx 10^{12} \text{ cm}^{-3}$.

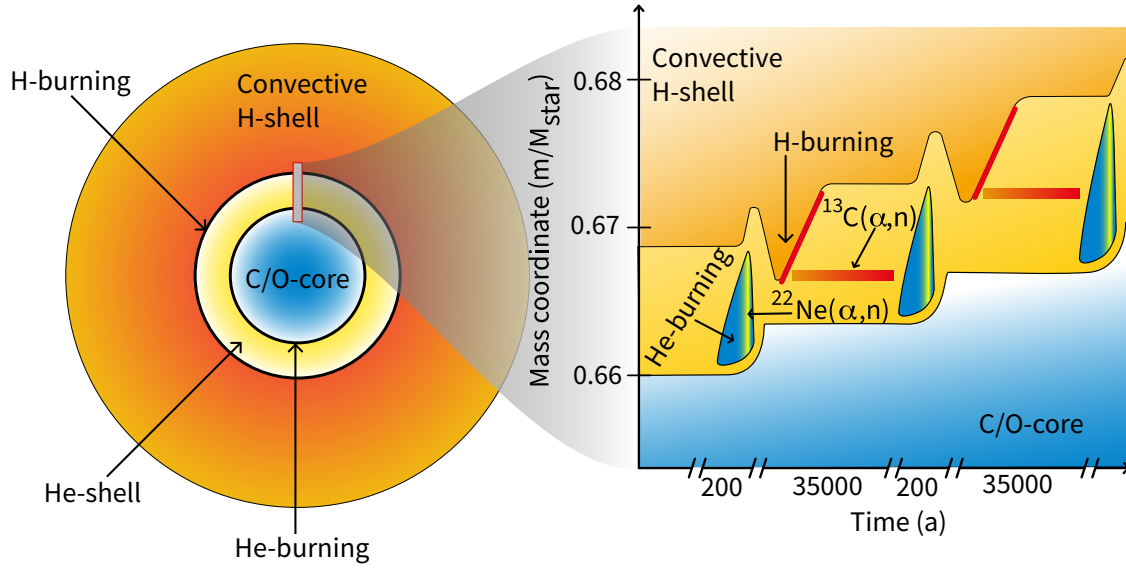


Figure 1.2.: Schematic of an AGB-star (left) and its different burning phases (right). Based on [58].

Compared to the main component the weak s-process has a low neutron fluence. Therefore, it becomes impossible to reach reaction flow equilibrium. As a consequence, a particular neutron capture cross section not only determines the abundance of the respective isotope, which is mostly the case in the main s-process, but also affects the abundances of all heavier isotopes as well [58, 54].

1.2. Determination of neutron capture cross sections relevant for the s-process nucleosynthesis

For the determination of neutron capture cross sections of astrophysical interest, neutrons within an energy range between one to several hundred keV are needed. For measurements of these cross sections, two methods are most commonly used. These are the time-of-flight- (ToF) and the activation method [58]. The ToF method relies on the detection of prompt γ -ray emission, following neutron captures. The energy of the neutrons are determined by measuring the time difference, between their production and reaction on the sample. Therefore, the energy differential neutron capture cross sections can be obtained. Depending on the stellar scenario of interest, the differential cross section can be convolved with the respective Maxwell-Boltzmann energy distribution. Another possible method to determine the neutron capture

1. Introduction

cross sections of astrophysical interest is the activation method. With this method a sample is irradiated with a high intensity neutron source and subsequently analyzed. Therefore, this method is only feasible if the produced nucleus is radioactive. The advantage of this method is the high neutron flux through the sample and, the therefore higher sensitivity. The disadvantage, however, is the dependence of the determined capture cross section on the used neutron spectrum. In order to determine cross sections for different nucleosynthesis sites, different neutron spectra and sources are needed. A prominent neutron source which features very high intensities due to the rapid rise of the (p,n) cross section, right above the neutron production threshold, is the ${}^7\text{Li}(p,n){}^7\text{Be}$ reaction. In section 2.5 the experimental methods are further elaborated.

1.3. The case of gallium

With mass numbers of $A = 69$ and $A = 71$, gallium is mostly produced in the weak s-process. Nucleosynthesis simulations designate gallium as the most overabundant s-element at the end of shell carbon burning [54]. Previous measurements, to determine the neutron capture cross section in the keV regime, show large differences. The influence of the correct neutron capture cross section of gallium on nucleosynthesis simulations is significant. Simulations with the online tool NETZ [75] can be utilized to visualize the impact of uncertainties on the abundances. For this the neutron capture cross sections were varied by 50 %. Figure 1.3 shows the sensitivities to the propagation effect of cross section uncertainties during the weak s-process. If the capture cross section of one isotope is changed by 50 %, this leads to changes up to 20 % for the s-abundances of following isotopes, while the abundances of the respective gallium isotopes are changed up to a factor of two.

Previously, neutron capture cross sections for both isotopes of gallium have been measured using the activation method with different neutron sources. For ${}^{69}\text{Ga}$ two measurements were carried out using a Sb-Be neutron source which produces nearly mono-energetic neutrons with dominant peaks at 23 keV and 378 keV and respective intensities of 97% and 3%. Kononov *et al.* determined the capture cross section to be (148.4 ± 1.2) mb [42, 52]. However, a value of (50 ± 5) mb was obtained by [26, 52], using the same neutron source, giving rise to a disagreement by a factor of three. Additionally, two cross section values for ${}^{71}\text{Ga}$ using the same neutron source type

are available. A measurement by Macklin *et al.* determined the cross section to be (140 ± 30) mb [49, 52] while Chaubey *et al.* measured (75 ± 10) mb [26, 52].

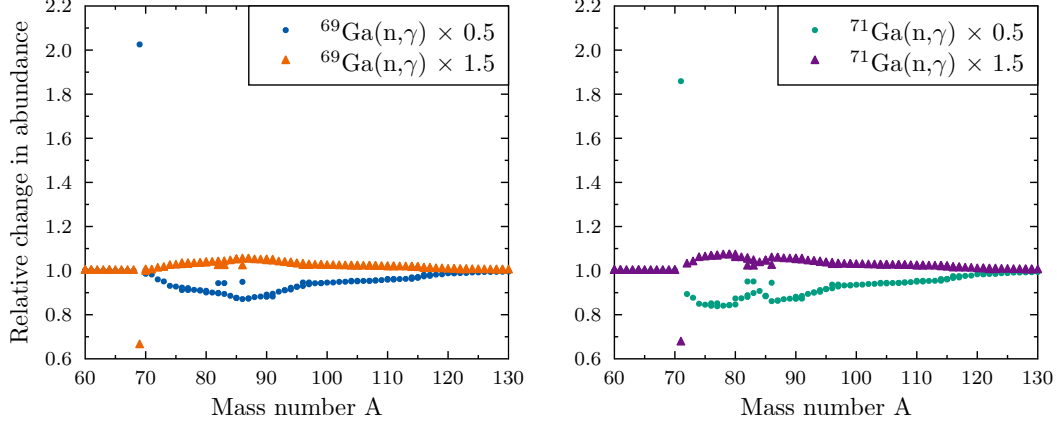


Figure 1.3.: Impact of the cross section uncertainties of the $^{69,71}\text{Ga}(n,\gamma)$ reactions on the abundances of the weak s-process. The simulations were conducted using the online tool NETZ.

An activation using a mono energetic neutron beam with $E_n = 25$ keV was carried out by Anand *et al.* determining a cross section of (104 ± 14) mb [5, 52] for ^{71}Ga . References [73, 28] indicate a cross section of 138 mb for ^{71}Ga using integral measurements with a neutron energy distribution corresponding to a quasi-stellar distribution at $k_B T = 25$ keV. Several activation measurements at different energies were carried out by Dovbenko *et al.* At an energy of (27 ± 5.3) keV the cross section for ^{69}Ga was determined to be (172 ± 49) mb [30, 52] and for ^{71}Ga (159 ± 45) mb [30, 52]. In addition to the activation measurements, time-of-flight measurements for natural gallium are available [72]. However, the neutron capture cross sections of other nuclei investigated in the same measurement campaign show large discrepancies with more recent measurements [28].

To provide more clarity into the data situation for $^{69,71}\text{Ga}$ a first activation experiment was carried out by Göbel *et al.* at the European Joint Research Centre (EC-JRC) in Geel. The cross section values obtained by activating a natural gallium sample did

1. Introduction

significantly differ from the values previously determined. The cross section ratio of the respective gallium isotope and gold were determined to be

$$\frac{\sigma_{69\text{Ga}}}{\sigma_{197\text{Au}}} = 0.29 \pm 0.02$$

$$\frac{\sigma_{71\text{Ga}}}{\sigma_{197\text{Au}}} = 0.17 \pm 0.01$$

[35].

1.4. Aim of the thesis

The possibility to use the neutron activation method featuring the ${}^7\text{Li}(\text{p},\text{n}){}^7\text{Be}$ reaction, which is mostly used to recreate a quasi-stellar neutron spectrum at an energy of $k_{\text{B}}T = 25\text{ keV}$, needs to be investigated for its use to recreate quasi-stellar neutron spectra with different energies. Simulations utilizing the PINO code [57] suggest a possible recreation of quasi-stellar neutron spectra at different energies relying on a linear combination of neutron spectra, obtained at different proton energies. While previous studies by Ratinsky *et al.*, Feinberg *et al.* and Lederer *et al.* show a good agreement of the simulations at proton energies of $E_{\text{p}} = 1912\text{ keV}$ [56, 31, 44], recent studies by Pachua *et al.* show large deviations between measurement and simulations using the PINO code at energies $E_{\text{p}} = 3500\text{ keV}$ [53]. These deviations implicate a possible incorrect simulation at proton energies higher than $E_{\text{p}} = 1912\text{ keV}$. This thesis aims at providing information, verification and foundations for improvements for the PINO code obtained by measurements of the ${}^7\text{Li}(\text{p},\text{n}){}^7\text{Be}$ neutron fields, in the proton energy range between 1887 keV and 2800 keV. The experimental campaign was carried out at the PTB Ion Accelerator facility at the Physikalisch-Technische Bundesanstalt PTB in Braunschweig.

An application for the ${}^7\text{Li}(\text{p},\text{n}){}^7\text{Be}$ neutron fields was a series of neutron activation experiments on gallium, with the goal to investigate the neutron capture cross sections of both stable isotopes: ${}^{69,71}\text{Ga}$. As previously stated, the data situation in the keV regime is very indecisive. To improve this situation and to provide better inputs for nucleosynthesis simulations, the precise neutron capture cross sections need to be known. This thesis aims at providing quasi-stellar neutron capture cross sections for ${}^{69}\text{Ga}$ and ${}^{71}\text{Ga}$ at an energy of $k_{\text{B}}T = 25\text{ keV}$ mimicking the ${}^{22}\text{Ne}(\alpha,\text{n}){}^{25}\text{Mg}$ phase during the convective helium core burning phase in massive stars.

2. General principles

2.1. Cross section and astrophysical rate

The quantity of interest in nuclear reaction experiments is the probability of the reaction called the cross section, which is defined as an area with the unit barn ($1 \text{ b} = 10^{-24} \text{ cm}^2$). For illustration a simplification can be made. Considering only the geometric parameters of the reaction participants, the geometrical cross section is defined as

$$\sigma_{\text{geo}} = \pi \cdot (r_{\text{projectile}} + r_{\text{target}})^2. \quad (2.1)$$

If the projectile and target nucleus are considered to be of spherical shape, where $r_{\text{projectile}}$ denotes the projectile and r_{target} the target nucleus radius. Due to the quantum nature of matter the energy dependent De-Broglie wave length λ has to be considered. Therefore, the cross section becomes

$$\sigma = \pi \cdot \lambda^2. \quad (2.2)$$

The cross section in nuclear physics is defined as

$$\sigma = \frac{N_{\text{react.}}}{N_{\text{target}} \cdot \frac{N_{\text{projectile}}}{A}}, \quad (2.3)$$

where $N_{\text{react.}}$ denotes the number of reactions, N_{target} the number of target nuclei and $N_{\text{projectile}}/A$ the number of projectiles per area. [55] [60].

The reaction cross section is strongly dependent on the energy of the projectile, and therefore, also velocity dependent $\sigma = \sigma(\nu)$, where ν denotes the relative velocity between the projectile and the target.

The rate of nuclear reactions r in a volume filled with particles X and Y and a density N_X and N_Y can be written as

$$r = N_X \cdot N_Y \cdot \nu \cdot \sigma(\nu), \quad (2.4)$$

2. General principles

where ν denotes the relative velocities.

In a stellar environment the velocity of the particles varies and follows the distribution function $\phi(\nu)$. The probability of a particle having a velocity ν in the interval $(\nu, \nu+1)$ is given by $\phi(\nu)d\nu$. The integral of the velocity distribution over all velocities is

$$\int_0^\infty \phi(\nu) d\nu = 1. \quad (2.5)$$

To determine the effective cross sections as a function of the temperature, ν and σ have to be convolved, which is then called the reaction rate per particle pair

$$\langle \sigma \nu \rangle = \int_0^\infty \phi(\nu) \nu \sigma(\nu) d\nu. \quad (2.6)$$

With Equation 2.6 the expression for the total reaction rate becomes

$$r = N_X \cdot N_Y \cdot \langle \sigma \nu \rangle (1 + \delta_{XY})^{-1} \quad (2.7)$$

with a correction term to account for reactions with the same particle types [60].

Stellar gas is non-degenerate, meaning the nuclei move non-relativistic. The gas is in thermodynamic equilibrium allowing the velocity of the nuclei to be described by a Maxwell-Boltzmann velocity distribution, which only relies on the mass of the particle m and the temperature of the surrounding area T

$$\phi(\nu) = 4\pi\nu^2 \left(\frac{m}{2\pi k_B T} \right)^{3/2} \exp \left(-\frac{m\nu^2}{2k_B T} \right). \quad (2.8)$$

The most probable velocity is derived from $d\phi/d\nu = 0$

$$\nu_T = \sqrt{\frac{2k_B T}{m}}. \quad (2.9)$$

The reaction rate per particle pair in stars, accounting for particles following a Maxwell-Boltzmann velocity distribution, can then be written as:

$$\langle \sigma \nu \rangle = 4\pi \left(\frac{\mu}{2\pi k_B T} \right)^{\frac{3}{2}} \cdot \int_0^\infty \nu^3 \sigma(\nu) \cdot \exp \left(-\frac{\mu\nu^2}{2k_B T} \right) d\nu, \quad (2.10)$$

or using the center of mass energy $E_{cm} = 1/2\mu\nu^2$

$$\langle \sigma \nu \rangle = \left(\frac{8}{\pi\nu} \right)^{\frac{1}{2}} \left(\frac{1}{k_B T} \right)^{\frac{3}{2}} \cdot \int_0^\infty E \sigma(E) \cdot \exp \left(-\frac{E}{k_B T} \right) dE, \quad (2.11)$$

where μ denotes the reduced mass $\mu = m_x m_y / (m_x + m_y)$.

The Maxwell Averaged Cross Section (MACS) is defined as the reaction rate scaled with the most probable velocity. Using Equation 2.9 and Equation 2.11 it can be written as

$$\sigma_{\text{MACS}} = \frac{\langle \sigma \nu \rangle}{\nu_T} = \frac{2}{\sqrt{\pi}} \frac{1}{(k_B T)^2} \cdot \int_0^\infty E \sigma(E) \cdot \exp\left(-\frac{E}{k_B T}\right) dE \quad (2.12)$$

[60, 58].

2.2. Radiation interaction with matter

In order to determine the cross section of a reaction, most experiments depend on the detection of radiation. The different detection mechanisms rely on the interaction of radiation with matter. Whether charged particles, neutrons or photons, all have the effect of triggering various reactions when penetrating matter. In order to choose the right detector, the nature of the radiation of interest is important, since different types of radiation require a different detector.

2.2.1. Charged particles interactions

The nature of the interaction depends strongly on the charge of the projectile particle. For particles heavier than electrons (e^-), such as alpha-particles (α), the main interaction with matter is the Coulomb interaction, the electromagnetic interaction between the charged particle and the shell-electrons of the matter atoms. Two scenarios are possible for the charged particle to transfer its energy to the shell electrons. The momentum the electron receives when the projectile is passing can lead to two different effects: excitation or ionization. Excitation of the material raises a bound electron to a higher shell, while ionization ejects the electron from the atom. Since only a small amount of the projectile's energy is lost per interaction, many can occur. As a result the projectile has a well defined range in the material, which is dependent on the kind of projectile and the matter itself. The heavier the projectile and or the denser the matter, the smaller the range [45, 41].

The stopping power S for charged particles in a given absorber is defined as

$$S = -\frac{dE}{dx}. \quad (2.13)$$

2. General principles

For particles with a given charge state, the stopping power S increases with decreasing particle velocity. The specific energy loss can be determined using the Bethe formula:

$$-\frac{dE}{dx} = \frac{4\pi e^4 z^2}{m_0 \nu^2} N Z \left[\ln \left(\frac{2m_0 \nu^2}{I} \right) - \ln \left(1 - \frac{\nu^2}{c^2} \right) - \frac{\nu^2}{c^2} \right], \quad (2.14)$$

where e denotes the charge of the projectile particle, N and Z the number density and the atomic number of the absorber atoms, m_0 the electron rest mass, ν the velocity of the projectile and I the average excitation and ionization potential of the absorber material [41].

2.2.2. Photon interactions

The interactions between photons and matter differ from charged particle interactions. The main interaction mechanisms between photons and matter are:

- Photoelectric effect
- Compton scattering
- Pair production.

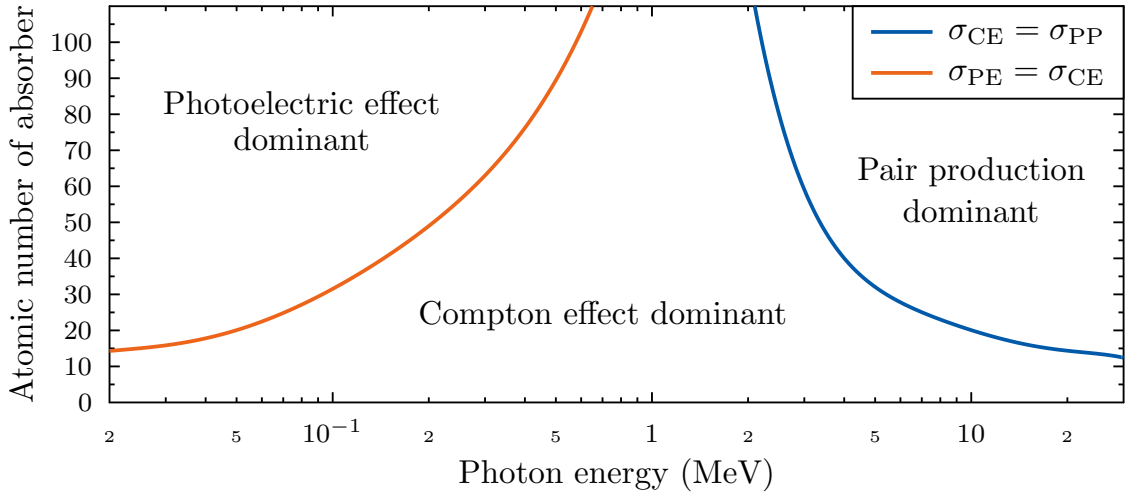


Figure 2.1.: Energy and atomic number dependence of the different interactions of photons with matter. At the continuous lines the cross sections of the two interaction mechanisms next to each other are equal. Data taken from XCOM [8].

Photoelectric effect

The photoelectric effect describes the absorption of a photon by an atom and the immediate ejection of the electron from the atom. The energy of the ejected electron can be approximated by

$$E = h\nu - E_b, \quad (2.15)$$

where E_b describes the binding energy of the electron, ν the frequency of the incident photon and h the Planck constant. The Photoelectric effect is typically the dominant interaction between photons and matter at incident photon energies up to approximately 100 keV, since the photons can only interact with bound electrons. When the incident photon energy reaches energies above the highest electron binding energy of the atom, the cross section of this reaction drops drastically [45].

Compton scattering

Compton scattering is dominant for photons with energies E_γ between 100 keV and 10 MeV. The incident photon scatters with a quasi-free electron. The electron can be considered free since the incident photon energy is much higher than the binding energy of the electron. During the scattering process, the photon transfers a part of its energy onto the electron. The photon energy after scattering E'_γ is dependent on the initial energy of the photon E_γ and the scattering angle θ . The photon energy after scattering is given as

$$E'_\gamma = \frac{E_\gamma}{1 + \frac{E_\gamma}{m_e c^2} (1 - \cos \theta)}. \quad (2.16)$$

Considering Equation 2.16, the energy transfer from photon to the electron reaches a maximum at a scattering angle of $\theta = 180^\circ$. However, even then the transferred energy is less than the incident photons energy. If the scattered photon leaves the detector-volume, the deposited energy corresponds to the electron, giving rise to two phenomena visible in the γ -spectrum: the Compton continuum and the Compton edge [45].

Pair production

If the energy of the photon exceeds 1022 keV, which equals $2 m_e$, another interaction mechanism becomes likely, the pair production. The incident photon is transformed

2. General principles

into an electron-positron pair, which is only possible in the vicinity of a nucleus in order to conserve momentum. Energy exceeding the 1022 keV threshold is transferred to the electron and positron in form of kinetic energy. While the electron is stopped in the material, the positron will annihilate with an electron after being slowed down sufficiently. The annihilation will create two photons with an energy of $E_\gamma = 511$ keV corresponding to the electron/positron mass. If both of these photons are stopped in a detector volume, the full energy of the incident photon is detected. If one of them escapes the volume, a so called single-escape line with an energy of $E_\gamma - 511$ keV, and if both escape a double-escape line $E_\gamma - 1022$ keV will become visible in the energy spectrum [45, 41].

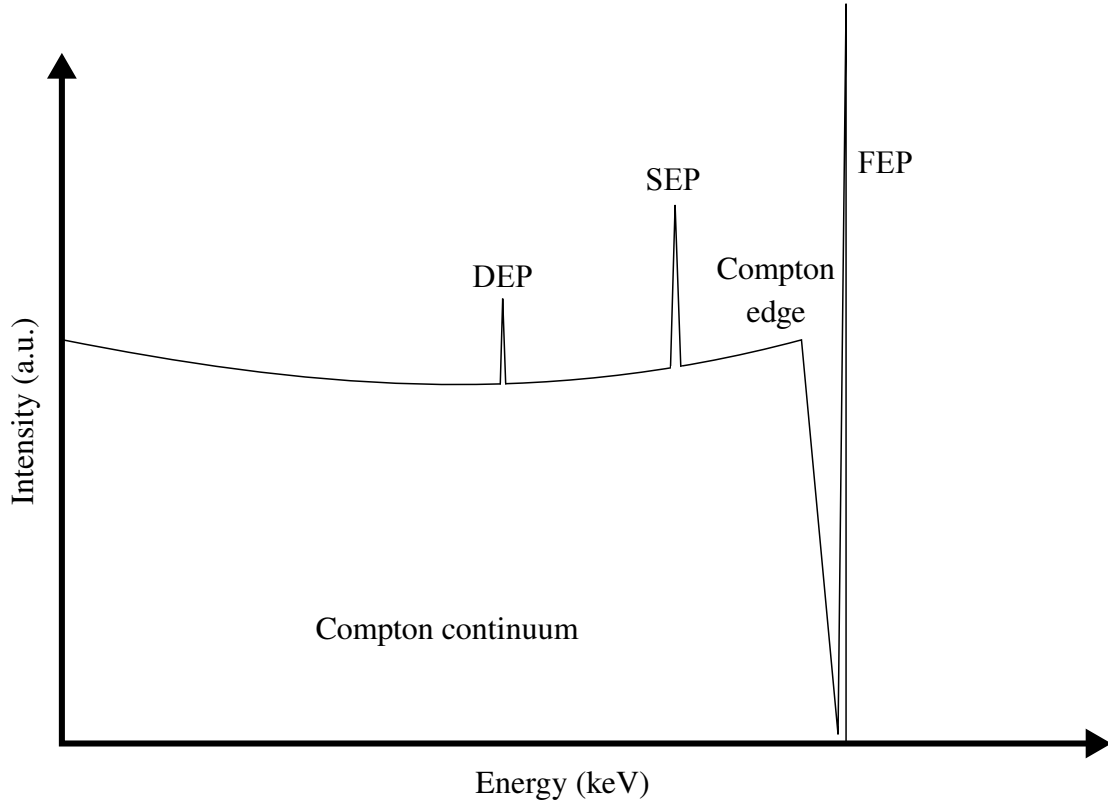


Figure 2.2.: Simplified illustration of a possible γ -ray spectrum in a detector. The Compton continuum and edge, the single- and double-escape (SEP and DEP) lines as well as the full energy peak (FEP) are marked.

2.2.3. Neutron interactions

Neutron interactions with matter rely on the strong force. Due to the small range of the strong force ($\approx 10^{-15}$ m), neutrons feature a very long range inside matter. However, when the neutron interacts, there are six main interaction principles: Elastic and inelastic scattering on nuclei, radiative neutron capture, neutron induced reactions, fission and high-energy hadron shower production. Since all these methods are strongly dependent on the energy of the neutron, neutrons are classified in respect to their energy. Additionally, neutrons penetrating matter experience exponential attenuation.

The total probability for a neutron to interact with matter is given by

$$\sigma_{\text{total}} = \sigma_{\text{elastic}} + \sigma_{\text{inelastic}} + \sigma_{\text{capture}} + \sigma_{\text{induced}} + \sigma_{\text{fission}} + \sigma_{\text{hadronic}}. \quad (2.17)$$

The effect of neutron moderation occurs when neutrons enter material and are not stopped immediately by one of the above mechanisms. The neutrons are then interacting with the material mostly by elastic- and inelastic scattering until it has lost enough energy to undergo radiative capture, neutron-induced or fission reactions [45].

2.3. Detector technologies

For the detection of radiation a detection device (detector) is needed. These instruments rely on the interaction mechanisms of radiation with matter. Depending on the type of radiation to be detected, a specific detector material is needed, which ensures the most efficient and correct detection of the radiation of interest. In case of photons in an energy range between 10 and 2000 keV High purity germanium (HPGe) detectors are commonly used. The basic function of any kind of detector is the registration of secondary particles created by the impinging radiation. Most detectors are capable of providing two types of information, time and pulse height.

2.3.1. Scintillation detectors

One of two detector types most common in nuclear physics applications are scintillation detectors. This detector type features a simple setup consisting of a scintillation

2. General principles

crystal or liquid, an optic coupling, a photomultiplier tube (PMT) and a voltage divider. Radiation impinging on a scintillation crystal creates a flash of light (scintillation). These flashes are then processed into an electronic signal by the PMT. To gather further information of the incident radiation, additional electronics are used.

Scintillation materials

Scintillation materials are sorted into different categories. Scintillators made from hydrocarbon compounds are classified as organic scintillators, where the scintillation process arises from transitions made by the free valence electrons of the molecules. A large advantage of these kind of materials is their use in many physical forms without their loss of scintillation properties.

The most widely used material are inorganic crystals. A prominent example for these are thallium-doped sodium iodine crystals (NaI(Tl)). These scintillators are most commonly used for the detection of β - and γ -radiation due to their high atomic number. The scintillation mechanism in inorganic scintillators relies on the band structure of the crystal. The detection of an impinging particle can occur in two ways. The crystal can be ionized by exciting an electron from the valence into the conduction band, resulting in the creation of a free electron and a free hole. Another possibility is the creation of a so called exciton, by exciting an electron to the exciton band located just below the conduction band, where the electron and the hole remain bound together as a electron-hole pair, which can move freely through the crystal. Now the so called activator or dopant becomes important. If the electron-hole pair encounters such an activator, former forbidden energy levels in the band gap become available. The ionization of the activator atom leads to a transition from excited to ground state, resulting in the creation of scintillation light.

For neutron detection, glass scintillators are of great importance. These scintillators are made from cerium activated lithium or boron silicates. For neutron detection the lithium component of these glasses is enriched by ^6Li . Since lithium silicates are also capable of detecting γ -rays, a discrimination between γ -and neutron-radiation is possible. The neutron detection mechanism for these glasses relies on $^6\text{Li}(n,\alpha)^3\text{H}$ reaction, where the α -particle ionizes the scintillator material and scintillation light is created [45].

Photo multiplier tube

The produced scintillation light needs to be analyzed in order to give information of the incident radiation. This becomes possible using a photomultiplier tube (PMT). The scintillator is coupled to the PMT with optical glue or connected via a light guide. A PMT consists of three main stage: the photo cathode, a focus mechanism and the dynode string encased in a vacuum tube. Photons created during the scintillation process react with the photocathode material, usually made from alkali metals, via the outer photoelectric effect, resulting in the emission of an electron. The material of the photocathode has to be selected depending on the wavelength of the scintillation light. Since the momentum vector of the electrons can be in various directions, a focus stage is needed. Via an electric field the produced electrons are guided to the first of many (between 5 and 10) dynode stages. Electrons striking the dynode material deposit a fraction of their energy inside, resulting in the emission of secondary electrons, which are subsequently accelerated to the next dynode stage, where the procedure is repeated. This ensures a multiplication process until the electrons are collected at the anode of the PMT to give rise to a measurable electric signal [45]. The voltage for the PMT is delivered via a voltage divider. This device ensures the correct voltages are applied to the dynode stages, which makes it responsible for the photo multiplication and acceleration processes of the electrons.

2.3.2. Semiconductor detectors

The second detector type used for the experiments presented in this thesis are semiconductor detectors. Based on crystalline semiconductor materials these detector types are most suitable for γ -ray detection. The detection mechanism of radiation is based on the creation of electron-hole pairs after the passage of ionizing radiation through the material. These pairs are then collected by an electric field in order to create a signal. Semiconductor crystals feature an energy band structure. In contrast to a conductor where energy levels of the outer atomic shell form a continuum, insulators and semiconductors feature an energy gap, also known as the forbidden band. The only difference between an insulator and a semiconductor is the width of this gap. It is determined by the lattice spacing of the crystal and is therefore dependent on temperature and pressure. In contrast to an insulator, where there is no excitation of electrons from valence to conduction band, even if an electric field is applied, in semiconductors due to the small band gap a small current can be observed [45]. The cooling of the semiconductor however reduces this current dramatically.

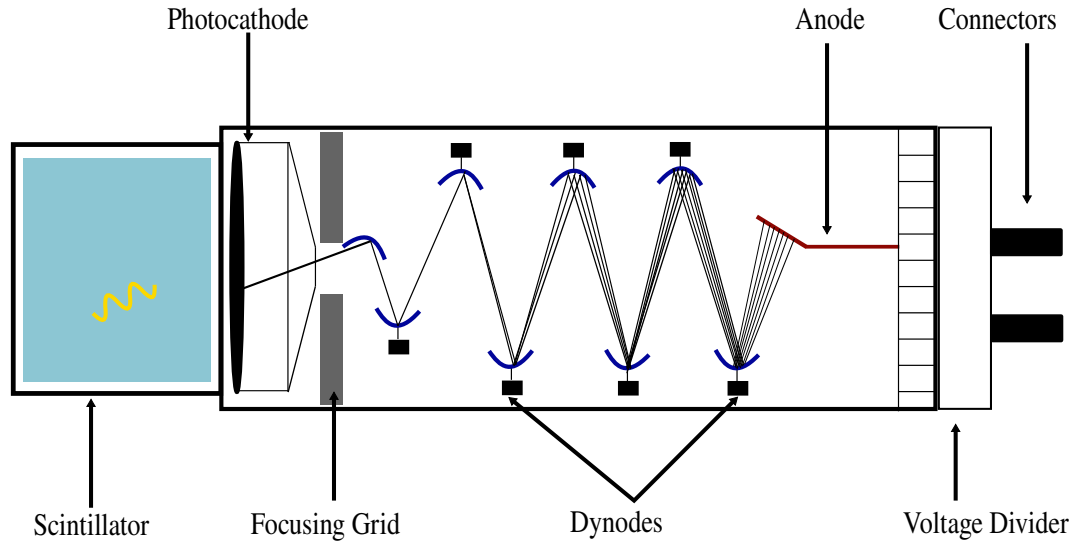


Figure 2.3.: Schematic of a scintillation detector for γ -detection.

Therefore, signal noise is reduced and only electron-hole pairs created by ionizing radiation will be detected. Since the current is very small, low noise electronics for signal amplification are needed. This is usually done by a charge-sensitive pre-amplifier.

2.4. Data acquisition systems

The signals provided by different variants of detectors have to be processed in order to achieve the information of interest. This is most commonly done by computer systems, which require the analog detector signal to be transformed into a digital signal. Widely used acquisition systems are presented hereinafter.

2.4.1. Analog data acquisition systems

The analog data acquisition system used for this work consists of a chain of different analog signal processing devices using the Nuclear Instrumentation Module (NIM)

format. For γ -spectroscopy the signal processing chain consists of a pre-amplifier, a spectroscopic amplifier and an analog-to-digital converter (ADC). In case of a semiconductor detector a charge-sensitive pre-amplifier is often used to amplify and pre-shape the small signal for the spectroscopic amplifier. The spectroscopic amplifier shapes the signal to reduce electronic noise. Also the signal can be further amplified and several other corrections, such as the elimination of cross-over or undershoots of the baseline after pulse shaping, can be applied [41, 34]. Once the signal has the designated shape required by the ADC it is converted into a digital signal after measuring the pulse amplitude. The multichannel analyzer (MCA) as the last piece of the chain is then responsible for the creation of the pulse height spectrum, which can be used for further analysis.

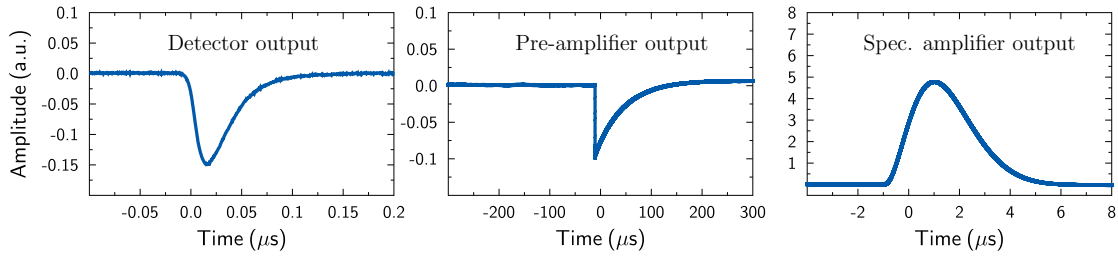


Figure 2.4.: Visualization of analog signal processing using a $\text{LaBr}_3\text{:Ce}$ scintillation detector. The output signals, from left to right, show the basic stages of an analog signal processing chain.

2.4.2. Digital data acquisition systems

The use of a digital data acquisition system is another possibility in detector signal processing. In contrast to the many different parts in an analog chain, digital signal processing systems often only consist of one part, the so called digitizer. Often featuring a flash analog to digital converter (FADC) and a field-programmable gate array (FPGA). The digitizers available are capable of combining all of the needed analog electronics on one board and may therefore be superior to analog measurement chains. One of the advantages is the form factor of these modules and the possibility to use specially designed firm- and software already during the signal detection phase.

2.5. Neutron sources and experimental techniques

Experiments to investigate neutron induced reactions, require freshly produced neutrons. These can be created by various neutron sources. Depending on the desired energy of the neutrons, different experimental techniques become available. For the determination of neutron capture cross sections in the thermal energy region at $k_B T = 0.025 \text{ eV}$, reactor experiments are favourable. For higher neutron energies accelerator-driven neutron sources become a possibility for neutron production. For experiments relying on a wide spread of neutron energies, for example at time-of-flight facilities to investigate the energy-dependent neutron capture cross section, spallation sources are used. These consist of Ion beams with high energies (several GeV) impinging on heavy tungsten or lead spallation targets. This leads to the creation of a variety of particles, including neutrons, which are subsequently collimated and guided to the sample to be irradiated.

A prominent neutron source available at lower energy accelerators (such as Van-de-Graaff accelerators) is the ${}^7\text{Li}(\text{p},\text{n}){}^7\text{Be}$ reaction, which has been proven to be a working horse for the determination of neutron capture cross sections relevant for the s-process nucleosynthesis using the activation method[58].

2.5.1. The ${}^7\text{Li}(\text{p},\text{n}){}^7\text{Be}$ reaction

The ${}^7\text{Li}(\text{p},\text{n}){}^7\text{Be}$ reaction is a compound nucleus reaction. The impinging protons react with the ${}^7\text{Li}$ and form a compound nucleus, meaning an intermediate nucleus with a lifetime longer than the passing time of the incident particle. In this reaction ${}^8\text{Be}^*$ with a lifetime of $\tau = (192 \pm 25) \times 10^{-15} \text{ s}$ [3]. While the possibility of a single nucleon-nucleon reaction exists, it is fairly small. Therefore, a large number of nucleon-nucleon collisions, where the binding energy of the incoming particle is distributed among the nucleons, take place. Upon reaching thermal equilibrium the compound nucleus state is achieved [55].



Due to the statistical distribution of the excitation energy among the nucleons, the decay of the compound nucleus is de-coupled from its creation. The information about the creation is lost and the neutron beam properties can be considered independent from the proton beam properties [10, 77].

Neutron production

The proton energy needed for neutron production, the neutron production threshold $E_{\text{thresh.}}$, can be determined using the special relativity relation, of the independence of the reference frames for scalar values. This allows the comparison between laboratory and center of mass frame.

$$(\mathbf{P}_p + \mathbf{P}_{\text{Li}})_{\text{lab}}^2 = (\mathbf{P}_{\text{Be}} + \mathbf{P}_n)_{\text{CM}}^2 \quad (2.18)$$

$$\left[\begin{pmatrix} \frac{E_p}{c} + m_p c \\ \mathbf{p}_p \end{pmatrix} + \begin{pmatrix} m_{\text{Li}} c \\ \mathbf{0} \end{pmatrix} \right]^2 = \left[\begin{pmatrix} m_{\text{Be}} c \\ \mathbf{0} \end{pmatrix} + \begin{pmatrix} m_n c \\ \mathbf{0} \end{pmatrix} \right]^2, \quad (2.19)$$

The particle momenta in the center of mass frame are $\mathbf{0}$, due to the requirement of the absence of energy left for relative motion to the center of mass. Therefore, the threshold energy is equal to the proton energy $E_p = E_{\text{thresh.}}$. Now Equation 2.18 can be written as, using the relation $\mathbf{P}^2 = m^2 c^2$:

$$m_p^2 c^2 + 2 \left(\frac{E_{\text{thresh.}}}{c} m_{\text{Li}} c + m_p m_{\text{Li}} c^2 \right) + m_{\text{Li}}^2 c^2 = (m_n c + m_{\text{Be}} c)^2$$

$$2m_{\text{Li}} E_{\text{thresh.}} + 2m_p m_{\text{Li}} c^2 + m_p^2 c^2 + m_{\text{Li}}^2 c^2 = m_n^2 c^2 + 2m_n m_{\text{Be}} c^2 + m_{\text{Be}}^2 c^2,$$

solving for $E_{\text{thresh.}}$ leads to:

$$E_{\text{thresh.}} = \frac{1}{2m_{\text{Li}}} \left[(m_n^2 + m_{\text{Be}}^2 - m_p^2 - m_{\text{Li}}^2 + 2m_n m_{\text{Be}}) c^2 \right] - m_p c^2. \quad (2.20)$$

Using the nuclear masses for each of the reaction participant taken from [74]:

$m_p = 938.786$	$\frac{\text{MeV}}{c^2}$	$m_{\text{Be}} = 6536.225$	$\frac{\text{MeV}}{c^2}$
$m_{\text{Li}} = 6535.362$	$\frac{\text{MeV}}{c^2}$	$m_n = 939.565$	$\frac{\text{MeV}}{c^2},$

the threshold energy can be determined to be

$$E_{\text{thresh.}} = 1880.631 \text{ keV}. \quad (2.21)$$

This values is in very good agreement with the experimental value determined by White *et al.* [76]

$$E_{\text{thresh. exp.}} = 1880.443 \pm 0.020 \text{ keV}. \quad (2.22)$$

2. General principles

If the proton energy exceeds approximately $E_p = 2370 \text{ keV}$, another reaction is possible. The ${}^7\text{Be}$, nucleus produced by the bombardment of lithium with protons, may be excited to the energy level $E_{7\text{mBe}} = 429.08 \text{ keV}$ [3], giving rise to a second neutron production channel in the reaction ${}^7\text{Li}(p,n){}^7\text{mBe}$. The threshold energy of this reaction can be solved via Equation 2.20 with the substitution of m_{Be} with

$$m_{\text{Be}}^{\text{iso}} = m_{\text{Be}} + E^{\text{iso}}/c^2 = 6536.654 \frac{\text{MeV}}{c^2}, \quad (2.23)$$

leading to a neutron production threshold energy of

$$E_{\text{thresh, iso}} = 2372.156 \text{ keV}. \quad (2.24)$$

2.5.2. The neutron activation method

As its name implies, the activation method is based on the irradiation of a sample with, in this case, neutrons. As a result of neutron captures on nuclei in the sample, the isotopic composition of the sample changes. If the created isotopes are radioactive, the analysis of the decay process can be utilized to determine the number of produced nuclei, which is usually done by γ -spectroscopy. Using the number of produced nuclei during the activation, the number of sample nuclei and the neutron flux, the cross section can be determined. However, this gives rise of the main limitation of the activation method, which are short (smaller than 1 s) or extremely long half-lives of the reaction products. Furthermore, the determined neutron capture cross section takes the total neutron energy distribution exposing the sample into account. For experiments with astrophysical interest, such as the s-process nucleosynthesis, the neutron spectrum should correspond to the thermal spectrum at the respective s-process site [58]. The ${}^7\text{Li}(p,n){}^7\text{Be}$ reaction is commonly used at low-energy accelerators. The necessary protons with an energy of $E_p = 1912 \text{ keV}$, about 30 keV above the neutron production threshold, create a quasi-stellar neutron spectrum with an energy dependence close to

$$\Phi_n = E \exp\left(-\frac{E}{25 \text{ keV}}\right), \quad (2.25)$$

as required to mimic the ${}^{22}\text{Ne}(\alpha,n){}^{25}\text{Mg}$ phase during the helium flashes in TP-AGB stars or the helium core burning in massive stars. The neutrons produced at this proton energy are emitted in a forward facing cone with an opening angle of $\theta \approx 120^\circ$, allowing the positioning of the sample directly onto the neutron source.

The consequence is a high neutron flux through the sample allowing the measurement of very small cross sections [58].

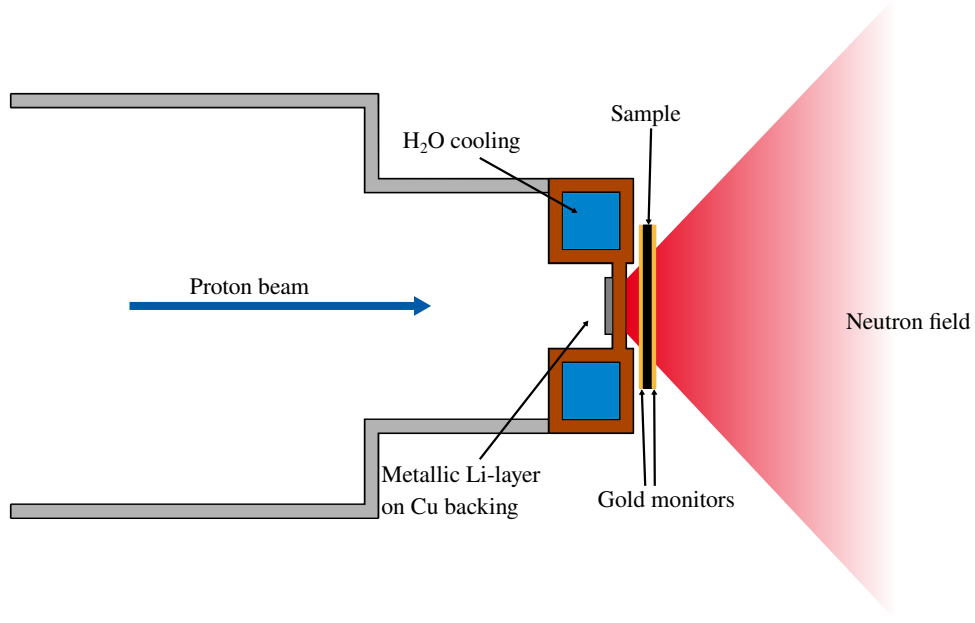


Figure 2.5.: Schematic of a typical activation setup at a low-energy accelerator featuring the ${}^7\text{Li}(p,n){}^7\text{Be}$ reaction as a neutron source at a proton energy of $E_p = 1912\text{ keV}$. The sample is placed between gold neutron monitors which will be analyzed by γ -spectroscopy to determine the produced nuclei during the activation.

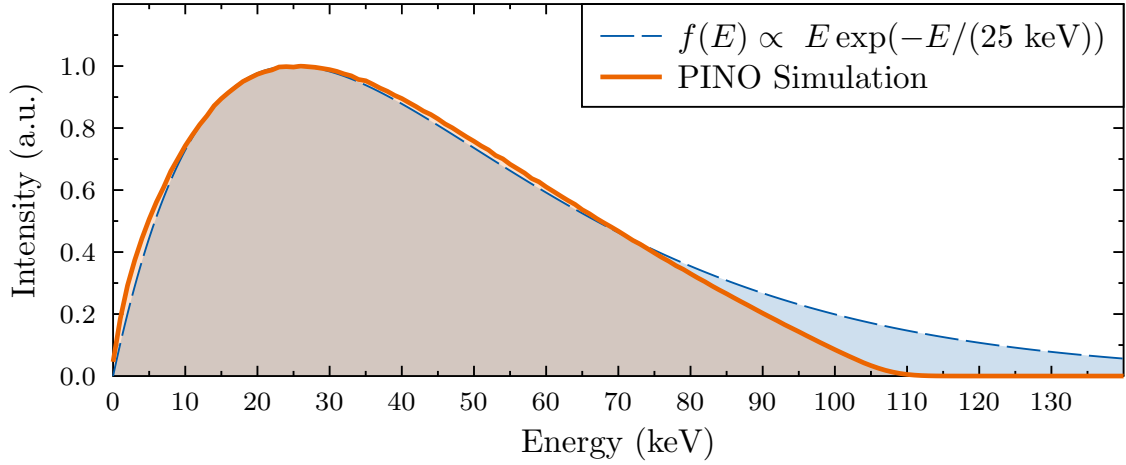


Figure 2.6.: Simulated neutron energy spectrum using the PINO tool [57]. The simulated neutron spectrum produced by the ${}^7\text{Li}(p,n){}^7\text{Be}$ reaction, at a proton energy of $E_p = 1912 \pm 2\text{ keV}$.

2.5.3. The neutron time-of-flight technique

Another method to measure the neutron capture cross section is the time-of-flight technique (ToF). The great advantage is the determination of the cross section as a function of neutron energy. The foundation of this method is the neutron production at well defined times using a pulsed beam. The determination of the neutron energy relies on the accurate knowledge of the flight path d_{flight} and the measurement of the flight time of the neutron t_{tof} . The energy of the neutron can then be determined by

$$E_n = (\gamma - 1)m_n c^2 = \left(\frac{1}{\sqrt{1 - \left(\frac{v_n}{c}\right)^2}} - 1 \right) m_n c^2, \quad (2.26)$$

using

$$v_n = \frac{d_{\text{flight}}}{t_{\text{tof}}}. \quad (2.27)$$

In most cases the relativistic effects can be neglected and Equation 2.28 can be written as

$$E_n = \frac{1}{2} m_n v_n^2. \quad (2.28)$$

The energy resolution of the neutrons recorded via the ToF method is determined by the uncertainties of the flight path and the flight time. It can be derived from Equation 2.28 and written as

$$\frac{\Delta E_n}{E_n} = 2 \sqrt{\frac{\Delta t_{\text{tof}}^2}{t_{\text{tof}}^2} + \frac{\Delta d_{\text{flight}}^2}{d_{\text{flight}}^2}}. \quad (2.29)$$

The energy resolution can be improved by increasing the flight path. This however has the disadvantage of reducing the neutron flux, which scales roughly with $1/d_{\text{flight}}^2$. Therefore, a compromise between energy resolution and neutron flux has to be found [58]. The capture cross sections during ToF experiments are usually determined using in-beam γ -spectroscopy, measuring the prompt γ -cascade emitted in the decay of the compound nucleus [58]. Additionally, the ToF method can be used to investigate neutron sources such as the ${}^7\text{Li}(p,n){}^7\text{Be}$ reaction. An example for such an investigation campaign is presented in the following.

3. Investigation of the ${}^7\text{Li}(\text{p},\text{n}){}^7\text{Be}$ neutron fields

Neutron activation experiments with non-monoenergetic neutron beams rely on the correct understanding of the neutron energy distribution of the neutron source. The preferred neutron source for these experiments with astrophysical motivation is the ${}^7\text{Li}(\text{p},\text{n}){}^7\text{Be}$ reaction, which has been investigated to a great extent [56, 31, 44]. Originally, it has only been used to mimic the ${}^{22}\text{Ne}(\alpha,\text{n}){}^{25}\text{Mg}$ phase in TP-AGB or massive stars, representing a neutron energy distribution corresponding to $k_{\text{B}}T = 25$ keV at proton energies approximately 30 keV above the reaction threshold. Recent studies by Reifarth *et al.* show a possibility to use this neutron source to recreate other energy distributions of astrophysical interest, such as $k_{\text{B}}T = 90$ keV [59]. One result of these studies is presented in Figure 3.1, where the neutron energy distribution with $k_{\text{B}}T = 90$ keV is approximated by a linear combination of different neutron spectra with the combination factors α_i . These studies rely on the PINO tool [57], which has been tested and improved over time using measurements of the neutron energy distribution at $E_{\text{p}} = 1912$ keV.

However, recent studies by Pachuau *et al.*, who compared the PINO code with measurements at proton energies of $E_{\text{p}} = 3500$ keV, show large differences between measurement and simulations [53]. In order to validate the PINO simulations at different proton energies the code needed to be tested between $E_{\text{p}} = 1880$ and 2800 keV. The following chapter describes the measurements of the neutron fields at ten different proton energies in this range using the ToF method at the PTB Ion Accelerator Facility at the PTB in Braunschweig. During the measurements the problem of an uncertainty in the true proton energy arose, the discussed proton energy values hereinafter refer to the set values of the accelerator.

3. Investigation of the ${}^7\text{Li}(p,n){}^7\text{Be}$ neutron fields

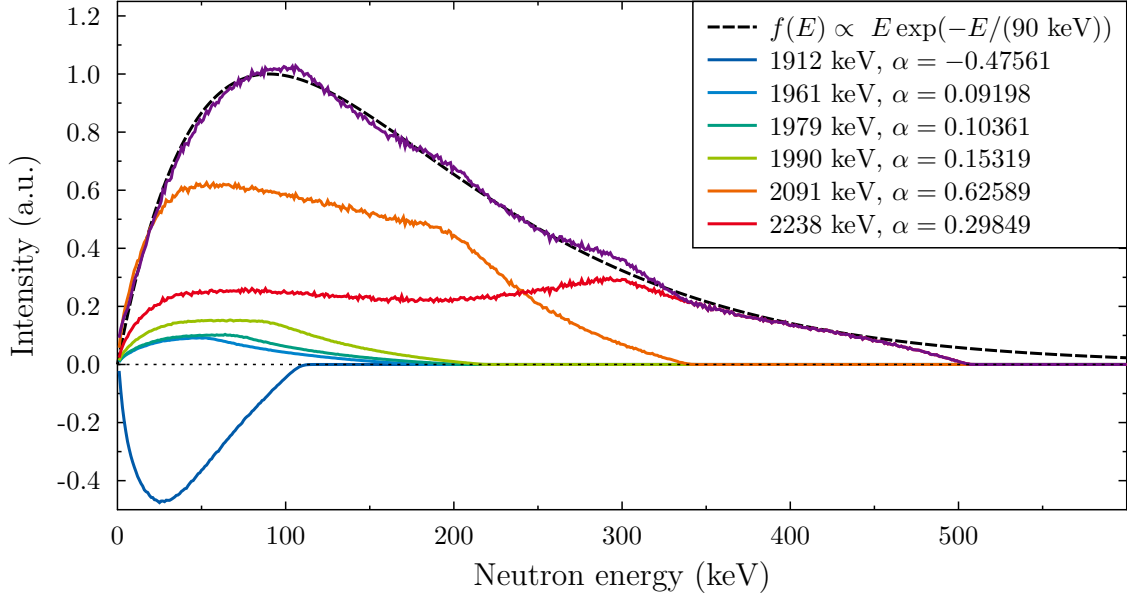


Figure 3.1.: Simulation results from PINO for the recreation of a $k_{\text{B}}T = 90 \text{ keV}$ quasi-stellar neutron spectrum using the ${}^7\text{Li}(p,n){}^7\text{Be}$ neutron source.

3.1. Experimental preparations

To determine the neutron fields of the ${}^7\text{Li}(p,n){}^7\text{Be}$ reaction, and subsequently compare these with the PINO simulation tool, neutron energy spectra need to be measured at different angular positions, preferably covering the full solid angle. For the minimization of the detection of scattered neutrons, which could be mistaken for direct neutrons of the reaction and cause a rise in background of the measured neutron spectra, the measurements were conducted at the PTB Ion Accelerator Facility (PIAF), located at the Physikalisch-Technische Bundesanstalt (PTB) in Braunschweig, Germany. The as low-scatter site classified facility, features a large open area surrounding the neutron production target and the experimental area, which reduces the influence of scattered neutrons significantly and allows to investigate different neutron sources with the utmost accuracy [61]. The properties of neutrons make a direct energy determination challenging. Therefore, the method of choice for energy resolved neutron spectra is the ToF method as described in subsection 2.5.3.

The required proton beam, for the neutron production, is delivered by a 2 MV High Voltage Engineering Europe HVEE tandem accelerator, capable of delivering proton beams with an energy $E_{\text{p}} = 0.2 - 4.0 \text{ MeV}$. The beam can either be delivered in continuous mode where a proton current of up to $50 \mu\text{A}$ is reachable or as a pulsed proton beam with a maximum repetition rate of 2.5 MHz and a nominal

pulse width of 1.5 ns [18]. During the experiment the neutron yield and the beam charge are monitored throughout the experimental area. The neutron yield is measured using three neutron monitors: A long counter neutron monitor (NM) with a central ^3He tube located at $\varphi = 16^\circ$ and distance to target $d_{\text{target}} = 6\text{ m}$, a second precision long counter (PLC) located at $\varphi = 100^\circ$ and $d_{\text{target}} = 5.5\text{ m}$ and a ^3He counter encased by polyethylene at $\varphi = 145^\circ$ and $d_{\text{target}} = 0.85\text{ m}$. The accumulated beam charge is determined using a current integrator and a frequency converter. For the angle dependent measurements of a neutron source, three movable (angle φ , and distance d) detector arms can be used. Onto these stands detectors for ToF measurements can be mounted [12].

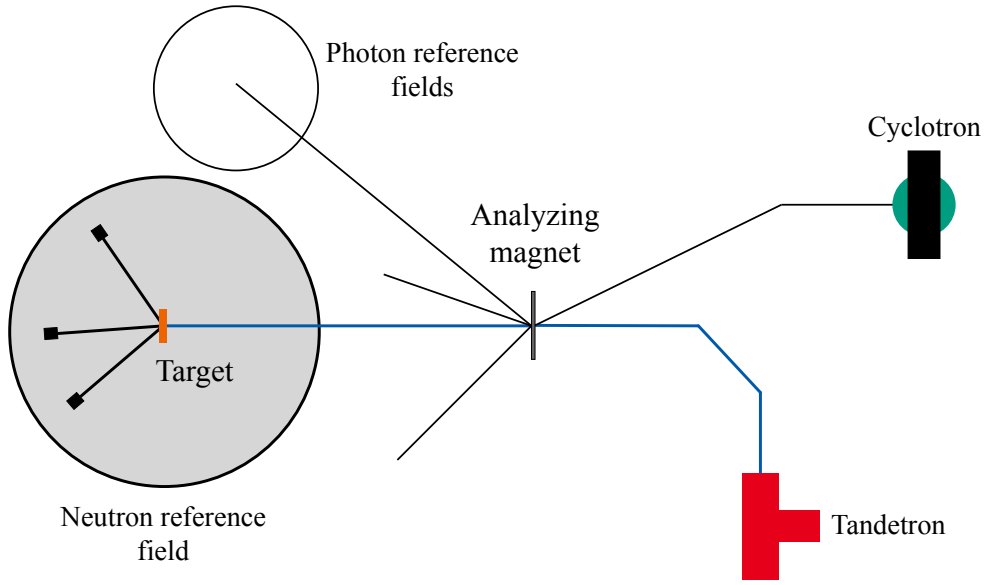


Figure 3.2.: Full schatic layout of the PTB Ion Accelerator Facility PIAF. Various different experimental sites are shown. Beamline used for the experimental campaign presented in this thesis is marked in blue. The beam was delivered by the 2 MV tandem accelerator. The proton beam energy was determined using the analyzing magnet. Following, the beam was lead to the neutron production target at the neutron reference field experimental area.

3. Investigation of the ${}^7\text{Li}(p,n){}^7\text{Be}$ neutron fields

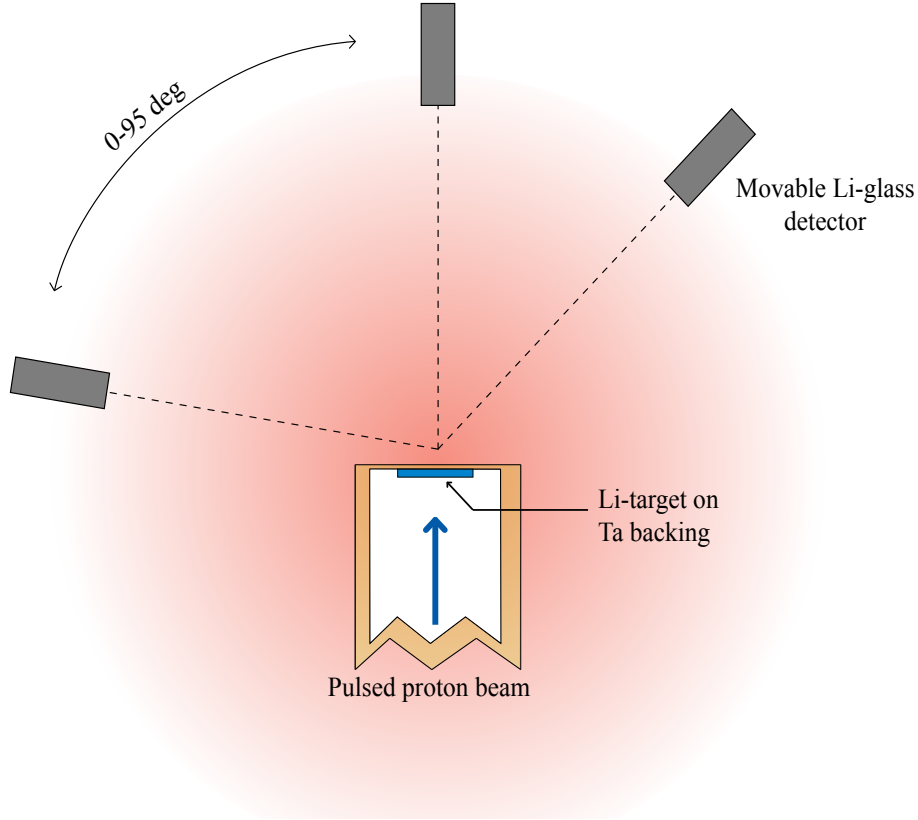


Figure 3.3.: Schematic of the experimental area for the measurement of the neutron fields. Three detectors are used, which were positioned around the neutron production target at different angles between 0° and 95° .

3.1.1. ${}^6\text{Li}$ -Glass detectors

For the neutron detection during the ToF measurements a fast detector is necessary to ensure the best possible time resolution. The detectors of choice are glass scintillators. During the experiment three similar ${}^6\text{Li}$ -glass detectors were used and are named detector I-III in the following. The specifications of the scintillation glasses can be found in Table 3.5. Detector III, including the specifications, was provided by the PIAF team at the PTB [51]. The other two detectors were assembled and tested at Goethe University Frankfurt. Both of the scintillation glasses were optically coupled to Philips XP 2020 photomultiplier tubes, featuring photocathodes matching the wavelength of the emitted scintillation light. Silicon oil was used for the optical coupling because of the similar refractive index to the face plate of the PMT. The detector assembly was finalized by wrapping the glasses with white Teflon tape, aluminum foil and black tape. The first two steps were done in order to ensure the reflection of the scintillation light into the PMT, while the black outer tape ensured



(a) XP 2020 PMT.



(b) Top view including scintillator.

Figure 3.4.: Part of the scintillation detector assembly: On the left side in figure (a) the Philips XP 2020 PMT ist shown without further wrapping. On the right side in figure (b) the ^6Li -glass disk is positioned in the middle of the PTM window. The coupling was ensured by silicon oil.

a complete shielding from light sources different than the scintillation light. This guarantees a low signal noise. Part of the assembly is presented in Figure 3.4.

The detectors were tested at Goethe University, Frankfurt. The required neutrons were produced by a 2.5 MV Van-de-Graaff accelerator with a continuous proton beam at an energy of $E_p = 1912 \text{ keV}$ impinging on a metallic lithium target, making use of the $^7\text{Li}(p,n)^7\text{Be}$ reaction. The detectors were mounted facing the target in a distance of 30 cm. The resulting pulse-height spectra are shown in Figure 3.5a and Figure 3.5b. The peak corresponding to the neutron interaction events in the detectors is clearly visible. The range of the spectra as well as the width of the neutron peak differs between the two detectors. Several possibilities for the deviations may be the reasons. One being the efficiency of the scintillator, another one being the PMT performance. Even though two similar PMTs were used, due to the old age several effects on the performance are possible. For example, a degradation of the photocathode or the dynode structures are possible, which leads to a reduced signal gain and, hence, reduced efficiency of the PMT. Apart from slight deviations in the

3. Investigation of the ${}^7\text{Li}(p,n){}^7\text{Be}$ neutron fields

pulse-height spectra the detectors performed well and were thought to be ready for the measurement of the neutron fields.

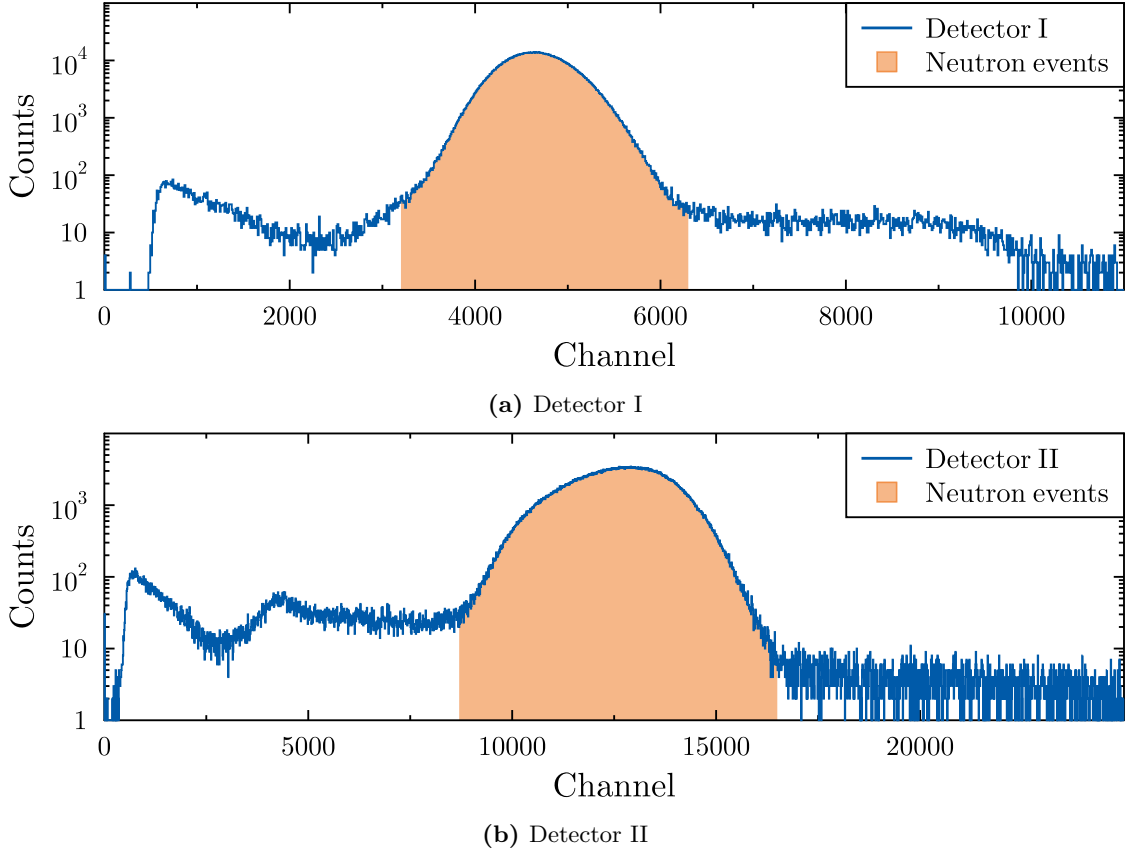


Figure 3.5.: Pulse height spectra of the assembled detectors I and II. The spectra show the response for neutrons created by the ${}^7\text{Li}(p,n){}^7\text{Be}$ reaction at a proton energy of $E_p = 1912$ keV.

3.1.2. Detector mounting

In order to use detectors I and II during the measurement of the neutron fields at the PIAF facility, the detectors had to be mounted on the spectrometer arms. To minimize the neutron induced background it is favorable to have as little material as possible inside the neutron fields and close to the detector. Since the detector arms are massive and made from stainless steel, the material of choice for the detector holder was carbon fiber-reinforced polymer (CFRP). The detector holders were designed to bring the detectors onto the same level as the neutron production target and to achieve a possible target to detector distance as close as 0.5 m.

The used construction features a base plate with a thickness of 5 mm, which ensures the detector to be as far away from the stainless steel spectrometer arms as possible. The vertical supports, with a thickness of 2 mm, were designed as truss in order to minimize the amount of material close to the detector. The construction is presented as a rendered CAD model in Figure 3.6. To ensure a safe positioning of the detector onto the detector holder, the detectors were strapped onto the vertical supports by cable ties. A final assembly on the spectrometer arm is presented in Figure 3.7.

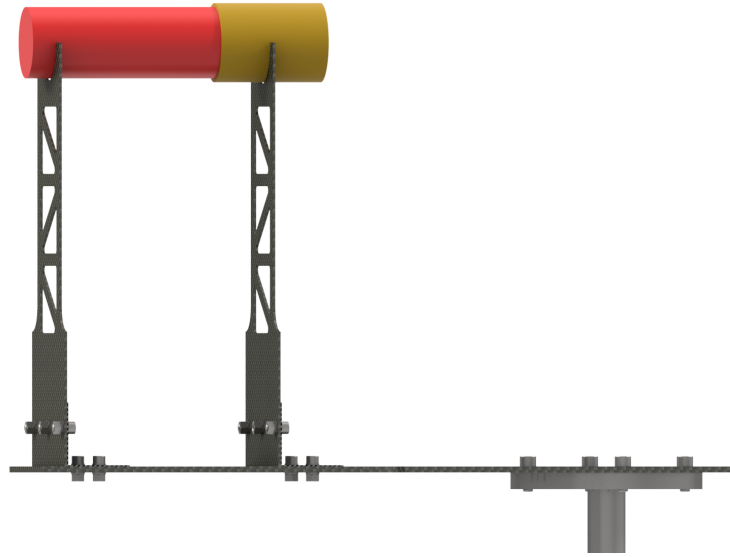


Figure 3.6.: Rendered CAD design of the neutron detector holder. The structure was optimized for minimal material to ensure a minimum neutron background.

3.1.3. Data acquisition

The data acquisition for a ToF experiment has special demands, especially using a short flight path. Typical experimental sites for neutron ToF experiments feature a flight path of several meters, ensuring a good neutron energy resolution. During the experiment at PIAF the flight path was expected to be between 0.5 and 1.5 m. Therefore, a fast data acquisition system (DAQ) was needed. The DAQ selected features a fast CAEN v1751 waveform digitizer using a pulse shape discrimination firmware, originally designed for the Frankfurter Neutronenquelle am Stern Gerlach Zentrum (FRANZ) project [4, 58]. The DAQ has been previously investigated for its use in ToF experiments with a short flight path [78].

3. Investigation of the ${}^7\text{Li}(p,n){}^7\text{Be}$ neutron fields

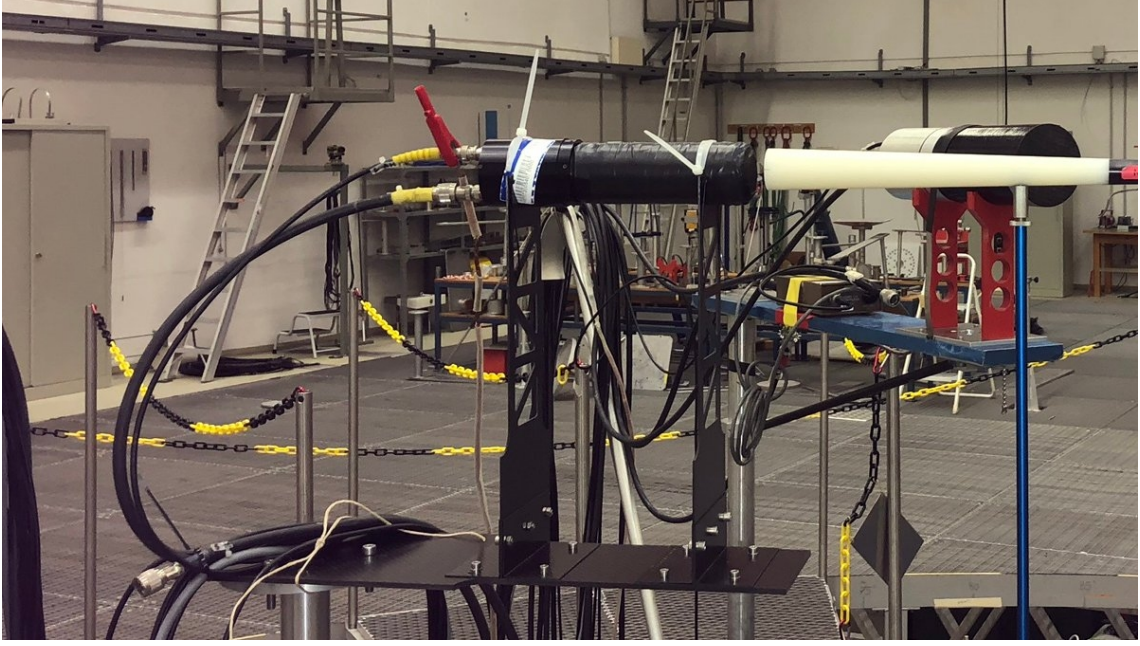


Figure 3.7.: ${}^6\text{Li}$ -glass detector mounted on the CFRP detector holder on the spectrometer arm at the PIAF facility. A shadow cone was placed in front of the detector for the measurement of scattered neutrons.

The CAEN v1715 VME module features a 8 channel 10 bit 1 GS/s flash ADC waveform digitizer with a dynamic input range of 1 V [66]. The combination of detector, digitizer and firmware can reach a time resolution of 1 ns, which makes it suitable for ToF measurements with short flight paths.

The detector signals are recorded when the signal amplitude exceeds a certain height, called the trigger. The signal can then be integrated, choosing two different integration length for pulse shape discrimination, the so called short gate and long gate. The timing information of the signal is saved the signal crosses the threshold. The software used for the data acquisition was the MIDAS framework [38]. Together with the digitizer these two parts ensured a smooth data acquisition with a maximum possible data rate of 80 MB/s. A schematic of the signal processing is presented in Figure 3.8.

Data acquisition at PIAF

For the determination of the neutron time of flight, the energy and timing signals of three ${}^6\text{Li}$ -glass detectors, as well as the signals of the proton bunch (called pickup) needed to be recorded. Due to the high repetition rate of the pickup signal (up to 2.5 MHz) a coincidence circuit was used to minimize the data output.

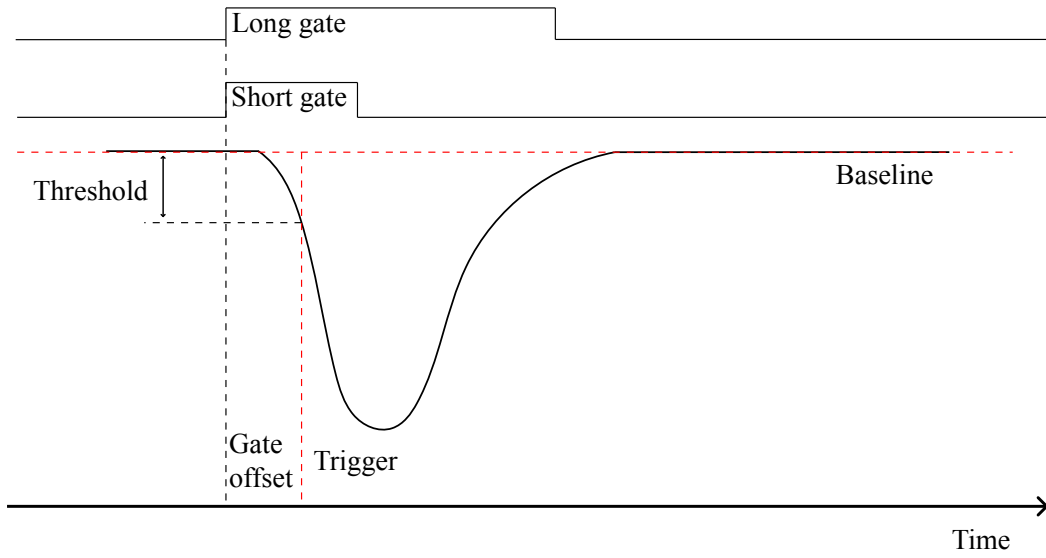


Figure 3.8.: Simplified schematic of the signal processing using a CAEN v1751 digitizer and the DPP-PSD firmware. Based on [66].

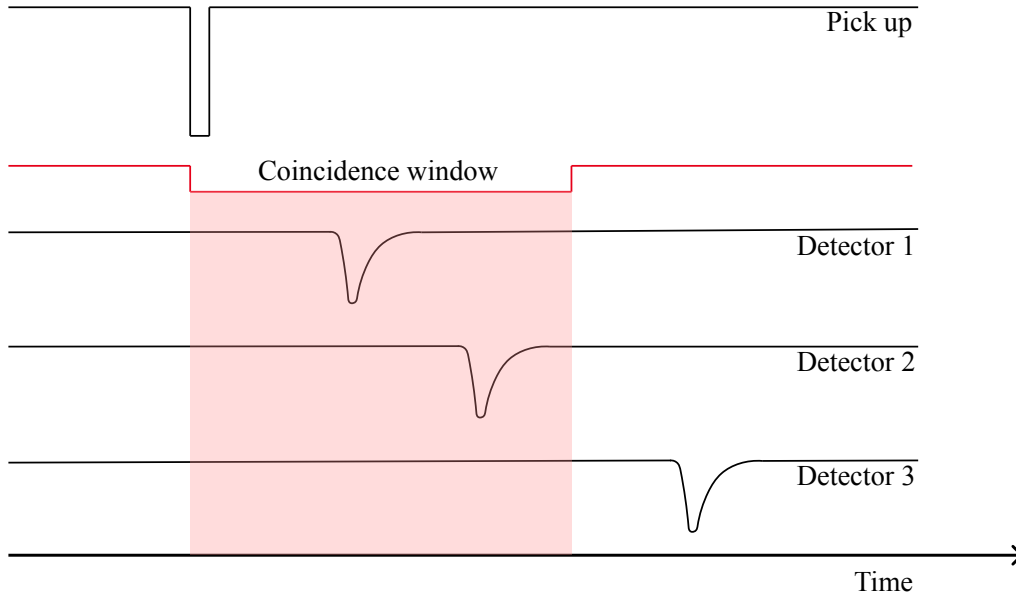


Figure 3.9.: Simplified schematic of the used coincidence logic during the measurement of the neutron fields using the pick up signal as main signal and the signals of the three ^6Li -glass detectors. Signals are only recorded if in the set coincidence window.

3. Investigation of the ${}^7\text{Li}(p,n){}^7\text{Be}$ neutron fields

The logic of the coincidence circuit is presented in Figure 3.9. The accelerator pickup signal creates a coincidence window. The length of the window was determined using the expected flight times of the neutrons and the pickup frequency. If during the coincidence windows of time $t_{\text{coinc.}}$ at least one signal from another signal channel is detected, the signals are recorded. This ensured a high count rate, only considering events of interest and discarding random events. Using this method the number of random coincidences was kept at a minimum and therefore the background in the spectra was improved.

In order to monitor the neutron flux throughout the experiment and, hence, monitor the target behavior, the neutron yield was constantly recorded by a data acquisition system of the PTB staff. For the subsequent normalization of the ToF spectra, the accumulated beam charge during each run was also recorded using a current integrator.

3.2. ${}^7\text{Li}(p,n){}^7\text{Be}$ neutron fields - Experiment

The neutron fields of the ${}^7\text{Li}(p,n){}^7\text{Be}$ reaction were measured using three ${}^6\text{Li}$ -glass detectors. Detectors I and II were mounted on the previously described carbon fiber detector holders onto the spectrometer arms. Detector III, which was provided by the PTB, was mounted using a poly-ethylene holder onto the center spectrometer arm. ToF spectra were acquired by moving two detectors between 27° and 95° and one detector between 0° and 25° degrees in steps of 5° . To detect differences in flight path or performance, spectra were additionally acquired for detectors at the same position. Detector I and II were compared positioned at $\varphi = 27^\circ$ and detector II and III at $\varphi = 15^\circ$. The flight path d_{flight} was selected to be 0.7 m, as a compromise between energy resolution and sufficient statistics. The distance between the detectors and the target was determined by a laser measurement system, which has an uncertainty of 1 mm. The angles of the spectrometer arms were set using a computer based angle positioning system. With this system it was also possible to adjust the flight path once correctly calibrated. Once calibrated, the flight path was checked prior to each new proton energy setting.

For the duration of the experimental campaign two neutron production targets were prepared by the PTB staff. The metallic lithium used as target material was evaporated onto a 0.5 mm thick tantalum backing. Following the evaporation process the target was mounted onto the beamline. This was done without breaking the vacuum, ensuring no oxidation of the lithium layer. To cool the target during the irradiation, a jet of compressed air was used. Additionally, the target was rotated with a speed of 1 rotation per second to maximize the cooling. The lithium targets, named RLi0319 and RLi0411, with an area density of $\tau_{\text{target 1}} = 260 \mu\text{g}/\text{cm}^2$ and $\tau_{\text{target 2}} = 276 \mu\text{g}/\text{cm}^2$ were each used for half of the duration of the measurement to ensure a stable neutron yield.

3. Investigation of the ${}^7\text{Li}(p,n){}^7\text{Be}$ neutron fields

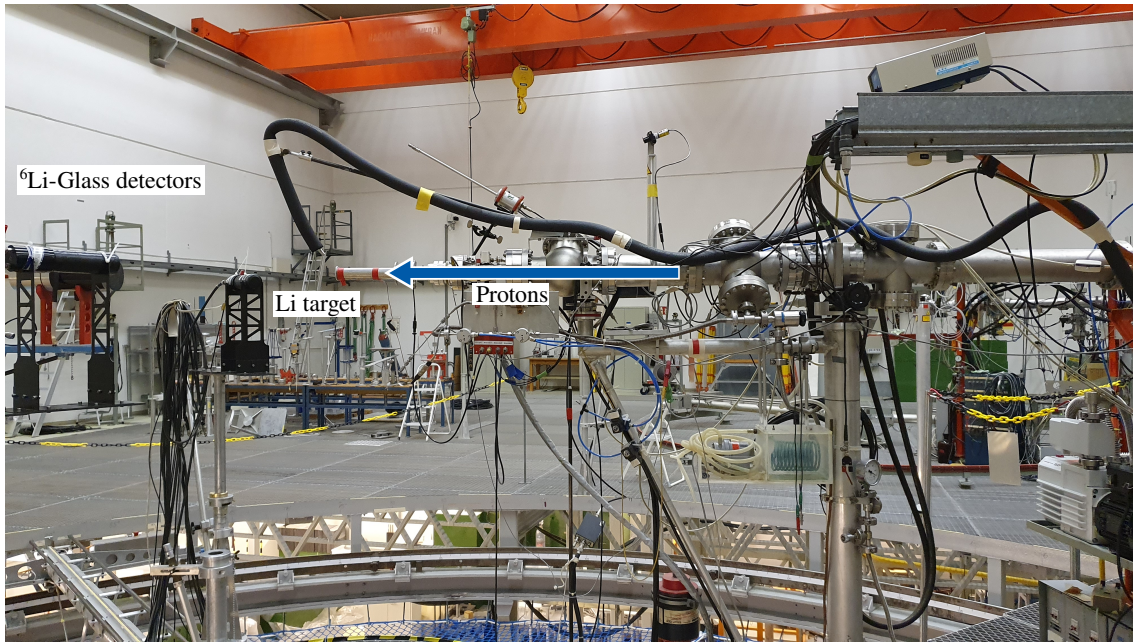


Figure 3.10.: Experimental setup: In the center the lithium target cooled by an air jet is visible. On the left edge of the picture two ${}^6\text{Li}$ -glass detectors mounted onto the carbon fiber detector holders can be seen.

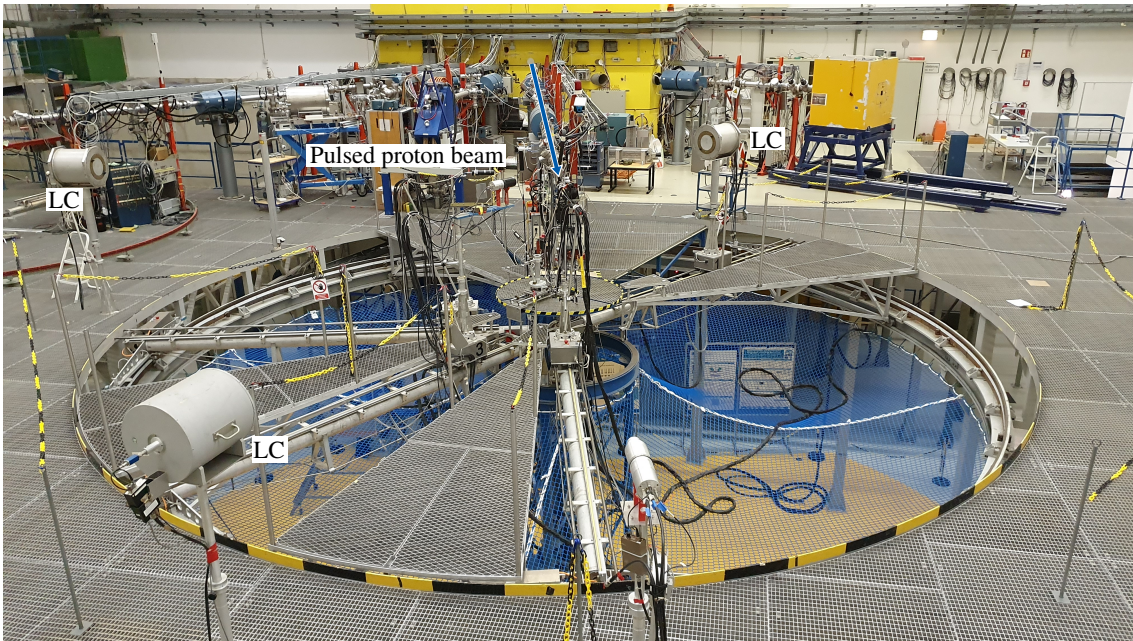


Figure 3.11.: Experimental area: Marked in the center is the proton beam line with the lithium target mounted. Surrounding the open pitch to minimize the effects of scattered neutrons. Three static neutron monitors are marked, which are responsible for monitoring the neutron yield during the irradiations.

E_p (keV)	Target	Frequency (kHz)	Detector I	Angle (deg)	Detector III
1887	RLi0411	312.5, 625	27, 50	27, 25, 20, 15	0, 5, 10, 15
1897	RLi0411	312.5	27, 35, 45, 40, 50	27, 30, 40, 25, 20, 15	0, 5, 10, 15
1907	RLi0411	625	27, 35, 45, 55, 65, 60	27, 30, 40, 50, 60, 25, 20, 15, 0	0, 5, 10, 15, 30
1912	RLi0319	1250, 625, 312.5	27, 35, 45, 55, 65	27, 30, 40, 50, 60, 0, 5, 10, 15	0, 27, 25, 20, 15
2000	RLi0411	1250	27, 35, 45, 55, 65, 75, 85, 95	27, 30, 40, 50, 60, 70, 80, 90, 25, 20, 15	0, 15, 5, 10
2100	RLi0319	1250	27, 35, 45, 55, 65, 75, 85, 95	27, 30, 40, 50, 60, 70, 80, 90, 25, 20, 15	0, 5, 10, 15
2200	RLi0411	1250	27, 30, 50, 70, 90, 50	27, 40, 60, 80, 15	0, 15, 20
2300	RLi0319	1250	27, 35, 45, 55, 65, 75, 85, 95	27, 30, 40, 50, 60, 25, 20, 15, 0	0, 5, 10, 15
2500	RLi0319	1250	27, 35, 45, 55, 65, 75, 85, 95	27, 30, 40, 50, 60, 25, 20, 15, 0	0, 5, 10, 15
2800	RLi0411	1250	27, 35, 45, 55, 65, 75, 85, 95	27, 30, 40, 50, 60, 25, 20, 15, 0	0, 5, 10, 15

Table 3.1.: Proton energy settings, targets, accelerator frequencies and angle settings for the detectors used during the experimental campaign.

3.2.1. Accelerator time resolution

The time resolution of the accelerator is defined by the length of the proton bunches on the neutron production target. To reach the best possible time resolution during the ToF measurements the pulsation mechanism of the accelerator needed to be tuned following each new proton energy and accelerator settings. The bunch length was determined recording a ToF spectrum with a BaF_2 scintillation detector. Even though this detector is not sensitive for neutrons, they are capable of detecting γ -rays with a superior time resolution than ${}^6\text{Li}$ -glass detectors. The resulting ToF spectrum only shows the γ -flash, which is a result of the protons impinging on the lithium target creating high energy γ -rays covering the source to detector distance with the speed of light. Using the BaF_2 detector, the sub-nanosecond time resolution allows the accurate determination of the width of the γ -flash. A typical γ -spectrum of the time resolution measurement is presented in Figure 3.12. The sharp peak was analyzed using a Gaussian fit. The determined FWHM depicts the bunch length and therefore the accelerator time resolution. The recorded γ -flash spectra, for each investigation run, are shown in Figure 3.13 and the corresponding accelerator time resolutions are listed in Table 3.2.

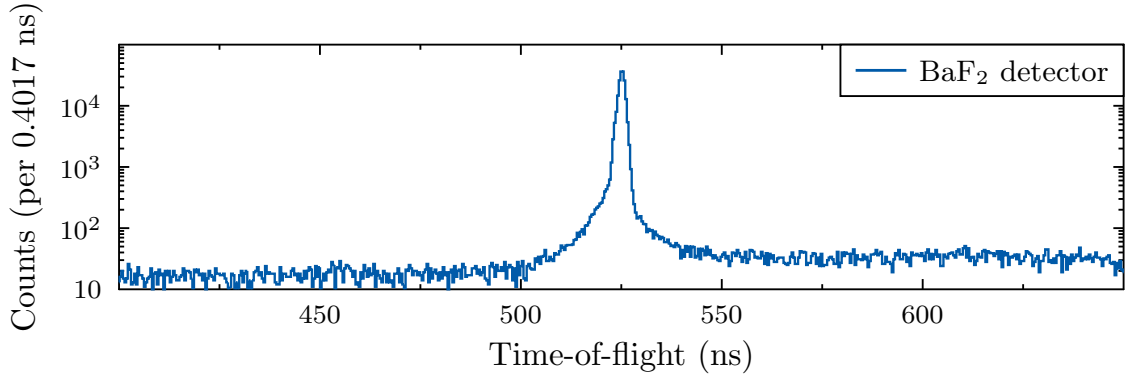


Figure 3.12.: Time-of-flight spectrum recorded using a BaF_2 detector at a proton energy of $E_p = 1912(1)$ keV. Only a single peak is visible in the spectrum, the γ -flash.

3.2.2. Total time resolution

The total time resolution $t_{\text{res. tot.}}$ is defined as the combined time resolution of the used components during the measurements. Each element of the measurement chain contributes to the total time resolution, which can be determined during the ToF measurements using the ${}^6\text{Li}$ -glass detectors. Due to the minor differences of the detectors, it has to be determined separately for each detector. The procedure to

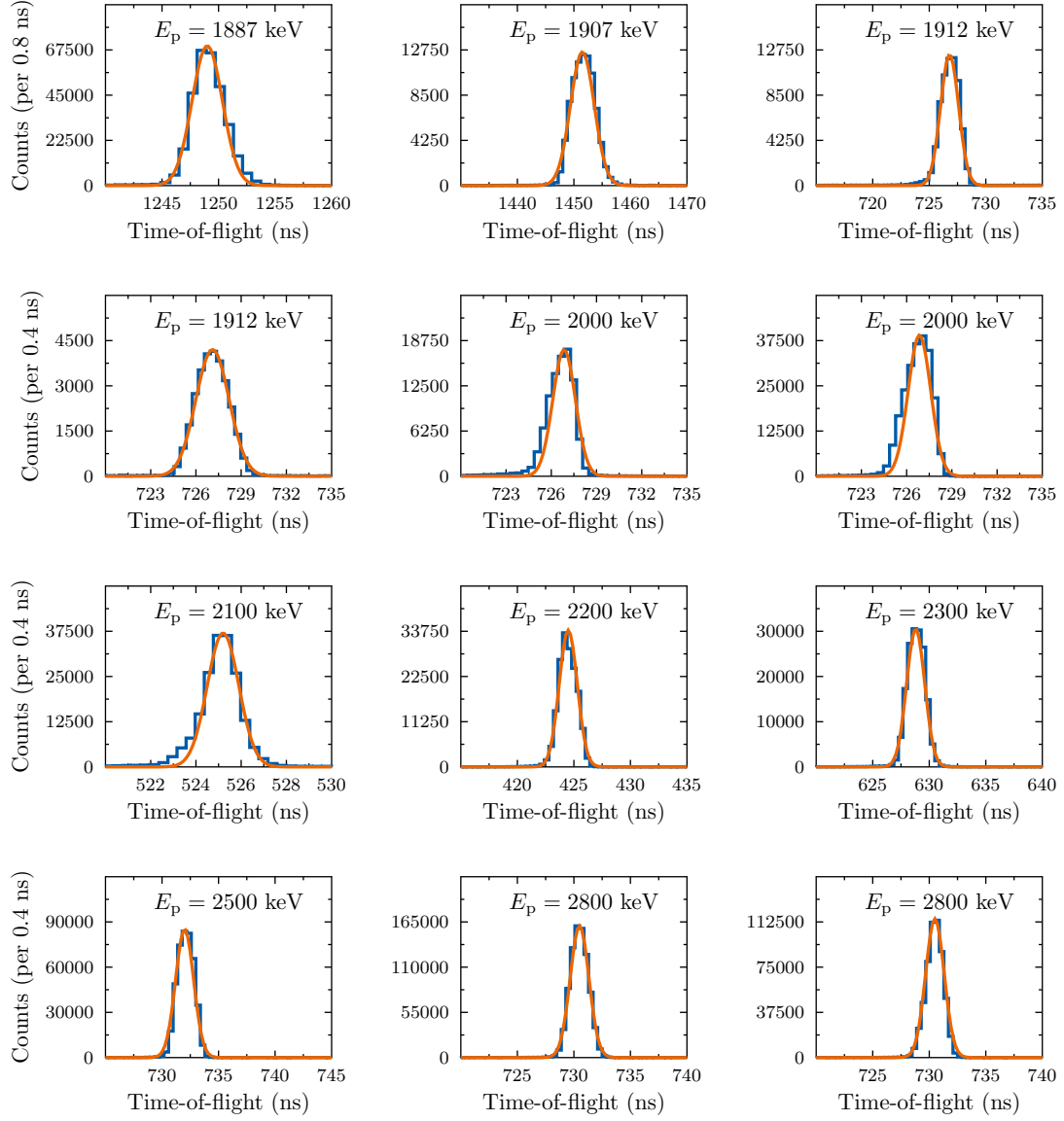


Figure 3.13.: Measurements for the accelerator time resolution. The blue line denotes the spectra measured using a BaF_2 detector, while the orange line is the Gaussian fit of the γ -flash. The FWHM denotes the time resolution of the accelerator.

3. Investigation of the ${}^7\text{Li}(p,n){}^7\text{Be}$ neutron fields

Day	E_p (keV)	Target	$t_{\text{res. acc.}}$ (ns)
1	2100	RLi0319	1.812(3)
2	2300	RLi0319	1.765(3)
2	2500	RLi0391	1.633(2)
3	2500	RLi0319	1.597(3)
4	1912	RLi0319	1.804(1)
5	1912	RLi0319	2.423(1)
6	1887, 1897	RLi0411	1.698(1)
7	1907	RLi0411	2.318(1)
7	2000	RLi0411	1.847(1)
8	2000	RLi0411	1.891(3)
8	2800	RLi0411	1.816(1)
9	2800	RLi0411	1.734(2)
9	2200	RLi0411	1.809(3)

Table 3.2.: Accelerator time resolutions measured using the BaF₂ detector.

determine the total time resolution is equal the determination of the accelerator time resolution presented in subsection 3.2.1. The FWHM of the γ -flash, visible in the measured ToF spectra, was obtained using a Gaussian fit with the ROOT analysis environment [17]. An excerpt from the analysis is shown in Figure 3.14. The values obtained are presented in Table 3.3. Additionally, the time resolution is also an important input parameter for the comparison between measured and simulated neutron spectra using the PINO tool, which are presented in section 3.5.

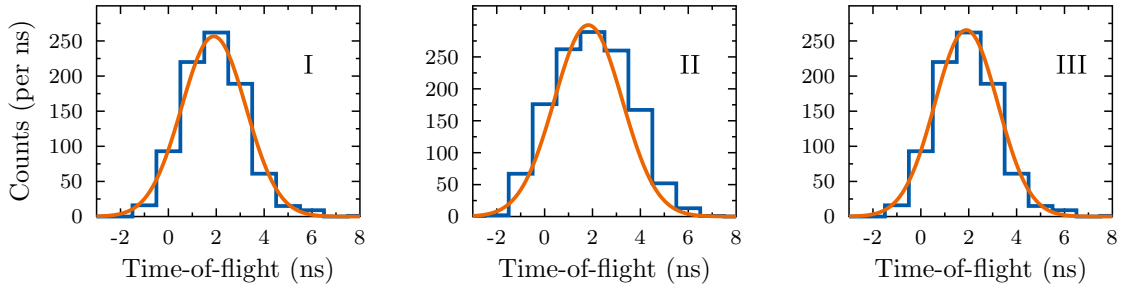


Figure 3.14.: Total time resolution for each ${}^6\text{Li}$ -glass detector during the measurement of the neutron fields at a proton energy of $E_p = 1912\text{ keV}$. The blue lines denotes the measurement, the orange line the Gaussian fit of the γ -flash.

3.2.3. Neutron yield

During the measurements, the neutron yield was monitored using the monitors described in section 3.1. It gives important insights in the lithium target behavior. A drastic decline in the neutron yield while the beam current remains stable, would indicate a rapid decrease in target quality. This becomes especially important when

E_p (keV)	Time resolution (ns)		
	Detector I	Detector II	Detector III
1887	2.28(10)	2.42(5)	2.41(9)
1897	2.91(10)	3.10(6)	2.75(11)
1907	3.38(5)	3.25(5)	3.23(6)
1912	3.33(5)	3.09(4)	3.08(7)
2000	4.06(3)	3.67(2)	3.92(3)
2100	4.56(7)	4.06(5)	3.75(8)
2200	3.32(5)	3.30(4)	3.24(5)
2300	3.04(4)	2.86(4)	2.98(5)
2500	3.15(7)	3.00(6)	2.95(4)
2800	3.22(4)	3.15(4)	3.04(5)

Table 3.3.: Total time resolution of the system determined using ${}^6\text{Li}$ -glass detectors positioned at $\varphi = 0^\circ$.

using high proton energies, where the protons are not decelerated below the neutron production threshold in the lithium layer. Considering the stopping power of protons in lithium, which is shown in Figure 3.15, the impinging protons with the energies used in this experiment are not fully stopped but only slowed down. Since the target is fairly thin, the protons do not lose a sufficient amount of energy depending on the penetration depth. For example, at a set proton energy of $E_p = 1912\text{ keV}$, the protons are slowed down in approximately $5.5\mu\text{m}$ to energies below the neutron production threshold. The analysis of the long counters did not give any hints of severe target degradation during the measurements, as presented in Figure 3.16. However, reference runs at a specific energy before each energy change would have given more insights in the target behavior over the entire beam time.

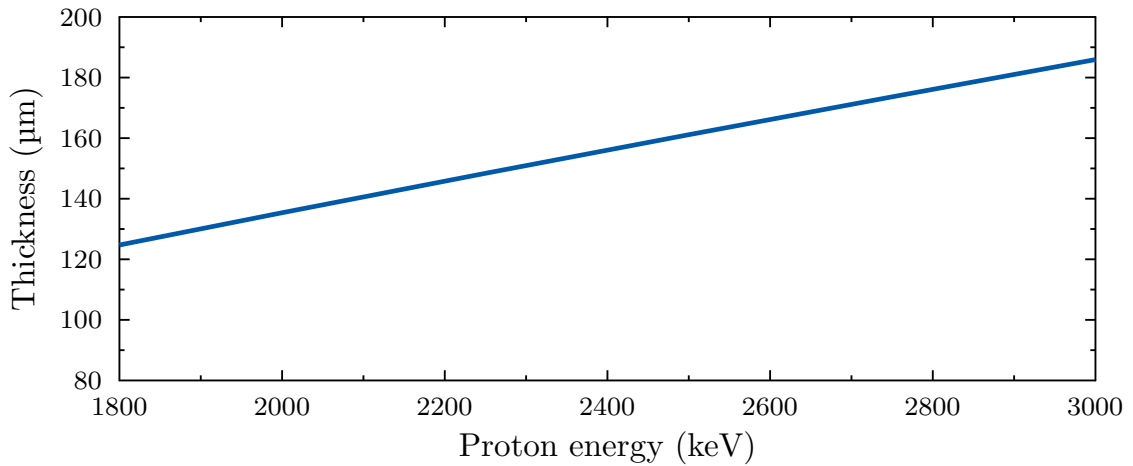


Figure 3.15.: Stopping power of protons in lithium. The data presented are taken from the SRIM simulation tool [79].

3. Investigation of the ${}^7\text{Li}(p,n){}^7\text{Be}$ neutron fields

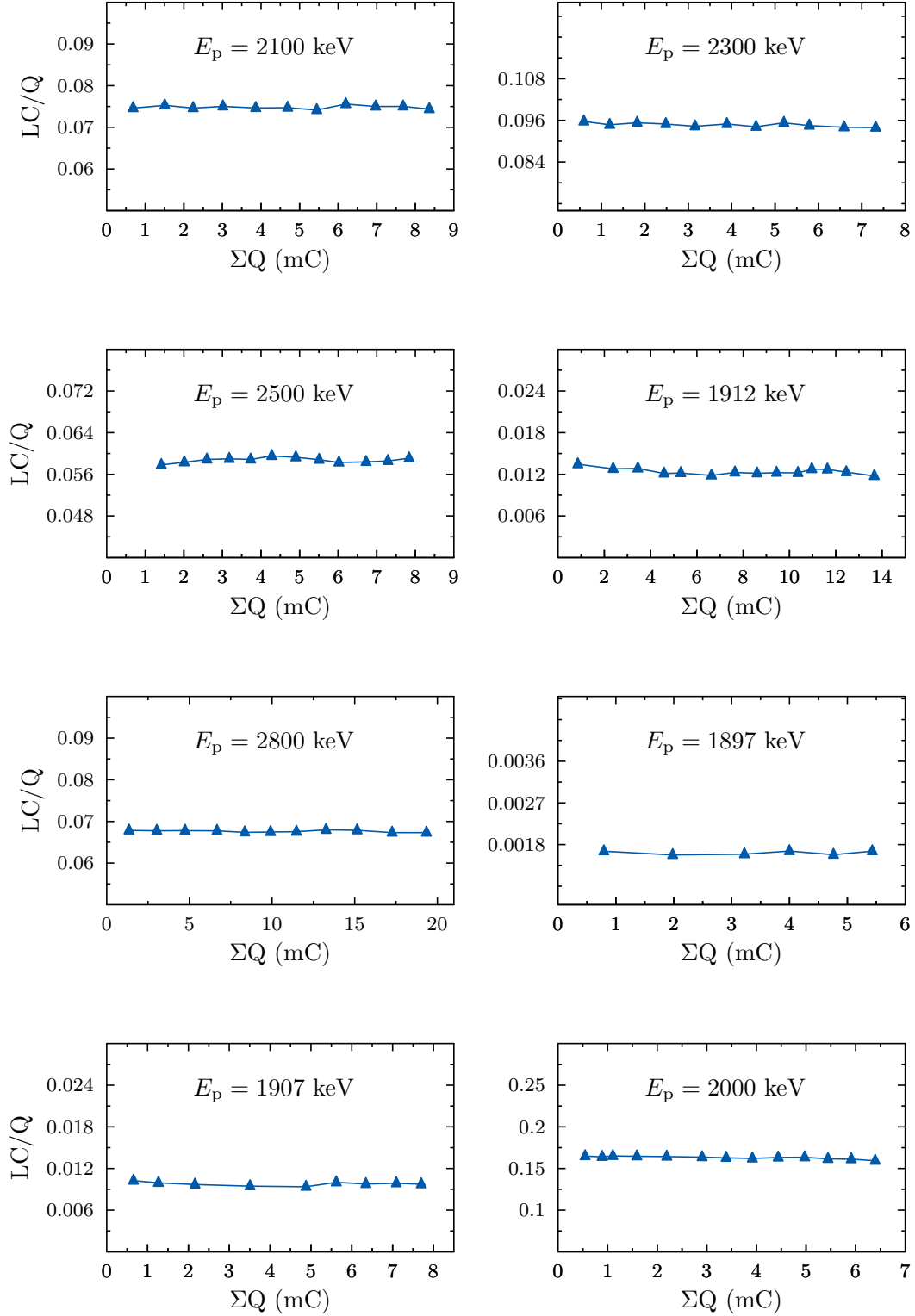


Figure 3.16.: Long counter readings per charge vs. the total accumulated beam charge on target during the measurements at different proton energies. No significant target degradation during the runs could be observed.

3.3. Time-of-flight analysis

Time-of-flight measurements were performed with the described setup at the energies and angles described in Table 3.1. The ToF data was acquired using the CAEN v1751 digitizer. Each recorded event gives information about the signal origin (channel), the time-stamp, the short gate and the long gate. The channel number denotes the associated input channel, the time-stamp the time the signal crossed the threshold, the short integration and the long integration of the signal. The signal processing is presented in Figure 3.8. For the analysis the short gate information was neglected, since no pulse-shape discrimination technique was possible using the ^6Li -glass detectors during the measurements. To transform the raw data into ToF spectra, the events needed to be sorted by event and time first. Due to the applied coincidence logic, only signals from the detectors during the coincidence window were recorded. The flight time of the neutrons was determined by subtracting the initial time at the pickup from the stopping time at the detector. The analysis was carried out using the software framework ROOT. In this section an overview of the acquired data and the data processing is given for selected proton energies of $E_p = 1907, 2100$ and 2500 keV. The procedure for analysis remains equal for all measurements.

To investigate the correct detection and performance of the used ^6Li -glass detectors, the pulse height spectra as shown in Figures 3.17a - 3.17c were reviewed. They show a clean peak corresponding to the neutron events for every detector. The width of the neutron peak becomes important when generating the ToF spectra. To enclose mostly neutron induced events, areas outside the regions of interest were discarded. This improves the signal to noise ratio dramatically. As presented in Figure 3.17a, detector I shows a shift in the neutron peak with increasing angular position. This is thought to be a gain shift of the detector, however another possibility is the effect of different neutron energies at different angles. Since the other detectors do not show this behavior at a proton energy of $E_p = 1907$ keV to an equal extend, detector I was investigated further. As presented in Figure 3.18 this behavior was also observed at different proton energies. At set proton energies above 2 MeV the two remaining detectors II and III show a similar behavior. Therefore, it is thought to be the result of a rate induced gain shift effect or since the efficiency of the detector varies with neutron energy, the seen shift is the result of the detector efficiency.

3. Investigation of the ${}^7\text{Li}(p,n){}^7\text{Be}$ neutron fields

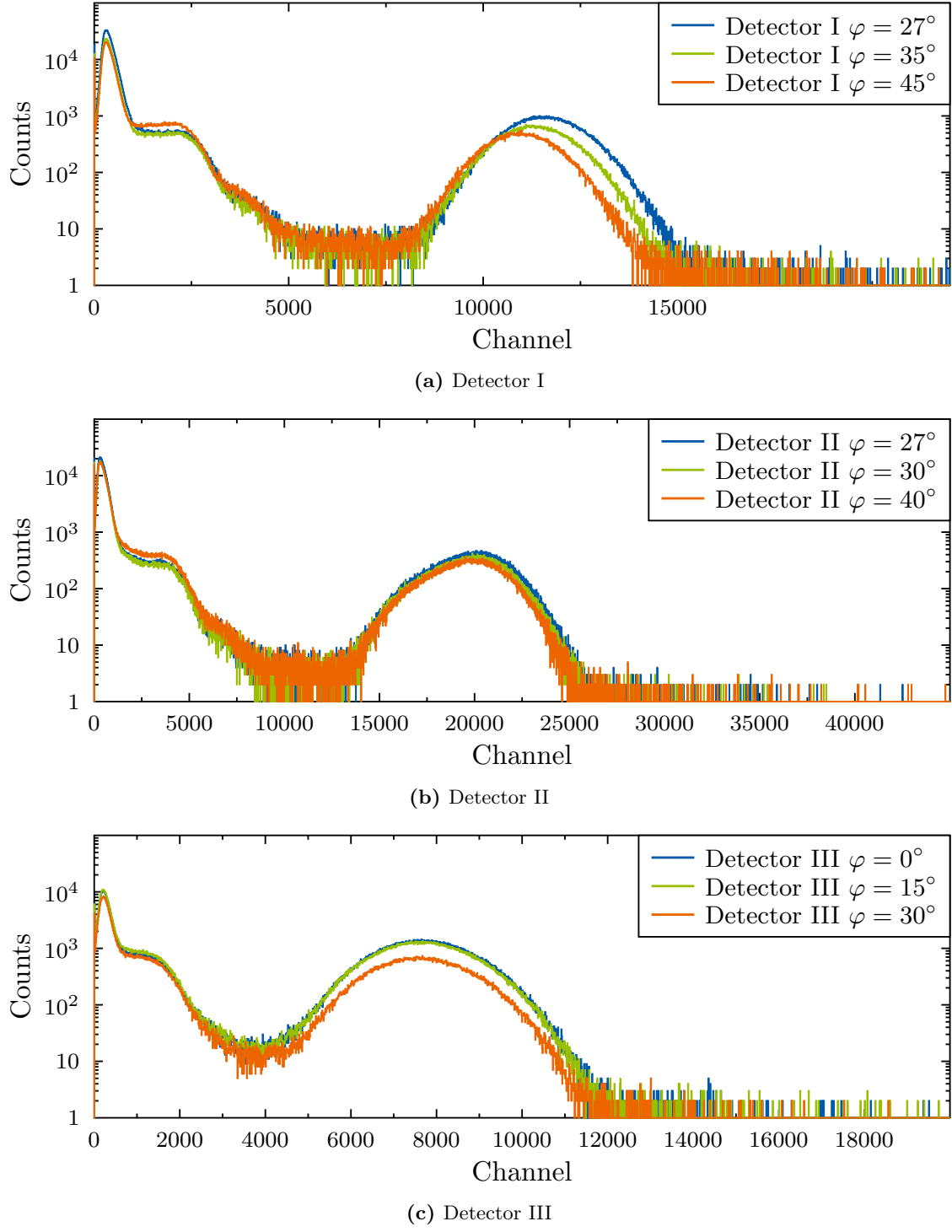


Figure 3.17.: Pulse height spectra for detectors I - III at a selected proton energy of $E_p = 1907$ keV at different angles.

For the creation of the ToF spectra only the neutron events are of interest. ToF spectra obtained using the timing and long gate information of the events are presented in Figures 3.19a - 3.19c. In the ToF spectra the effects of the kinematic collimation become clearly visible. The neutron energies decreases with larger angular position of the detector, which is visible as an increase in flight time. This can also be observed in Figure 3.19b and Figure 3.19c.

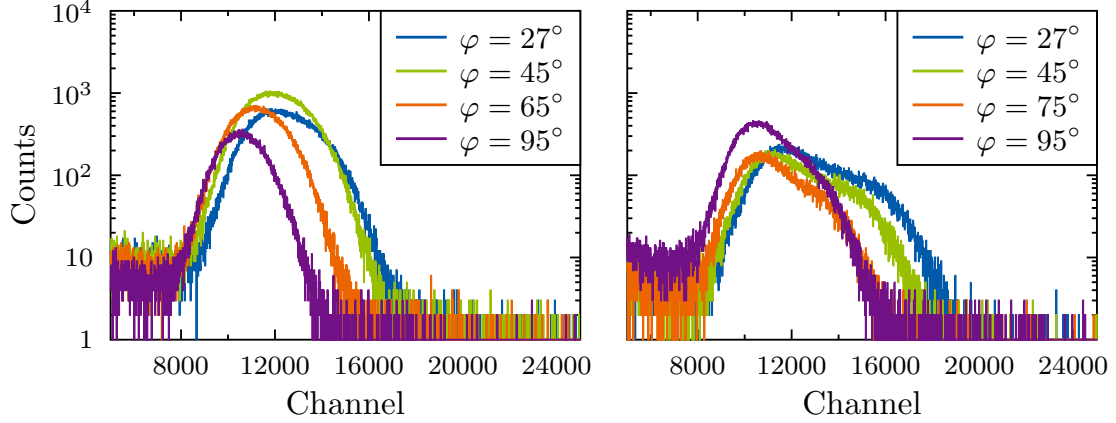
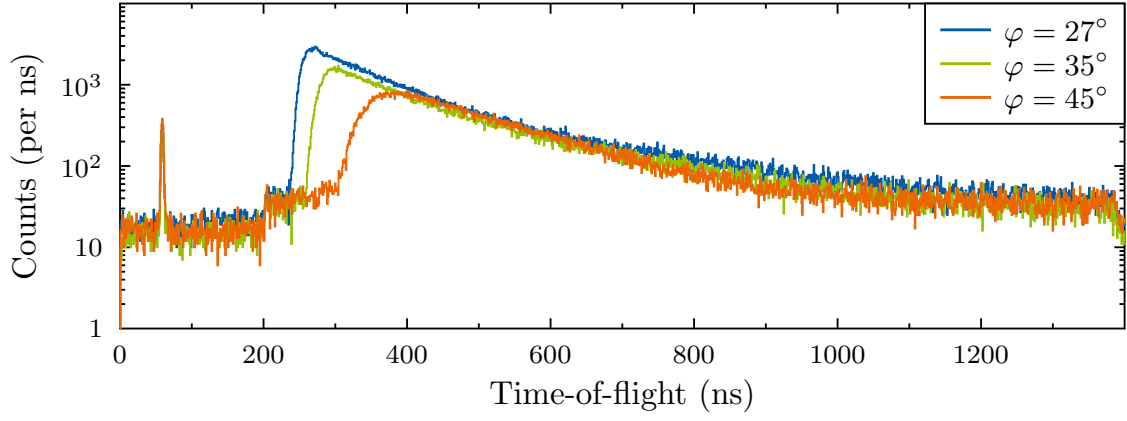


Figure 3.18.: Pulse height spectra for detector I at $E_p = 2100$ keV (left) and $E_p = 2500$ keV (right) at different angles.

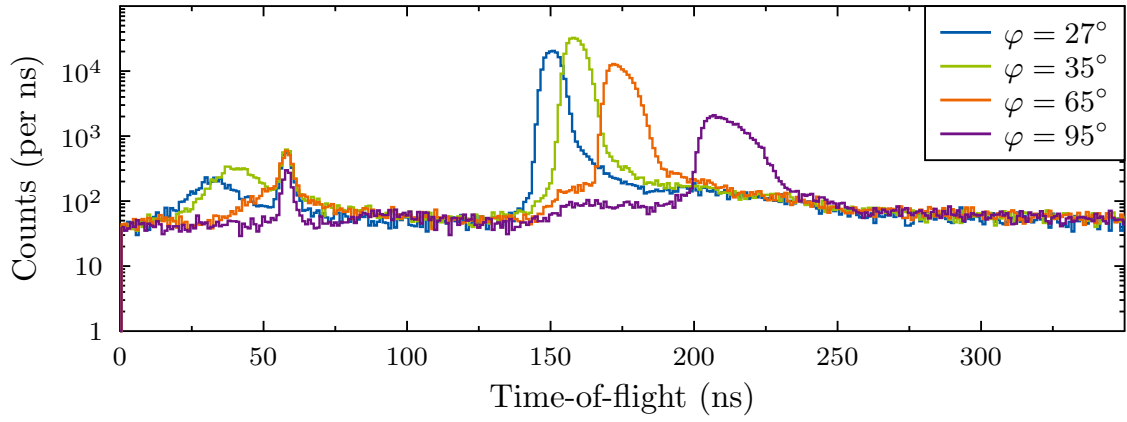
At a proton energy of $E_p = 2500$ keV the second neutron production channel, described in subsection 2.5.1, becomes available and is visible in the spectrum in form of a second neutron energy distribution. In Figure 3.19b, at a proton energy of $E_p = 2100$ keV, an additional peak structure in front of the γ -flash is noticeable. Following an inspection of the ToF spectra and the accelerator beamline, the origin of this structure was an fault of the pulsing mechanism of the accelerator causing the proton beam to interfere with the beamline. This resulted in the production of bremsstrahlung, which became visible as a second γ -flash.

In Figure 3.19a the centroid of the γ -flash lies at approximately 60 ns. The expected centroid of the peak, considering the speed of light and the flight-path of 0.7 m, is expected to be at 2.3 ns. The shift can also be observed in ToF spectra at different proton energies and using different detectors. This is caused by the different cable lengths of the respective detectors. The ToF data were corrected by shifting the γ -flash to the expected position.

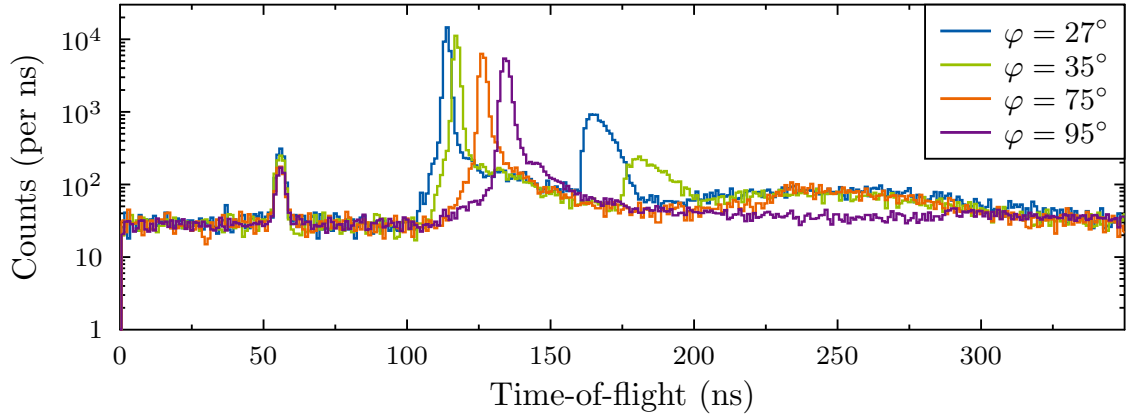
3. Investigation of the ${}^7\text{Li}(p,n){}^7\text{Be}$ neutron fields



(a) $E_p = 1907$ keV



(b) $E_p = 2100$ keV



(c) $E_p = 2500$ keV

Figure 3.19.: ToF spectra measured by detector I at set proton energies of (a) 1907 keV, (b) 2100 keV and (c) 2500 keV.

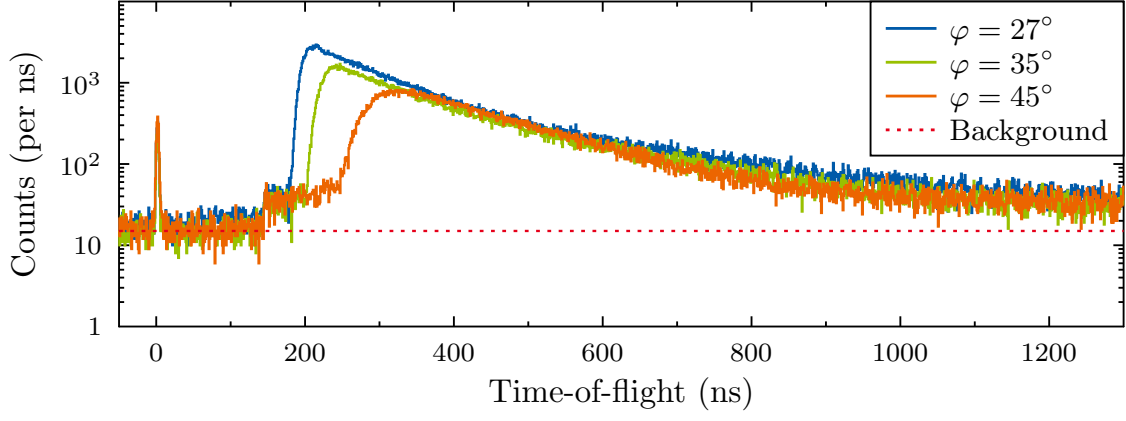
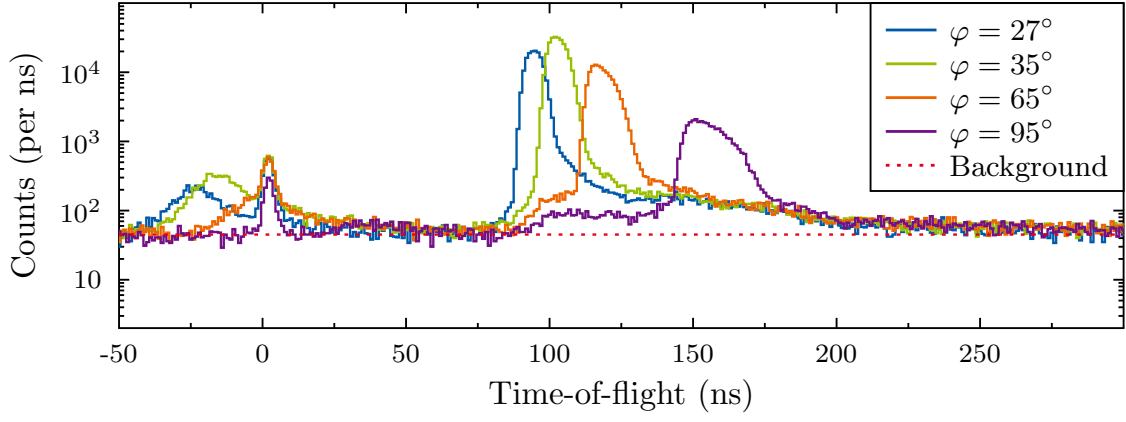
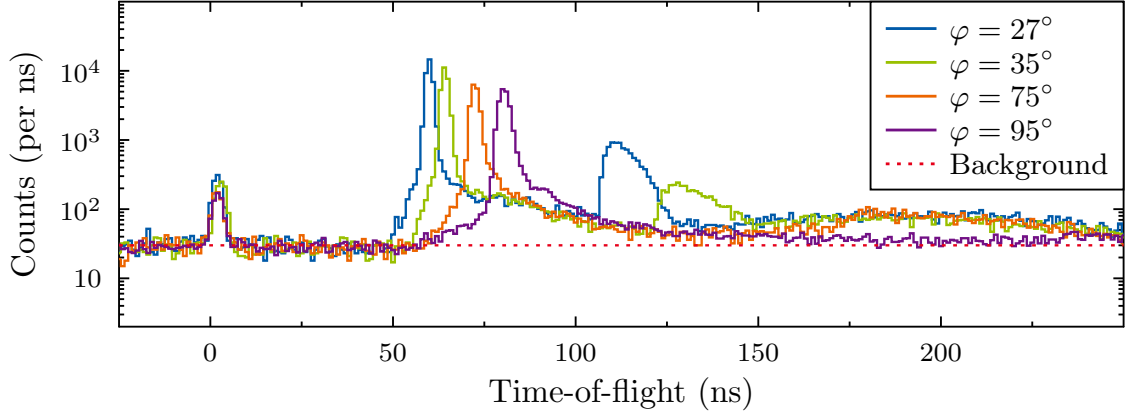
(a) $E_p = 1907$ keV(b) $E_p = 2100$ keV(c) $E_p = 2500$ keV

Figure 3.20.: ToF spectra, corrected for the cable lengths, measured by detector I at set proton energies of (a) 1907 keV, (b) 2100 keV and (c) 2500 keV.

3. Investigation of the ${}^7\text{Li}(p,n){}^7\text{Be}$ neutron fields

Prior to further analysis, such as the ToF to energy conversion and the assembly of the neutron fields, the time corrected spectra had to be corrected for ambient and scattering background. As presented in Figure 3.20a and Figure 3.20c the flat background around the γ -flash can be used for the background correction. However, due to the beamline interference this was problematic at a proton energy of $E_p = 2100$ keV. At this energy the events between 10 and 50 ns of flight time were selected to be background events. The weighted mean background per bin was determined taking the statistical uncertainties per bin into account.

The mean background per bin was then subsequently subtracted from each bin in the spectrum. The result of the background corrections are presented in Figures 3.21a - 3.21c. The background corrected spectra still show a remnant background. This background is two to four orders of magnitude smaller than the maximum of the neutron peaks, and hence, will be neglected in the following. However, the remaining background is also a limitation, especially for the correct detection of the second neutron production channel at a proton energy of $E_p = 2500$ keV. As presented in Figure 3.21c, with the increasing angle of the detector, the second visible neutron distribution vanishes above $\varphi = 30^\circ$.

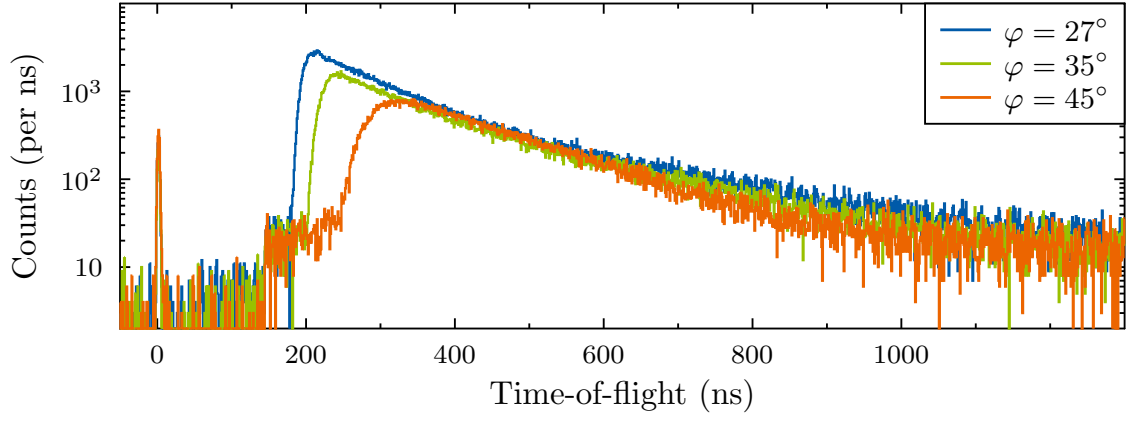
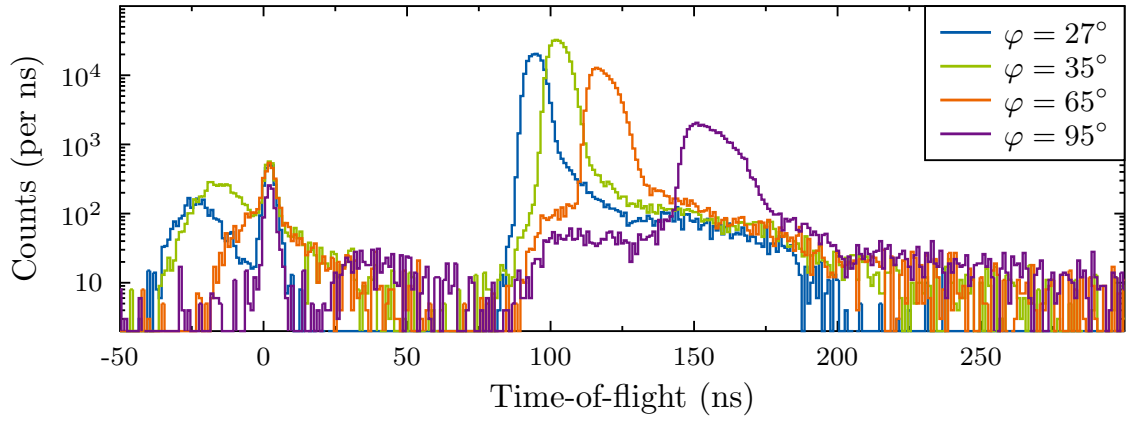
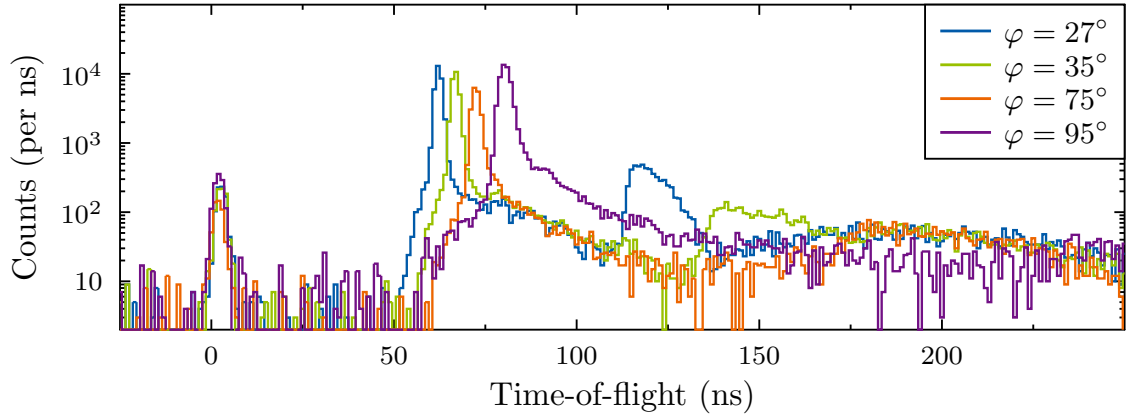
(a) $E_p = 1907$ keV(b) $E_p = 2100$ keV(c) $E_p = 2500$ keV

Figure 3.21.: Background corrected ToF spectra measured using detector I at set proton energies of (a) 1907 keV, (b) 2100 keV and (c) 2500 keV.

3.3.1. Time of flight to energy conversion

To determine the neutron energy, the background corrected ToF spectra were converted using Equation 2.28. The most crucial input, apart from the time-of-flight, for the conversion is the exact knowledge of the flight path, which was checked by a laser distance measurement system prior to each new proton energy setting. The measured flight path values are presented in Table 3.4. In addition, the target backing thickness of 0.5 mm and the half of the scintillator thickness were taken into account. In Figures 3.22a - 3.22c the neutron energy spectra are presented without further rebinning of the energy axis. Considering a linear binning of the x-axis in the ToF spectra with a bin width of 1 ns, the binning of the created energy spectra is quadratic.

First half of the experiment using target RLi0319		
Flight path I (mm)	Flight path II (mm)	Flight path III (mm)
706.6	701.5	716.1
Second half of the experiment using target RLi0411		
701.6	701.5	716.1

Table 3.4.: Used flight path values for the time to energy conversion. The values of the flight path include the target backing thickness, the measured distance between target and detector, and half of the scintillator thickness.

To create an equidistant binning with a bin width of 1 keV, the raw energy spectra were rebinned using the spline interpolation method from the ROOT framework. The results are shown in Figures 3.23a - 3.23c. In the spectra obtained at a set proton energy of $E_p = 2500$ keV the problematics of the nonlinear binning become clear. This is a direct result of the rapid decline of the neutron energy resolution because of the high neutron energies, the short flight path and the limited time resolution. The neutron energy resolution in the presented energy range is in the magnitude of several tens of keV. Thereupon the spline interpolation method becomes fairly unreliable. For an improvement of the neutron energy resolution a second measurement series at an increased flight path at proton energies above $E_p = 2200$ keV would have been useful. In the highest set proton energies a second neutron distribution in the spectrum becomes visible. Presented in Figure 3.23c, recorded at a set proton energy of $E_p = 2500$ keV, the origin of the visible distribution in the energy range between 30 and 300 keV is the second neutron production channel ${}^7\text{Li}(p,n){}^7\text{mBe}$. The main production channel is responsible for the energy distribution between 380 and 800 keV. Additionally, another structure between 0 and 20 keV is visible. The origin

of this structure is believed to be scattered neutrons, due to the high energies of the neutrons originating in the ${}^7\text{Li}(\text{p},\text{n}){}^7\text{Be}$ reaction.

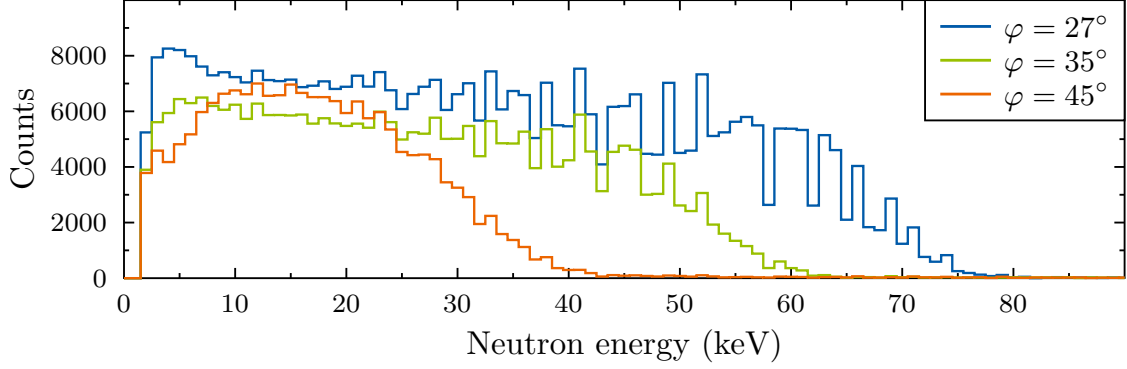
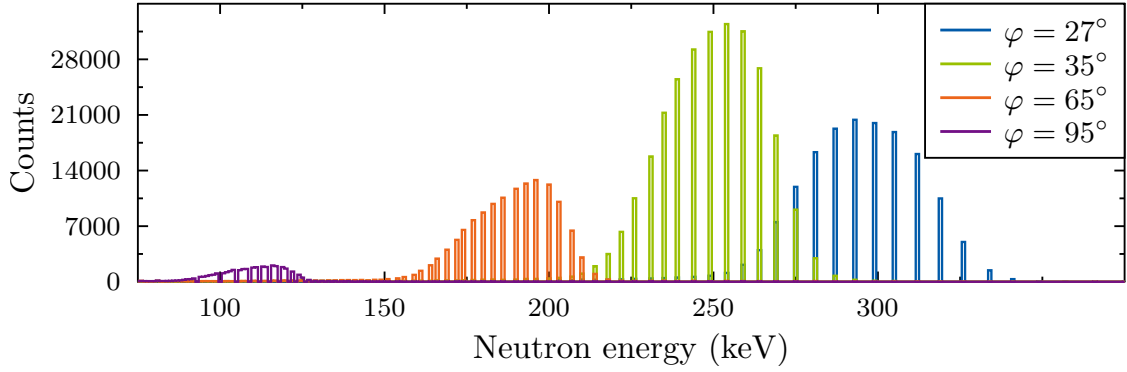
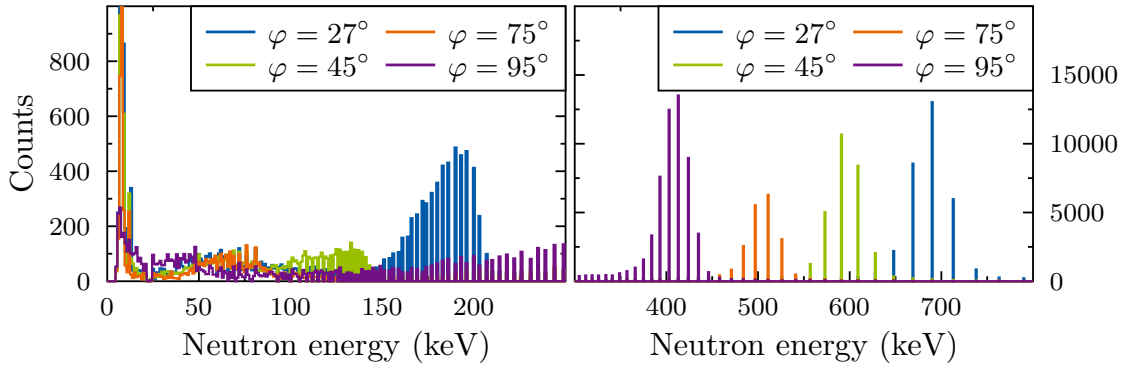
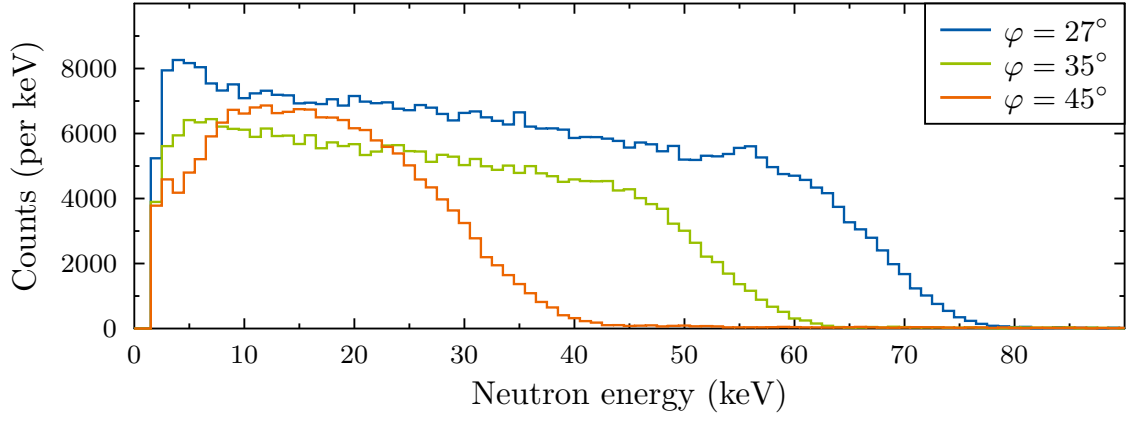
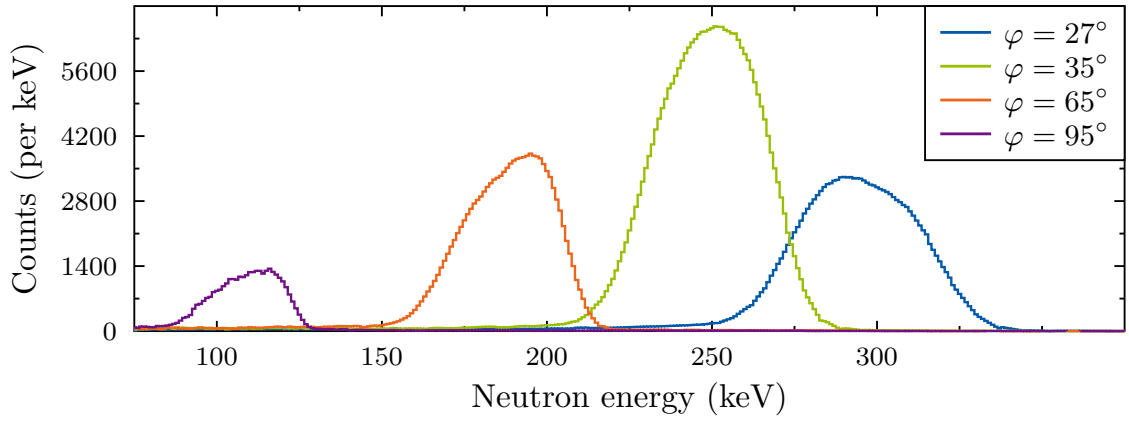
(a) $E_p = 1907 \text{ keV}$ (b) $E_p = 2100 \text{ keV}$ (c) $E_p = 2500 \text{ keV}$

Figure 3.22.: Energy spectra obtained using detector I at set proton energies of (a) 1907 keV, (b) 2100 keV and (c) 2500 keV.

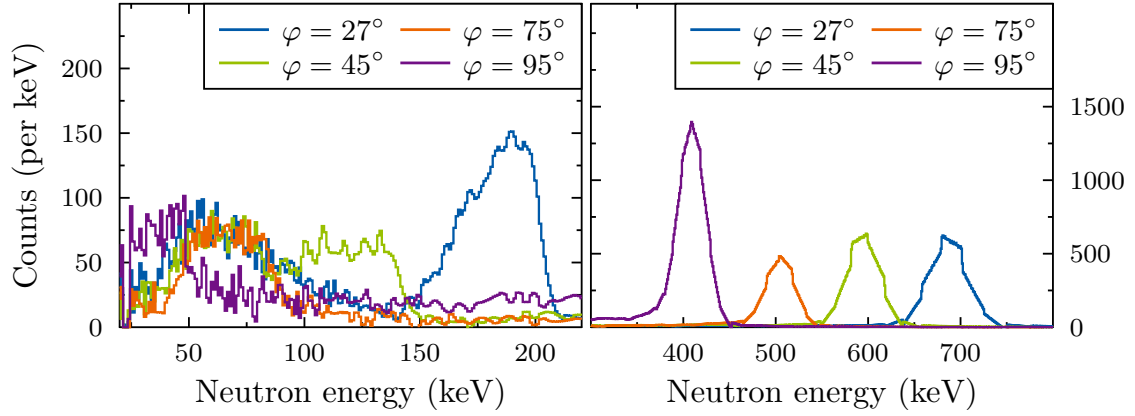
3. Investigation of the ${}^7\text{Li}(p,n){}^7\text{Be}$ neutron fields



(a) $E_p = 1907 \text{ keV}$



(b) $E_p = 2100 \text{ keV}$



(c) $E_p = 2500 \text{ keV}$

Figure 3.23.: Rebinned energy spectra using detector I at set proton energies of (a) 1907 keV, (b) 2100 keV and (c) 2500 keV.

3.4. Neutron fields

The neutron field is characterized as the angle-integrated neutron spectrum. For proton energies, where the center of mass velocity of the compound nucleus ${}^8\text{Be}^*$ exceeds the velocity of the emitted neutron, neutrons are emitted in a well defined cone of a specific opening angle θ . For proton energies above approximately 1940 keV, the cone opening half angle becomes $\theta/2 = 180^\circ$ [56, 31, 44, 53]. For the determination of the angle-integrated neutron spectra covering the entire solid angle, neutron spectra would have to be measured between 0° and 180° , which leads to several difficulties. One of which is the positioning of the detectors. Especially at an angle of 180° , where the beamline would make a positioning impossible. Furthermore, at angles above 85° material would be in between the detector and the neutron production target, such as the target itself or other accelerator and monitoring equipment. For activation measurements, where the samples, are placed directly in front of the neutron production target, a field determination up to 85° is considered to be sufficient. The positions under which the neutron spectra were measured during the experiment can be found in Table 3.1. The neutron fields can be constructed either using the background corrected ToF- or the neutron energy spectra. These spectra for each run need to be normalized by the accumulated beam charge on the lithium target, taking into account different measurement durations and beam current differences. The accumulated beam charge for each run is presented in section B. Using the charge corrected spectra, the neutron fields for each detector and proton energy can be created. The combined neutron field, consisting of all three detectors, can only be considered to be an approximation due to the slightly different flight paths and different detector specifications. Therefore, each detector has a slight difference in the solid angle coverage and thus is exposed to a slightly different neutron spectrum. To investigate the influence of the differences between the detectors, for each set proton energy, the detectors were directly compared with each other. The differences in the recorded ToF spectra at the same angular position for the detectors, at set proton energies of $E_p = 1907, 2100$ and 2500 keV, are shown in Figures 3.24 - 3.29. The uncertainties of the measured spectra considered in the following are strictly statistical. The statistical uncertainties are composed of the uncertainties of the raw spectra, the background and the accumulated beam charge. These combined uncertainties of the spectra have been determined by Gaussian error propagation.

3. Investigation of the ${}^7\text{Li}(p,n){}^7\text{Be}$ neutron fields

The difference at low energies, in the presented case at $E_p = 1907\text{ keV}$, is only marginal, however the effects of the different flight paths become noticeable especially between detectors II and III. Comparing the spectra of detectors II and III both recorded at an angle of $\varphi = 15^\circ$, the difference in the fast neutron flank of the spectrum is noticeable and is a result of the different flight paths of the neutrons. For a better visibility the uncertainties of the spectra are only presented in the ratio between the compared spectra. These uncertainties were determined by Gaussian error propagation from the statistical uncertainties of the compared measurements.

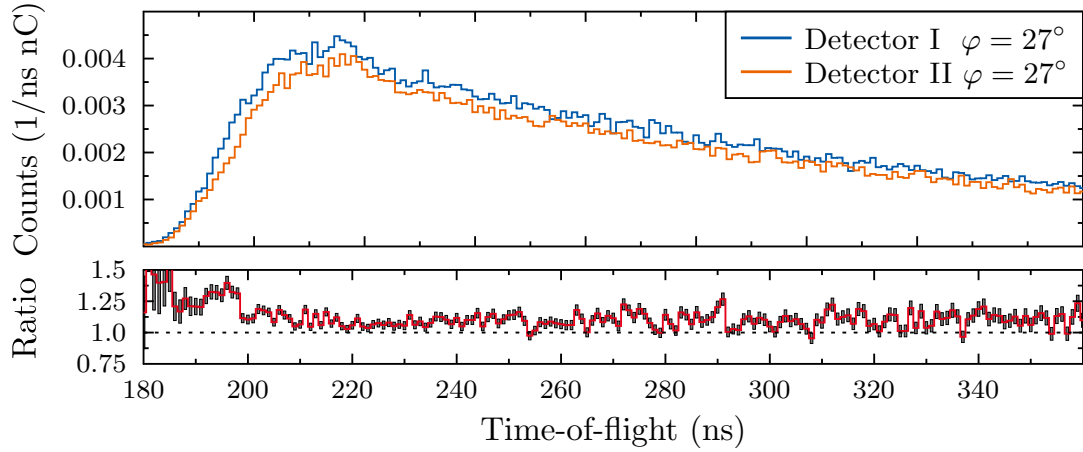


Figure 3.24.: Comparison of ToF spectra obtained using detector I and II, measured under the same angle $\varphi = 27^\circ$ at $E_p = 1907\text{ keV}$. A slight difference is noticeable due to a different flight path and detector specification.

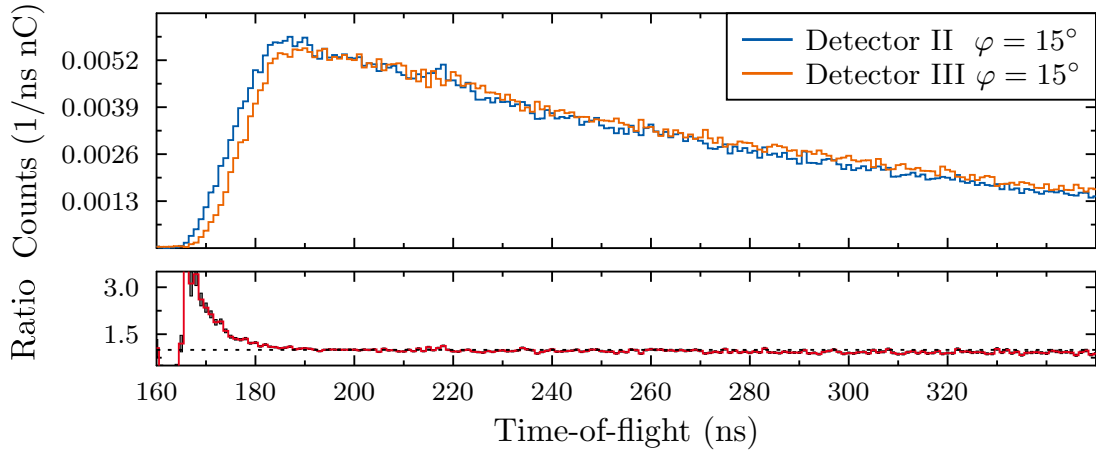


Figure 3.25.: Comparison of ToF spectra obtained using detector II and III, measured under the same angle $\varphi = 15^\circ$ at $E_p = 1907\text{ keV}$. The difference a result of the different flight path and detector specification.

At higher proton energies, such as $E_p = 2100$ keV, the differences between the detectors are small due to the decreasing neutron energy resolution of the detection setup. As presented in Figure 3.26 and Figure 3.27 the differences in the spectra recorded by different detectors under the same detector position, except for the flight path, show only minor disagreements. The uncertainty of the flight time of 1 ns has a clear impact on the spectra obtained at these energies. The differences between the detectors are within the margin of uncertainty for the time resolution.

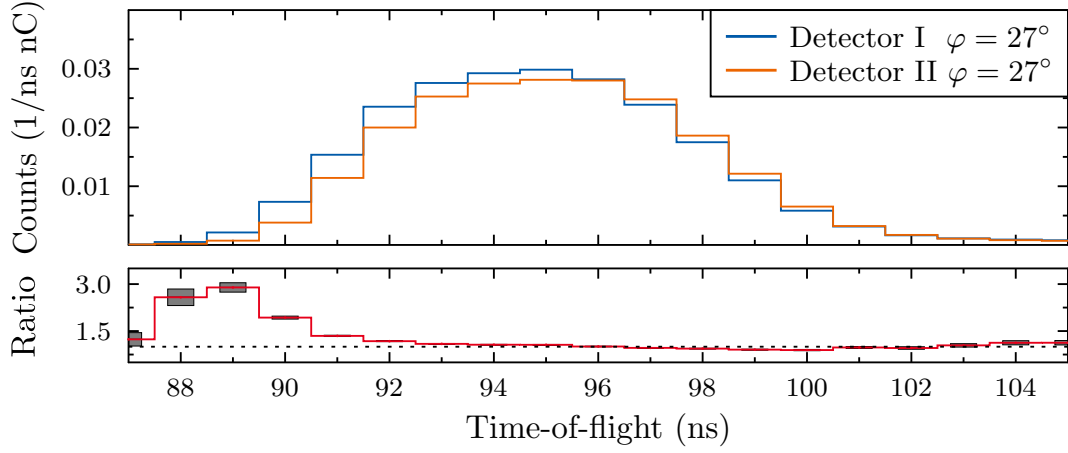


Figure 3.26.: Comparison of ToF spectra obtained using detector I and II, measured under the same angle $\varphi = 27^\circ$ at $E_p = 2100$ keV. A slight difference is noticeable due to a different flight path and detector specification.

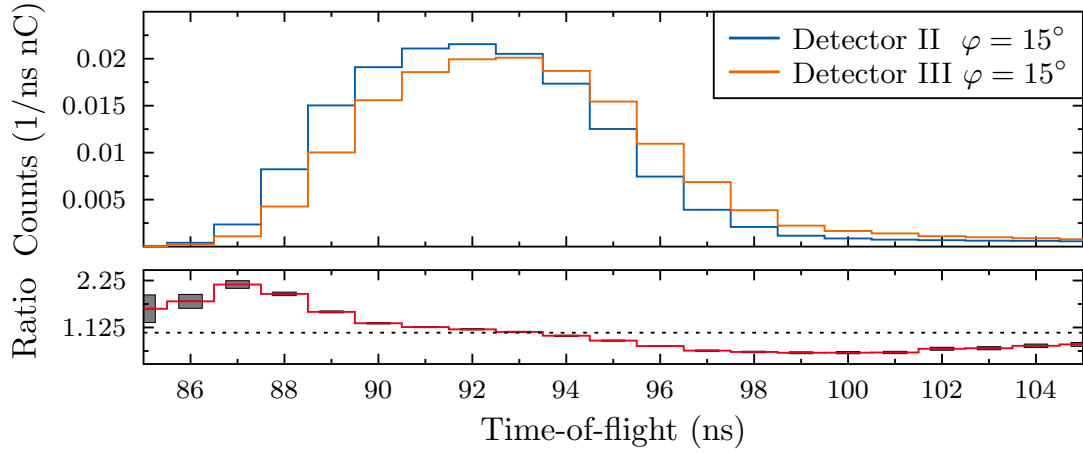


Figure 3.27.: Comparison of ToF spectra obtained using detector II and III, measured under the same angle $\varphi = 15^\circ$ at $E_p = 2100$ keV. A difference is noticeable due to a different flight path and detector specification.

3. Investigation of the ${}^7\text{Li}(p,n){}^7\text{Be}$ neutron fields

At even higher proton energies, above $E_p = 2350$ keV, where the second neutron production channel becomes available, the neutron energy distribution, coming from the main production channel, becomes even more narrow. At this proton energy the time resolution of 1 ns is equal to more than 40 keV in neutron energy. For the purpose of these measurements however, mainly the angle-integrated neutron yield is of interest, which lowers the importance of the energy resolution. In retrospect increasing the flight path for a second series of measurements would have been useful to gain more sensitivity for the neutron energy. This problem becomes even more severe at the highest measured set proton energy of $E_p = 2800$ keV.

The comparison of the different detectors at the equivalent angular position supported the approximation of the combined neutron fields with energy spectra measured by the different detectors, due to the solid angle corrections and considering the margin of uncertainties of the time resolution and the flight paths.

Final neutron fields

In the final step to create the angle-integrated neutron fields, the energy spectra obtained at various angular positions, have to be scaled with the respective solid angle coverage of the detector.

With the definition of the solid angle Ω

$$\Omega = 2\pi (1 - \cos(\theta)), \quad (3.1)$$

follows as a solid angle correction for the detector at position $\varphi = 0$

$$f_{\text{scaling},0^\circ} = \frac{2\pi(1 - \cos(\alpha))}{2\pi(1 - \cos(\theta + \alpha))} = \frac{(1 - \cos(\alpha))}{(1 - \cos(\theta + \alpha))}, \quad (3.2)$$

where α denotes the half of the step size (for most measured proton energies $\alpha = 2.5$) and θ the maximum angle. For detector positions at $\varphi \neq 0^\circ$ Equation 3.2 becomes

$$f_{\text{scaling}} = \frac{[(1 - \cos(\varphi - \alpha)) - (1 - \cos(\varphi + \alpha))]}{(1 - \cos(\theta + \alpha))}. \quad (3.3)$$

Once scaled, the neutron spectra measured at each angle, normalized for the accumulated beam charge during the respective run, are integrated to create the final neutron field. The angular correction factors are presented in section B, Tables B.11 and B.12.

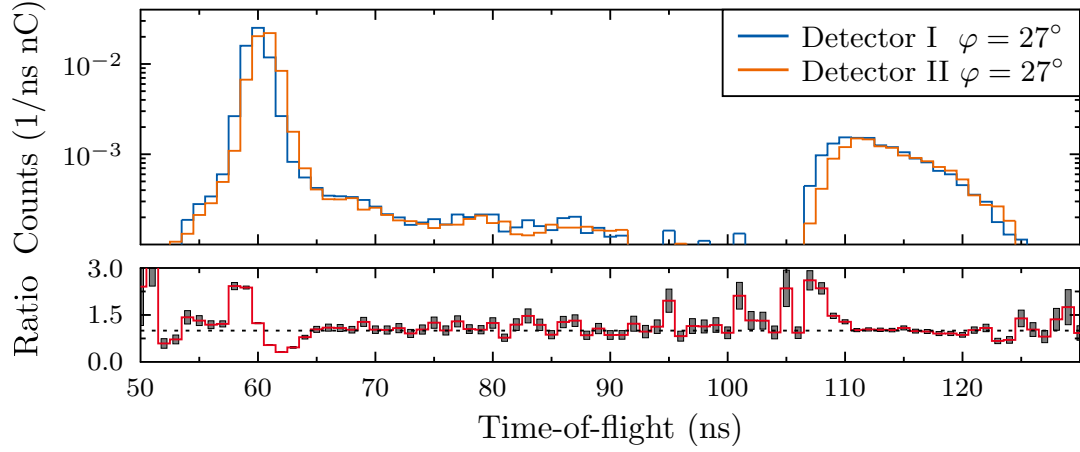


Figure 3.28.: Comparison of ToF spectra obtained using detector I and II, measured under the same angle $\varphi = 27^\circ$ at $E_p = 2500$ keV. A slight difference is noticeable due to a different flight path and detector specification.

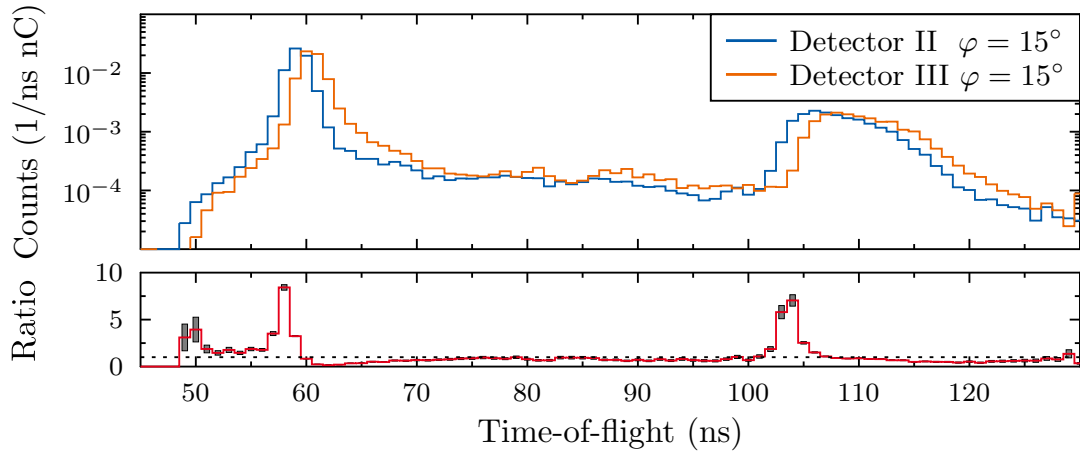


Figure 3.29.: Comparison of ToF spectra obtained using detector II and III, measured under the same angle $\varphi = 15^\circ$ at $E_p = 2500$ keV. A difference is noticeable due to a different flight path and detector specification.

3.5. Comparison with the PINO tool

A major aim of the experimental campaign was the comparison of the measured neutron spectra, at proton energies different than $E_p = 1912\text{ keV}$, with the simulation tool PINO. This tool is used as the foundation to recreate a quasi-stellar neutron spectrum produced by the ${}^7\text{Li}(p,n){}^7\text{Be}$ reaction at various energies. The PINO tool relies on the Monte Carlo method to simulate the transformation from proton to neutron. In the simulation several simplifications are made, such as the assumption of the absence of proton scattering inside a thin lithium layer. Additionally, the code only relies on the ionization of lithium. Therefore, the stopping of the protons is a result of only electronic interactions and (p,n) reactions. The stopping power data used during the simulations are taken from the well-established program SRIM [79]. For the determination of the neutron spectrum, the tool relies on double differential cross sections for the ${}^7\text{Li}(p,n){}^7\text{Be}$ reaction, compiled by Liskien and Paulsen [47]. The transport of the simulated neutron is also simplified. The simplifications include the hypothesis of a neutron transmission greater than 95% for the lithium target backing. Additionally, neutrons are not tracked but ray-traced, meaning only the initial position and the angle at time of production are considered. In order to receive the desired simulated spectrum, the tool has to be provided with certain input parameters, such as the stopping power, (p,n) cross sections, lithium target geometry, sample geometry, proton beam specifications and the number of simulated samples [57].

Using the base version of PINO, the output is given in two files: the neutron yield as a function of energy and the neutron spectrum passing through the sample. For the comparison of the measurements presented in this thesis, the code was adapted to support the simulation of ToF spectra at various positions in space. To use this adapted version the input file was extended to support the specifications of the time resolution and the flight path. In addition, the code was further improved to simulate the neutron spectrum passing a disk, square or sphere at a certain position in space. Using this code the simulation of a neutron spectrum passing through a detector at a certain position as in the measurements becomes possible. This version of PINO will be denoted PINO v2. In Figures 3.30a - 3.30c, the simulated PINO ToF spectra for three proton energies $E_p = 1907, 2100$ and 2500 keV are presented. The resemblance to the measured spectra, shown in Figures 3.21a - 3.21c, is remarkable. However, these spectra are not yet corrected for the detector efficiency. As a first

step in the comparison between the simulation and the measurement, a crucial input, the simulated time resolution of the system was investigated.

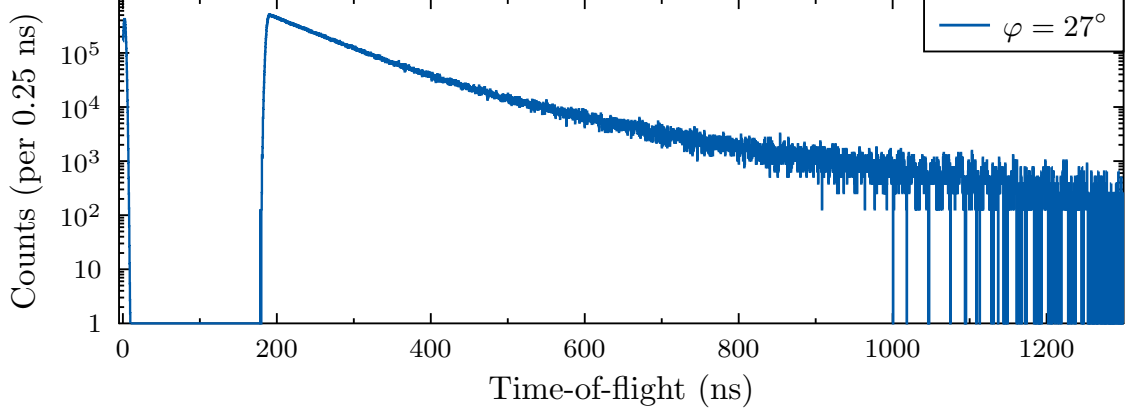
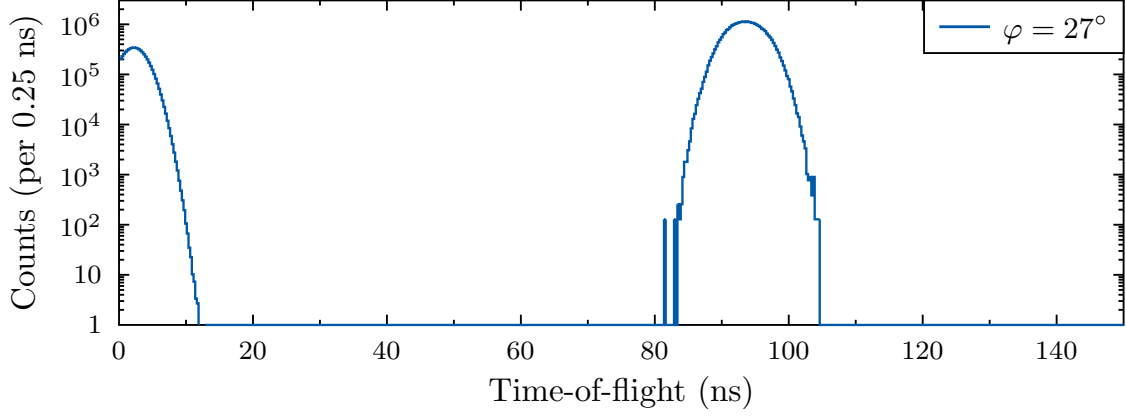
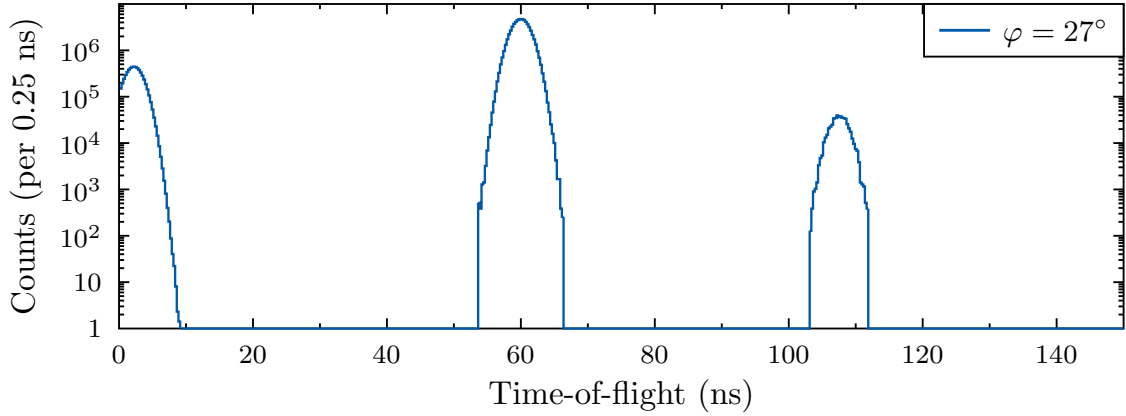
(a) $E_p = 1907$ keV(b) $E_p = 2100$ keV(c) $E_p = 2500$ keV

Figure 3.30.: Time-of-flight spectra simulated using the PINO tool at proton energies of (a) $E_p = 1907$, (b) $E_p = 2100$ and (c) $E_p = 2500$ keV.

3.5.1. Time resolution

The time resolution, which has a direct influence on the ToF spectra, is given as a parameter in the input file for the PINO v2 simulation tool. The time resolution responsible for the simulated width of the γ -flash. It is approximated by a Gaussian shaped peak. The broader this peak and therefore the larger the time resolution, the broader is the resulting simulated neutron energy distribution.

When comparing the simulation with the measurements, for example at set proton energies of $E_p = 1907, 2100$ and 2500 keV, presented in Figure 3.31, the simulation and the measurement show a very good agreement. The input for the simulations were taken from Table 3.3. The only difference visible is a slight shift of the centroid of the γ -flash, which is a result of the slightly non-Gaussian shape of the γ -flash during the measurements. The differences in flight time are below 0.5 ns, which is within the margin of uncertainty of the time resolution of 1 ns. The match between simulation and measurement was equally well for all measured and simulated energies.

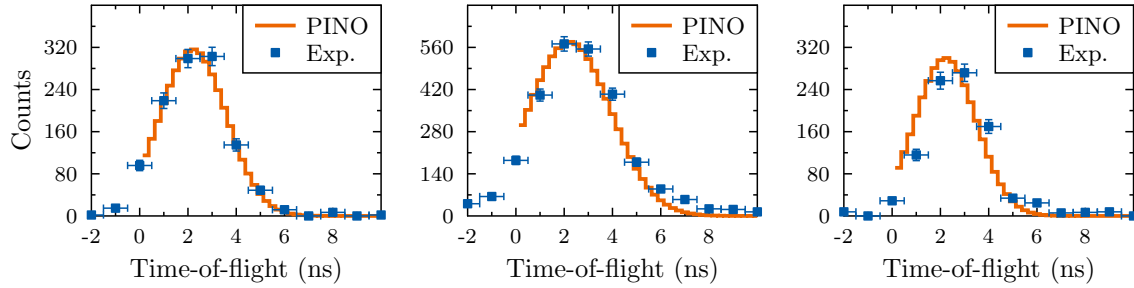


Figure 3.31.: Simulated vs. measured γ -flash for time resolution comparison. From left to right: $E_p = 1907, 2100$ and 2500 keV. Measurements are scaled to fit the simulation.

3.5.2. Detector efficiency

For the correct comparison between simulation and measurement, either the simulated or the measured spectra need to be corrected for the respective detector efficiency. It was chosen to correct the simulated spectra with the detector efficiency for further comparisons and to simplify comparisons in the future. The detection efficiency for ${}^6\text{Li}$ -glass detectors can not easily be determined using calibration sources. Since this detector type is not suitable to resolve neutron energies, a different method is needed. One possibility is the detection of strict mono-energetic neutrons or tagged neutrons. If the energy of the neutrons is known, the detection efficiency can be determined analog to the efficiency of a γ -detector. However, given the energy

	No. 1	No. 2	No. 3
Material	NE908 (GS20)	NE908 (GS20)	NE912 (KG2)
Total Li (wt%)	6.6	6.6	7.5
^6Li enrichment (%)	95	95	95
Diameter (mm)	38.8	38.0	39.9
Thickness (mm)	3.1	3.0	2.85

Table 3.5.: Specification of the used scintillation glasses. The values are taken from [62].

Material designation	Type of Li	Weight (%)				
		SiO ₂	MgO ₂	Al ₂ O ₃	Ce ₂ O ₃	Li ₂ O
GS20	Enriched	56	4	18	3	18
KG2	Enriched	74	0	0	5	21

Table 3.6.: Lithium glass specification as input for the GEANT-4 simulations. The presented values are taken from [68].

range of the needed detector calibration, the safest way to determine efficiency is a simulation of the detector. This was done taking advantage of the Monte Carlo method, using the toolkit GEANT-4 [2]. The detector geometry and specification could not easily be recreated, since the two detectors I and II, which were assembled in Frankfurt, are about 30 years old and thus missing most of the specifications. However, the markings on the detectors gave indication for the chemical composition of the glasses. The detectors were then designed in the GEANT-4 framework with their specifications and the glass composition as presented in Table 3.5 and Table 3.6. Only the scintillation glasses were simulated. The results of the efficiency simulations are shown in Figure 3.32. The resulting efficiency curves are very similar. While detector I and II are equal in their scintillator composition and very similar in the size of the glass, the efficiencies for them are almost equal. Detector III shows an efficiency up to 20% larger than detectors I and II. The statistical uncertainty of the simulation ranged between 0.5% in the resonance region and up to 6% in the high energy region above 800 keV. Including the uncertainties of the theoretical cross section inputs taken from [13] a maximal uncertainty of 7.8% arises above a neutron energy of 800 keV. The systematic uncertainties, depending on the energy range of the neutron, are presented in Table 3.7. The high statistical uncertainty is a result of the very thin lithium glass scintillators and the declining cross section of the $^6\text{Li}(n,\alpha)^3\text{H}$ reaction.

3. Investigation of the ${}^7\text{Li}(p,n){}^7\text{Be}$ neutron fields

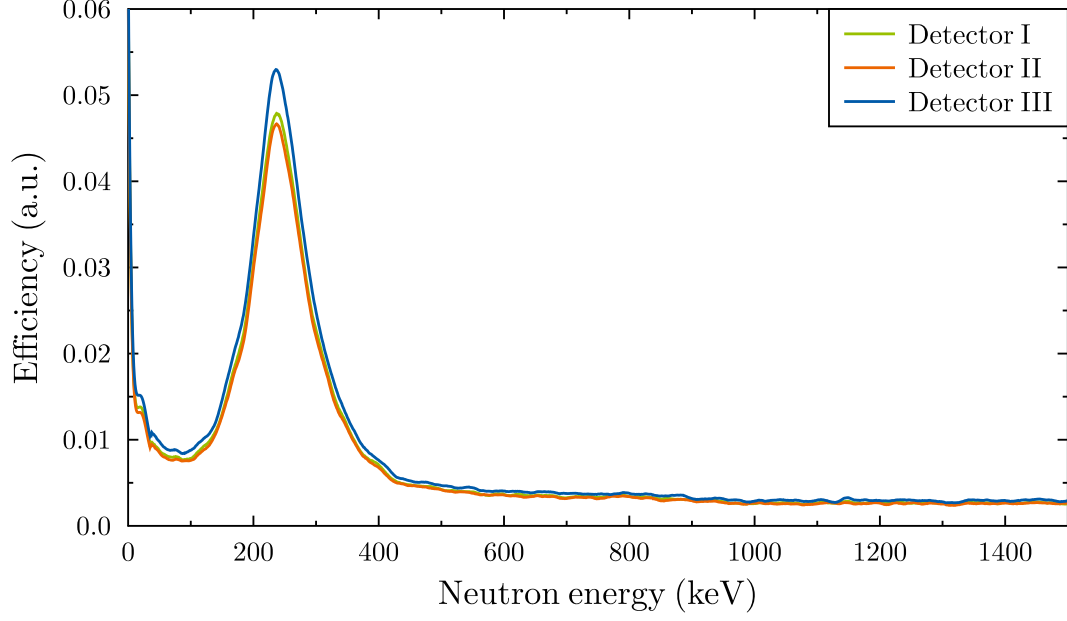


Figure 3.32.: Simulated detector efficiencies for the used detectors during the experiment. The specifications for the simulation inputs are shown in Table 3.5 and Table 3.6.

Energy range (keV)	Systematic uncertainty (%)
0.1 - 1.0	0.3
1.0 - 10	0.5
10 - 50	0.7
50 - 90	1.1
90 - 150	1.5
150 - 450	2.0
450 - 650	5.0
650 - 800	2.0
800 - 1000	5.0

Table 3.7.: Presented are the systematic uncertainties for the detector efficiency. Values taken from [13].

3.5.3. Proton beam energy

As mentioned in the beginning of chapter 3, during the the measurement of the neutron fields the problem of a large uncertainty in the proton beam energy arose. For some selected proton energies the accelerator staff noticed deviations of up to 10 keV from the selected values. With the thin lithium targets used, and the resulting narrow neutron energy distribution, these differences would impact the possibility of the comparison with PINO tremendously. A possibility to determine the correct proton energy was the use of the PINO code, but ignoring the comparison of the angular neutron yield in the first step. The kinematics of the reaction are well known and implemented in PINO. A set of ToF spectra were simulated varying the proton energy in 1 keV steps. Afterwards, the measured and simulated ToF spectra were compared bin per bin using a χ^2 -test.

$$\chi^2 = \sum_{n=1}^n \frac{(C_{n,\text{mes.}} - C_{n,\text{sim.}})^2}{\sigma_{n,\text{mes.}}^2}, \quad (3.4)$$

where $C_{n,\text{mes.}}$ denotes the measured intensity, $C_{n,\text{sim.}}$ the simulated intensity and $\sigma_{n,\text{mes.}}$ variance of the measured intensity at bin n .

To exclude possible differences in the spectra for this test only the rising flank of the ToF spectra, representing the fastest neutrons at a specific proton energy and angle, were compared. Prior to the comparison, the maximum of the spectra were normalized to 1.

For the proton energy determination a set of assumptions had to be made. Variables such as the lithium target thickness, which can not be determined without a specific unknown uncertainty and the accelerator energy spread were considered to be constant for this check. These important input variables also have an effect on the simulated spectrum. The target thickness has only been determined during the evaporation. During irradiation however, the target will degrade and most likely a carbon layer will build up onto the target. Another possibility is the deposition of lithium inside the target backing over time. All these effects may change the measured neutron energy distribution.

The accelerator energy spread may also vary during measurement and for different proton energies. The value given by the accelerator staff was: $\Delta E = 1$ keV. The differences in the ToF spectra by a variation of the proton energy in 1 keV steps is shown in Figures 3.33a - 3.33c. The variation of 1 keV does show a difference in

3. Investigation of the ${}^7\text{Li}(p,n){}^7\text{Be}$ neutron fields

ToF of up to 2.5 ns at a proton energy of $E_p = 1907$ keV. At higher energies, such as 2100 keV, a variation of the proton energy of 5 keV means a difference of up to 1.5 ns in ToF. For even higher proton energies, the ToF of the neutron distribution coming from the ${}^7\text{Li}(p,n){}^7\text{Be}$ reaction shows almost no difference between variations of up to 5 keV. The slower neutrons originating in the isomeric state reaction show a maximum deviation of 2 ns. This is a result of the limited time resolution of the acquisition system.

As a first step towards the determination of the correct proton energy only the spectra obtained using detector III were used, since this detector was positioned at an angle of 0° . Afterwards, the other detectors were used for comparison under the remaining angles measured. The deviation between the determined proton energies between the detectors was 1 keV at maximum, which is within the margin of error of the accelerator energy spread. The differences between set and actual energy were determined to be 2 keV - 3 keV up to a proton energy of $E_p = 2000$ keV. At higher proton energies, a more prominent difference between set and measured energy arises when using PINO to approximate the true proton energy. A direct comparison between simulation and measurement for the proton energy approximation is presented in Figure 3.34.

Proton energy set (keV)	Proton energy measured (keV)
1887	1884(1)
1897	1894(1)
1907	1904(1)
1912	1909(1)
2000	1998(1)
2100	2100(1)
2200	2202(1)
2300	2305(1)
2500	2490(1)
2800	2791(1)

Table 3.8.: Determined proton beam energies using PINO. Except for energies higher than 2200 keV, the proton energies deviate between 2 and 3 keV.

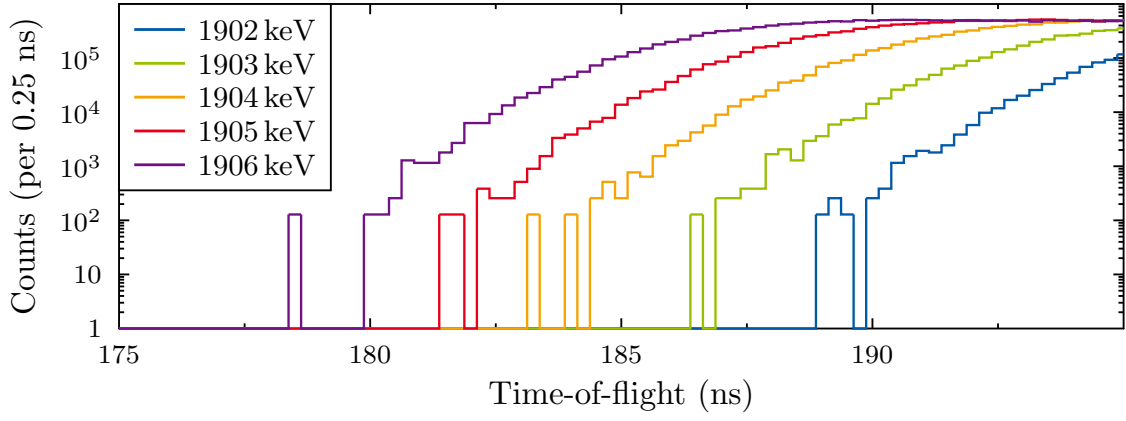
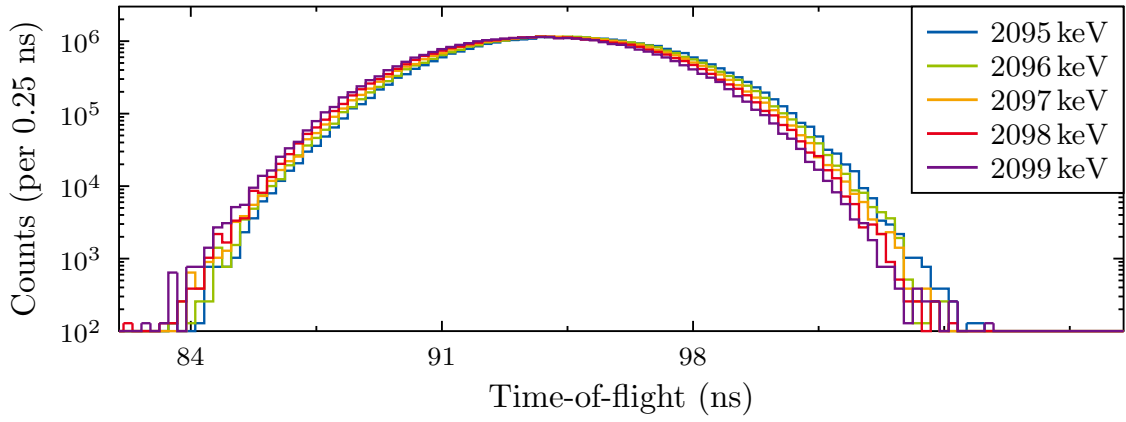
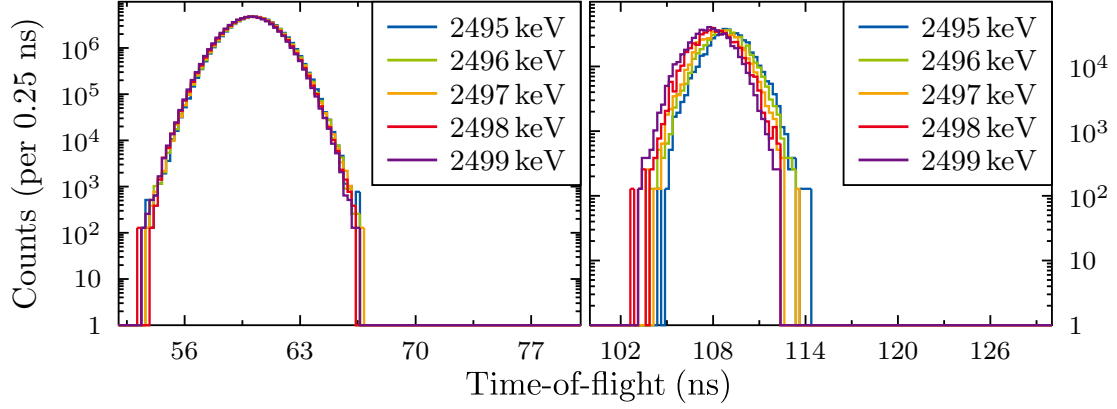
(a) $E_p = 1907$ keV(b) $E_p = 2100$ keV(c) $E_p = 2500$ keV

Figure 3.33.: Simulated ToF spectra to demonstrate a variation of the proton energy around a set value of (a) $E_p = 1907$, (b) $E_p = 2100$ and (c) $E_p = 2500$ keV.

3. Investigation of the ${}^7\text{Li}(p,n){}^7\text{Be}$ neutron fields

The comparison presented in Figure 3.34, shows that the match between simulation and measurement is excellent. The deviation observable at $E_p = 1897$ keV is due to the limited statistics in the measurement and simulation. Therefore, the normalization to 1 leads to uncertainties. At proton energies above the second neutron production threshold, a deviation of up to 10 keV between set and measured proton energy has been determined. The comparison between measurement and simulation are overall in a good agreement at $E_p = 2490$ keV for the main neutron production channel. The neutron emission originating in the second neutron production channel however, deviates to a large extend from the simulation. Due to the short flight path the energy resolution, especially for spectra measured at high proton energies, is the largest uncertainty. An additional reason for the deviations between measurement and simulation, especially at high proton energies, is the target degradation over the course of the measurement campaign.

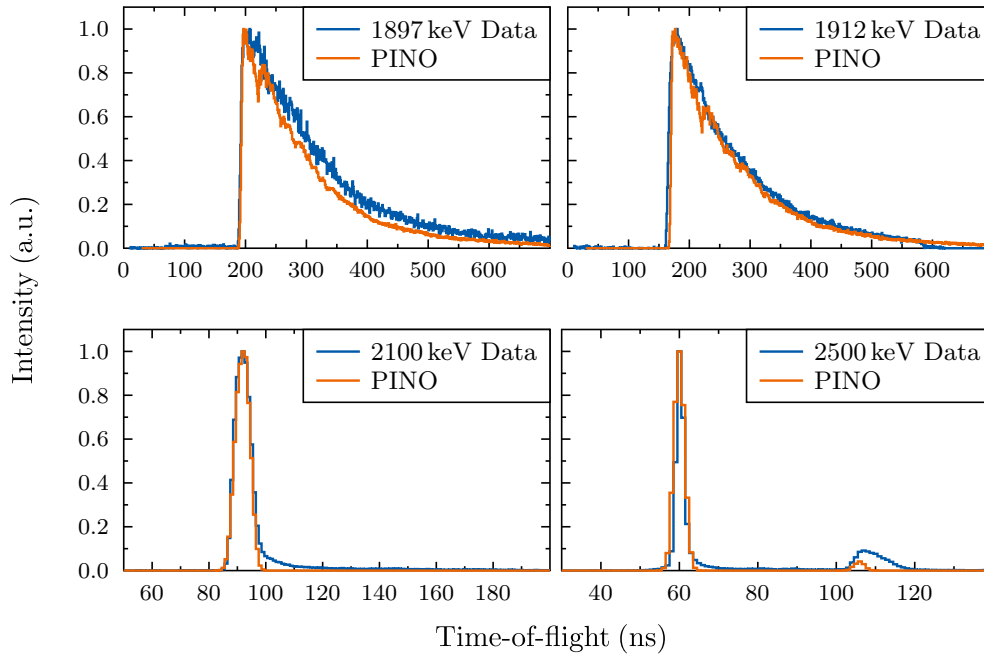


Figure 3.34.: Excerpt from the proton energy determination. Spectra obtained by simulation and measurement are compared. For better comparison the measured and simulated spectra were normalized to 1.

Additionally to the proton energy approximation using the PINO code, the neutron production threshold was investigated. Since the cross section of the ${}^7\text{Li}(p,n){}^7\text{Be}$ reaction rises rapidly within a few keV of the neutron production threshold, this was thought to be a metric for the difference between selected and true proton energy.

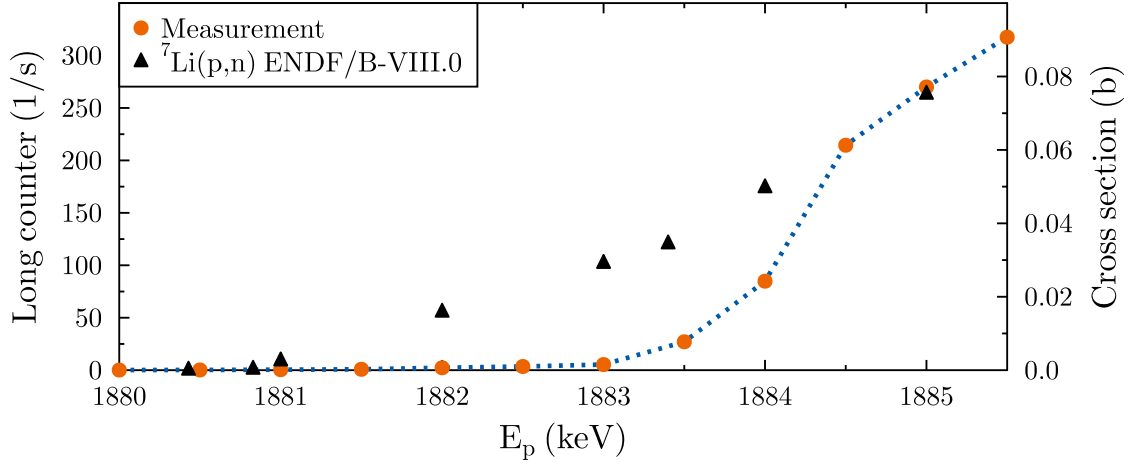


Figure 3.35.: Results of the neutron production threshold scan. A proton energy deviation of approximately 2-3 keV is visible. The values for the ${}^7\text{Li}(p,n){}^7\text{Be}$ cross section were taken from [13].

For the investigation one of the long counters, usually used to monitor the neutron yield throughout the experiment, was positioned directly in front of the lithium target. The proton energy of the accelerator was first set to 1880 keV and successively increased in steps of 0.5 keV. As presented in Figure 3.35, a difference between 2-3 keV proton energy between expected neutron emission and detection is visible. These findings are in good agreement with the results of the PINO simulation at an energy of 1887 keV.

3.5.4. Comparison of the ${}^7\text{Li}(\text{p},\text{n}){}^7\text{Be}$ neutron fields

The measured angle-integrated neutron energy spectra were compared with PINO v2. The results are presented in the following subsections.

The code simulates the neutron spectrum at the detector position. The detector itself is considered to be a sphere, with the center of the sphere at detector position. For the comparison the measured neutron spectra were normalized by the accumulated beam charge, as previously shown. Additionally, the maximum of the final constructed neutron fields was normalized to 1. The simulated neutron energy spectra were normalized by the number of simulated protons and the constructed field maximums were normalized to 1.

In the following four different spectra are presented for each proton energy: A 2D spectrum of the measurement, a 2D spectrum of the simulation, a 2D spectrum showing the difference ratio and an x-axis projection showing a comparison of the angle-integrated neutron spectrum determined by measurement and PINO v2.

The difference ratio Δ_w between the measurement and simulation was determined by

$$\Delta_w = \frac{I_{\text{PINO}} - I_{\text{mes.}}}{0.5 \cdot (I_{\text{PINO}} + I_{\text{mes.}})}, \quad (3.5)$$

where I_{PINO} denotes the simulated intensity and $I_{\text{mes.}}$ the measured intensity.

The considered uncertainties are presented in the figures containing the angle-integrated spectra. Presented are the uncertainties for the PINO v2 simulation, taking the statistical as well as the systematic uncertainties originating in the detector efficiency into account. The systematic uncertainties for the neutron energy ranges of the lithium glass detectors are shown in Table 3.7. The uncertainties of the angle-integrated measured spectra are strictly statistical.

3. Investigation of the ${}^7\text{Li}(p,n){}^7\text{Be}$ neutron fields

$$E_{p, \text{ set}} = 1887 \text{ keV}$$

The lowest determined true proton energy was $E_p = 1884 \text{ keV}$, about 3 keV above the neutron production threshold, which was the first energy to produce a significant amount of neutrons. The neutron spectrum covered a small solid angle and was measured by detectors II and III.

The resulting angle-integrated neutron energy spectra presented in Figure 3.36 show a very good agreement between measurement and simulation. The slight deviations are most likely a result of the simulation geometry and the low statistics of the measurement.

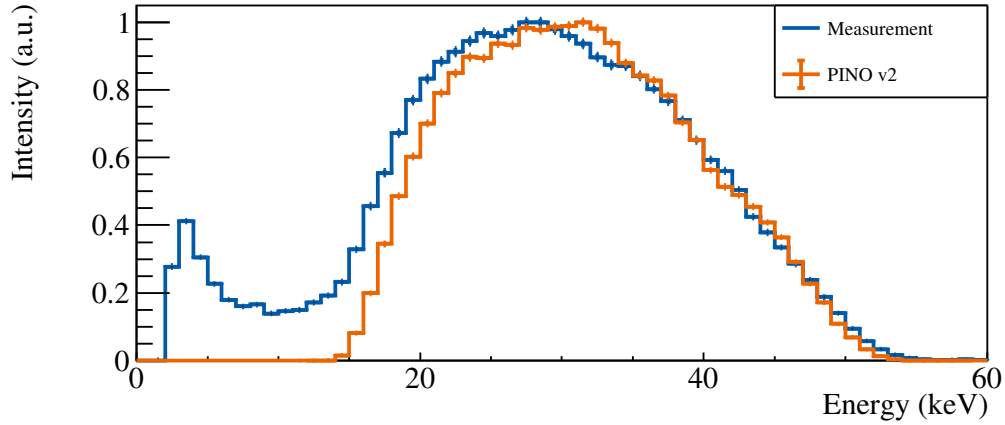


Figure 3.36.: Measured and simulated neutron energy spectra determined using detectors II and III at a proton energy of $E_p = 1884 \text{ keV}$. Detector I was positioned outside the neutron cone.

For a bin per bin comparison the heat maps of the measurement, simulation and the difference ratios are shown in Figure 3.37. In the high energy range the simulation seems to underestimate the number of neutrons slightly. However, in the energy range between 45 and 50 keV slightly less neutrons than expected by the simulation were measured. During the measurement a fair amount of noise was visible in the low energy region of the measured spectrum. This is most likely a result of the non optimized experimental setup for the low energies and scattered low energy neutrons. Overall a very good agreement between simulation and measurement is visible.

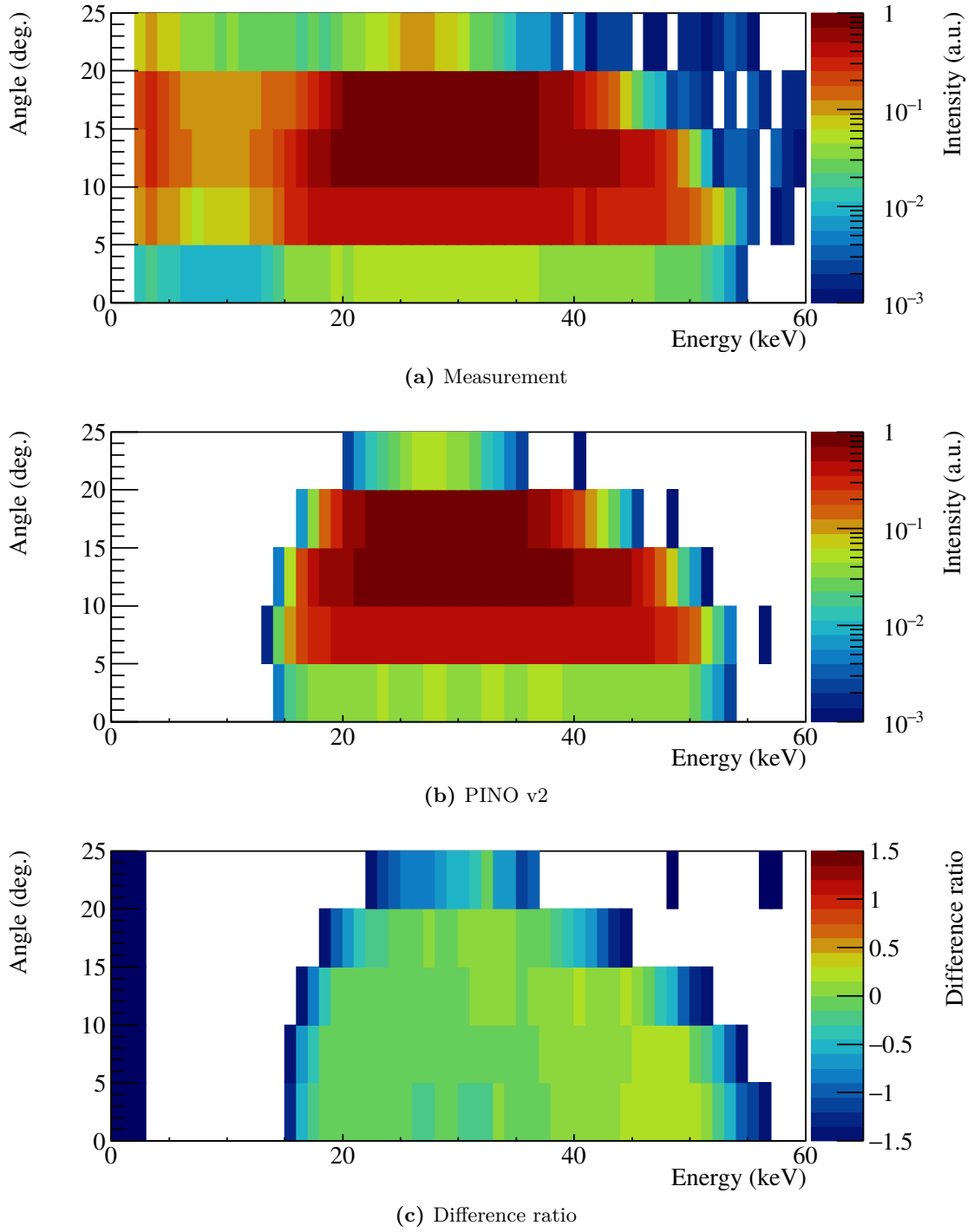


Figure 3.37.: Heat maps for comparison between simulation and measurements. Proton energy $E_p = 1884$ keV.

3. Investigation of the ${}^7\text{Li}(p,n){}^7\text{Be}$ neutron fields

$E_{p, \text{ set}} = 1897 \text{ keV}$

The next energy measured during the campaign, 10 keV above the previous setting, was determined to be $E_p = 1894 \text{ keV}$. The neutron spectrum now covers a larger solid angle and was measured using all three detectors. The resulting angle-integrated neutron spectrum is presented in Figure 3.38, and shows overall a reasonable agreement between measurement and simulation. In total, the measured spectrum is shifted approximately 5 keV towards lower energies.

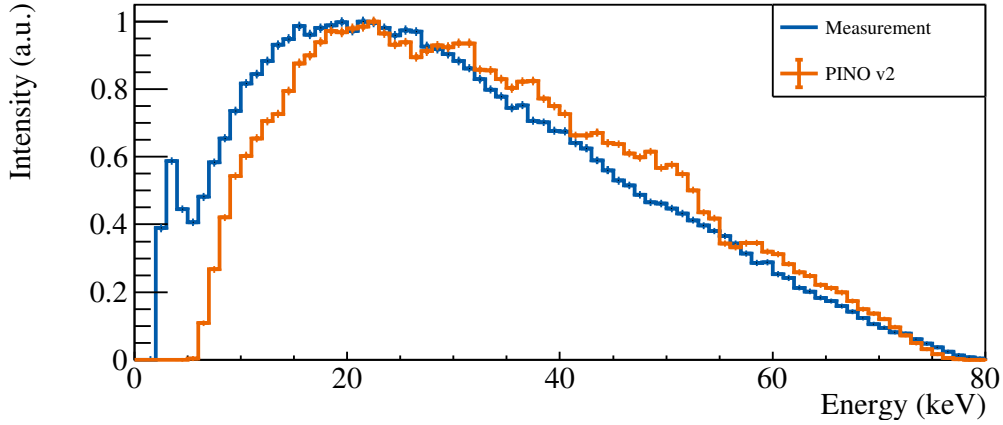


Figure 3.38.: Measured and simulated neutron energy distribution at a proton energy of $E_p = 1894 \text{ keV}$. A shift of the maximum between simulated and measured spectra of 5 keV towards lower energies is clearly visible.

For a bin per bin comparison the heat maps of the measurement, simulation and difference ratio are shown in Figure 3.39. As already noticed during the measurement of the previous energy, the simulation seems to underestimate the number of neutrons in the highest energy region slightly. The spectra obtained at 0° , 5° , and 10° degrees however show significantly less neutrons than predicted by the simulation, especially between 60 and 70 keV. This might be due to an incorrect setting of detector III since this detector was responsible for the coverage of these angles. During the measurement a fair amount of noise was visible in the low energy region of the spectrum, which is again most likely linked to a non-optimized experimental setting and scattered low energy neutron. This makes the correct measurement of the low energy region of the presented spectra difficult. Expect for the contribution of detector III a good agreement between simulation and measurement is visible.

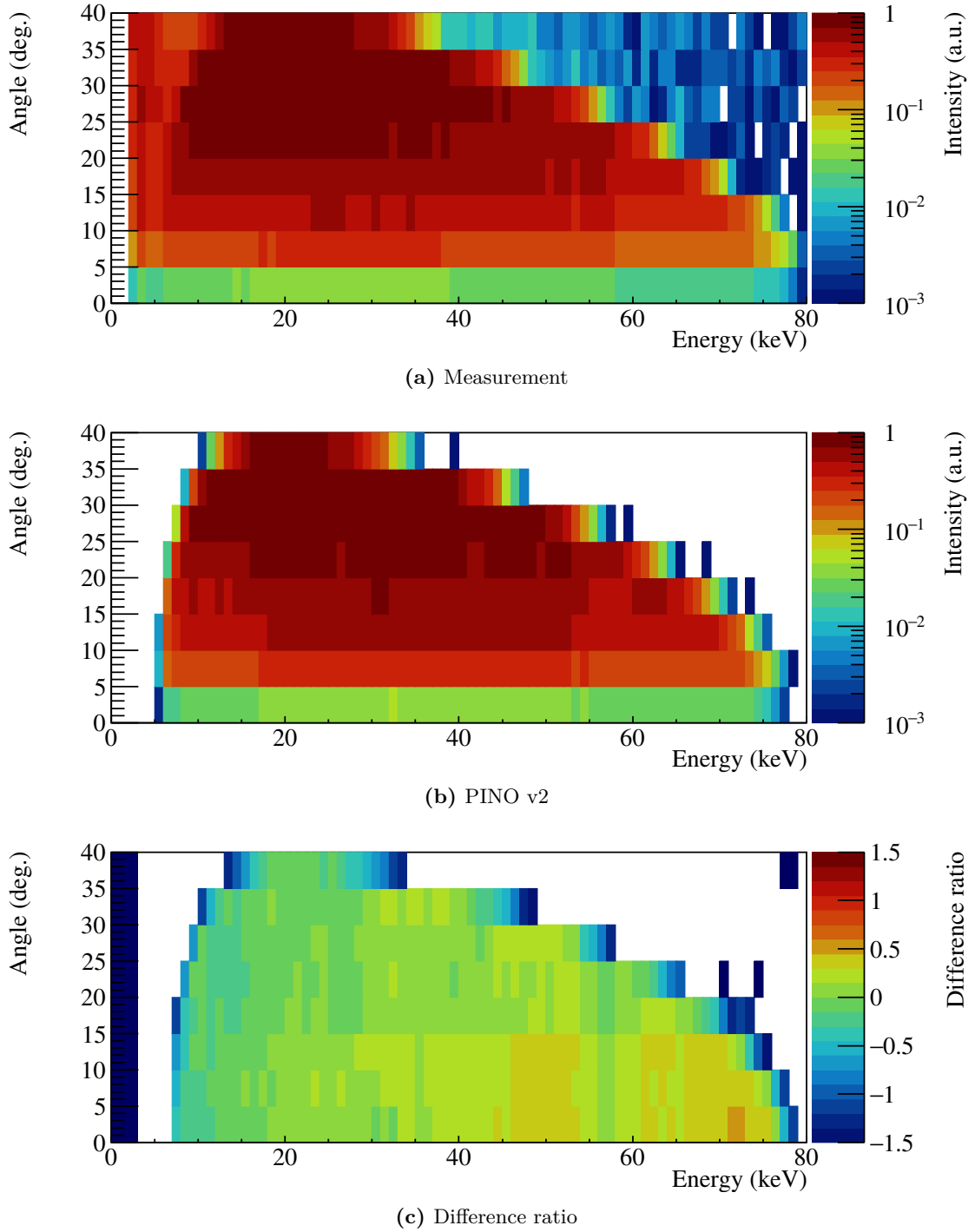


Figure 3.39.: Heats maps for better comparison between simulation and measurements. Proton energy $E_p = 1894$ keV.

3. Investigation of the ${}^7\text{Li}(p,n){}^7\text{Be}$ neutron fields

$$E_{p, \text{ set}} = 1907 \text{ keV}$$

Following the determination of the true proton energy of 1904 keV, 10 keV above the previous measurement, the neutron fields were investigated. The resulting angle-integrated neutron spectra are presented in Figure 3.40, which shows significant differences when comparing simulation and measurement. As previously seen, in the lower energies the amount of noise detected during this energy was a severe problem. For better comparison the low energy part was cut off. For a bin per bin comparison

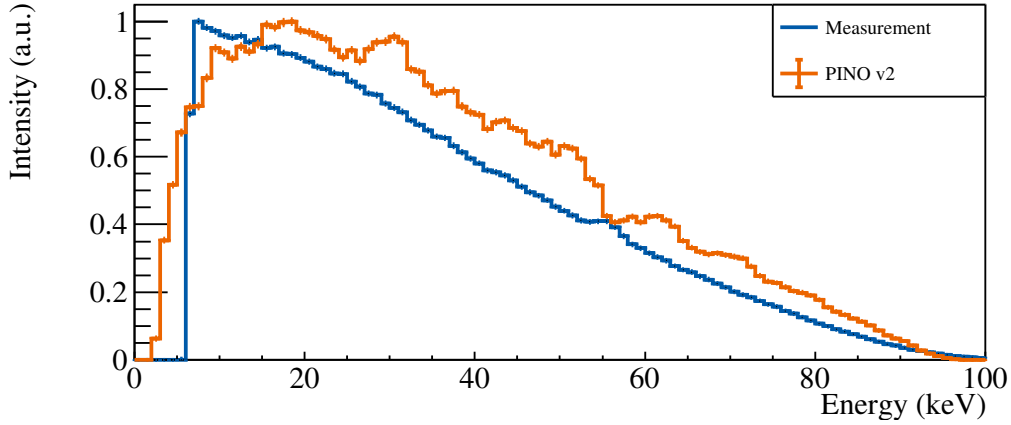


Figure 3.40.: Measured and simulated neutron energy distribution for a determined proton energy of $E_p = 1904 \text{ keV}$. The detector angles are given in Table 3.1. A direct comparison is difficult because of the noise cut off in the measured spectrum at 8 keV.

the heat maps of the measurement, simulation and the difference ratios are shown in Figure 3.41. Due to the cutoff at lower energies in the measured spectrum a large deviation is shown between measurement and simulation in the low energy part of the spectra. Additionally, the simulation underestimates the number of high-energy neutrons in the highest energy regions for each angle. As previously noticed, spectra determined at positions 0° , 5° , and 10° , which were measured using detector III, show significantly less neutrons than anticipated.

During the measurement the accelerator showed severe problems, which even caused some shut downs. In order to fix the problem and to re-tune the pulsing mechanism detector III was unmounted which most likely lead to a slightly different flight path and therefore the visible differences between simulation and measurement.

Overall the amount of noise in the spectra made the comparison nearly impossible. Only the falling edge of the spectrum, towards high energies, can be used as a benchmark.

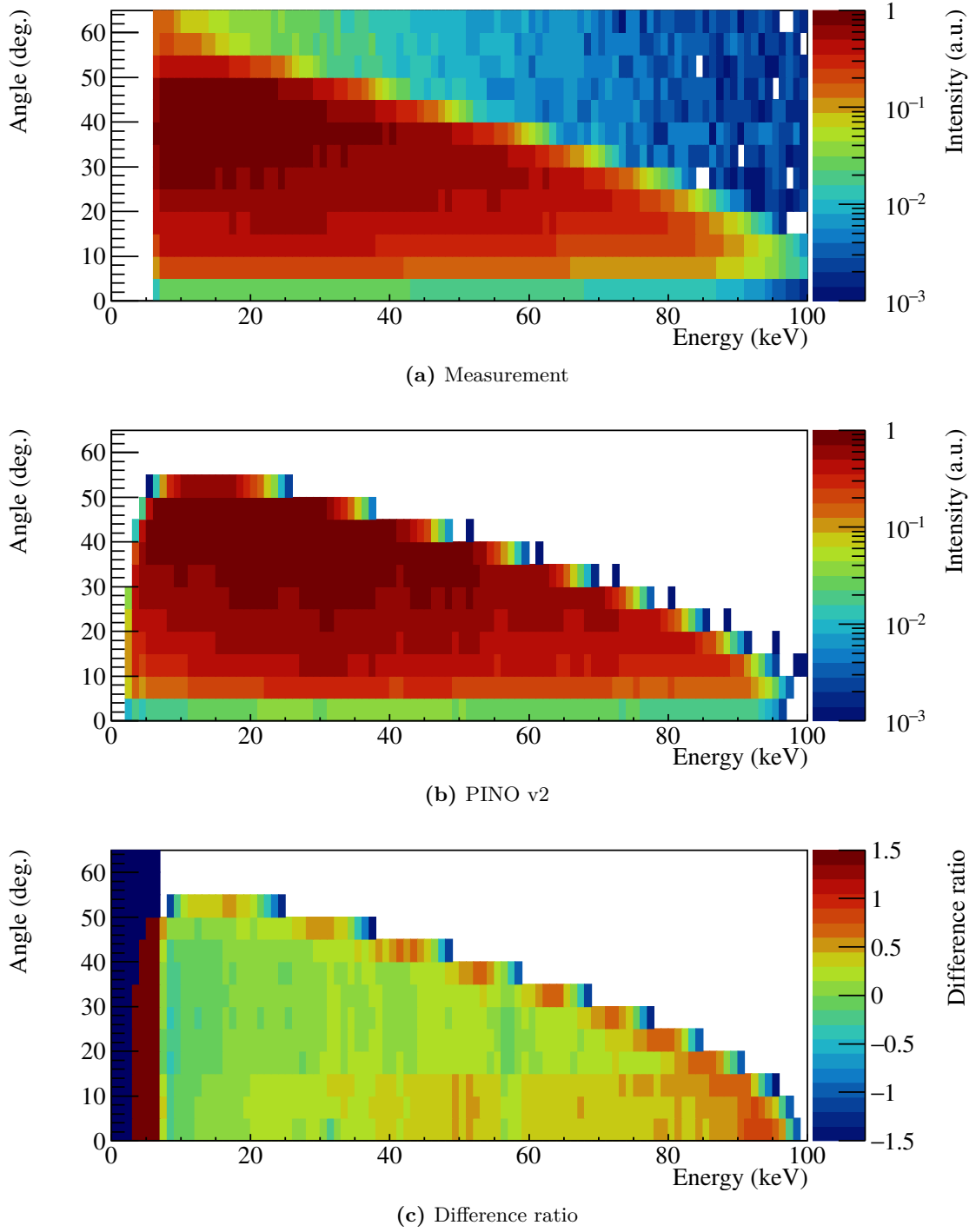


Figure 3.41.: Heat maps for better comparison between simulation and measurements. Proton energy $E_p = 1904$ keV.

3. Investigation of the ${}^7\text{Li}(p,n){}^7\text{Be}$ neutron fields

$E_{p, \text{ set}} = 1912 \text{ keV}$

The true proton energy of $E_p = 1909 \text{ keV}$ was measured as a benchmark and test of the measurement and analysis routines. The selected proton energy of interest was actually $E_p = 1912 \text{ keV}$ which has previously been measured among others by Ratinsky *et al.* and Lederer *et al.*. At a proton energy of $E_p = 1912 \text{ keV}$ the resulting angle-integrated neutron energy spectrum resembles a quasi-stellar neutron energy spectrum at $k_B T = 25 \text{ keV}$. The PINO code, which was written following the measurements of Ratinsky *et al.* was initially checked with these measurements. Lederer *et al.* remeasured the neutron fields at this proton energy with higher accuracy at the PTB.

The angle-integrated neutron spectra are presented in Figure 3.42. Apart from the low energy region, which was cut off because of excess noise in the spectrum, a good agreement between simulation and measurement is visible. For a bin per

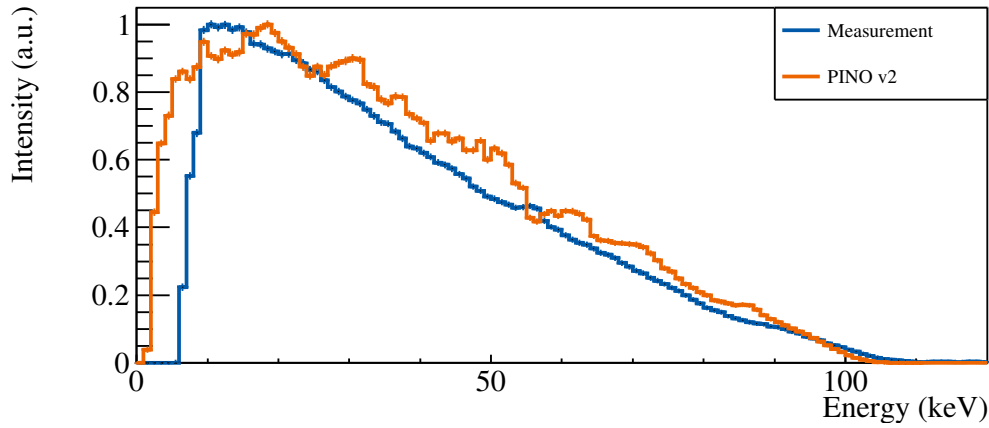


Figure 3.42.: Measured vs simulated energy spectra at a measured proton energy of $E_p = 1909 \text{ keV}$.

bin comparison the heat maps of the measurement, simulation and the difference ratio are presented in Figure 3.43. Again, the spectra measured using detector III show significantly less neutrons than predicted by the simulation, while the other detectors seem to be in good agreement between measurement and simulation. A large problem for the overall comparison at this energy as well as for the previous two lower energies is the amount of noise in the spectra. Therefore, the normalization of the maximum in the spectrum to 1 becomes very unreliable. However, because of the many measurements already been conducted to investigate this energy to a great extend, the visible agreements in the energy range above 25 keV were though to be sufficient.

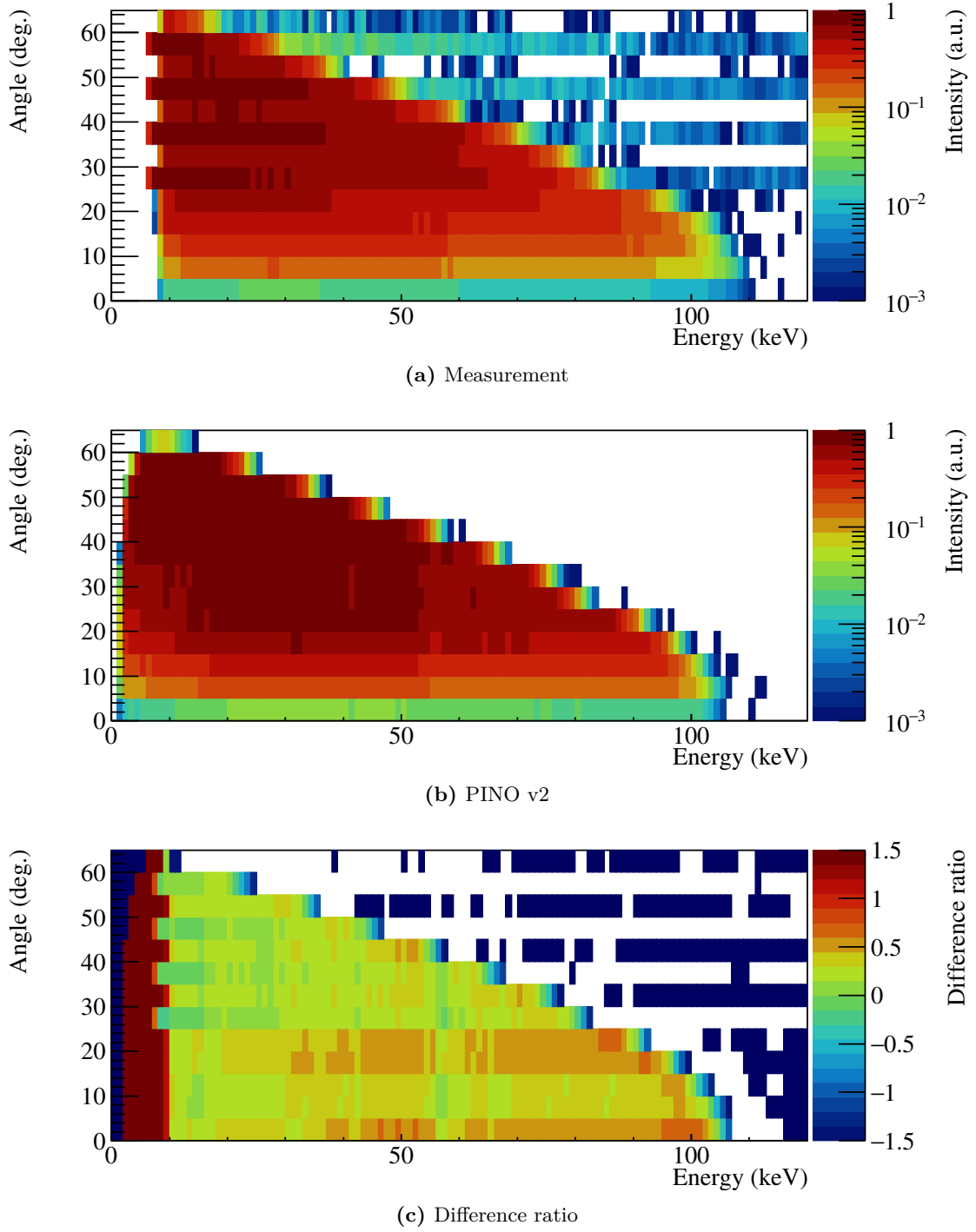


Figure 3.43.: Heat maps for better comparison between simulation and measurements. Proton energy $E_p = 1909$ keV.

3. Investigation of the ${}^7\text{Li}(p,n){}^7\text{Be}$ neutron fields

$$E_{p, \text{ set}} = 2000 \text{ keV}$$

The first energy of the high energy investigation series above 1912 keV was the set proton energy of $E_p = 2000$ keV. Using the PINO tool a true proton energy of $E_p = 1998$ keV was approximated. The neutron spectrum now covers the full solid angle.

The resulting angle-integrated neutron energy spectra presented in Figure 3.44. At this energy, differences between simulation and measurement are clearly visible. While the spectra show a good agreement in the high energy region, beginning at 160 keV on to lower energies a difference of up to 50% becomes visible. Additionally, noise is visible between 0 and 50 keV.

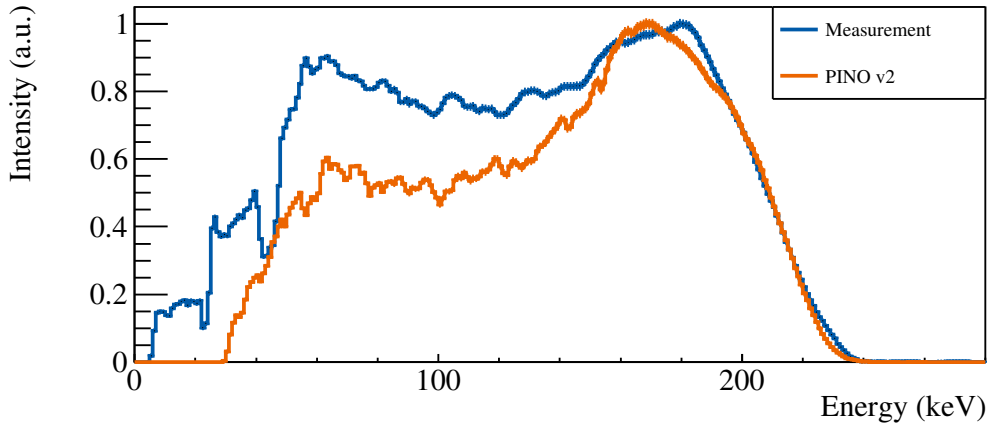


Figure 3.44.: Comparison of the angle-integrated neutron spectra at a selected proton energy of $E_p = 1998$ keV. A clear difference between simulation and measurement is visible in the intermediate energy range and the low energy range of the spectrum.

For a bin per bin comparison the heat maps of the measurement, simulation and the difference ratios are shown in Figure 3.45. The missing entries in the energy region between 40 and 50 keV are a result of a wrong calibration of the data acquisition. As previously noticed the spectra determined by detector III show the largest deviations between measurement and simulation. In the lower energy regions, measured with this detector, the simulation shows significantly more events than measured and less neutrons than expected in the low energy regions. The spectra determined using detectors I and II show a better agreement between simulation and measurement. Especially at high angles more neutrons were measured than predicted by the simulation. An overall comparison shows that, the measured neutron spectrum is slightly more narrow than the simulated one.

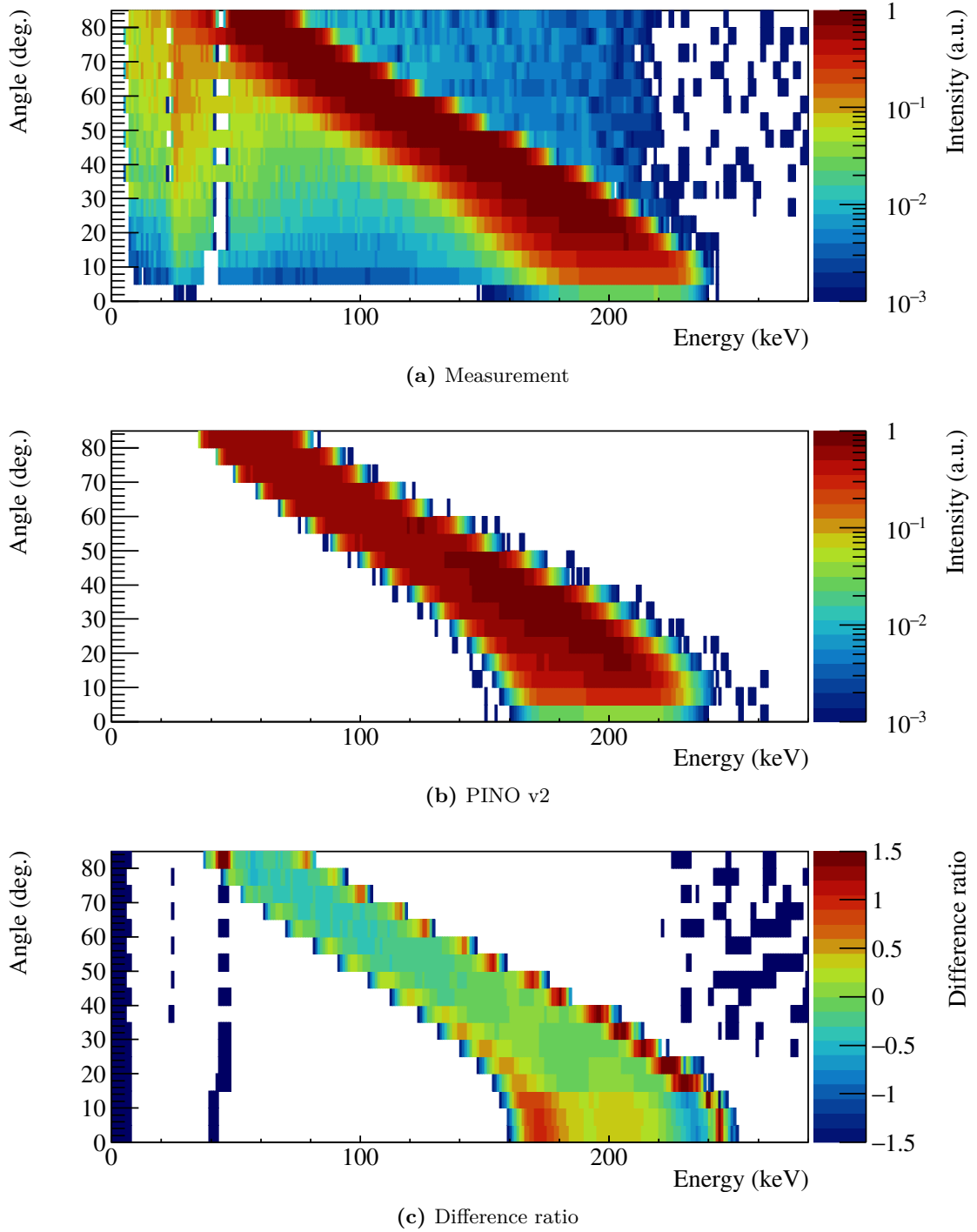


Figure 3.45.: Heat maps for better comparison between simulation and measurements. Proton energy $E_p = 1998$ keV.

3. Investigation of the ${}^7\text{Li}(p,n){}^7\text{Be}$ neutron fields

$$E_{p, \text{ set}} = 2100 \text{ keV}$$

The first energy of the experimental campaign at PIAF was $E_p = 2100 \text{ keV}$. The resulting angle-integrated neutron spectra are presented in Figure 3.46. Apart from the high energy flank a good agreement between measurement and simulation is visible. At 250 keV a dip in the measured spectrum is noticeable.

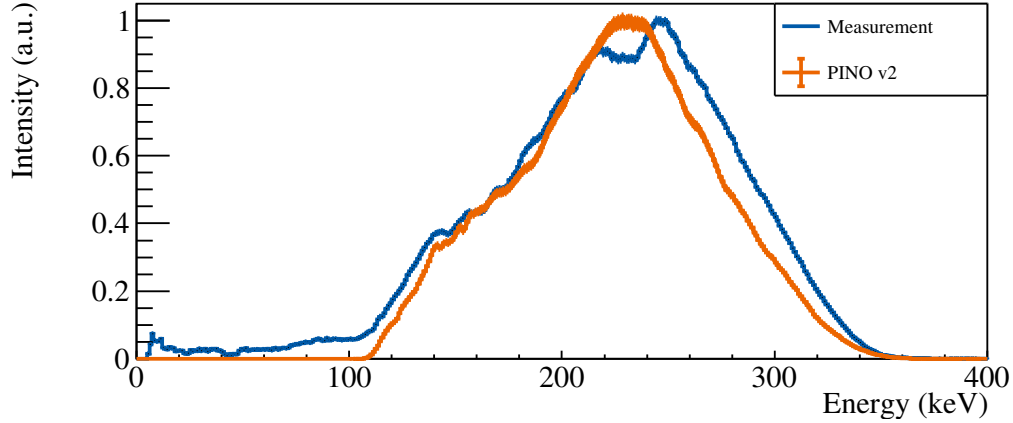


Figure 3.46.: Comparison of the angle integrated neutron spectra. As can be seen in the heat maps for this proton energy the match between simulation and measurement is very good except for the high energy flank.

For a bin per bin comparison the heat maps of the measurement, simulation and the difference ratios are shown in Figure 3.47. Spectra measured at angles above 55° show less detected neutrons in the high-energy region as predicted by the simulation. This is most likely due to an overestimated detection efficiency in this region. Spectra measured between 45° and 55° show neutron energies where the detector efficiency becomes maximal. The good agreement between simulation and measurement is therefore a direct benchmark for the simulated detector efficiencies. In contrast to the overestimation of the number of neutrons by the simulation above 55° , between 0° and 45° more neutrons were measured than expected. At the presented neutron energies the rapidly declining neutron energy resolution also becomes an uncertainty, which has to be considered when comparing the spectra. Overall a good agreement between simulation and measurement is visible.

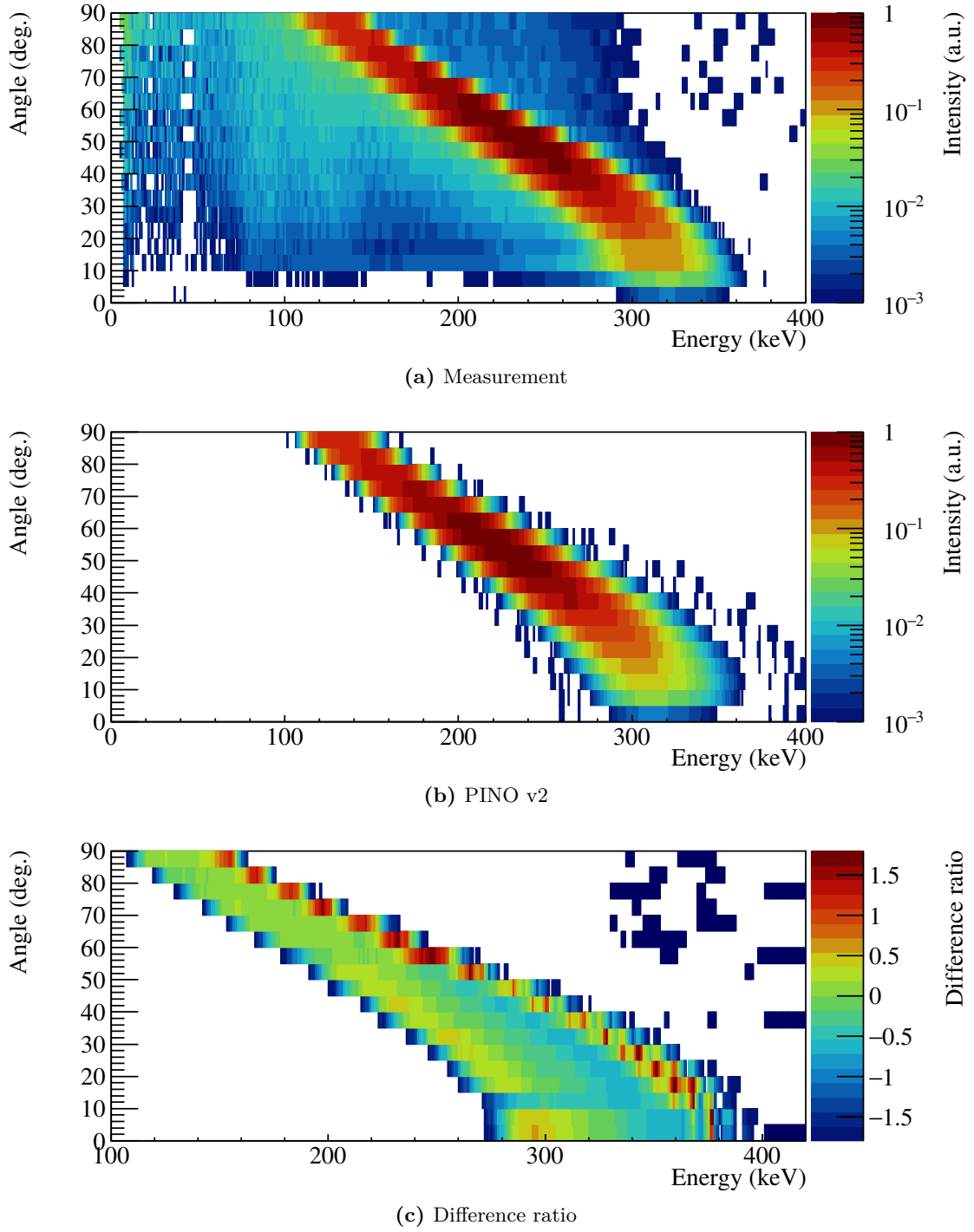


Figure 3.47.: Heat maps for better comparison between simulation and measurements. Proton energy $E_p = 2100$ keV.

3. Investigation of the ${}^7\text{Li}(p,n){}^7\text{Be}$ neutron fields

$$E_{p, \text{ set}} = 2200 \text{ keV}$$

The final proton energy during the experimental campaign was approximated to be $E_p = 2202 \text{ keV}$. Prior to the measurements, during the accelerator tuning phase, several problems regarding the neutron yield were noticed. It was concluded that the lithium target was severely degraded. In order to record a minimum of data, the angular steps were increased from 5° to 10° . During the measurements the accelerator showed problems, which also lead to shut downs and resulted in re-tunes during the measurements. This gave rise to additional uncertainties, especially in the proton energy and proton pulse length.

The angle-integrated spectra are presented in Figure 3.48. Considering the problems during the measurement a fairly good agreement between simulation and measurement is visible.

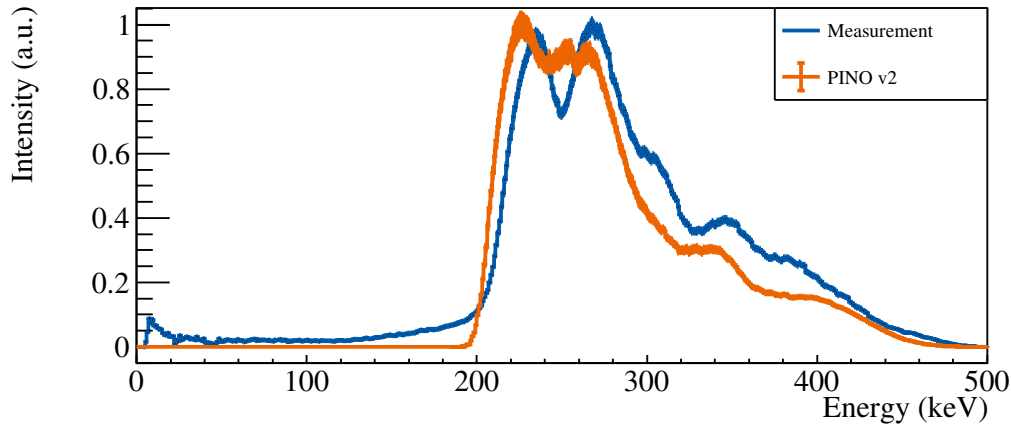


Figure 3.48.: Comparison of the angle integrated neutron spectra at a selected proton energy of $E_p = 2202 \text{ keV}$. Despite the problems during the measurement an agreement is visible.

For a bin per bin comparison the heat maps of the measurement, simulation and the difference ratios are shown in Figure 3.49. It becomes evident that at an angle of 20° almost no neutrons were detected. The reason for this remains unknown. Additionally, the spectra for each detector show more neutrons than predicted in the high energy regions at each angle but less in the lower energy regions. This is most likely a shift due to the target degradation. Overall it can be concluded, due to the problems during the measurements these results should be used carefully for further adjustments to the simulation code.

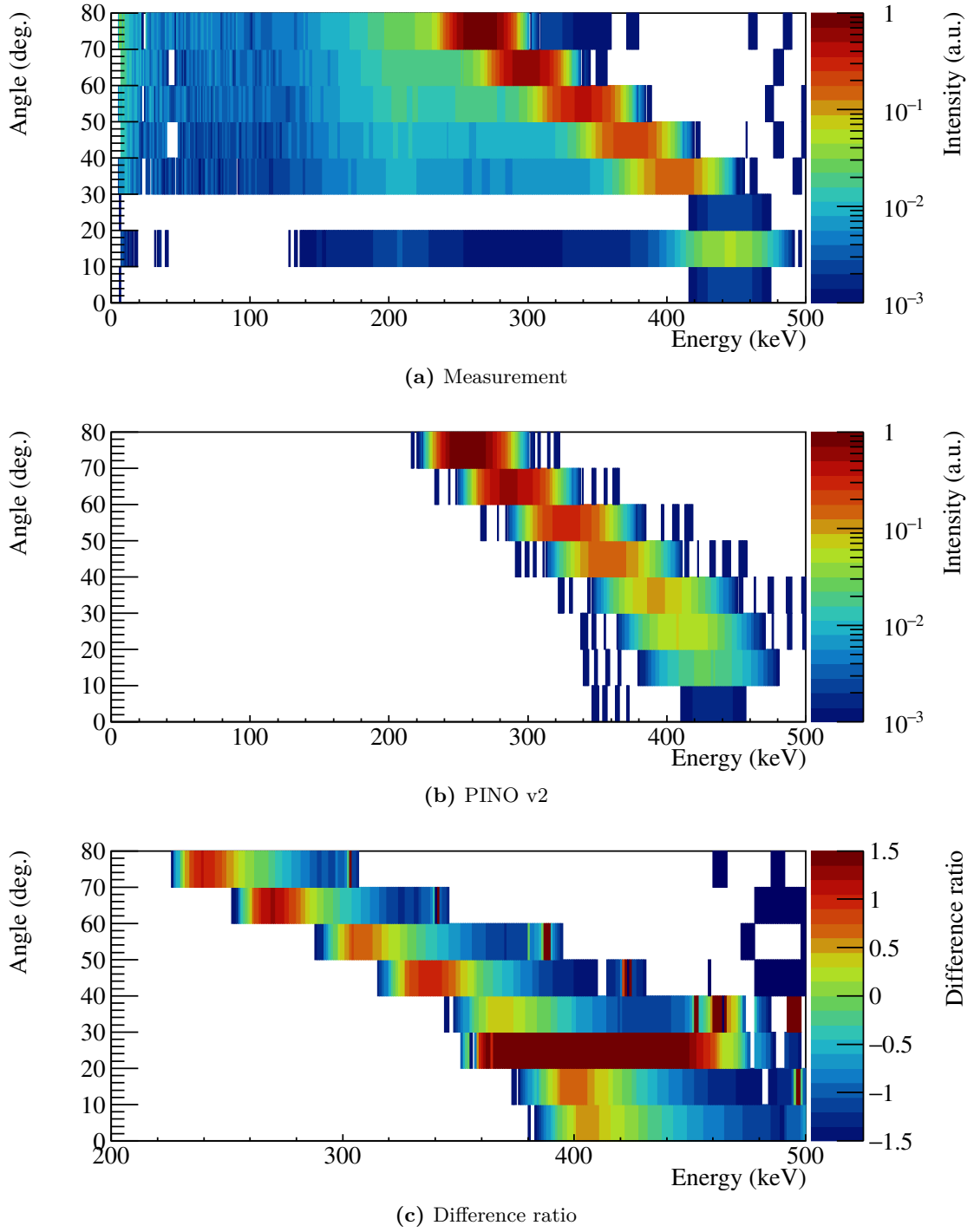


Figure 3.49.: Heat maps for better comparison between simulation and measurements. Proton energy $E_p = 2202$ keV.

3. Investigation of the ${}^7\text{Li}(p,n){}^7\text{Be}$ neutron fields

$$E_{p, \text{ set}} = 2300 \text{ keV}$$

The measurement of the neutrons fields at the last proton energy, below the second neutron production threshold, was approximated to be $E_p = 2305 \text{ keV}$. The resulting angle-integrated neutron spectra are presented in Figure 3.50, where a good agreement between simulation and measurement is noticeable. However, a peak structure is visible in the measured energy spectrum that does not occur in the simulation. Additionally, a structure is visible between 200 and 250 keV with unknown origin. For

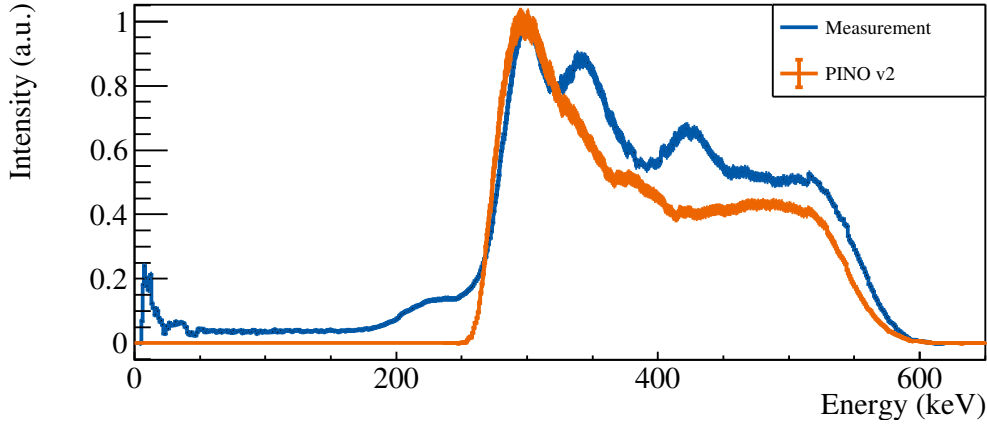


Figure 3.50.: Angle-integrated neutron spectra for $E_p = 2305 \text{ keV}$.

a further bin per bin comparison the heat maps are shown in Figure 3.51. Considering the measured spectra shown in the heat map, two minor peaks are noticeable, which are though to be responsible for the structure visible at this energy region in the angle-integrated neutron spectrum. The origin is unknown but this is probably the result of scattered neutrons. Overall the difference ratio shows a slight overestimation by the simulation on the low energy end of the neutron spectra at positions up to 45° . The two peaks visible in the angle-integrated neutron spectrum, in the energy range between 300 and 400 keV in Figure 3.50, are most likely the result of an incorrect angle setting. During the measurement the computer system responsible for the correct angle settings crashed and the angles had to be set manually, which most likely resulted in an error. Therefore, the step size between the measurements was smaller resulting in the creation of a peak structure. An additional uncertainty in the comparison arises due to the limited neutron energy resolution. Despite some problems the resemblance between simulation and measurement is very good, but as presented the measurement shows more neutrons than predicted in the high energy range of each spectrum.

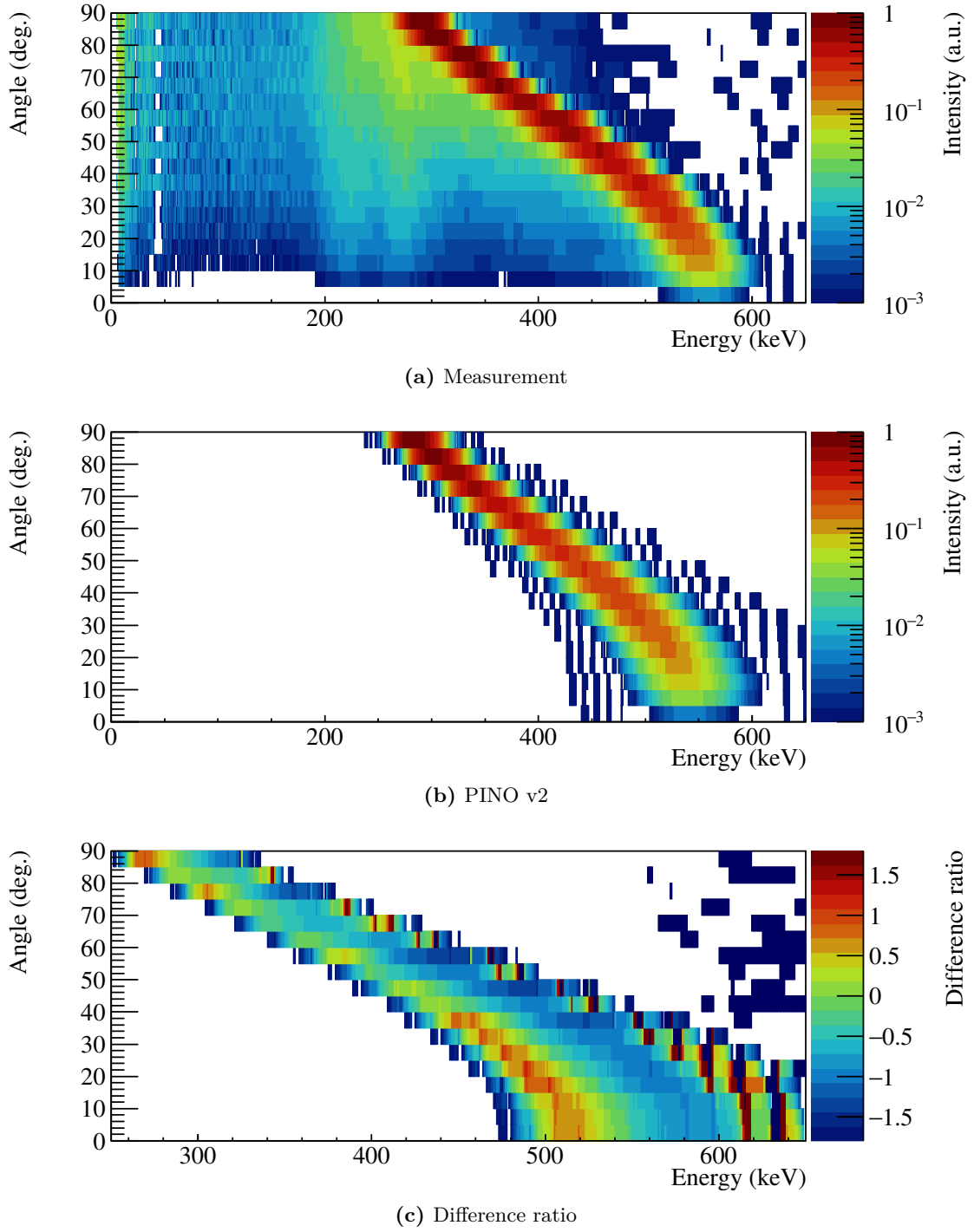


Figure 3.51.: Heat maps for better comparison between simulation and measurements. Proton energy $E_p = 2305$ keV.

3. Investigation of the ${}^7\text{Li}(p,n){}^7\text{Be}$ neutron fields

$$E_{p, \text{ set}} = 2500 \text{ keV}$$

For the measurement of the neutron fields at the set proton energy of $E_p = 2500 \text{ keV}$, a true proton energy of $E_p = 2490 \text{ keV}$ was approximated. At this energy the second neutron production channel becomes available. During the analysis of the measurement the limited neutron-energy resolution becomes clearly visible. The angle-integrated neutron spectra are presented in Figure 3.52. Additionally, to a neutron energy distribution between 400 and 800 keV originating from the main neutron production channel, two other structures are visible. One of the structures

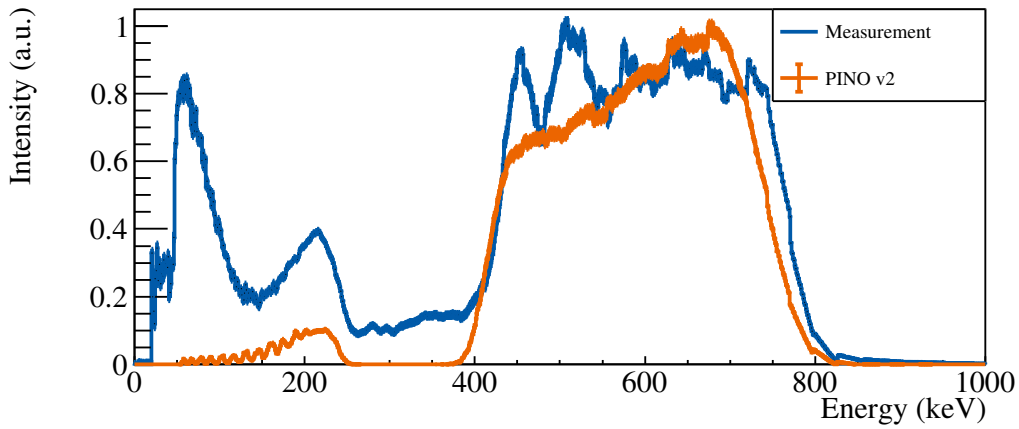


Figure 3.52.: Angle-integrated neutron spectra for $E_p = 2490 \text{ keV}$.

between 50 and 250 keV originates in the second neutron production channel as described in section 2.5.1. The peak structure in the beginning of the measured spectrum is most likely a product of scattered neutrons. In the measured energy spectrum a peak structure becomes evident in the energy range of the main neutron production channel, between 400 and 800 keV. For the bin per bin comparison heat maps of the measurement, simulation and the difference ratio are shown in Figure 3.53. The difference ratio shows each measured spectrum covers a narrower energy range than predicted. This is the reason for the peak structure visible in Figure 3.52. Additionally, the true proton energy might have been slightly higher than 2490 keV. Due to the limited neutron energy resolution the correct determination of the true proton energy was challenging. Furthermore, it is clearly visible that the neutron distribution from the second neutron production channel is underestimated by the simulation. Overall a good agreement for the main neutron production channel is visible. This is not the case for the second neutron production channel. The narrower

energy range of the measured spectra gives rise to further investigations at a longer flight path and therefore, a better energy resolution.

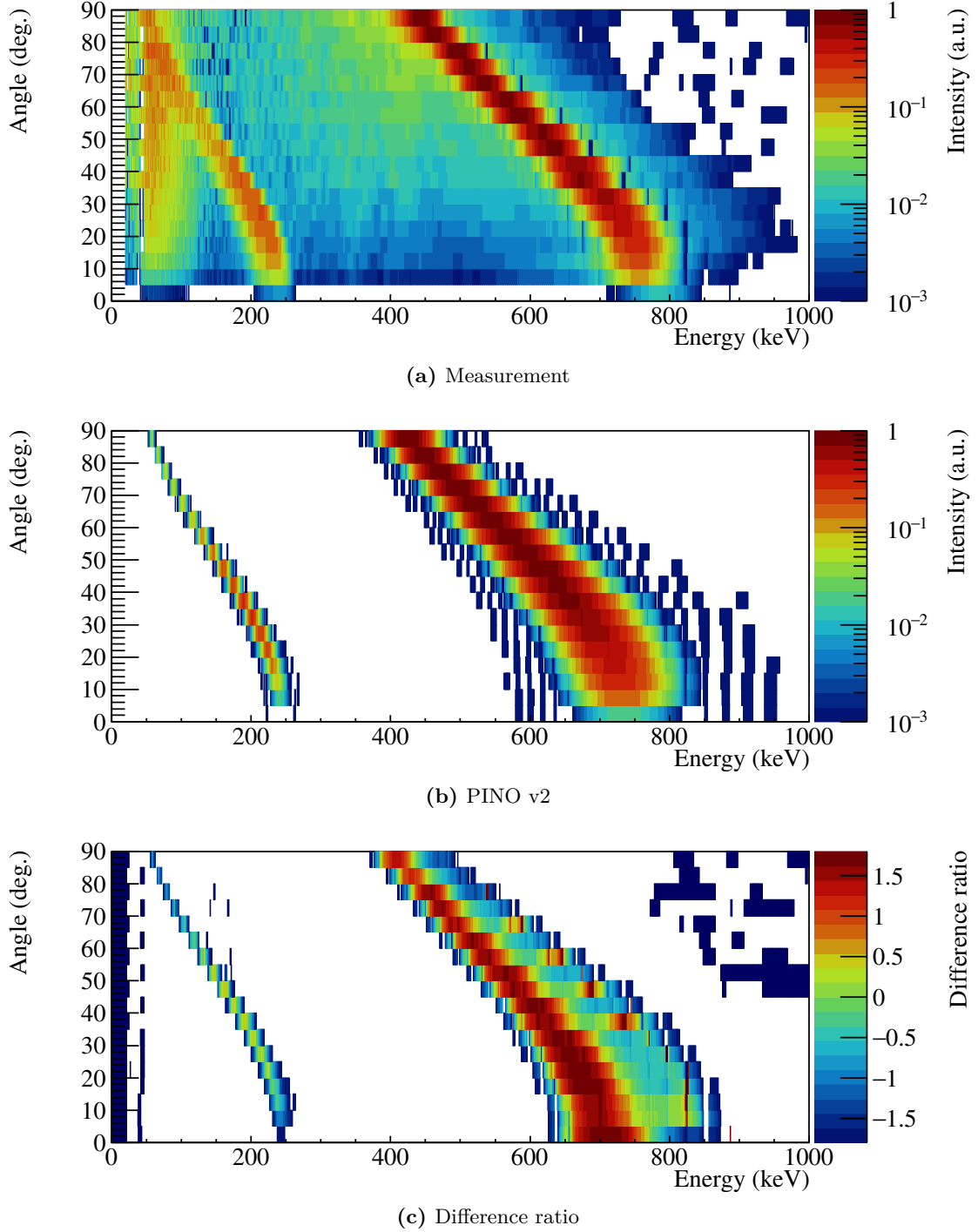


Figure 3.53.: Heat maps for better comparison between simulation and measurements. Proton energy $E_p = 2490$ keV.

3. Investigation of the ${}^7\text{Li}(p,n){}^7\text{Be}$ neutron fields

$$E_{p, \text{ set}} = 2800 \text{ keV}$$

The highest proton energy measured during the experimental campaign was $E_p = 2791 \text{ keV}$. Again, the approximation of the true proton energy was challenging due to the narrow neutron energy distribution and the limited time resolution of the data acquisition system. The angle-integrated neutron spectra are presented in Figure 3.54. Several differences between simulation and measurement become obvious. The most prominent is the significant underestimation of the intensity of the second neutron distribution. For the bin per bin comparison the heat maps of

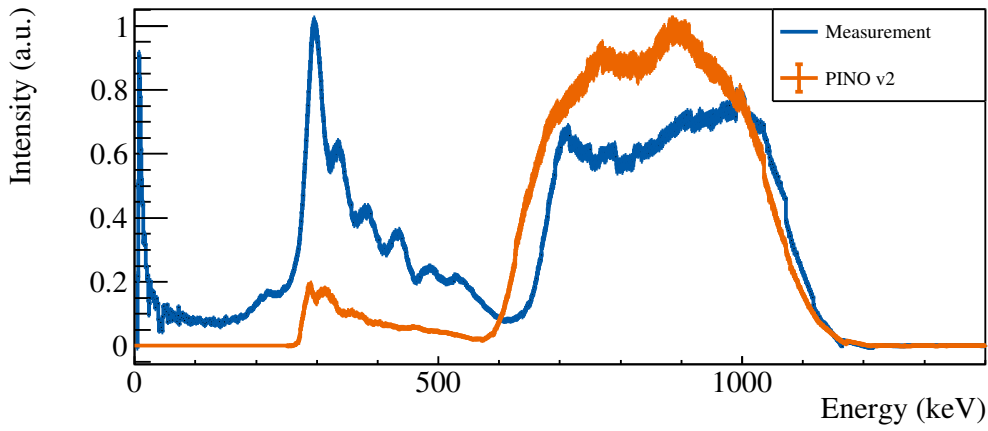


Figure 3.54.: Angle-integrated neutron spectra for $E_p = 2791 \text{ keV}$.

the measurement, simulation and the difference ratio are shown in Figure 3.55. The differences between measurement and simulation become very clear and not only lie in the second neutron-production channel, which is severely underestimated by the simulation, but also in the main neutron-production channel. The simulated spectrum for each angular setting is significantly broader than the measured neutron distribution. Regarding the angle-integrated neutron spectrum the effects of the broader simulated neutron spectra are in the range of 100 keV. The measurement at this proton energy shows a 80% higher intensity of the neutrons originating the second neutron-production channel than simulated. Overall, only a slight resemblance between measurement and simulation is visible up to a neutron energy of 500 keV. Above 500 keV the match of the main neutron production channel is satisfactory. Further investigations are needed to fully understand the simulation at this proton energy setting.

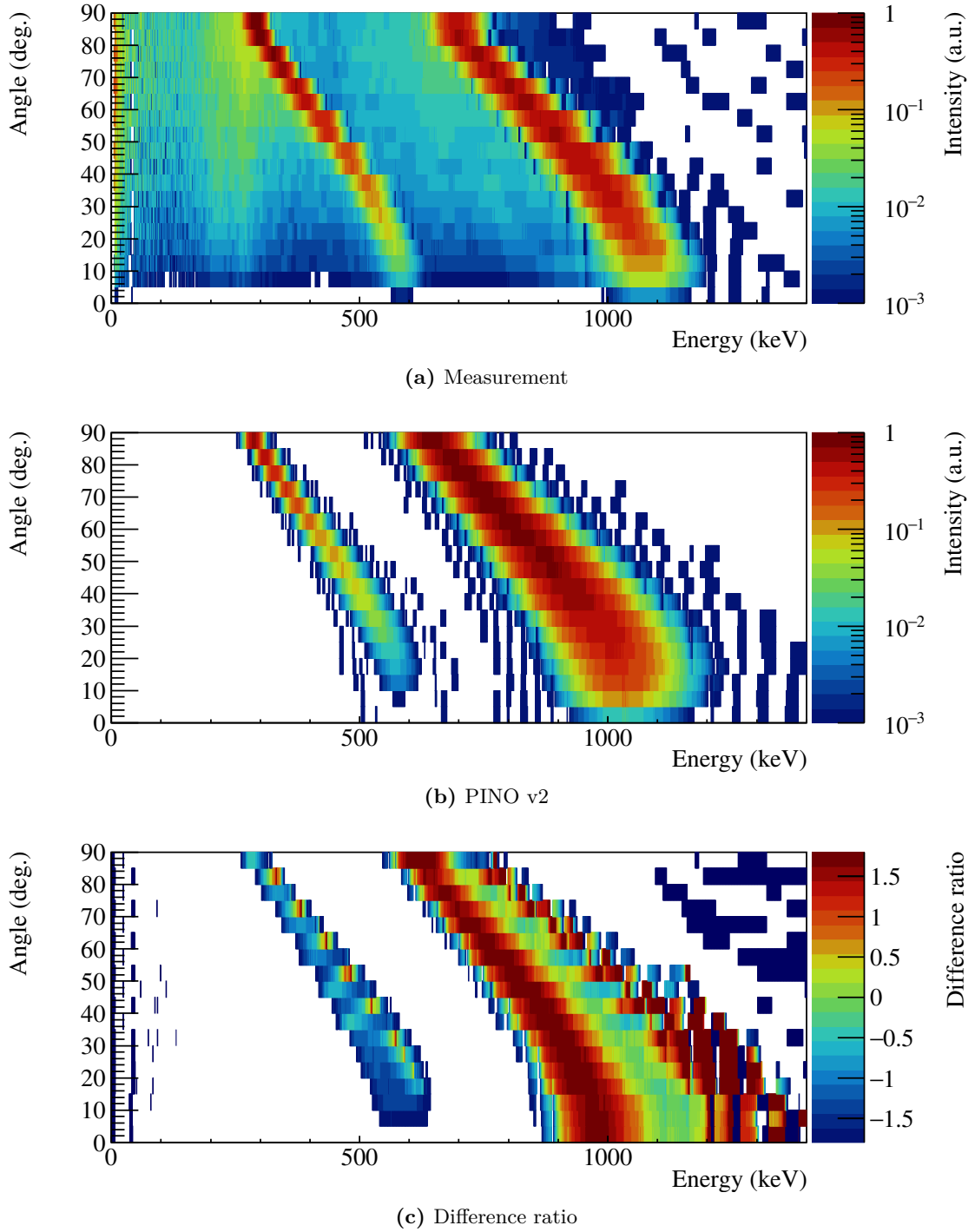


Figure 3.55.: Heat maps for better comparison between simulation and measurements. Proton energy $E_p = 2791$ keV.

4. Neutron activation of Gallium

An application for the ${}^7\text{Li}(\text{p},\text{n}){}^7\text{Be}$ neutron fields with an astrophysical motivation was the neutron activation campaign of gallium. To verify the obtained values by Göbel *et al.*, presented in section 1.3, a series of neutron activation experiments using various gallium samples was carried out at the 2.5 MV Van-de-Graaff accelerator at Goethe University Frankfurt. The accelerator is able to produce a continuous proton beam with a maximum energy of $E_p = 2.5 \text{ MeV}$ and an energy spread of $\Delta E = 2 \text{ keV}$ at an average beam current between 6 and 8 μA on the target. The ${}^7\text{Li}(\text{p},\text{n}){}^7\text{Be}$ reaction was used as the neutron source for all of the activation experiments described in the following.

When irradiated with protons at an energy of $E_p = 1912 \text{ keV}$, the created neutron spectrum mimics a quasi-stellar neutron spectrum at $k_B T \approx 25 \text{ keV}$. The expected neutron spectrum at the sample position was simulated using the PINO tool with the input values given in Table C.6 and is presented in Figure 2.6. The sample was placed between two neutron flux monitors at the end of the beamline very close to the neutron production target. Since the neutrons at this energy are emitted in a forward cone with an opening angle of 120° , this ensured the total coverage of the neutron cone by the sample. During the irradiation the proton current was continuously monitored and recorded using a current integrator. The time-dependent neutron flux during the activation was recorded using a ${}^6\text{Li}$ -glass scintillator as a neutron detector. A schematic of the experimental setup during the activation is shown in Figure 2.5. Four different activation experiments were carried out. During the first three activations gallium samples with a thickness of 0.5 mm were used. During the last experiment elastic neutron scattering inside the sample as well as the neutron transmission of the samples were investigated and therefore, samples with different thicknesses were used. As a simplification the experiments will be henceforth called: Activation I, II, III and IV. The properties of the activated samples are shown in Table C.2. During all of the presented activations, thin gold foils were used as neutron flux monitors, due to the well known neutron capture cross section of ${}^{197}\text{Au}$.

4.1. Activation analysis

The determination of the neutron capture cross section ratios between gallium and gold is the main goal of the following activations. This value can be calculated via

$$\frac{\sigma_{\text{Ga}}}{\sigma_{\text{Au}}} = \frac{\frac{N_{\text{Ga,prod.}}}{N_{\text{Ga,sample}}}}{0.5 \cdot \left(\frac{N_{\text{Au,front,prod.}}}{N_{\text{Au,front,sample}}} + \frac{N_{\text{Au,back,prod.}}}{N_{\text{Au,back,sample}}} \right)}, \quad (4.1)$$

where $N_{\text{prod.}}$ denotes the number of nuclei produced during the activation and N_{sample} the number of sample nuclei. The sample nuclei N_{sample} were determined using the sample masses and isotopic abundances. The number of produced nuclei $N_{\text{prod.}}$ were determined by γ -spectroscopy. The radioactive reaction products were investigated using a head-to-head setup of two almost identical, cylindrical, Broad Energy Germanium detectors (BEGe) [67]. The number of produced nuclei during the activation can be determined by

$$N_{\text{prod.}} = \frac{N_{\gamma}}{\varepsilon(E_{\gamma}) I_{\gamma} \kappa f_{\text{b}} f_{\text{wm}} f_{\text{dt}} f_{\text{casc}}}, \quad (4.2)$$

where N_{γ} denotes the counts in the investigated γ -line, $\varepsilon(E_{\gamma})$ the detector efficiency at energy E_{γ} , κ the sample γ -self-absorption, I_{γ} the γ -line intensity, f_{b} the correction factor for the decays during the activation, f_{wm} the correction factor for decaying nuclei between the stop of the activation and the start of the measurement as well as the correction for decaying nuclei after the measurement, f_{dt} the correction for the detector dead time and $f_{\text{casc.}}$ the cascade and summing correction. The correction factor f_{wm} relies on correct time keeping, which was ensured by the use of synchronized clocks.

For the analysis the correction factors for the γ -intensity I_{γ} , the self absorption κ , the cascade correction f_{casc} and the efficiency were determined by GEANT-3 [16] simulations. These correction factors were combined into the simulation correction factor f_{sim} which leads to

$$N_{\text{prod.}} = \frac{N_{\gamma}}{f_{\text{b}} f_{\text{wm}} f_{\text{dt}} f_{\text{sim}}}. \quad (4.3)$$

The uncertainties of the simulation correction factors f_{sim} were determined by Gaussian error propagation between the uncertainties of the respective γ -line intensities and the simulation itself. The uncertainty of the simulation was assumed to be 5%.

The dead time correction factor was determined by comparing real and live time of the measurement. These values were given by the data acquisition system

$$f_{\text{dt}} = \frac{t_{\text{live}}}{t_{\text{real}}}. \quad (4.4)$$

The correction for the decaying nuclei during waiting time and the measurement are calculated by

$$f_{\text{wm}} = \exp(-\lambda t_{\text{w}}) [1 - \exp(-\lambda t_{\text{m}})], \quad (4.5)$$

where λ is the decay constant for the respective isotope. The correction for the decays during the activation f_{b} takes the fluctuations of the neutron flux into account. The flux was monitored continuously in time intervals of 1 ns with a ^6Li -Glass detector. The correction factors have to be calculated for the respective isotopes of gallium and gold via

$$f_{\text{b}} = \frac{\sum_i \Phi_i \exp[-\lambda(t_a - i\Delta t)]}{\sum_i \Phi_i}, \quad (4.6)$$

where Φ_i denotes the counts in the neutron detector for each time interval Δt , the activation duration t_a and the decay constant of the activation product λ .

Additionally to the cross sections ratio, following the determination of the produced nuclei, the spectrum averaged cross sections can be determined by

$$\sigma_{\text{SACS}} = \frac{N_{\text{prod.}}}{N_{\text{sample}} \cdot \Phi_{\text{n}}}, \quad (4.7)$$

where Φ_{n} denotes the total neutron flux through the sample which can be determined using the gold monitors in front and behind the sample of interest. Because of the well known neutron capture cross section of ^{197}Au , Equation 4.7 can be adjusted to determine the neutron flux through the respective neutron flux monitor

$$\Phi_{\text{n}} = \frac{N_{\text{prod.}}^{\text{Au}}}{N_{\text{sample}}^{\text{Au}} \cdot \sigma_{\text{SACS}}^{\text{Au}}}. \quad (4.8)$$

The neutron flux differs slightly between the upstream (front) and downstream (back) monitor. A median value representing the neutron flux through the sample has to be determined by

$$\bar{\Phi}_{\text{n}} = \frac{1}{2} \cdot (\Phi_{\text{n}}^{\text{upstream}} + \Phi_{\text{n}}^{\text{downstream}}) \quad (4.9)$$

The values for the $\sigma_{\text{SACS}}^{\text{Au}}$ at the respective positions can be taken from the simulation tool PINO.

4.1.1. Ga analysis

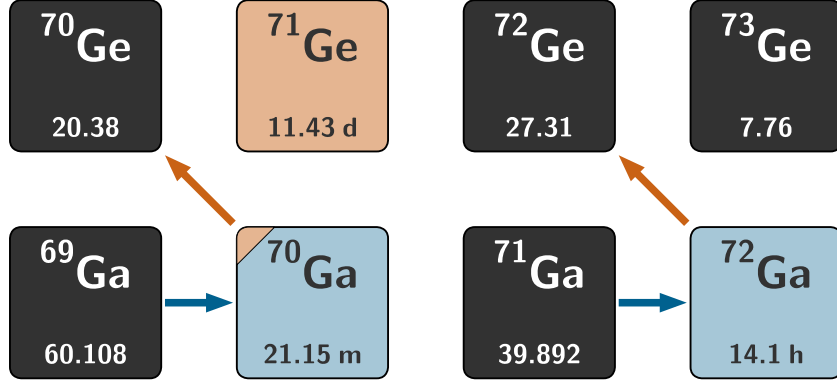


Figure 4.1.: Excerpt from the chart of nuclides in the region of the reactions of interest. The neutron capture reactions are marked with a blue arrow. The subsequent β^- -decay is depicted with a red arrow.

The decay of the produced gallium isotopes ^{70}Ga and ^{72}Ga can be investigated by analyzing various γ -lines. The neutron capture reactions and the subsequent decay are shown in Figure 4.1. The γ -lines of interest during the following activation analysis are presented in Table 4.1. For the analysis of the decay of ^{72}Ga only γ -lines between 600 and 1100 keV are considered, due to imprecise efficiency values above these energies. This is a result of the limited number of efficiency calibration samples. Therefore, the simulations can not be verified above 1400 keV and would be an additional source of uncertainty. To determine the number of produced ^{198}Au nuclei and therefore, the neutron flux the 411.8 keV γ -line was used.

Decay of	γ energy (keV)	Intensity I_γ (%)	Reference
^{70}Ga	176.115 (13)	0.294 (9)	[36]
	1039.513 (10)	0.65 (5)	
^{72}Ga	629.967 (19)	26.13 (4)	[1]
	834.13 (4)	95.45 (8)	
	894.327 (18)	10.136 (15)	
	1050.794 (17)	6.991 (11)	
^{198}Au	411.80205 (17)	95.62	[39]

Table 4.1.: γ -emission lines of interest during the analysis of the following activation measurements.

4.2. Experimental preparations

Prior to the execution of the activation experiments, the samples and gold monitors were prepared. This included the re-weighting of each sample and gold monitor, as well as the correct positioning of the sample and neutron monitors on Kapton foil and onto stainless steel sample holder rings. Additionally, the gallium samples were covered with a second layer of Kapton, as a safety measure to prevent possible molten gallium contamination due to the low melting point of 29.8°C . In Figures 4.2 and 4.3 two gallium samples are shown during the sample preparation. The gallium samples and the gold monitors feature the same diameter in order to simplify the determination of the neutron flux analysis.

The neutron production target was produced by vapor deposition of metallic lithium onto a copper backing. For the offline analysis of the activation products the used detectors for γ -spectroscopy were calibrated, using calibration sources presented in Table C.1, to ensure a correct detection of the photons of interest. The schematic of the used detector setup is presented in Figure 4.4.

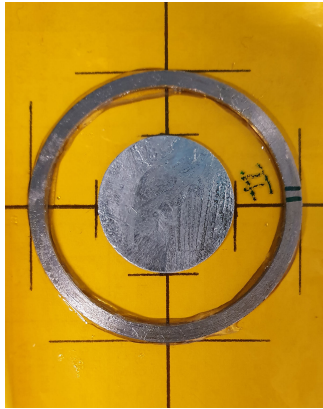


Figure 4.2.: Natural gallium sample glued onto Kapton foil and fenced in by a stainless steel sample ring.

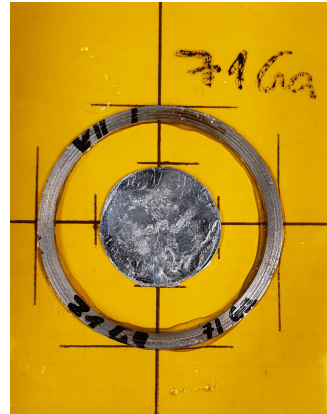


Figure 4.3.: Enriched ^{71}Ga sample glued onto Kapton foil and fenced in by a sample ring.

4.2.1. Detector energy calibration

For the analysis of the activated samples, two BEGe-detectors were coupled to an analog data acquisition system as described in subsection 2.4.1. To reach the best possible experimental results, the detectors were calibrated before each activation experiment. The first step of a series of calibrations is the energy calibration. The output of the spectroscopy amplifiers is handed over to the ADCs, which are connected

4. Neutron activation of Gallium

to the Multiparameter System (MPA), which is a fast list mode system with a total of four inputs. This system is connected to a computer via IDE connection. Using the MPA software the spectra can be recorded and analyzed via the sorting of events depending on their signal amplitude. The result is a pulse-height spectrum, which is not yet suitable for further analysis. The conversion from pulse-height to energy spectrum is carried out using radioactive calibration sources. These sources emit γ -quanta with well known energies. The preferred correlation between channel and energy is linear. To verify the linearity between signal amplitude and γ -energy, spectra with several different calibration sources have to be recorded. The linear energy calibration function is defined as

$$E_\gamma = \alpha \cdot \text{Channel} + \beta, \quad (4.10)$$

where α and β denote the calibration parameters, which can be evaluated by a linear fit of the function to the data points.

4.2.2. Detector energy resolution

The energy resolution of the detector is crucial for the analysis of γ -emitters with more than one γ -line. The energy resolution determines the ability to distinguish between two close lying γ -energy lines. Since peaks in the spectrum have a Gaussian shape due to fluctuations in the number of produced ionizations and excitations, the energy resolution at a specific energy, ΔE_γ , is determined by the full width at half maximum (FWHM) in keV [45]. The relative energy resolution is

$$R = \frac{\Delta E_\gamma}{E_\gamma}. \quad (4.11)$$

A small peak width is also crucial to differentiate γ -lines originating from the decay of interest or other decays, such as natural background or possible contamination of the sample.

4.2.3. Detector efficiency

The detector efficiency is an important value for the correct analysis of γ -spectra. The full energy peak efficiency ε_{FEP} takes only events corresponding to a full energy peak in the γ -spectrum into account [41]. To determine the detector efficiency over

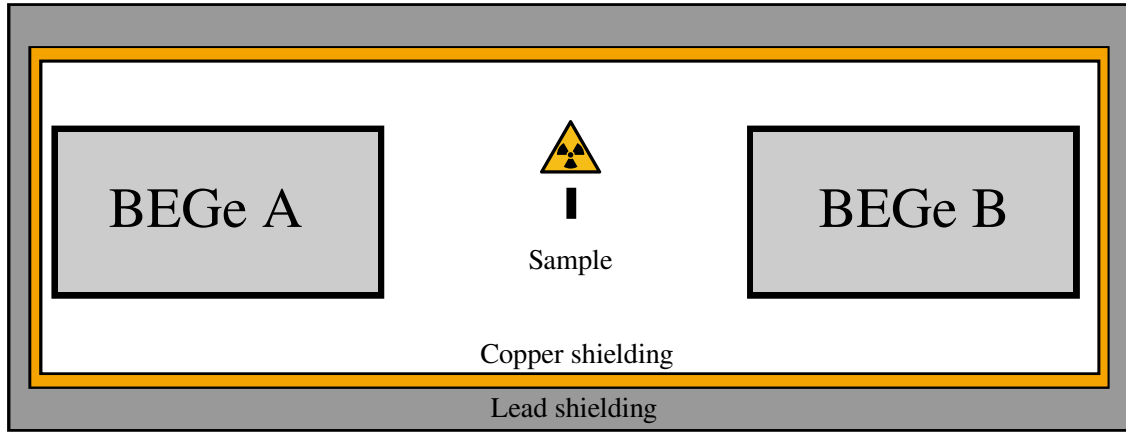


Figure 4.4.: Schematic of the BEGe detector setup used for γ -spectrometry. The detectors are placed inside copper and lead shielding to lower the ambient background.

a broad energy range, various calibration sources with well-known γ -emission line energies and activity are used. By analyzing the obtained spectra of these sources the full energy peak efficiency can be determined by

$$\varepsilon_{\text{FEP}}(E) = \frac{N_{\text{FEP}}(E)}{A_0^{\text{ref}} \exp(-\lambda t_w) I_\gamma(E) t_m f_{\text{dt}}}, \quad (4.12)$$

where $N_{\text{FEP}}(E)$ is the number of counts in the full energy photo peak, A_0^{ref} the activity of the radioactive source in decays per second (Bq) at the time of the calibration, t_w the duration between reference time of the calibration source and the time of measurement in seconds, $I_\gamma(E)$ the emission probability of a photon with energy E , t_m the duration of the measurement and f_{dt} the dead time correction factor. If the γ -quanta are emitted in a cascade, the efficiency has to be corrected for this. Equally for summing effects, which is the detection of two or more γ -quanta in a time frame which is too short for the detector to distinguish between two separate events. While summing corrections can be avoided by reducing the source activity, for example by increasing the distance between source and detector, cascade effects can not easily be avoided. In order to correct the events in the full energy photo peak for cascade effects, Monte Carlo simulations of the detector geometry and of the decay of the radionuclides used are commonly used.

4.3. Activation I

The first experiment of the activation campaign took place in December 2019 at Goethe University, Frankfurt. A total of four different activations were carried out. The properties of the used samples are listed in Table C.2. For the natural gallium sample the isotopic abundance was taken from [50]. For the enriched samples the isotopic abundance of the respective gallium isotope was taken from the specifications provided by the manufacturer [23, 24]. As neutron flux monitors two gold foils with a matching diameter to the sample and a thickness of 0.00125 mm were used for each activation. Identically to the gallium samples, the sample nuclei of the gold samples were determined by their weight and isotopic abundance. The specification of the used gold samples for this activation are presented in Table C.5. The neutron production target for the activation, a metallic lithium target, was prepared by evaporation onto a copper backing with a thickness of 0.5 mm. The thickness of the lithium layer was determined by a quartz crystal monitoring system to be approximately 22 μm . The accelerator energy was set to $E_p = 1912 \pm 2 \text{ keV}$ for the production of a quasi-stellar neutron spectrum with $k_B T \approx 25 \text{ keV}$. During the activation the proton current on the lithium target and the neutron flux were recorded using a current integrator and a ^6Li -glass scintillator mounted behind the activation setup at the end of the beamline at a distance of 30 cm from the lithium target.

Following the activation of samples with different durations, presented in Table 4.2, the irradiated samples were transported and placed before the two BEGe-detectors to record the decay of the reaction products. In order to minimize summing and cascade effects the distance between the detectors and the sample was set to 10.3 cm, ensuring a good compromise between efficiency and summing effects.

Sample	Activation	Activation time
natGa I	I	42.0 min
^{69}Ga	I	42.0 min
^{71}Ga	I	2.0 h
^{69}Ga	II	41.5 min

Table 4.2.: Activated samples and the irradiation times during the activation experiment. The durations for the activations were chosen in reference to the half life of the produced isotopes.

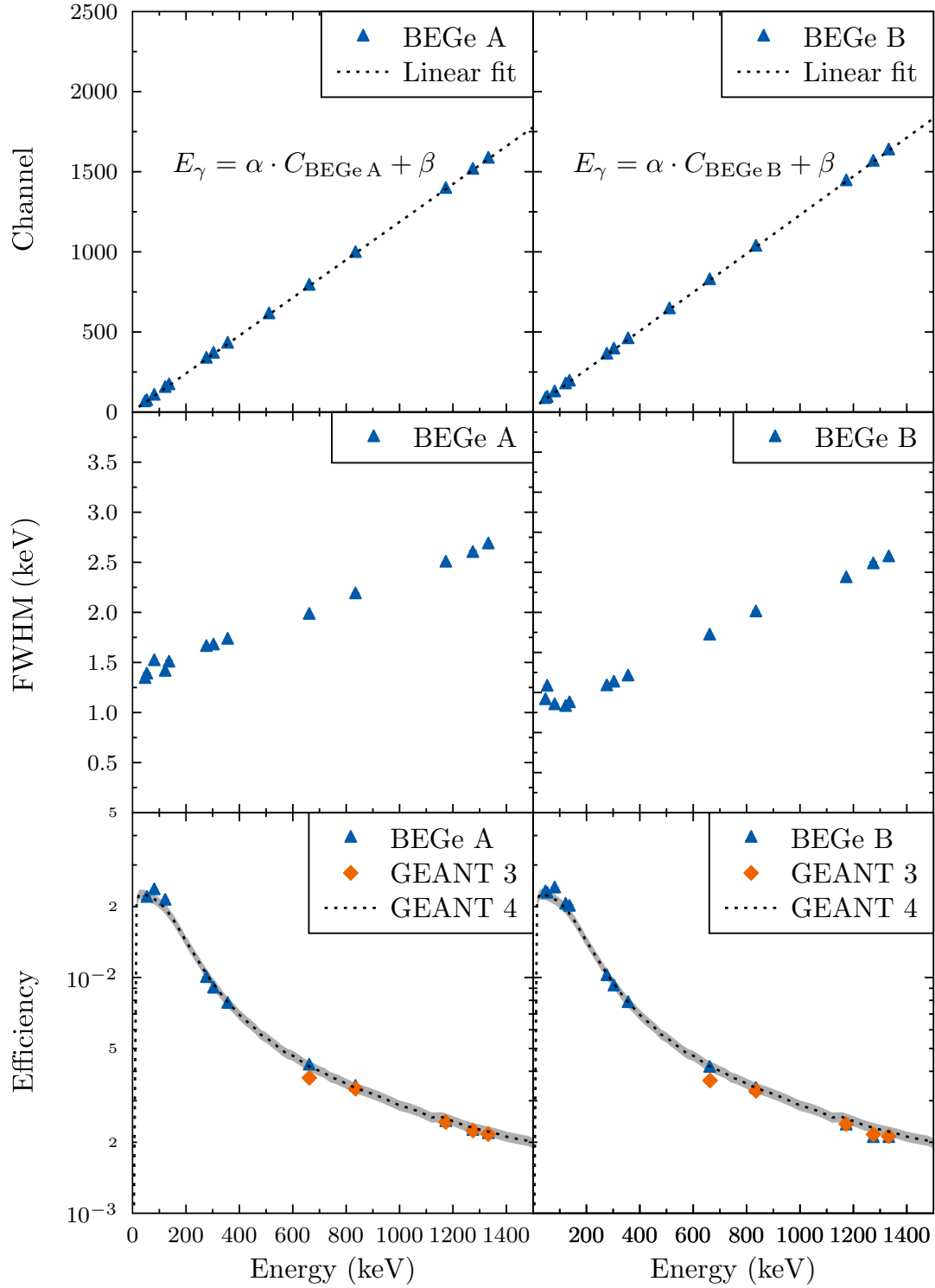


Figure 4.5.: Results of the detector calibration for both BEGe detectors. From top to bottom: Energy calibration, resolution calibration and the efficiency measurements.

Ga Analysis I

Following the irradiation of the samples, the recorded γ -spectra were analyzed using the spectrum analyzing tool *tv* [27]. This program allows to identify, background correct, fit and integrate peaks of interest in a spectrum. Prior to the analysis the two BEGe-detectors were calibrated at the selected sample to detector distance of 10.3 cm. The results of the calibration are shown in Figure 4.5. The detector calibration was performed using the calibration sources listed in Table C.1. The channel to energy conversion was performed using a linear fit function for each detector. The conversion functions were determined to be

$$E_{\gamma} = (0.85 \cdot C_{\text{BEGe A}} - 3.92) \text{ keV}$$

$$E_{\gamma} = (0.83 \cdot C_{\text{BEGe B}} - 19.73) \text{ keV}.$$

The detector energy resolution was determined to be between 1 keV and 3 keV in the region of interest, which ensured the identification of the gallium peaks with great accuracy. The measured efficiencies of both detectors are in good agreement with simulations using the GEANT-3 and GEANT-4 simulation toolkits [16, 2]. This reflects the sufficient understanding of the detector geometry and its performance and, therefore leads to a well known correction factor needed for the analysis of the activation measurement.

The recorded γ -spectra following the counting of the activated gallium samples and the gold monitors are presented in Figures 4.7 - 4.10. The difference of the spectra between the natural and enriched samples is clearly visible. The analysis of the enriched samples show a dramatic improvement of the sensitivity over the natural gallium sample. This leads to an easier identification of the peaks of interest, and to higher counting statistics in the region of interest. This reduces the statistical uncertainty. Additionally, a large number of peaks from the ^{72}Ga decay are clearly visible in the decay spectrum of the enriched sample, whereas the natural sample spectrum is dominated by the electron induced background of the ^{70}Ga β^- -decay. However, due to the low emission probability of these lines, they were not used for analysis. The γ -lines used for the analysis are provided with a colored marker in the spectrum. For the analysis of the $^{69}\text{Ga}(\text{n}, \gamma)$ reaction the γ -lines at 176 keV and 1039 keV were used since these are the only γ -lines originating in the decay of ^{70}Ga . In case of $^{71}\text{Ga}(\text{n}, \gamma)$ the lines of interest are 630, 834, 894 and 1050 keV. For the determination of the neutron flux, the 411 keV γ -emission line of ^{198}Au was used.

The determined number of counts for each detector and the simulation correction factors are presented in Table C.3 and Table C.4.

In addition to the analysis of the γ -emission spectra of the activated samples the f_b -correction factor was determined using the neutron flux measured by the ^6Li -glass detector during the activation. A typical time-dependent neutron flux spectrum is presented in Figure 4.6. The f_b factor was calculated using Equation 4.6. The correction factors for each sample and activation are shown in Table C.7. The waiting-time correction factor f_{wm} was determined analytically using Equation 4.5 and synchronized timing measurement. Source of uncertainty for the time-correction factor are the uncertainties of the respective decay constants and a timing uncertainty of 1 s. The dead time of the detectors was determined using Equation 4.4. Where the uncertainty of the timing was estimated to be 1 s.

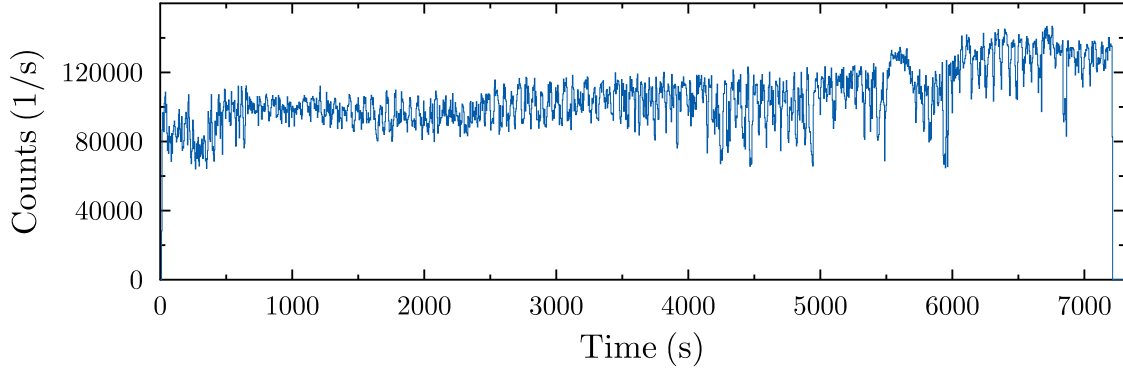


Figure 4.6.: Neutron flux recorded during the irradiation of the enriched ^{71}Ga sample.

With the correction factors and the determined counts in the γ -peaks, all the needed values for the determination of the number of the produced nuclei are given. They were determined for each γ -emission line and detector using Equation 4.3. From these values the weighted mean between the two detectors and the γ - emission lines $\langle N_{\text{prod.}} \rangle$ was calculated and is presented in Table C.8.

For the uncertainty calculation the statistical uncertainty of the values was determined by the number of counts in the γ -line of interest. The presented systematic uncertainties only account for the uncertainty of the simulation correction factor $f_{\text{sim.}}$, since the uncertainties of the remaining correction factors f_b , f_{wm} and f_{dt} were smaller than 1% and thus were neglected.

4. Neutron activation of Gallium

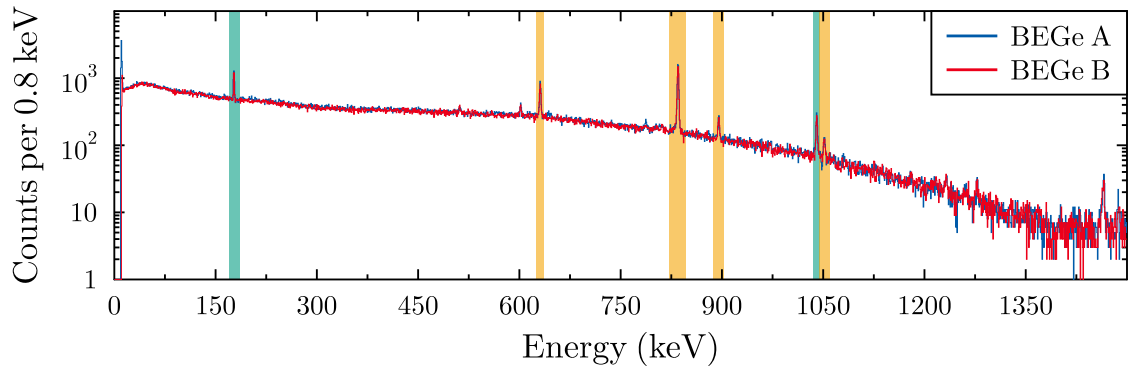


Figure 4.7.: Decay spectrum of the activated natural gallium sample.

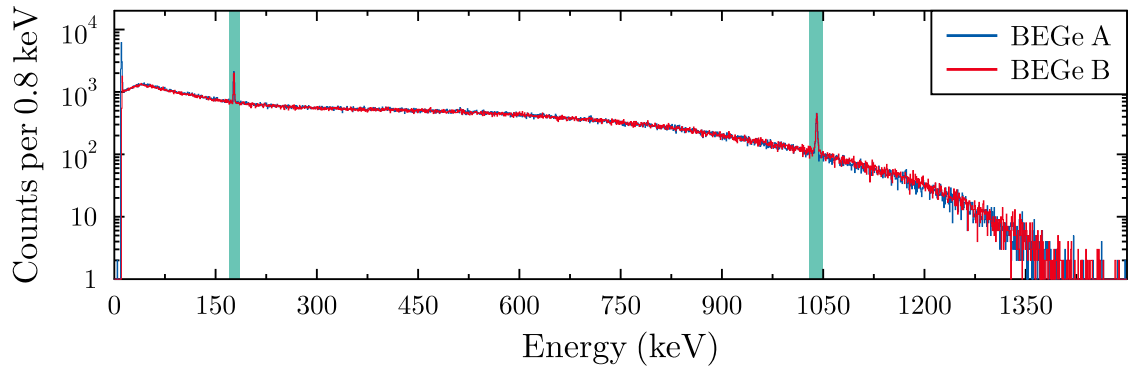


Figure 4.8.: Decay spectrum of the activated enriched ⁶⁹Ga sample.

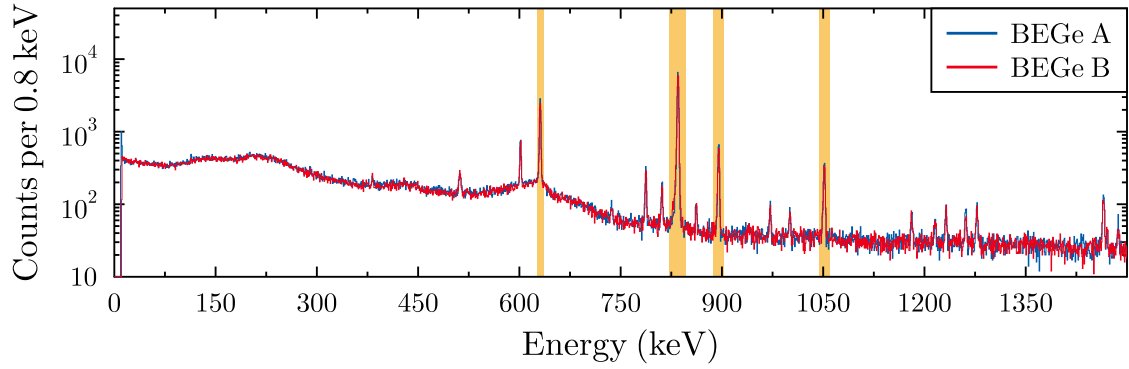


Figure 4.9.: Decay spectrum of the activated enriched ⁷¹Ga sample.

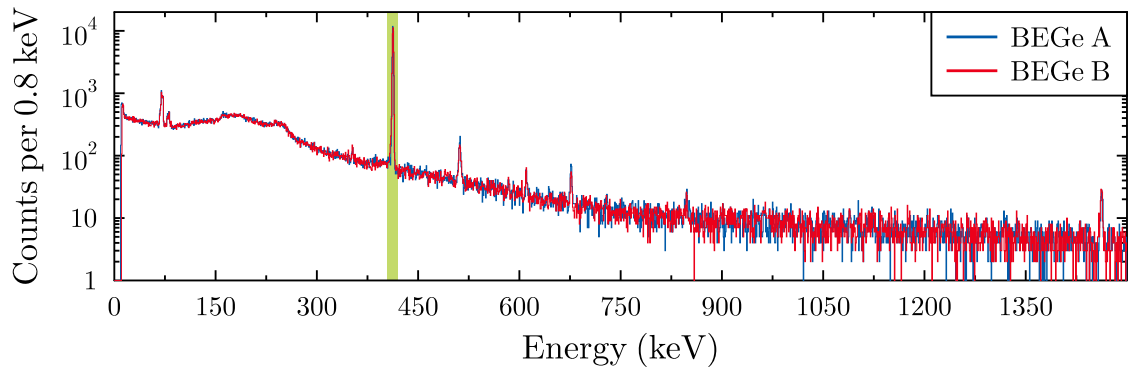


Figure 4.10.: Decay spectrum of one of the activated gold monitors used for neutron flux analysis.

Using the determined number of produced nuclei and the number of sample nuclei for the gold monitors and the activated samples, as well as the information provided by the manufacturer of the sample material, the weighted mean between the detectors and γ -lines, for the cross section ratios $\langle\sigma_{\text{Ga}}/\sigma_{\text{Au}}\rangle$ was determined using Equation 4.1. The results are presented in Table 4.3.

Reaction	Sample	Activation	$\langle\sigma_{\text{Ga}}/\sigma_{\text{Au}}\rangle$	u_{stat}	u_{syst}
$^{69}\text{Ga}(\text{n}, \gamma)$	natGa I	I	0.2827	0.0045	0.0187
	^{69}Ga	I	0.2597	0.0031	0.0165
	^{69}Ga	II	0.2624	0.0038	0.0168
$^{71}\text{Ga}(\text{n}, \gamma)$	natGa I	I	0.1728	0.0018	0.0106
	^{71}Ga	I	0.1179	0.0010	0.0073

Table 4.3.: Final values for the cross section ratios determined for the activation of each gallium sample. For ^{69}Ga the values are in good agreement within the margins of uncertainties. For ^{71}Ga there is a large discrepancy.

The values obtained for the cross section ratio of ^{69}Ga and ^{197}Au show a good agreement within in the uncertainties between the natural sample and the enriched sample. The values for ^{69}Ga are overall in a very good agreement with the results obtained by Göbel *et al.* [35], where the used neutron spectrum was similar and only natural gallium samples were investigated. In addition the ratio of ^{71}Ga and ^{197}Au was determined. The results obtained using the natural gallium sample is consistent with the value obtained by Göbel *et al.* [35]. However, the determined cross sections ratio of $^{71}\text{Ga}(\text{n}, \gamma)$ reaction show a 32% difference between the natural and the enriched sample.

Additionally, the spectrum-averaged neutron capture cross sections were calculated using the neutron flux through the gallium samples. To determine the neutron flux the produced number of nuclei $N_{\text{prod.}}$ and the sample nuclei N_{sample} of the gold monitors, which can be found in Table C.5 and Table C.8, are a crucial input. The neutron capture cross sections for gold at the respective positions are determined using the PINO tool. The values used are given in Table 4.4.

Spectrum averaged cross section	Gold upstream	Gold downstream
σ_{SACS} (mb)	648.5 ± 12.9	627.9 ± 12.6

Table 4.4.: Spectrum averaged gold cross sections for both neutron flux monitors. Values taken from a simulation using the PINO tool using the sample positions during the measurement.

4. Neutron activation of Gallium

Using Equation 4.8 the neutron flux through the gold monitors was determined and is presented in Table 4.5. These values can be directly used to determine the SACS of the reaction using Equation 4.7. The final results for this activation measurement, the SACS for each sample and reaction are presented in Table 4.6.

Activation	Monitor upstream	Flux / 10^{-16} downstream	Monitor upstream	Flux / 10^{-16} upstream	Sample flux / 10^{-16}
natGa I	44	1.1623 ± 0.064	VI	1.0662 ± 0.058	1.1142 ± 0.061
^{69}Ga act. I	38	1.1161 ± 0.061	26	1.0818 ± 0.085	1.0989 ± 0.060
^{69}Ga act. II	32	0.7973 ± 0.044	33	0.7940 ± 0.043	0.7956 ± 0.043
^{71}Ga	31	2.1453 ± 0.118	36	2.1532 ± 0.117	2.1493 ± 0.178

Table 4.5.: Determined neutron flux using the gold monitors during the activation.

Sample	Reaction	σ_{SACS}	$u_{\text{stat.}}$	$u_{\text{syst.}}$
natGa I	$^{69}\text{Ga}(\text{n}, \gamma)$	180.57	3.00	14.03
	$^{71}\text{Ga}(\text{n}, \gamma)$	110.88	1.25	8.14
^{71}Ga		75.41	0.82	5.60
^{69}Ga act. I	$^{69}\text{Ga}(\text{n}, \gamma)$	165.81	2.10	12.51
^{69}Ga act. II		167.51	2.57	12.67

Table 4.6.: Final results for the spectrum averaged cross sections for each activation and reaction. The values for the reaction $^{69}\text{Ga}(\text{n}, \gamma)$ are in good agreement. The values for $^{71}\text{Ga}(\text{n}, \gamma)$ show a difference of 32%.

4.4. Activation II

In order to resolve the disagreements of the cross section ratios of ^{71}Ga and ^{197}Au obtained during the previous activation experiment, another activation experiment was performed at Goethe University Frankfurt in November 2020. During this short experiment only the $^{71}\text{Ga}(n, \gamma)$ reaction was of interest. Therefore, the experimental setting was optimized for the measurement of this gallium isotope. To exclude a possible error during the experimental preparations, a different natural gallium sample was used, named natGa II. Due to limited resources, the same could not be done for the enriched ^{71}Ga sample. As in the previous experiment a metallic lithium target with a thickness of approximately 22 μm , evaporated onto a copper backing, was used as the neutron production target. To ensure a high activity of the produced ^{72}Ga , the samples were activated for the in Table 4.7 presented durations. Following the sample irradiation, the reaction products were analyzed using the two BEGe detectors with a sample to detector distance of 11.3 cm. During the activation the neutron flux and the proton current were recorded using a ^6Li -glass detector and a current integrator. No changes were made at the experimental setup in order to ensure equal conditions as during the previous activation measurement

Sample	Activation	Activation time
natGa II	I	2.0 h
^{71}Ga	I	4.2 h

Table 4.7.: Activated samples and the activation times for the activation experiment.

Ga Analysis II

Equally to the previous activation experiment, the spectra were recorded using the spectrum analysis program MPWin. The analysis of the peaks of interest was performed using the program *tv*. Prior to the activation analysis the detectors were calibrated at the exact same sample to detector distance that was later used for the gallium analysis, which was at 11.3 cm. The results of the calibrations are shown in Figure 4.11. A very well fitting linear correlation between channel number and γ -energy could be observed.

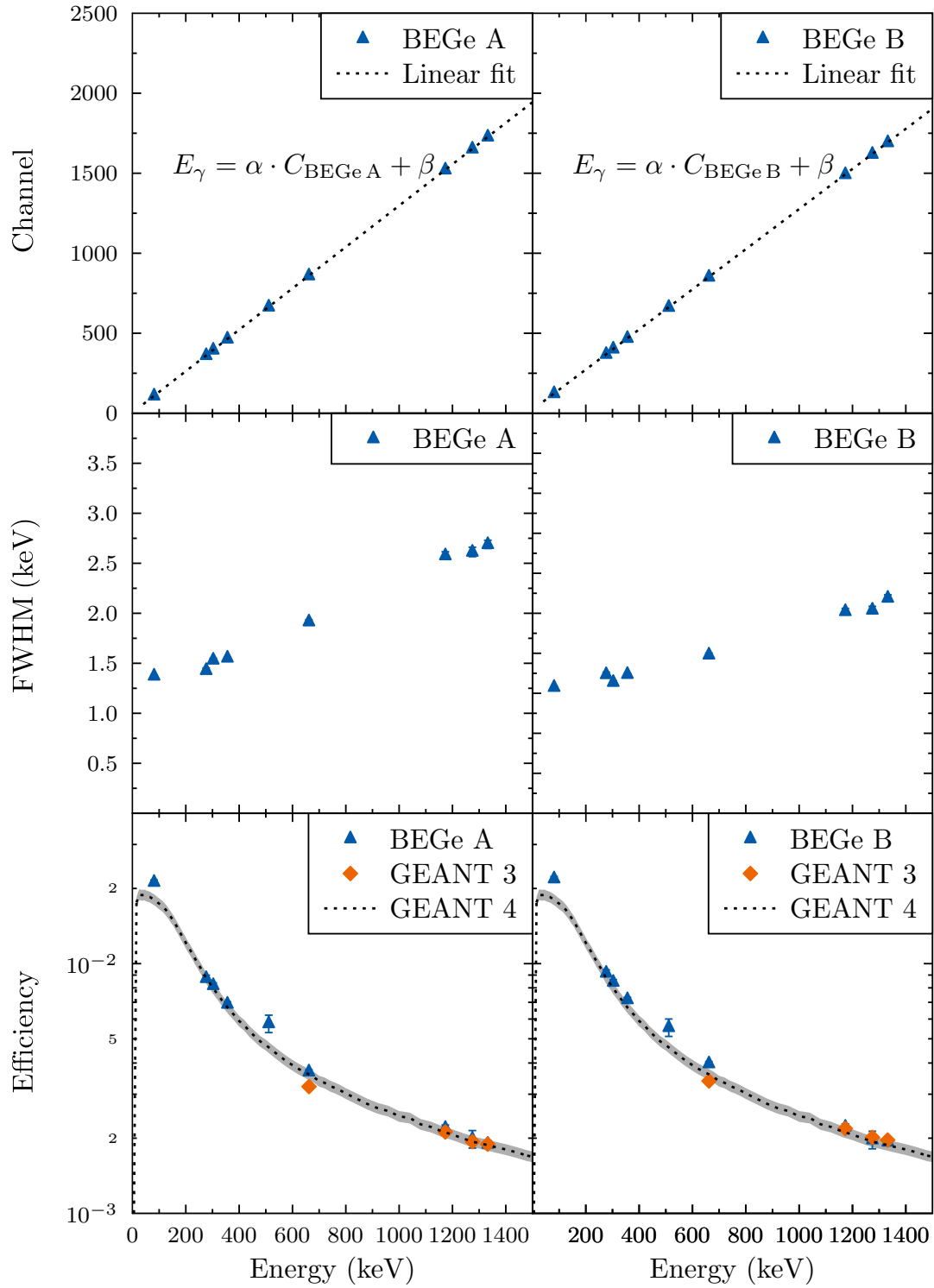


Figure 4.11.: Results of the detector calibration for both BEGe detectors. From top to bottom: Energy calibration, resolution calibration and the efficiency measurements.

The channel to energy conversion was performed using a linear fit for each detector with the functions:

$$E_{\gamma} = (0.77 \cdot C_{\text{BEGe A}} - 3.47) \text{ keV}$$

$$E_{\gamma} = (0.78 \cdot C_{\text{BEGe B}} - 18.27) \text{ keV}.$$

For the efficiency however one measurement value could not be well represented by the GEANT-3 simulations. This may be due to some misunderstandings of the sample-detector geometry or problems during the measurement. However, the energy range of interest (between 400 keV and 1200 keV) is very well represented by the simulations. The energy resolution of the detectors remains unchanged between 1 keV and 3 keV in the region of interest.

Analog to the previous activation experiment the neutron flux during the activation was recorded using a ^6Li -glass detector mounted in a distance of 30 cm behind the activation setup for the determination of the f_b -factor and the online neutron flux monitoring. In addition to the neutron flux, the proton current was recorded using a current integrator. During this activation the proton beam current varied between 6 and 10 μA . Following the irradiation of the samples for the in Table 4.7 shown durations, the samples were placed in front of the BEGe detectors for γ -spectroscopy. Since this activation was thought to be a sanity check for the previous results, only three γ -emission lines from the decay of ^{72}Ga were analyzed, namely 630 keV, 834 keV and 894 keV. The correction factors were determined using Equations 4.4 - 4.6. The simulation correction factor was taken from the GEANT-3 simulations of the detectors. As in the previous analysis the uncertainties of the correction factors were neglected except the simulation correction factor. The statistical uncertainties were determined by the counts in the respective γ -emission line.

With the correction factors, presented in Table C.12, and the determined counts in the γ -peaks, presented in Table C.10 and Table C.11, the produced nuclei during the activation were determined using Equation 4.3. The weighted mean for the produced nuclei $\langle N_{\text{prod.}} \rangle$ are shown in Table C.13. With the number of produced nuclei for each γ -line and each detector, and the number of sample nuclei for gallium and gold

4. Neutron activation of Gallium

presented in Table C.2 and Table C.9, the weighted mean of the cross section ratio $\langle \sigma_{71\text{Ga}}/\sigma_{\text{Au}} \rangle$ was determined to be

$$\left\langle \frac{\sigma_{71\text{Ga,natural}}}{\sigma_{197\text{Au}}} \right\rangle = 0.1755 \pm 0.0024_{\text{stat.}} \pm 0.0108_{\text{syst.}} \quad (4.13)$$

$$\left\langle \frac{\sigma_{71\text{Ga,enriched}}}{\sigma_{197\text{Au}}} \right\rangle = 0.1213 \pm 0.0010_{\text{stat.}} \pm 0.0075_{\text{syst.}} \quad (4.14)$$

Yet again a difference of approximately 31% arises between the enriched and the natural sample. Since the natural gallium sample was different from the sample used in the previous activation, the problem does not seem to be with the natural sample itself. Again the ratio obtained for the natural gallium sample does agree with the value obtained by Göbel *et al.* [35], measured at a different setup with different gallium samples. However, the presented disagreements may arise from the isotopic enriched gallium sample. The number of sample nuclei in this sample was determined using the mass of the sample and the isotopic abundance given by the manufacturer [24]. A possible way to check a faulty weight of the sample would have been the removal of the sample from the Kapton foil. Due to the price of the material and the occurring remaining residue on the Kapton foil it was concluded a re-weighting of the sample by itself was the only possibility. The method chosen was the weighing of the sample, including Kapton foil and stainless steel sample holder. Following the subtraction of the weight of a similar sample holder, as well as the weight of the same amount of Kapton. The weight difference between initial weighting and re-weighting was insignificant. Within the range of the scales uncertainty, the weight of the sample, determined before mounting in the previous activation, was confirmed. This lead to the idea of a false isotopic abundance or possible impurities in one the samples.

Searching for possible impurities in the gallium samples, the γ -spectra of the radioactive activation products were investigated closer. The energies of all visible peaks were investigated. During this analysis only γ -lines originating in the decay of reaction products from the gallium activation and natural background lines were observed. So the reason for the disagreements could not be solved by γ -spectroscopy.

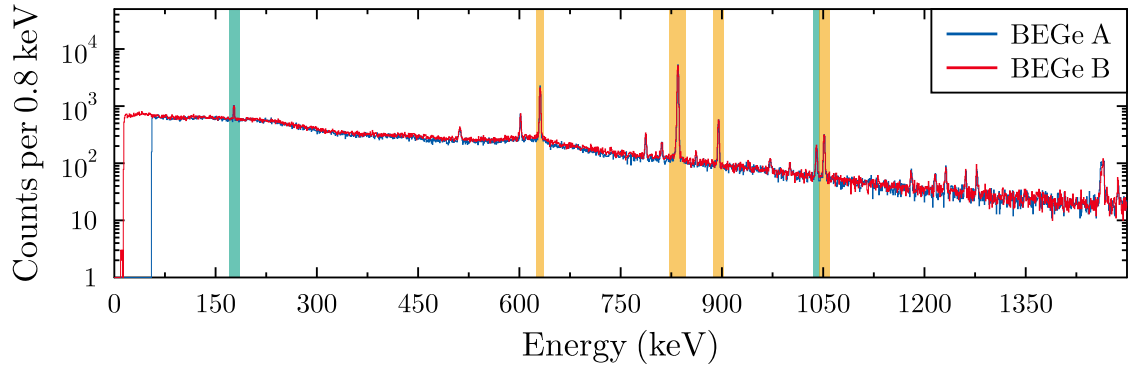


Figure 4.12.: Decay spectrum of the activated natural gallium sample.

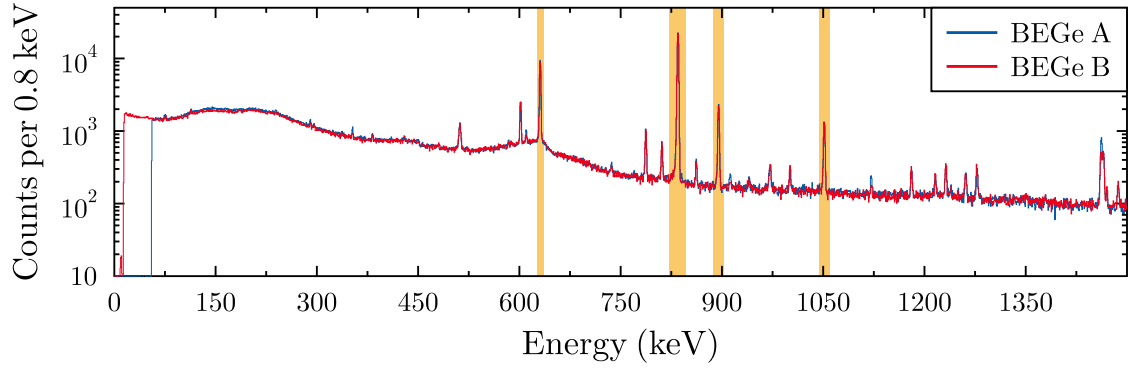


Figure 4.13.: Decay spectrum of the activated ⁷¹Ga enriched sample.

4.5. Non-destructive material analysis

A possible reason for the discrepancies in the cross section ratios using natural and enriched gallium samples could be a contamination of one or both samples with different material, which is not visible in the γ -emission spectra. This may be caused by several reasons, like very short half lives of the reaction product or the absence of γ -emission during the nuclear decay. Therefore, the samples of interest were investigated using the micro X-ray fluorescence (μ XRF) method.

The principle of the method is shown in Figure 4.14. A typical X-ray spectrometer consist of four main components. An excitation source producing ionizing radiation owing to photoelectric absorption of the atoms present in the sample, usually a X-ray tube, a sample presentation mechanism, a detection system responsible for the collection of the characteristic radiation emerging from the sample and a signal processing system responsible for the presentation of the gathered information [69].

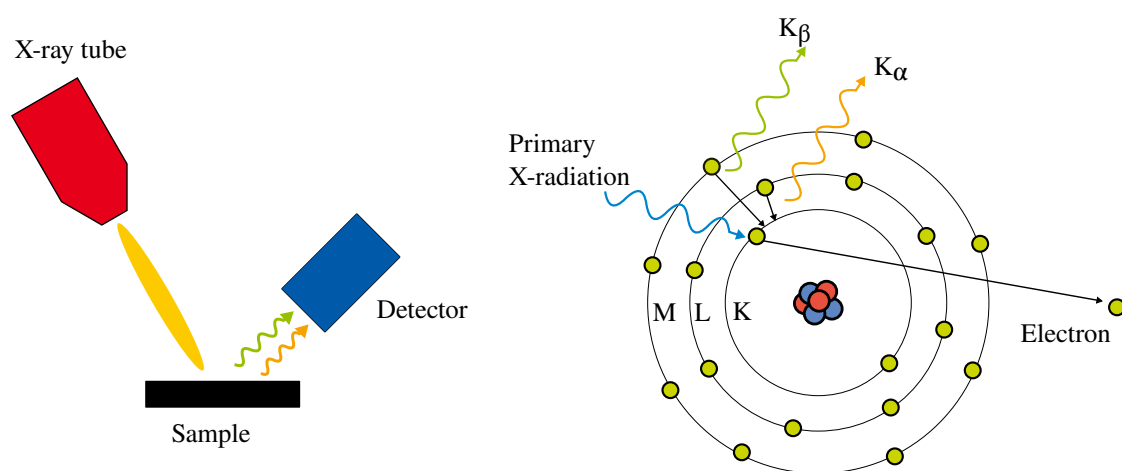


Figure 4.14.: Basic principle of XRF analysis. Based on [69].

If the energy of a photon impinging on the sample is larger than the binding energy of an inner shell electron, a part of its energy may be absorbed due to photoelectric absorption. The shell electron is subsequently ejected from its position leaving a vacancy on the shell orbital which leads to an ionized atom. This ionized state can be destroyed by two mechanisms: The first is the Auger effect, in which a rearrangement of electrons occurs which results in the emission of other photoelectrons.

The foundation of the second effect is the transfer of an electron from one of the outer orbitals to fill the vacant spot. The energy difference between the initial and the final state of the transferred electron is emitted in the form of an X-ray photon. These X-ray photons have specific energies for each element. The emitted characteristic X-rays can be used to identify the composition of materials, with the advantage that not only the presence of elements but also their abundance can be determined [69].

The used system for the investigation of the gallium samples was an EDAX Eagle II μ XRF spectrometer. The rhodium filament in the X-ray tube makes it possible to detect elements between $Z = 9$ and $Z = 86$. The advantage of μ XRF over the classical XRF is the improved spatial resolution diameter, which is many orders of magnitude smaller than that of conventional XRF [69]. Two gallium samples, the natural gallium sample natGa II and the enriched ^{71}Ga sample, were investigated. They were exposed by X-radiation, produced by a 40 kV X-ray tube, for 50 sec at 100 μA . The analysis of the obtained spectra is shown in Figure 4.15.

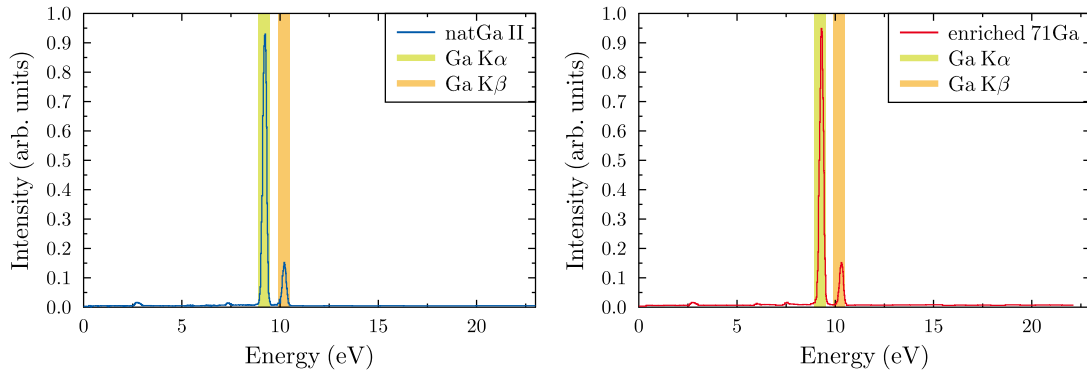


Figure 4.15.: Results obtained by μ XRF on two gallium samples. Clearly visible are the characteristic X-rays (K_α and K_β) from Gallium. No other significant X-rays are visible ensuring the purity of the samples.

It becomes evident that the investigated samples were free of any significant contamination, which could explain the difference in cross sections obtained by the activation method for the $^{71}\text{Ga}(n, \gamma)$ reaction. However, due to the limitation of the technique, elements with low Z , like oxygen or carbon could not be detected. The only hints for the absence of oxygen or carbon in the samples is the sample color, which would change with a high amount of carbon as well as the melting point for gallium(III)-oxide which would be much higher than the 29.8°C for pure gallium.

4.6. Activation III

Since, no major impurities were found during the μ XRF analysis of the gallium samples, the reason of the difference in cross sections has to be elsewhere. One possibility could be different neutron transmissions of the samples, which could be affected by contamination of the gallium samples with elements not visible using the μ XRF method, for example material with $Z < 8$.

While the contamination with light elements is highly unlikely, as pointed out in section 4.5, another possibility could be the influence of ^{69}Ga on the ^{71}Ga in the natural gallium sample. The data situation for the elastic neutron scattering cross sections as well as the total neutron cross section is very scarce for both stable isotopes of gallium. Only theoretical models can be used for simulations. A possibility to investigate the transmission and scattering of neutrons in the gallium samples, as well as the influence of the gallium isotopes on each other, was to activate the samples together as a sample stack, with gold foils as neutron flux monitors in between. This experiment was conducted at the accelerator of the Goethe University in Frankfurt. The lithium target, used as the neutron source, remained the same as during the previous activation measurement with a sufficient thickness of approximately 22 μm . The duration of each activation can be found in Table 4.8. The long activation times were chosen in order to gain a high activity of the ^{72}Ga . For the γ -spectroscopy the setup was untouched since activation II. The specifications of the used gold monitors are presented in Table C.14.

Sample upstream	Sample downstream	Activation time
^{71}Ga	natGa II	2.0 h
natGa II	^{71}Ga	2.1 h

Table 4.8.: Activated samples and the activation times for the activation experiment.

Activation Analysis III

The analysis of the activated samples was again based on γ -spectroscopy. Following the counting of each sample and gold monitors the determined counts, which are presented in Table C.16 and Table C.17, the weighted mean of the produced nuclei were determined. The results are shown in Table C.18. The determined correction factors are shown in Table C.15. The final values for the weighted mean of the ratios between the detectors and γ -lines were calculated and are presented in Table 4.9.

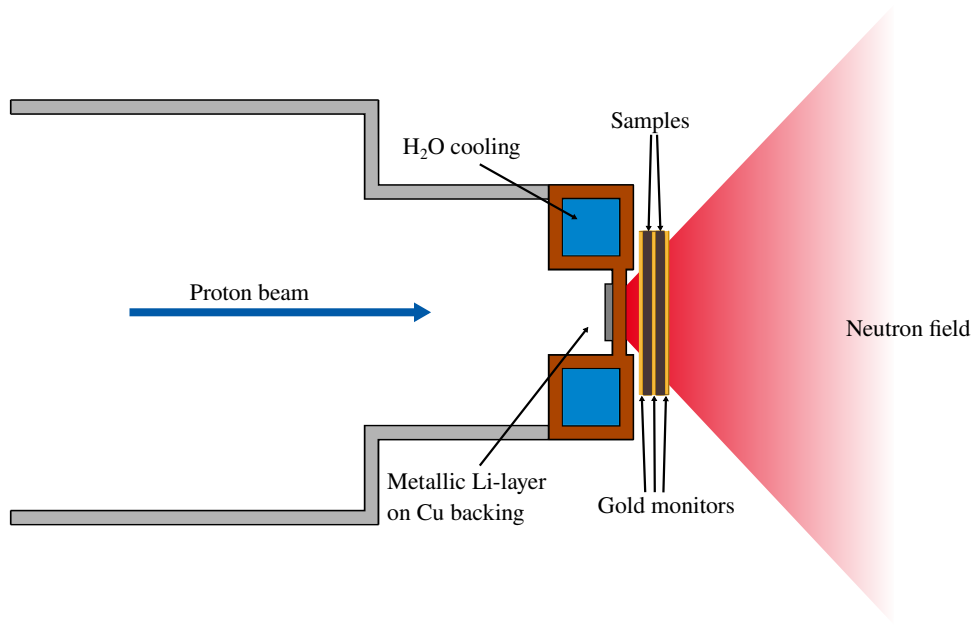


Figure 4.16.: Schematic of the used activation setup for the sample stack activation. No changes at the setup were made. The samples are stacked between gold monitors and placed inside the neutron cone.

Front	Back	$\langle \sigma_{\text{Ga}} / \sigma_{\text{Au}} \rangle_{\text{front}}$	$\langle \sigma_{\text{Ga}} / \sigma_{\text{Au}} \rangle_{\text{back}}$
^{71}Ga	natGa II	$0.1616 \pm 0.0008_{\text{stat.}} \pm 0.0099_{\text{syst.}}$	$0.1631 \pm 0.0009_{\text{stat.}} \pm 0.0099_{\text{syst.}}$
natGa II	^{71}Ga	$0.2134 \pm 0.0023_{\text{stat.}} \pm 0.0130_{\text{syst.}}$	$0.1205 \pm 0.0012_{\text{stat.}} \pm 0.0073_{\text{syst.}}$

Table 4.9.: Final results of the sample stack activations.

It becomes clearly visible that the sequence of the samples seems to have a large influence on the cross section ratios. While the ratios for the first activation with the enriched ^{71}Ga sample in the front are in good agreement with each other, the reverse order shows a difference of 56.5%. The nature of this was further investigated using the gold monitors. Usually because of the transmission and scattering in the gold monitors and sample, the ratio between produced Nuclei $N_{\text{prod.}}$ and the sample nuclei N_{sample} should constantly decline with increasing distance from the neutron production target to the sample of interest. The values shown in Table 4.10 and Figure 4.17 indicate a behavior just as expected.

4. Neutron activation of Gallium

$\langle N_{\text{prod.}}/N_{\text{Sample}} \rangle_{\text{front}}$	$\langle N_{\text{prod.}}/N_{\text{Sample}} \rangle_{\text{middle}}$	$\langle N_{\text{prod.}}/N_{\text{Sample}} \rangle_{\text{back}}$
$(3.9930 \pm 0.2014) \cdot 10^{-13}$	$(3.8335 \pm 0.1935) \cdot 10^{-13}$	$(3.4177 \pm 0.1719) \cdot 10^{-13}$
$(6.4251 \pm 0.3317) \cdot 10^{-14}$	$(6.2268 \pm 0.3217) \cdot 10^{-14}$	$(5.8652 \pm 0.2985) \cdot 10^{-14}$

Table 4.10.: Ratio of produced ^{198}Au nuclei during the activations as a check of neutron scattering by the gallium samples.

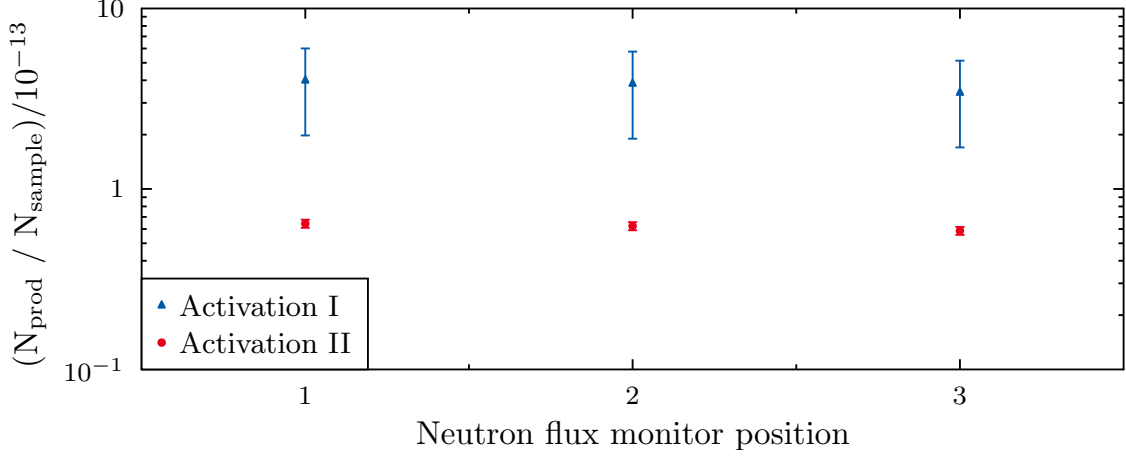


Figure 4.17.: Ratio between produced ^{198}Au nuclei and ^{197}Au sample nuclei. The values behave just as expected with a slight decline in ratio.

In the search for possible reasons of the behaviour of the cross sections ratios, neutron capture simulations were carried out. These simulations rely on the Monte Carlo method and use the neutron spectrum simulated by PINO, the sample specifications and the geometry of the sample stack at the end of the beamline. Another important input parameter is the scattering and the neutron capture cross section for the used isotopes. These cross sections were taken from the ENDF/B-VII.1 database [25]. The results of these simulations are shown in Table 4.11. The values determined by activation and simulation do not match. The differences in simulated cross sections ratios of ^{71}Ga and ^{197}Au mostly rely on the abundance of the isotopic enrichment. Additionally, simulations only considering one gallium sample at the different positions does not show a large influence on the neutron capture probability.

Sample stack configuration	$\langle \sigma_{71\text{Ga}} / \sigma_{197\text{Au}} \rangle_{\text{front}}$	$\langle \sigma_{71\text{Ga}} / \sigma_{197\text{Au}} \rangle_{\text{back}}$
Au \rightarrow ^{71}Ga \rightarrow Au \rightarrow natGa \rightarrow Au	0.199 ± 0.0028	0.200 ± 0.0032
Au \rightarrow natGa \rightarrow Au \rightarrow ^{71}Ga \rightarrow Au	0.206 ± 0.0032	0.196 ± 0.0029
Au \rightarrow ^{71}Ga \rightarrow Au \rightarrow no sample \rightarrow Au	0.198 ± 0.0028	
Au \rightarrow no sample \rightarrow Au \rightarrow ^{71}Ga \rightarrow Au		0.201 ± 0.0029
Au \rightarrow natGa \rightarrow Au \rightarrow no sample \rightarrow Au	0.205 ± 0.0032	
Au \rightarrow no sample \rightarrow Au \rightarrow natGa \rightarrow Au		0.209 ± 0.0033
Use $^{69}\text{Ga}(\text{n},\text{n}')$ cross section $\times 10$		
Au \rightarrow ^{71}Ga \rightarrow Au \rightarrow natGa \rightarrow Au	0.196 ± 0.0026	0.214 ± 0.0032
Au \rightarrow natGa \rightarrow Au \rightarrow ^{71}Ga \rightarrow Au	0.213 ± 0.0032	0.196 ± 0.0029

Table 4.11.: Results of neutron capture simulations using the sample stack specifications as input. No difference in cross section ratio depending on the sample position in the stack can be seen.

4.7. Activation IV

The difference of the cross section ratios could not be explained by the sample stack activation. Considering the neutron transmission and scattering of gallium not fully understood, another activation experiment was conducted. The multiple scattering of neutrons on atoms has an influence on the reaction probability, and is dependent on the number of sample nuclei. The more nuclei in a sample, the higher is the probability of neutron scattering and absorption in the sample. In the previous activations, described in the previous sections, the gallium samples had a thickness of 0.5 mm. Due to the use of enriched gallium samples, these enriched samples featured a significantly higher number of nuclei. To investigate this influence of the number of sample nuclei on the cross section, natural gallium samples were prepared by casting molten gallium, and activated. The samples with thicknesses of: 0.1, 0.2, 0.5, 1.0, 1.25 and 1.5 mm, and were prepared as part of the Masters thesis of Tabea Kuttner [43]. At a sample thickness of 1.25 mm the natural gallium sample has approximately the same amount ^{71}Ga nuclei as the enriched sample. Due to limited resources, producing several samples with different thicknesses could not be repeated for the enriched gallium. The samples were activated using the same sample holder geometry as during the previous activations at the Frankfurt Van-de-Graaff accelerator. Neutrons were produced via the $^7\text{Li}(\text{p},\text{n})^7\text{Be}$ reaction using a metallic lithium target with a thickness of 100 μm , evaporated onto a copper backing. During the activations the proton current fluctuated between 7 and 9 μA . The activation times, selected for high statistics from the $^{71}\text{Ga}(\text{n},\gamma)$ reaction, are shown in Table 4.12. During the irradiation of the samples the proton current as

4. Neutron activation of Gallium

Sample	Thickness	Activation	Activation time
natGa 0.2 (2)	0.2 mm	1	1.03 h
natGa 0.2 (1)	0.2 mm	1	4.29 h
natGa 0.1 (1)	0.1 mm	1	1.11 h
natGa 0.5 (1)	0.5 mm	1	1.25 h
natGa 0.2 (2)	0.2 mm	2	2.05 h
natGa 0.1 (1)	0.1 mm	2	4.03 h
natGa 0.2 (1)	0.2 mm	2	1.85 h
natGa 1	1.0 mm	1	1.93 h
natGa 1.25	1.25 mm	1	1.43 h
natGa 1.5	1.5 mm	1	1.53 h

Table 4.12.: Samples and the irradiation times.

well as the neutron flux were monitored, and the later used for the correction of the decays.

The detector to sample distance was set to 5.3 cm for detector A and 5.5 cm for detector B. As the quest to understand the cross section of the $^{71}\text{Ga}(n, \gamma)$ reaction only the γ -emission lines from the ^{72}Ga decay (630 keV, 834 keV and 839 keV) were used for the analysis. The specifications for the samples and gold monitors are presented in Table C.21 and Table C.20.

Activation analysis IV

During the experiment the neutron flux was observed using a ^6Li -Glass scintillator, which was mounted at an increased distance at 1 m, compared to the previous activations to ensure low pile-up in the data acquisition. The correction factors are presented in Table C.24. The determined counts for the samples and monitors were determined by γ -spectroscopy, and are presented in Table C.23 and Table C.22. The weighted mean, of the detectors and γ -lines, for the produced nuclei are shown in Table C.19. The statistical uncertainties were determined using the counts in the respective γ -emission line. The uncertainties for the correction factors except the simulation correction factor were smaller than 1% and were neglected. The final values for the cross section ratios, the weighted mean between the detectors and γ -lines, are shown in Table 4.13 and Figure 4.18. No significant relation between the cross section ratio for ^{71}Ga and the investigated sample thicknesses could be observed. One value obtained for the second activation of the gallium sample with a thickness of 0.1 mm thickness shows a difference to the median of 27%. Since this value could be falsified by the first activation of this sample, the difference is

most likely an error during the measurement. Neutron-capture simulations, based on the PINO tool and the scattering and capture cross sections for ^{71}Ga from the ENDF/B-VII.1 database [25], are presented in Figure 4.19. No significant relation between thickness and cross section ratio in the range between 0.01 and 1.5 mm is shown using the simulations. Again, the discrepancies between the ratio obtained using natural and enriched gallium samples cannot be explained.

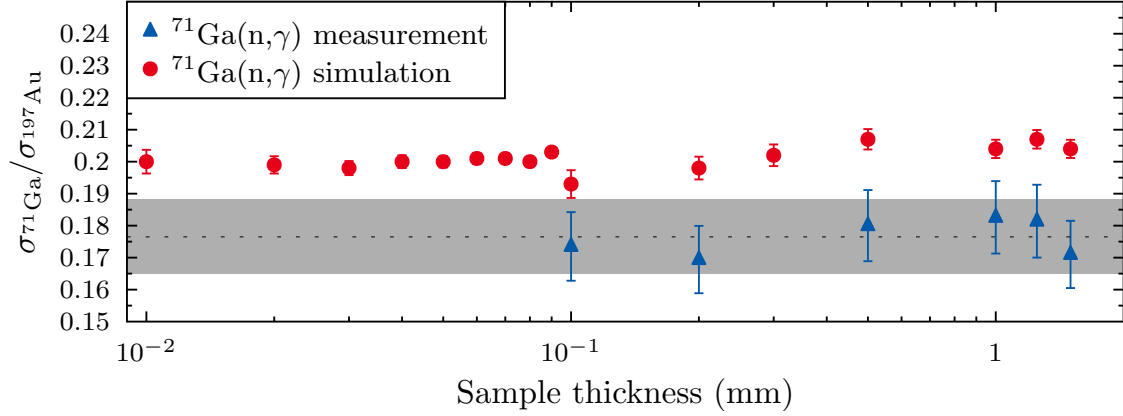


Figure 4.18.: Cross section ratios for the $^{71}\text{Ga}(n,\gamma)$ reaction. The simulation predicted larger cross section ratios than measured. However, no relation between the measured or simulated cross sections ratios and sample thickness could be observed. The dashed line denotes the weighted mean of the measurement values and the light blue area the uncertainty of the weighted mean.

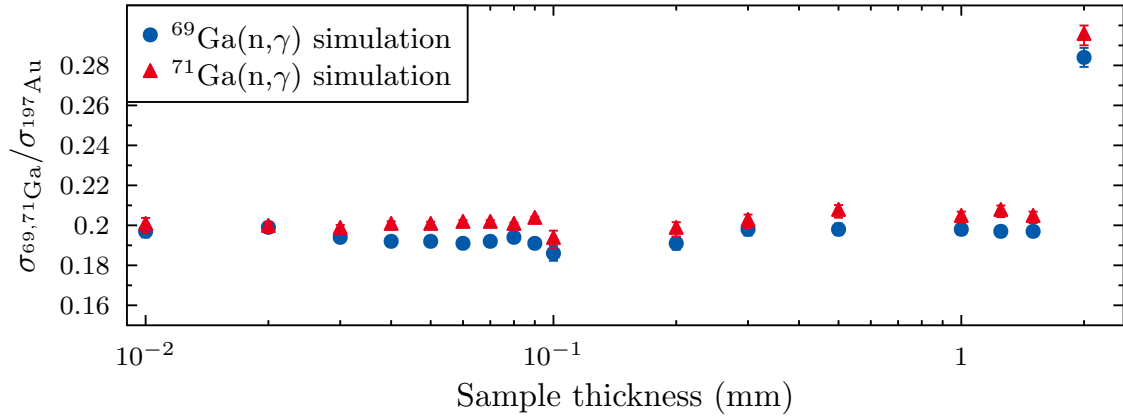


Figure 4.19.: Cross section ratios determined by neutron capture simulations of ^{69}Ga and ^{71}Ga . No significant dependence of the cross section ratio of either gallium isotope with the sample thickness can be determined up to 1.5 mm. At 2 mm sample thickness the simulated cross section ratios show a sudden increase.

4. Neutron activation of Gallium

Sample	Activation	$\langle\sigma_{\text{Ga}}/\sigma_{\text{Au}}\rangle$	u_{stat}	u_{syst}
natGa 0.2 mm II 1cm	I	0.1378	0.0006	0.0085
natGa 0.2 mm I 1cm	I	0.1712	0.0013	0.0105
natGa 0.2 mm I 5cm	I	0.1583	0.0006	0.0099
natGa 0.1 mm I 5cm	I	0.1760	0.0013	0.0110
natGa 0.1 mm I 5cm on	I	0.1735	0.0007	0.0107
natGa 0.3 mm I 5cm	I	0.1958	0.0007	0.0120
natGa 0.5 mm I 5cm	I	0.1800	0.0007	0.0111
natGa 0.2 mm II	II	0.1694	0.0007	0.0105
natGa 0.1 mm I	II	0.1150	0.0003	0.0068
natGa 1.0 mm I	I	0.1826	0.0006	0.0113
natGa 1.25 mm I	I	0.1814	0.0014	0.0113
natGa 1.5 mm I	I	0.1710	0.0004	0.0105

Table 4.13.: Final results for the cross section ratios between ^{71}Ga and ^{197}Au .

5. Conclusion and outlook

Neutron capture cross sections relevant for the s-process can be measured by the activation method using the ${}^7\text{Li}(\text{p},\text{n}){}^7\text{Be}$ reaction as the neutron source. For this reaction, a proton beam with an energy of 1912 ± 2 keV creates a quasi-stellar spectrum at $k_B T = 25$ keV. Simulations with the PINO tool suggest the possibility to determine neutron capture cross sections for $k_B T \neq 25$ keV by a linear combination of several spectrum-averaged cross sections. The accuracy of the PINO tool was investigated by measuring neutron fields of the ${}^7\text{Li}(\text{p},\text{n}){}^7\text{Be}$ reaction for proton energies up to 2800 keV.

Investigation of the ${}^7\text{Li}(\text{p},\text{n}){}^7\text{Be}$ neutron fields

The measurements of ${}^7\text{Li}(\text{p},\text{n}){}^7\text{Be}$ neutron fields were conducted at the low scatter facility PIAF at the PTB Braunschweig. The neutron energy distributions were determined using the neutron time-of-flight method. A pulsed proton beam was shot on a thin $5\mu\text{m}$ thick metallic lithium target, for ten different proton energies: 1887, 1897, 1907, 1912, 2000, 2100, 2200, 2300, 2500 and 2800 keV. The obtained ToF spectra were background corrected and normalized for the accumulated beam charge. For the determination of the angle-integrated neutron spectra, the neutron fields, the measurements were corrected for the respective solid angle coverage.

Several complications arose during the measurements, which made the comparison with the simulation challenging. The new proton accelerator showed a difference between selected and true proton energy of up to 10 keV. The determination of the true proton energy was demanding because of the short flight path of 70 cm and the limited time resolution of the data acquisition (1 ns). It was obtained using the ${}^7\text{Li}(\text{p},\text{n}){}^7\text{Be}$ reaction threshold as well as the PINO tool. While in good agreement, the limiting time resolution gave rise to a large uncertainty in the true proton energy. Another source of uncertainty was the angle-positioning system, which faulted during some measurements, resulting in the need of a manual angle setting. Additionally, the

5. Conclusion and outlook

detector holders slightly bent under the weight of the specially shielded high-voltage and signal cables during the experiment. The comparison between measurements and PINO simulations show a very good agreement for set proton energies $E_p = 1887, 1897, 1907, 1912$ and 2100 keV. The difference between simulation and measurement at $E_p = 2000$ keV is very interesting - it was already observed in the analysis of activation measurements conducted by Tabea Kuttner [43], where discrepancies between the simulated and measured neutron flux at $E_p = 1990$ keV arose.

At $E_p = 2200$ keV the problems with the accelerator and the lithium target prevented an exact measurement. Nevertheless the neutron fields could be compared to PINO and show a good resemblance. Above a proton energy of $E_p = 2300$ keV the differences between the PINO tool and the measurement become more severe. While the neutron fields measured at a proton energy of $E_p = 2300$ keV could differ from the simulations due to a wrong proton energy, the neutron fields measured at the two highest set proton energies $E_p = 2500$ and $E_p = 2800$ keV, could not be sufficiently reproduced by PINO. This became especially noticable for the second neutron production channel, which seems to be implemented incorrectly in the PINO code. This was already noticed by Pachau *et al.* [53]. Since the data for this reaction channel is scarce, a designated measurement campaign for the second neutron production channel could be helpful. Additionally, at the high energies the energy resolution was a limiting factor in the exact measurement and subsequent comparison. The neutron fields at high energies could not have been investigated with a second measurement series at the doubled flight path due to insufficient beam time.

To provide additional data and to further investigate this reaction the measurements presented should be compared to different neutron simulation codes. For future activation measurements, especially at high proton energies, it is recommended to investigate the neutron fields prior to each activation since small changes, such as target thickness or proton energy, have a large influence on the neutron energy distribution. Since, this is not possible at every facility, the dependency of accurate simulations arises. Therefore, the presented measurements need to be used to further improve simulation tools like PINO.

For further investigations of the presented measurement of the neutron fields, the efficiencies of the ^6Li -glass detectors should be measured in order to further investigate the accuracy of the GEANT-4 simulations of the detectors. This can improve the comparisons between simulation and measurement.

Neutron activation of Gallium

As an application of the ${}^7\text{Li}(\text{p},\text{n}){}^7\text{Be}$ neutron fields for astrophysics, the neutron capture cross sections of ${}^{69,71}\text{Ga}(\text{n},\gamma)$ at $k_B T = 25 \text{ keV}$ were investigated. The produced neutron energy distribution at a proton energy of $E_p = 1912 \text{ keV}$ mimicked a quasi-stellar spectrum relevant for the neutron capture cross sections during convective helium core burning in massive stars.

During the activation campaign samples with different compositions were used to minimize statistical uncertainties. Gallium samples with natural abundance, as well as enriched samples ${}^{69}\text{Ga}$ and ${}^{71}\text{Ga}$ were used. The activation of natural and enriched gallium was very successful. For ${}^{69}\text{Ga}(\text{n},\gamma)$ the measured values for samples with different gallium compositions were

$$\begin{aligned} \left\langle \frac{\sigma_{{}^{69}\text{Ga}}}{\sigma_{\text{Au}}} \right\rangle_{\text{natural sample}} &= 0.2827 \pm 0.0045_{\text{stat.}} \pm 0.0187_{\text{syst.}} \\ \left\langle \frac{\sigma_{{}^{69}\text{Ga}}}{\sigma_{\text{Au}}} \right\rangle_{\text{enriched act. I}} &= 0.2597 \pm 0.0031_{\text{stat.}} \pm 0.0165_{\text{syst.}} \\ \left\langle \frac{\sigma_{{}^{69}\text{Ga}}}{\sigma_{\text{Au}}} \right\rangle_{\text{enriched act. II}} &= 0.2624 \pm 0.0038_{\text{stat.}} \pm 0.0168_{\text{syst.}} \end{aligned}$$

These values agree within their uncertainties. Additionally, the values confirm the results presented by Göbel *et al.* during the activation measurement at the EC-JRC Geel [35].

The determined neutron capture cross sections ratios for the ${}^{71}\text{Ga}(\text{n},\gamma)$ reaction were inconsistent and lead to an extended activation campaign. The values determined during the first activation in 2019 were

$$\begin{aligned} \left\langle \frac{\sigma_{{}^{71}\text{Ga}}}{\sigma_{\text{Au}}} \right\rangle_{\text{natural sample}} &= 0.1728 \pm 0.0018_{\text{stat.}} \pm 0.0106_{\text{syst.}} \\ \left\langle \frac{\sigma_{{}^{71}\text{Ga}}}{\sigma_{\text{Au}}} \right\rangle_{\text{enriched}} &= 0.1179 \pm 0.0010_{\text{stat.}} \pm 0.0073_{\text{syst.}} \end{aligned}$$

As presented a difference in cross section ratio between natural and enriched sample of 32% arose. The value obtained using the natural composition however confirm the value presented by Göbel *et al.* for this reaction [35].

5. Conclusion and outlook

To exclude possible errors during the first activation, a different natural gallium sample and the enriched ^{71}Ga sample were activated. However, the difference of 32% remained. During the γ -spectroscopy of the activated spectra no impurities leading to an incorrect isotopic abundance in the samples could be determined. Additionally, the samples of natural and enriched gallium were investigated with non-destructive materials analysis. During the μXRF measurements no impurities could be determined.

Besides the possibility of impurities in the sample, the influence of the two gallium isotopes on one another were investigated by activating a stack of natural and enriched samples. The determined cross section ratios showed a clear difference depending on the position of the samples. However, using neutron capture simulations this could not be reproduced, which is most likely a result of the input cross sections due to the scarce data situation for gallium.

As an attempt to investigate the possible influence of ^{69}Ga on ^{71}Ga an activation of several natural gallium samples with different thicknesses was conducted. During the analysis no significant correlation of the cross section with sample thickness could be observed. Therefore, the situation remains far from being solved by activation measurements. The only remaining possibility to obtain a correct cross section for this reaction is the analysis of the time-of-flight measurements of the enriched and natural samples. This is done in the doctoral thesis of Deniz Kurtulgil. The results from these measurements conducted at the n_Tof experiment at CERN could bring light into the situation. Additionally, due to the overall scarce data situation, the measurement of the total cross section of gallium should be conducted, which is also important for neutron capture simulations. The measurements of the total cross sections of $^{69,71}\text{Ga}$ is proposed at the DICER facility at the Los Alamos National Laboratory, USA. With these additional data the mystery of the different cross sections for the same isotope in different samples could be solved.

6. Zusammenfassung

Im Rahmen dieser Arbeit wurden zwei Experimente geplant und durchgeführt.

Das erste Experiment diente der Vermessung der Energie- und Winkelverteilung der Neutronen, die bei der ${}^7\text{Li}(\text{p},\text{n}){}^7\text{Be}$ Reaktion entstehen. Das Experiment wurde bei verschiedenen Protonenenergien zwischen $E_p = 1887$ und 2800 keV an der Physikalisch-Technischen Bundesanstalt (PTB) in Braunschweig durchgeführt. Das Ziel dieser Messkampagne war das bessere Verständnis der Neutronenenergieverteilungen, um Simulationen zu überprüfen und zu verbessern. Ein zweites Experiment beschäftigte sich mit der Anwendung der Neutronenfelder der ${}^7\text{Li}(\text{p},\text{n}){}^7\text{Be}$ Reaktion für die Aktivierung von Gallium, um die Neutroneneinfangquerschnitte von ${}^{69}\text{Ga}$ und ${}^{71}\text{Ga}$ zu messen.

Untersuchung der ${}^7\text{Li}(\text{p},\text{n}){}^7\text{Be}$ Neutronenfelder

Die Messung der winkelabhängigen Neutronenspektren aus der ${}^7\text{Li}(\text{p},\text{n}){}^7\text{Be}$ Reaktion wurde bei zehn verschiedenen Protonenenergien durchgeführt: $1887, 1897, 1907, 1912, 2000, 2100, 2200, 2300, 2500, 2800$ keV. Zur Bestimmung der Neutronenenergie, wurde die Flugzeitmethode mit drei ${}^6\text{Li}$ -Glas Szintillationsdetektoren verwendet. Um Effekte gestreuter Neutronen zu minimieren, wurden die Experimente an der streuungsarmen PTB Ion Accelerator Facility der Physikalisch-Technischen Bundesanstalt in Braunschweig durchgeführt. Zusätzlich wurden zwei der verwendeten Detektoren auf Detektorhalterungen aus kohlenstofffaserverstärktem Kunststoff montiert, welche für dieses Experiment entworfen und gebaut wurden. Für die Messungen wurden die ${}^6\text{Li}$ -Glas Detektoren in einem Abstand von ca. 70 cm zu einem luftgekühlten metallischen Lithium Target montiert. Um einen möglichst konstanten Neutronenfluss zu sichern, wurden während des Experiments zwei metallische Lithium Targets mit einer Dicke von ca. $5\text{ }\mu\text{m}$ verwendet.

Vor jeder Messreihe wurde der Beschleuniger auf die bestmögliche Zeitaufösung eingestellt, um eine genaue Messung der Neutronenfelder zu ermöglichen. Die gemessene Zeitaufösung des gesamten Messaufbaus lag zwischen 2 und 4 ns. Diese Werte waren auch für weitere Vergleiche als Eingangsparameter für Simulation von Bedeutung. Anschließend wurden Flugzeitspektren für die beschriebenen Protonenenergie unter Winkeln in 5° Abstand gemessen. Während der Messungen wurde mit Hilfe von diversen Neutronenmonitoren der Neutronenfluss überwacht. In Kombination mit einem Ladungszähler, welcher den integrierten Protonenstrom während der Messungen aufzeichnet, wurde die Neutronenausbeute bestimmt. Die gemessenen Flugzeitspektren wurden für die weitere Untersuchung untergrundbereinigt. Dies war aufgrund des gleichbleibenden Untergrunds zwischen γ -flash und Neutronenereignissen möglich. Der sogenannte γ -flash entsteht, wenn während der Wechselwirkungen der Protonen mit dem Lithium-Target hochenergetische Photonen (γ s) entstehen, die mit Lichtgeschwindigkeit die Strecke bis zum Detektor zurücklegen und daher deutlich früher als die Neutronen ankommen.

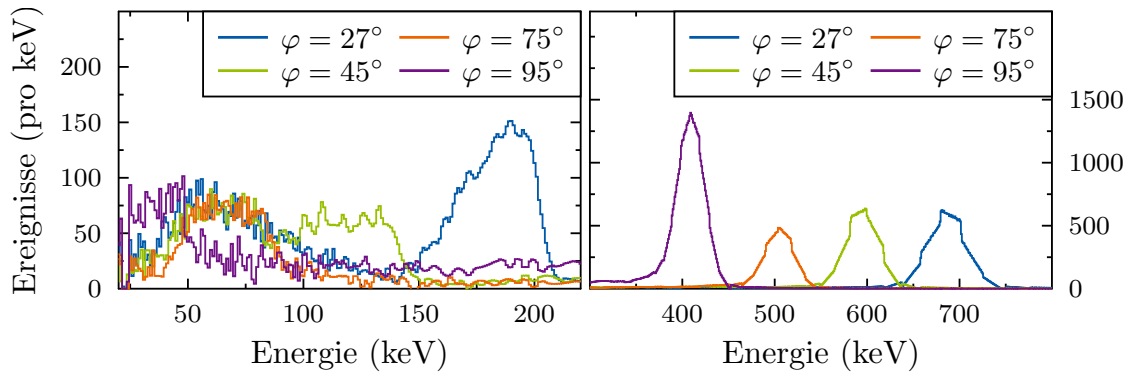


Abbildung 6.1.: Energiespektren erzeugt aus Flugzeitspektren unter verschiedenen Detektorwinkeln bei $E_p = 2500$ keV. Aufgrund der problematischen Energieauflösung bei hochenergetischen Neutronen, zeigen sich im rechten Teil der Grafik stufenartige Peaks.

Für die Erzeugung der winkelintegrierten Neutronenenspektren, den Neutronenfeldern, wurden die Energiespektren aufgrund unterschiedlicher Messdauern noch auf die während der Messung deponierten Ladungen auf dem Target normiert und entsprechend der Raumwinkelabdeckung skaliert. Im Anschluss wurden die gemessenen Spektren mit Simulationen verglichen, welche mit dem PINO Tool durchgeführt wurden. Dazu wurde das Tool weiterentwickelt, um die Energie- und Flugzeitspektren mit den Spezifikationen der Messungen nachzubilden. Während der Messungen wurde eine von der eingestellten abweichende Protonenenergie festgestellt. Die tat-

sächliche Protonenenergie wurde mit Hilfe des PINO Tools bestimmt. Dazu wurden die schnellen Neutronenflanken in den gemessenen Flugzeitspektren mit Simulationen bei verschiedenen Protonenenergien verglichen. Bei Energien bis 2200 keV ergab sich eine maximale Abweichung zwischen Einstellung und Messung von 3 keV. Bei den drei verbliebenen höheren Energien wurde eine maximale Abweichung von 10 keV bestimmt. Die durch den Abgleich bestimmte Protonenenergie wurde anschließend für die Vergleiche der Neutronenfelder zwischen Messung und Simulation verwendet.

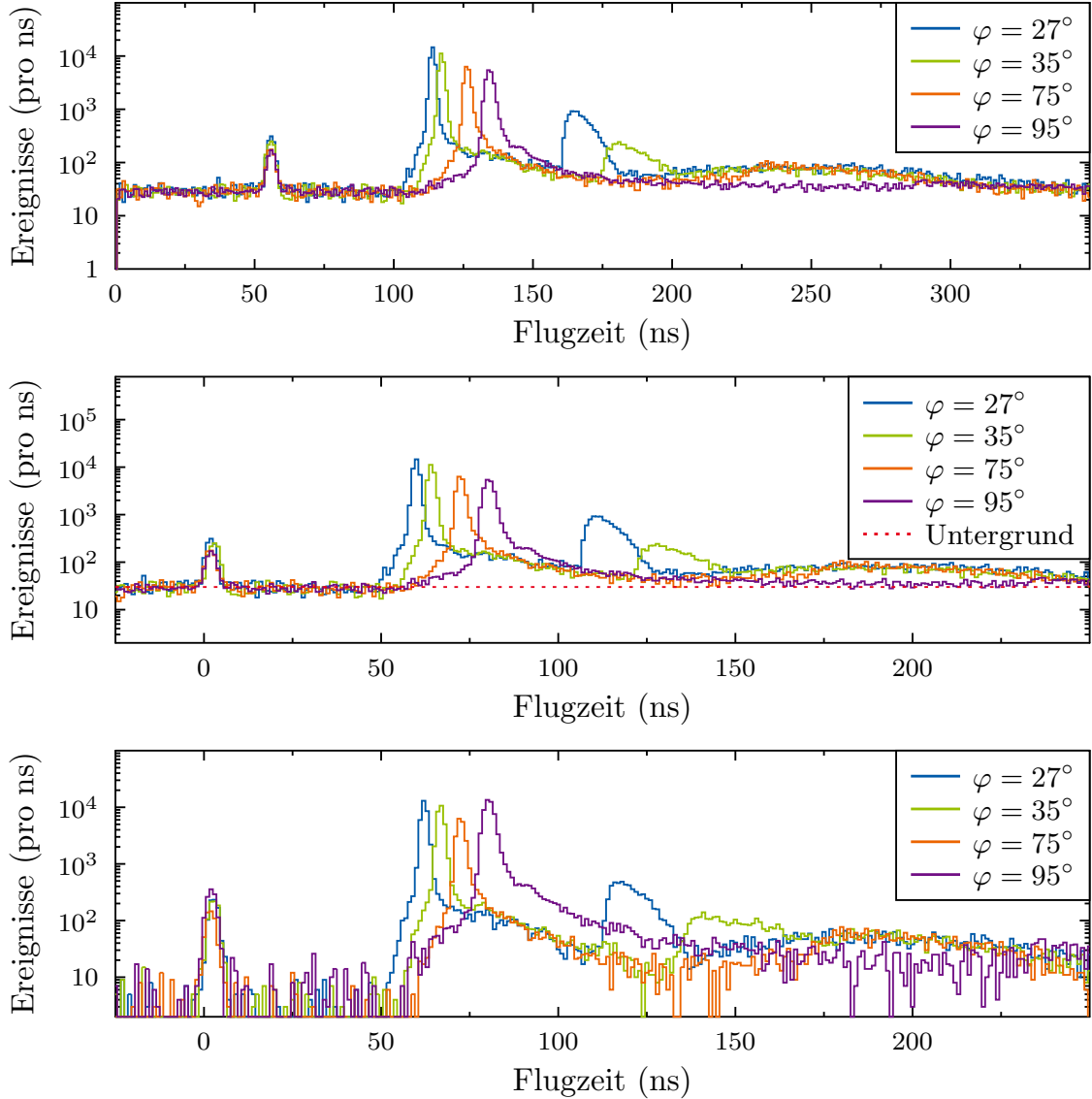


Abbildung 6.2.: Gezeigt sind die Flugzeitspektren für die verschiedenen Analyseschritte. Von oben nach unten: Die unkorrigierten, die γ -flash korrigierten und die untergrundbereinigten Flugzeitspektren bei einer eingestellten Protonenenergie von $E_p = 2500$ keV.

Die Neutronenspektren bei $E_p = 1887, 1897, 1907, 1912$ und 2100 keV zeigten eine sehr gute Übereinstimmung zwischen PINO und den Messungen. Bei den übrigen Energien ergaben sich Teils sehr große Differenzen zwischen Simulation und Messung. Eine mögliche Ursache hierfür ist die limitierte Energieauflösung aufgrund des kurzen Flugwegs. Eine andere ist die inkorrekte Simulation des zweiten Neutronenemissionskanals, welcher ab einer Protonenenergie von $E_p = 2372$ keV zur Verfügung steht. Zusätzlich könnten Probleme während des Experiments, wie zum Beispiel eine ungenaue Protonenenergie, inkorrekte Flugweg- oder Winkeleinstellung der Detektoren und die allmähliche Zerstörung des Lithiumtargets zu den Abweichungen beigetragen haben. Mit Hilfe der gewonnenen Erkenntnisse kann nun das PINO Tool bei hohen Protonenenergien weiter überprüft und verbessert werden, um genauere Vorhersagen für quasi-stellare Neutronenspektren zu treffen.

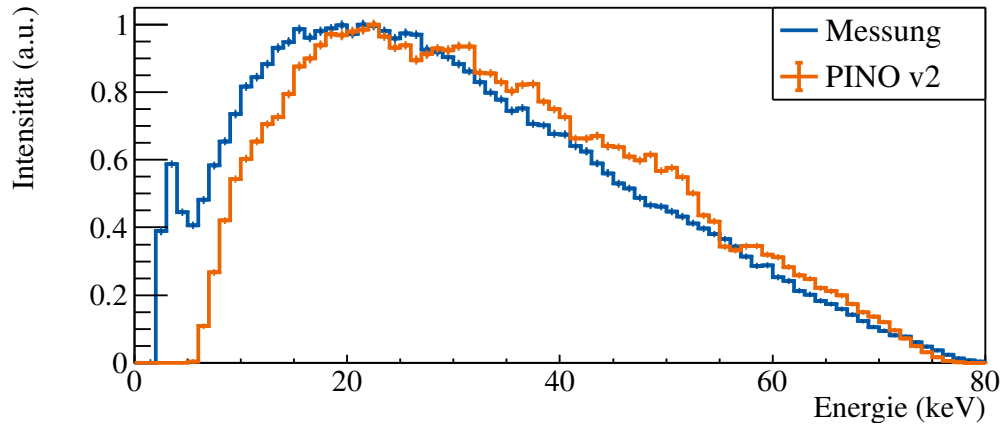


Abbildung 6.3.: Vergleich der winkelintegrierten Neutronenspektren bei $E_p = 1897$ keV.

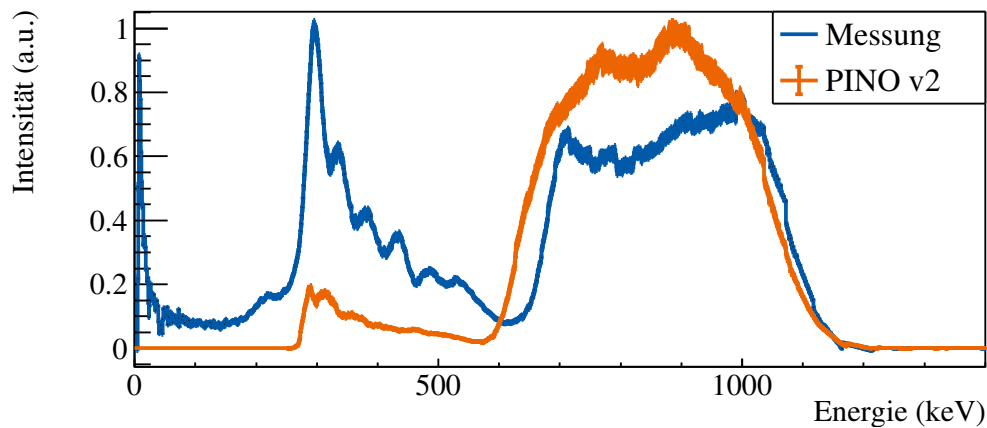


Abbildung 6.4.: Vergleich der winkelintegrierten Neutronenspektren bei $E_p = 2800$ keV.

Neutronenaktivierung von Gallium

Als eine Anwendung für die Neutronenfelder der ${}^7\text{Li}(\text{p},\text{n}){}^7\text{Be}$ Reaktion wurde Gallium aktiviert, ein Element, welches hauptsächlich während der schwachen Komponente des s-Prozesses in massiven Sternen gebildet wird. Die Aktivierungen wurden bei einer Protonenenergie von $E_p = 1912\text{ keV}$ durchgeführt. Das bei dieser Energie erzeugte Neutronenspektrum gleicht einer quasi-stellaren Neutronenenergieverteilung von $k_B T = 25\text{ keV}$. Dabei wurden sowohl natürliche Proben als auch angereicherte Proben untersucht, um die Neutroneneinfangsquerschnitte der Reaktionen ${}^{69,71}\text{Ga}(\text{n},\gamma)$ zu messen. Die Messung der Querschnitte der ${}^{69}\text{Ga}(\text{n},\gamma)$ Reaktion war sehr erfolgreich. Die Ergebnisse der Einfangsquerschnittverhältnisse zwischen Gallium und Gold, welche mit den verschiedenen Proben erhalten wurden, stimmen im Rahmen der jeweiligen Unsicherheiten überein:

$$\left\langle \frac{\sigma_{{}^{69}\text{Ga}}}{\sigma_{\text{Au}}} \right\rangle_{\text{natürliche Probe}} = 0.2827 \pm 0.0045_{\text{stat.}} \pm 0.0187_{\text{syst.}}$$

$$\left\langle \frac{\sigma_{{}^{69}\text{Ga}}}{\sigma_{\text{Au}}} \right\rangle_{\text{angereichert Akt. I}} = 0.2597 \pm 0.0031_{\text{stat.}} \pm 0.0165_{\text{syst.}}$$

$$\left\langle \frac{\sigma_{{}^{69}\text{Ga}}}{\sigma_{\text{Au}}} \right\rangle_{\text{angereichert Akt. II}} = 0.2624 \pm 0.0038_{\text{stat.}} \pm 0.0168_{\text{syst.}}$$

Die erhaltenen Ergebnisse für die ${}^{71}\text{Ga}(\text{n},\gamma)$ Reaktion, ermittelt mit natürlichen und angereicherten Problem, zeigen eine Differenz von 32%, deutlich außerhalb der abgeschätzten Unsicherheiten:

$$\left\langle \frac{\sigma_{{}^{71}\text{Ga}}}{\sigma_{\text{Au}}} \right\rangle_{\text{natürliche Probe}} = 0.1728 \pm 0.0018_{\text{stat.}} \pm 0.0106_{\text{syst.}}$$

$$\left\langle \frac{\sigma_{{}^{71}\text{Ga}}}{\sigma_{\text{Au}}} \right\rangle_{\text{angereicherte Probe}} = 0.1179 \pm 0.0010_{\text{stat.}} \pm 0.0073_{\text{syst.}}$$

Um die Ursache der Differenz zu ermitteln, wurden weitere Aktivierungsmessungen durchgeführt. Die Ursache für die Abweichungen konnte nicht abschließen ermittelt werden. Eine mögliche Kontamination mit Fremdelementen der Proben wurde mittels Mikro-Röntgenfluoreszenz ausgeschlossen. Der gegenseitige Einfluss von ${}^{69}\text{Ga}$ und ${}^{71}\text{Ga}$ wurde untersucht und die Proben als Stapel gleichzeitig aktiviert. Hierbei

zeigten sich deutliche Unterschiede. Diese konnten durch Neutroneneinfangssimulationen in ihrer Tendenz bestätigt, aber nicht vollständig erklärt werden. Weiterhin wurde die Neutronentransmission untersucht und dazu natürliche Galliumproben verschiedener Dicken untersucht. Ein Einfluss der Probendicke auf den Wirkungsquerschnitt konnte nicht festgestellt werden. Um diesem Phänomen auf den Grund zu gehen und den genauen Neutroneneinfangsquerschnitt von ^{71}Ga zu bestimmen, wird die Auswertung von Flugzeitsmessungen benötigt. Zusätzlich, um die Datenlage zu verbessern, sollten auch Messungen des totalen sowie des Streuquerschnitts durchgeführt werden, um auch verschiedene Simulationen zu verbessern. Eine Messung des totalen Wirkungsquerschnitts von ^{69}Ga und ^{71}Ga wurde an der DICER Anlage des Los Alamos National Laboratory vorgeschlagen.

A. Appendix

Uncertainty calculation

Each measured value has an uncertainty. The knowledge and understanding of these is crucial in order to fully understand the measured and determined values of interest. In general uncertainties can be divided into different categories as the statistical and the systematic uncertainties. Statistical uncertainties, as the name implies, are of statistical unpredictable nature. The second kind are the systematic uncertainties. Systematic uncertainties can not be minimized by higher statistics. An example for the systematic uncertainty is an incorrect time setting during a time critical experiment. If the clock is 10 seconds off, the uncertainty does not change even if the measurement is repeated.

Gaussian error propagation

Most values determined by an experiment are the product of using various calculations using the measured values. Since each of the measured values has an uncertainty also the value of interest has an uncertainty. This uncertainty can be determined using the Gaussian error propagation. The uncertainty of a determined value (y) u_y can be derived from the uncertainties of the values contributing to the value u_i :

$$u_y = \sqrt{\sum_{i=1}^n \left(\frac{\partial y}{\partial x_i} \cdot u_i \right)^2} \quad (\text{A.1})$$

where y denotes the value of interest and x_i the value afflicted with the uncertainty u_i . Equation A.1 however is only valid for independent variables. If variables are

A. Appendix

dependent, the covariance has to be taken into account. The covariance is defined as: $u(x_i, x_j)$. Equation A.1 then becomes

$$u_y = \sqrt{\sum_{i=1}^n \left(\frac{\partial y}{\partial x_i} \cdot u_i \right)^2 + 2 \sum_{i=1}^{n-1} \sum_{j=i+1}^n \left(\frac{\partial y}{\partial x_i} \right) \left(\frac{\partial y}{\partial x_j} \right) u(x_i, x_j)}. \quad (\text{A.2})$$

Weighted arithmetic mean

The weighted arithmetic mean takes the uncertainties of the values contributing to a mean value into account. A value with a higher uncertainty contributes less to the mean than a value with a lower uncertainty. The weighted arithmetic mean is defined as

$$\bar{x} = \frac{\sum_{i=1}^n x_i w_i}{\sum_{i=1}^n w_i} \quad (\text{A.3})$$

with

$$w_i = \frac{1}{\Delta u_i^2}, \quad (\text{A.4})$$

where Δu_i is the total uncertainty derived from statistic and systematic uncertainties. The total uncertainty can be determined via

$$\Delta u_{\text{tot.}}^2 = u_{\text{stat.}}^2 + u_{\text{syst.}}^2. \quad (\text{A.5})$$

The uncertainty of the weighted arithmetic mean was calculated as follows

$$\Delta \bar{x} = \sqrt{\frac{1}{\sum_{i=1}^n w_i}}. \quad (\text{A.6})$$

B. Appendix - Investigation of the ${}^7\text{Li}(\text{p},\text{n}){}^7\text{Be}$ neutron fields

Accumulated beam charge

In this section the accumulated beam charge determined by the current integrator during the measurements of the neutron fields are presented.

E_p (keV)	Run	Detector I φ (deg)	Detector II φ (deg)	Detector III φ (deg)	ΣQ (μC)
1887	102	27	27	0	1431487
	103	50	15	15	1876177
	105	50	20	10	1580980
	106	50	25	5	1417661

Table B.1.: Accumulated beam charge on the target during the measurements of the neutron fields at a proton energy of $E_p = 1887\text{ keV}$

E_p (keV)	Run	Detector I φ (deg)	Detector II φ (deg)	Detector III φ (deg)	ΣQ (μC)
1897	107	27	27	0	791556
	108	35	30	0	1189986
	109	45	40	0	1239245
	110	40	25	5	777321
	111	40	20	10	762138
	112	50	15	15	670327

Table B.2.: Accumulated beam charge on the target during the measurements of the neutron fields at a proton energy of $E_p = 1897\text{ keV}$

B. Appendix - Investigation of the ${}^7\text{Li}(p,n){}^7\text{Be}$ neutron fields

E_p (keV)	Run	Detector I φ (deg)	Detector II φ (deg)	Detector III φ (deg)	ΣQ (μC)
1907	114	27	27	0	654115
	115	35	30	0	611981
	116	45	40	0	895697
	117	55	50	0	1345898
	118	65	60	0	1370354
	119	55	25	5	742503
	120	55	20	10	723839
	121	55	15	15	746887
	122	60	30	30	610246

Table B.3.: Accumulated beam charge on the target during the measurements of the neutron fields at a proton energy of $E_p = 1907$ keV

E_p (keV)	Run	Detector I φ (deg)	Detector II φ (deg)	Detector III φ (deg)	ΣQ (μC)
1912	72	27	27	0	853772
	73	35	30	0	1526984
	74	45	40	0	1067096
	75	55	50	0	1132080
	77	55	50	0	723548
	78	65	60	0	1328181
	79	65	0	27	1011753
	80	65	5	25	955247
	81	65	10	20	842531
	82	65	15	15	923257
	83	27	27	0	599607
	84	35	30	0	672579
	85	45	40	0	816760
	87	55	50	0	1211264
	94	27	27	0	931800
	95	40	30	0	1130150
	96	40	20	10	947803
	97	60	50	0	1155877

Table B.4.: Accumulated beam charge on the target during the measurements of the neutron fields at a proton energy of $E_p = 1912$ keV

E_p (keV)	Run	Detector I φ (deg)	Detector II φ (deg)	Detector III φ (deg)	ΣQ (μC)
2000	123	27	27	0	545798
	124	35	30	0	344079
	125	35	30	0	215528
	126	27	27	0	484014
	127	45	40	0	602457
	128	55	50	0	712439
	129	55	25	5	484942
	130	55	20	10	528275
	131	55	15	15	521697
	132	65	60	0	533518
	133	75	70	0	469271
	134	85	80	0	470582
	135	95	90	0	481461
	136	95	90	0	752278
	137	95	90	0	440680
	138	85	80	0	689404
	139	75	70	0	797899

Table B.5.: Accumulated beam charge on the target during the measurements of the neutron fields at a proton energy of $E_p = 2000$ keV

E_p (keV)	Run	Detector I φ (deg)	Detector II φ (deg)	Detector III φ (deg)	ΣQ (μC)
2100	11	27	27	0	683437
	12	35	30	0	821616
	13	45	40	0	735895
	14	55	50	0	771170
	15	55	25	5	850982
	16	55	20	10	828752
	17	55	15	15	752161
	18	65	60	0	753132
	19	75	70	0	774415
	20	85	80	0	711794
	21	95	90	0	678740

Table B.6.: Accumulated beam charge on the target during the measurements of the neutron fields at a proton energy of $E_p = 2100$ keV

E_p (keV)	Run	Detector I φ (deg)	Detector II φ (deg)	Detector III φ (deg)	ΣQ (μC)
2200	153	27	27	0	575891
	154	30	40	0	619443
	155	50	60	0	627211
	156	70	80	0	539582
	157	90	10	20	583745
	158	50	15	15	850181

Table B.7.: $E_p = 2200$ keV

B. Appendix - Investigation of the ${}^7\text{Li}(p,n){}^7\text{Be}$ neutron fields

E_p (keV)	Run	Detector I φ (deg)	Detector II φ (deg)	Detector III φ (deg)	ΣQ (μC)
2300	23	27	27	0	595262
	24	35	30	0	594077
	25	45	40	0	632692
	26	55	50	0	660816
	27	55	25	5	674619
	28	55	20	10	732436
	29	55	15	15	672619
	30	65	60	0	641027
	31	75	70	0	585886
	32	85	80	0	802530
	33	95	90	0	727402

Table B.8.: Accumulated beam charge on the target during the measurements of the neutron fields at a proton energy of $E_p = 2300$ keV

E_p (keV)	Run	Detector I φ (deg)	Detector II φ (deg)	Detector III φ (deg)	ΣQ (μC)
2500	35	95	90	0	1414920
	36	85	80	0	595800
	38	85	80	0	585726
	39	27	27	0	580312
	41	35	30	0	555204
	44	45	40	0	546854
	52	55	50	0	623205
	53	55	25	5	603966
	54	55	20	10	513247
	55	55	15	15	703569
	56	65	60	0	565671
	57	75	70	0	549972

Table B.9.: Accumulated beam charge on the target during the measurements of the neutron fields at a proton energy of $E_p = 2500$ keV

E_p (keV)	Run	Detector I φ (deg)	Detector II φ (deg)	Detector III φ (deg)	ΣQ (μC)
2800	140	27	27	0	1345162
	141	35	30	0	1682312
	142	45	40	0	1706845
	143	55	50	0	1934658
	144	55	25	5	1679147
	145	55	20	10	1561219
	148	55	15	15	1565138
	149	65	60	0	1790586
	150	75	70	0	1879986
	151	85	80	0	2118399
	152	95	90	0	2076160

Table B.10.: Accumulated beam charge on the target during the measurements of the neutron fields at a proton energy of $E_p = 2800$ keV

Angular correction factors

Presented are the angular correction factors used for the scaling of the angle-integrated neutron spectra.

$E_p = 1887 \text{ keV}$		$E_p = 1897 \text{ keV}$		$E_p = 1907 \text{ keV}$		$E_p = 1912 \text{ keV}$	
Angle	Correction	Angle	Correction	Angle	Correction	Angle	Correction
0°	$5.26 \cdot 10^{-3}$	0°	$2.93 \cdot 10^{-3}$	0°	$1.77 \cdot 10^{-3}$	0°	$1.36 \cdot 10^{-3}$
5°	0.049	5°	0.023	5°	0.014	5°	0.011
10°	0.097	10°	0.047	10°	0.028	10°	0.022
15°	0.144	15°	0.070	15°	0.042	15°	0.032
20°	0.191	20°	0.092	20°	0.055	20°	0.043
25°	0.235	25°	0.114	25°	0.069	25°	0.053
30°	0.279	30°	0.134	30°	0.081	30°	0.062
		35°	0.153	35°	0.093	35°	0.072
		40°	0.173	40°	0.104	40°	0.080
		45°	0.190	45°	0.115	45°	0.088
				50°	0.124	50°	0.096
				55°	0.132	55°	0.102
				60°	0.140	60°	0.108
						65°	0.113
						70°	0.117

Table B.11.: Angular correction factors for the determination of the neutron fields.

Angle	Correction	Angle	Correction	Angle	Correction
0°	$9.95 \cdot 10^{-4}$	5°	$7.95 \cdot 10^{-3}$	10°	0.0160
15°	0.023	20°	0.031	25°	0.039
30°	0.046	35°	0.052	40°	0.059
45°	0.065	50°	0.070	55°	0.074
60°	0.079	65°	0.080	70°	0.086
75°	0.088	80°	0.090	85°	0.091

Table B.12.: Angular correction factors used for the determination of the neutron fields above proton energies of $E_p = 2000 \text{ keV}$.

Neutron energy sub plots

Presented are the scaled neutron spectra for each detector and angle.

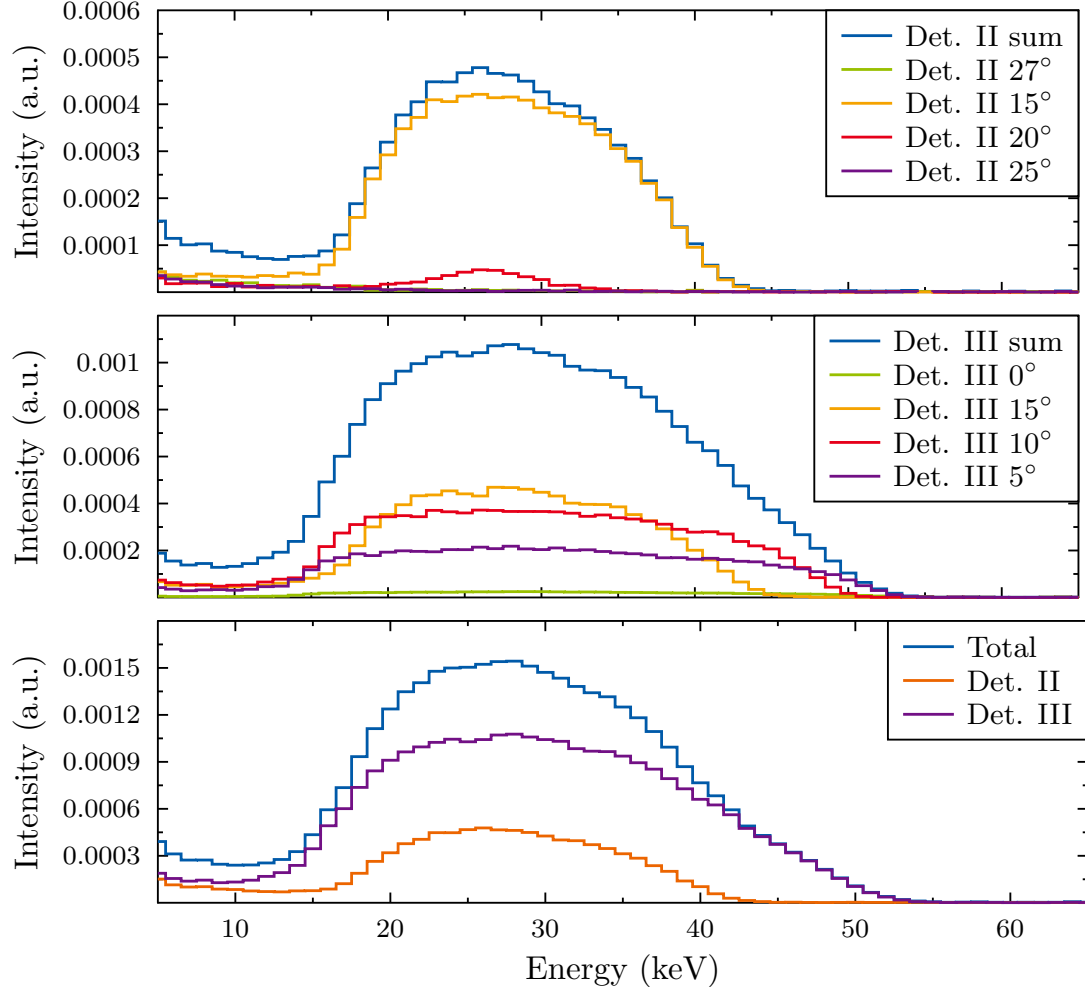


Figure B.1.: Measured neutron spectra for a set proton energy of $E_p = 1887$ keV

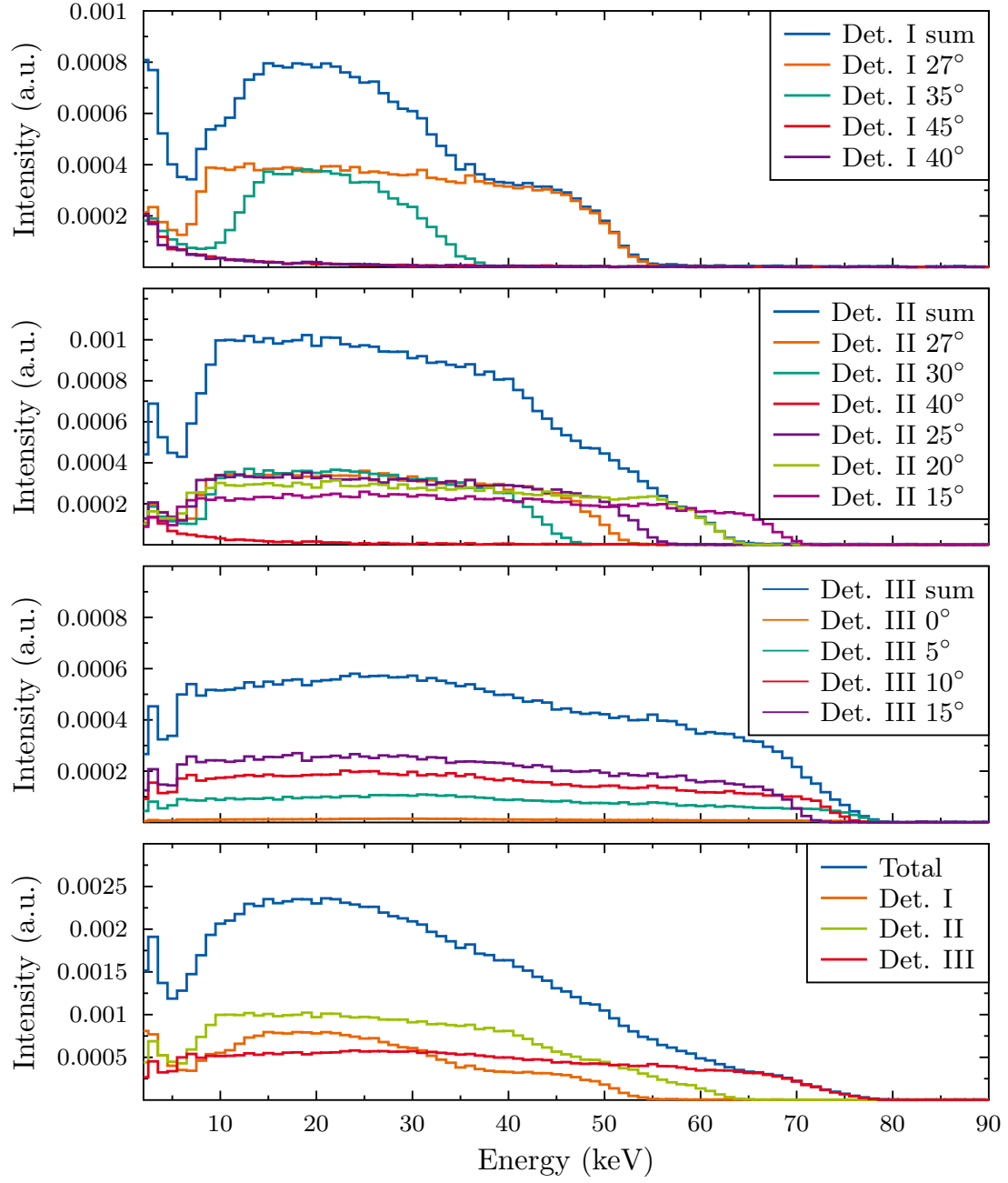


Figure B.2.: Measured neutron spectra for a set proton energy of $E_p = 1897$ keV

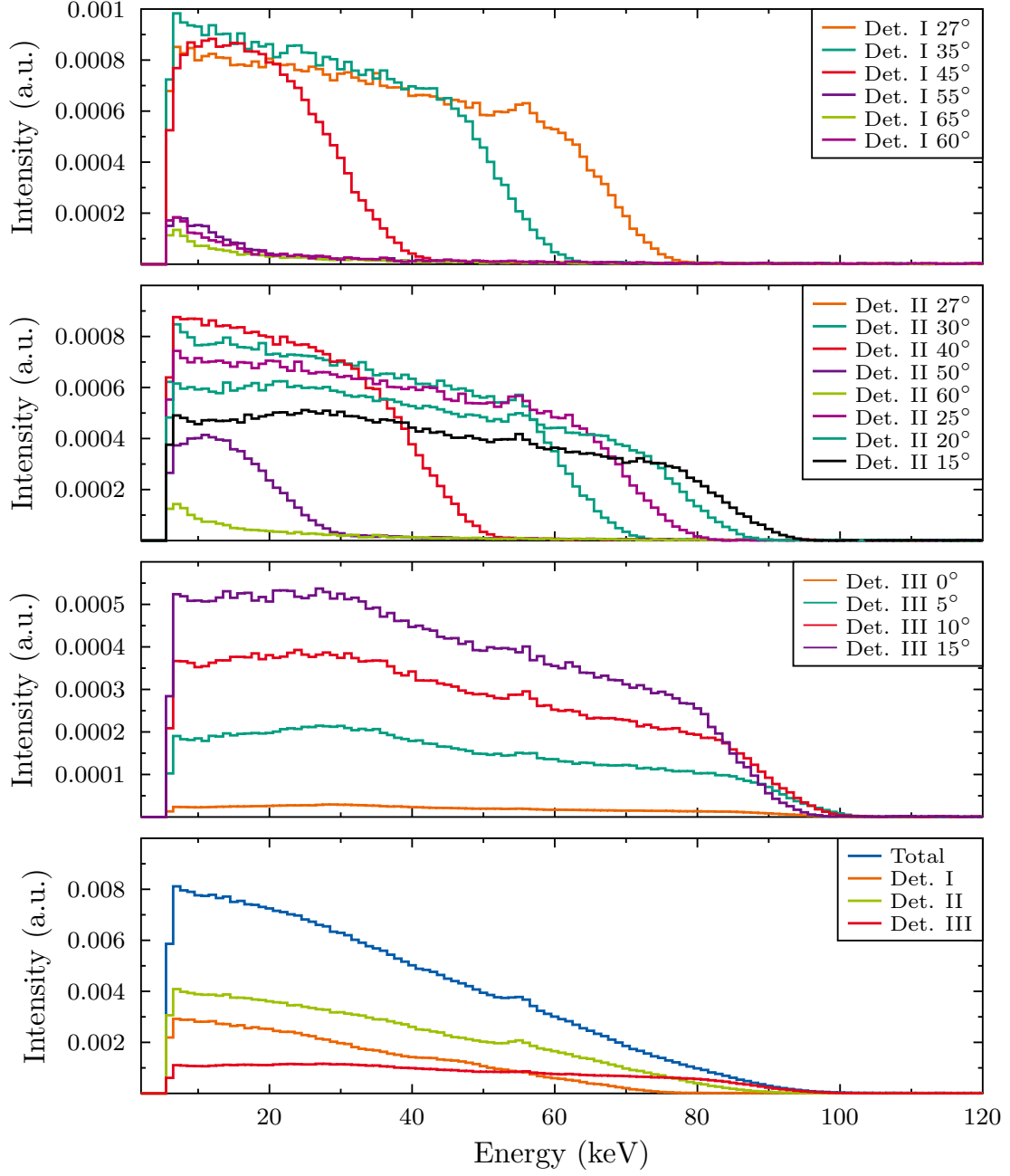


Figure B.3.: Measured neutron spectra for a set proton energy of $E_p = 1907$ keV

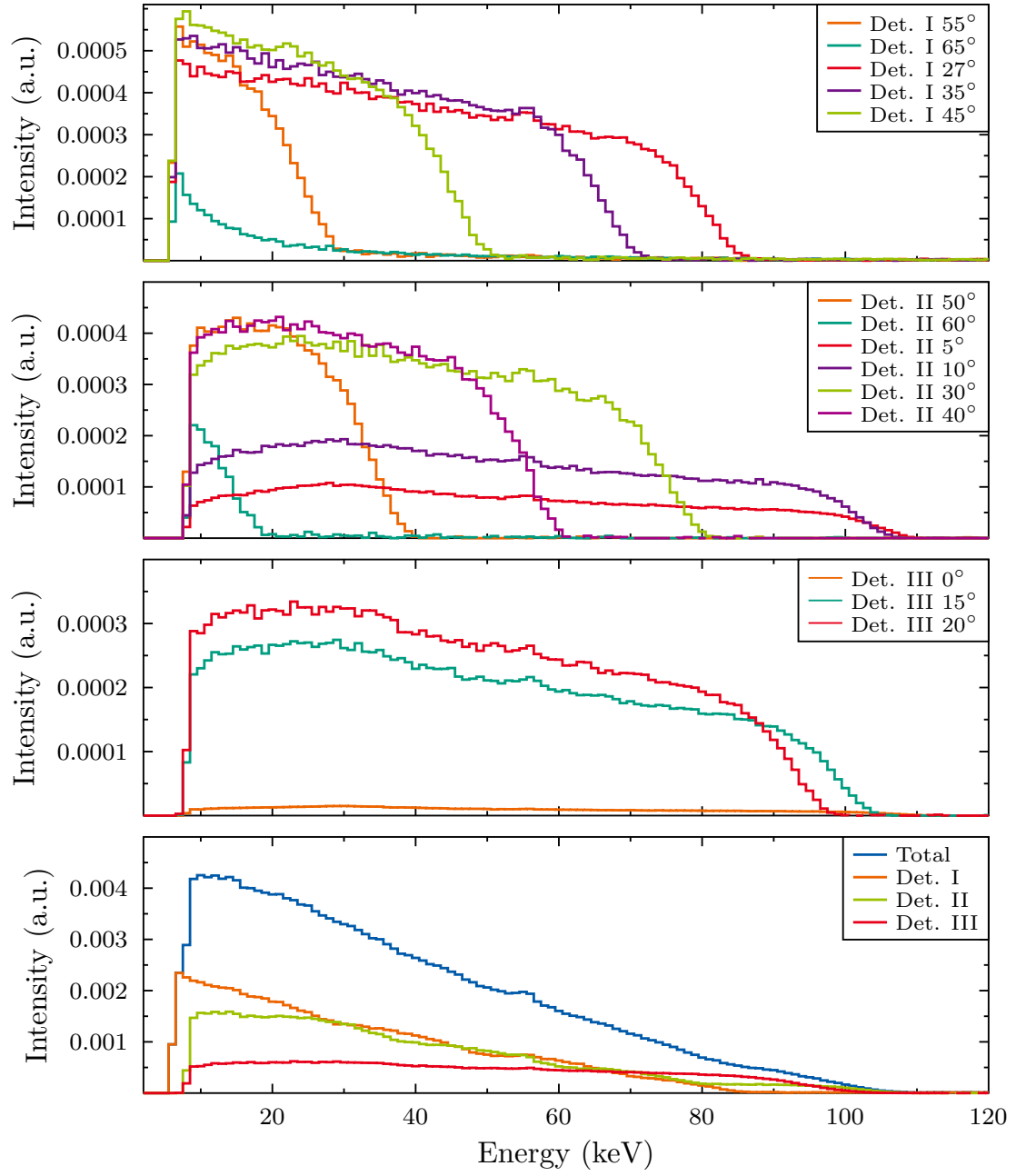


Figure B.4.: Measured neutron spectra for a set proton energy of $E_p = 1912$ keV

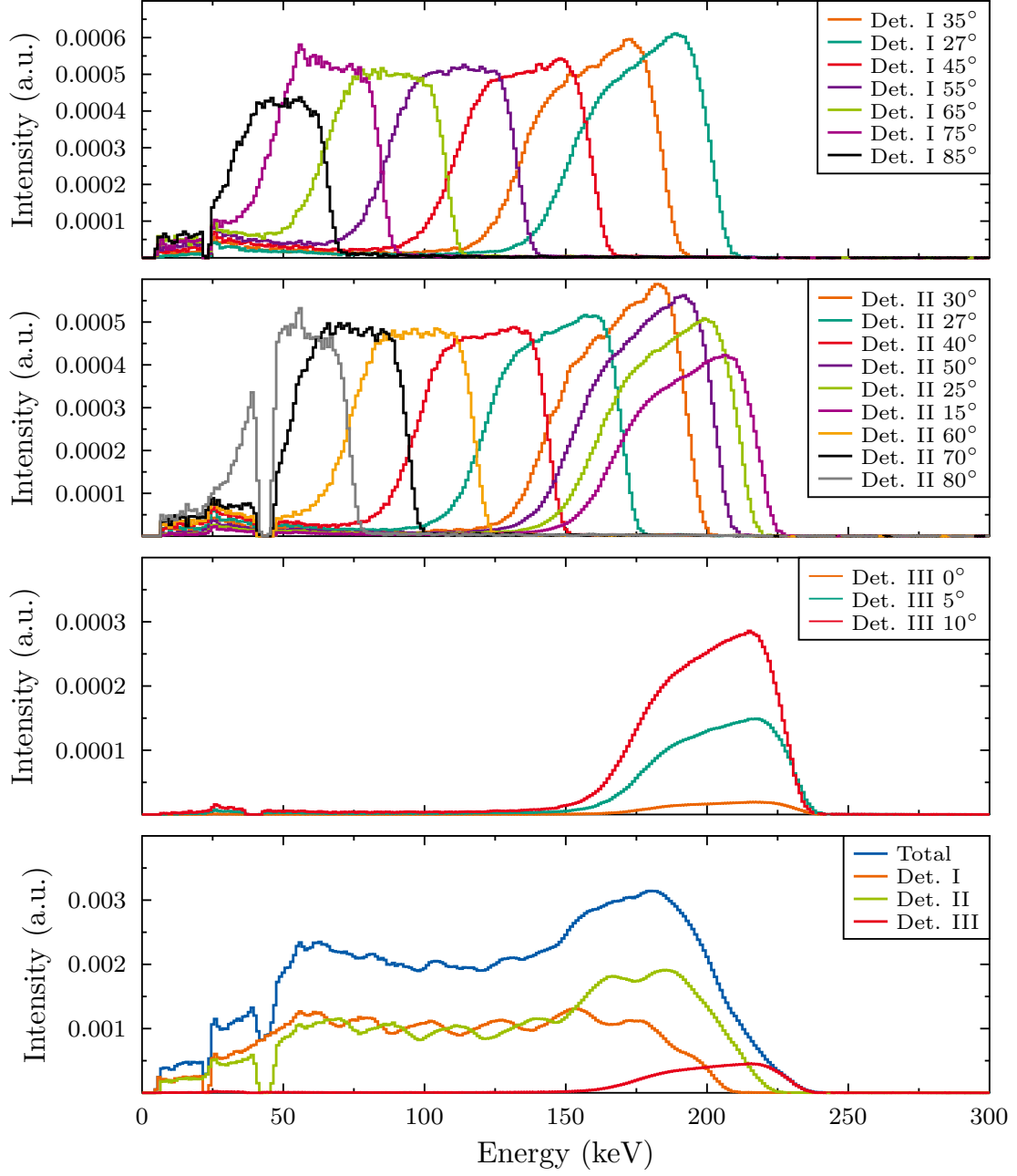


Figure B.5.: Measured neutron spectra for a set proton energy of $E_p = 2000$ keV

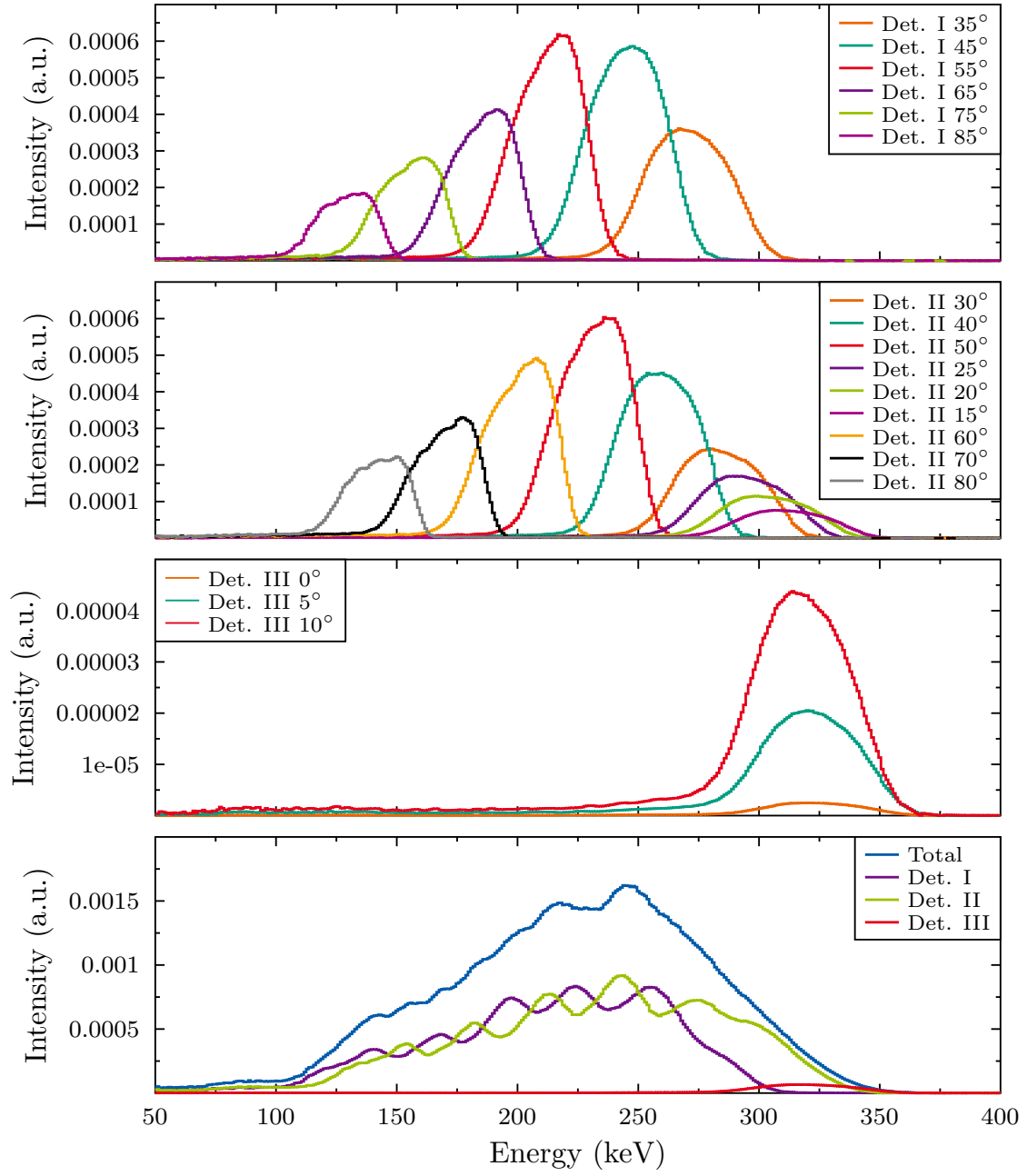


Figure B.6.: Measured neutron spectra for a set proton energy of $E_p = 2100$ keV

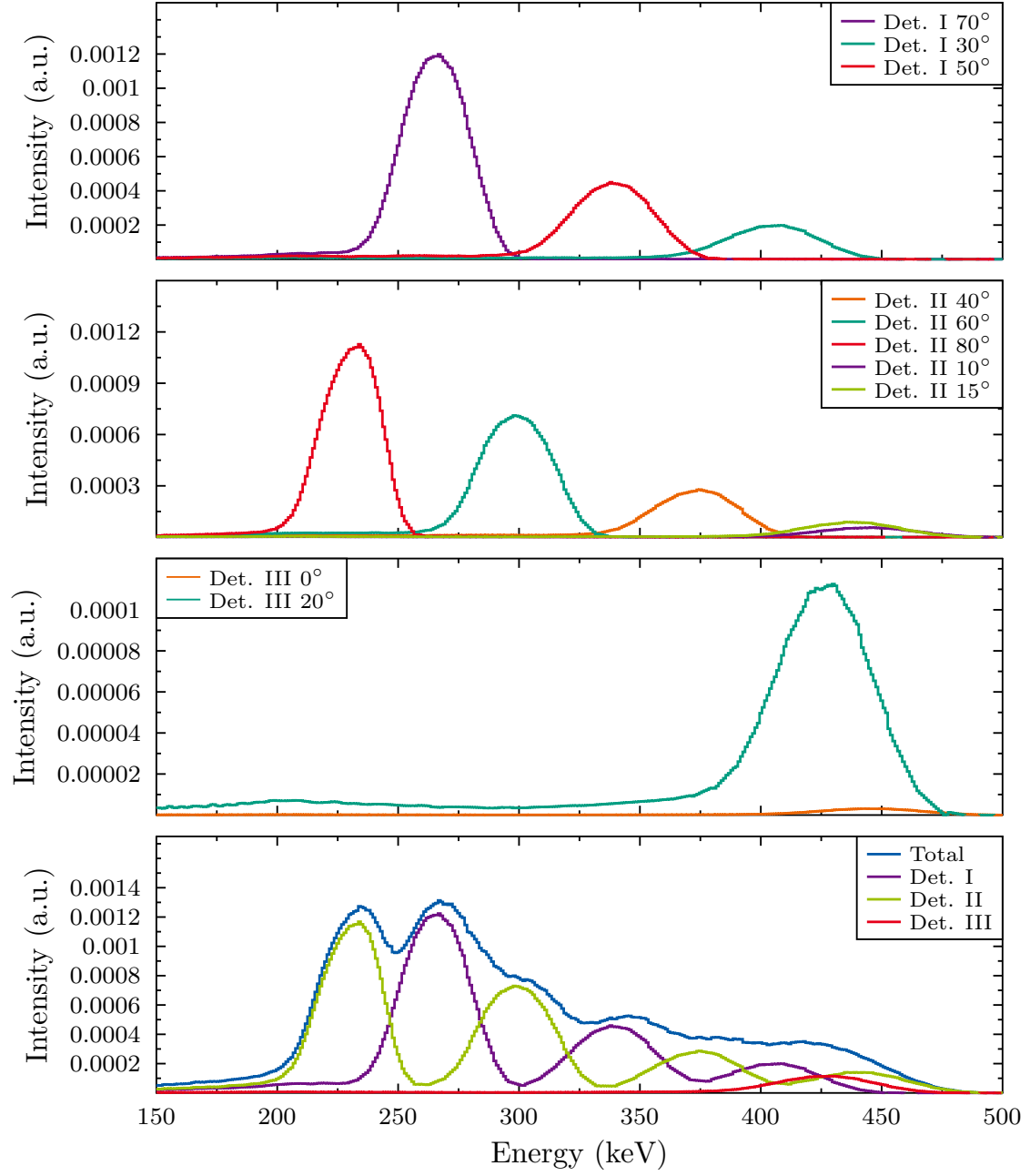


Figure B.7.: Measured neutron spectra for a set proton energy of $E_p = 2200$ keV

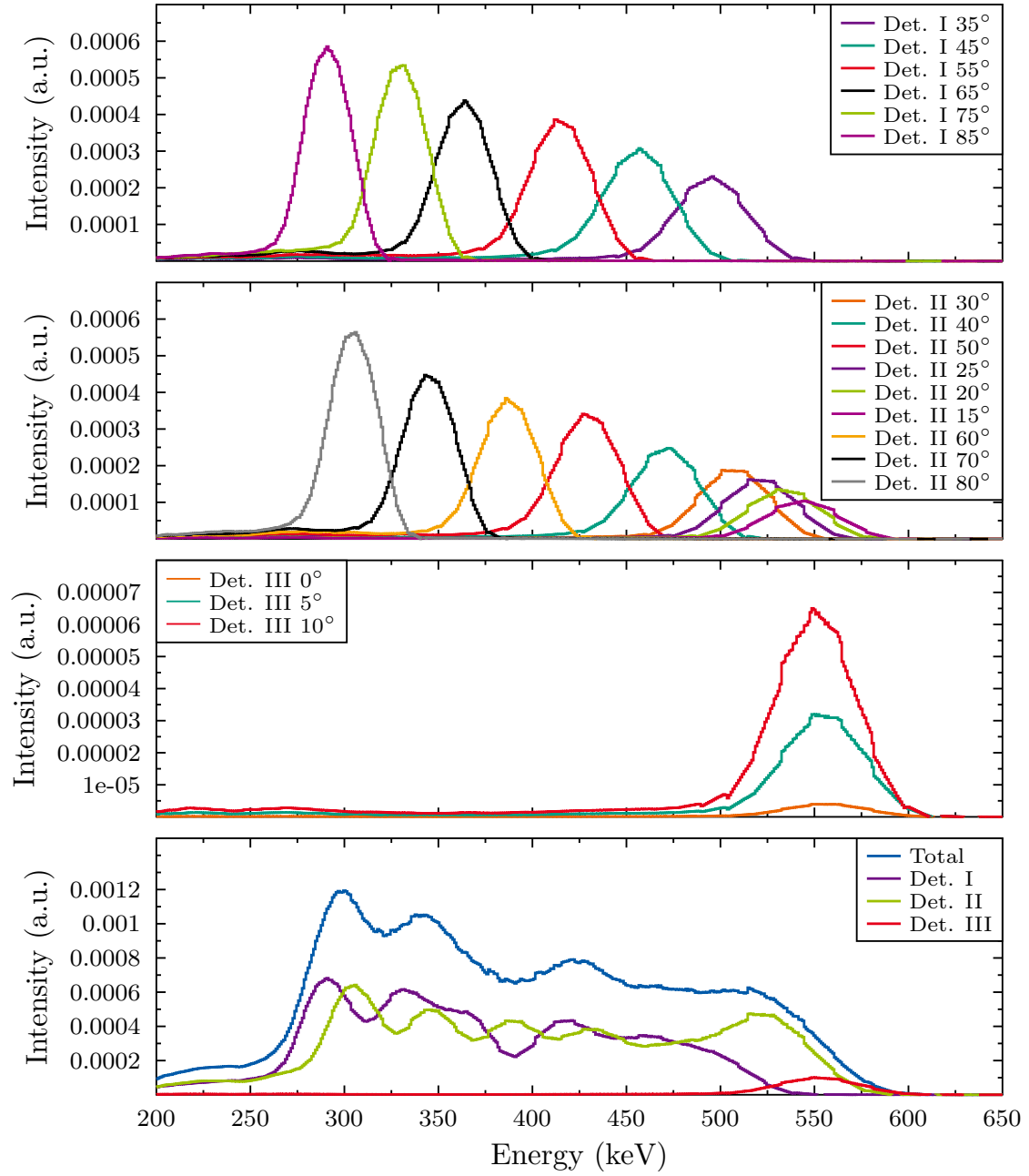


Figure B.8.: Measured neutron spectra for a set proton energy of $E_p = 2300$ keV

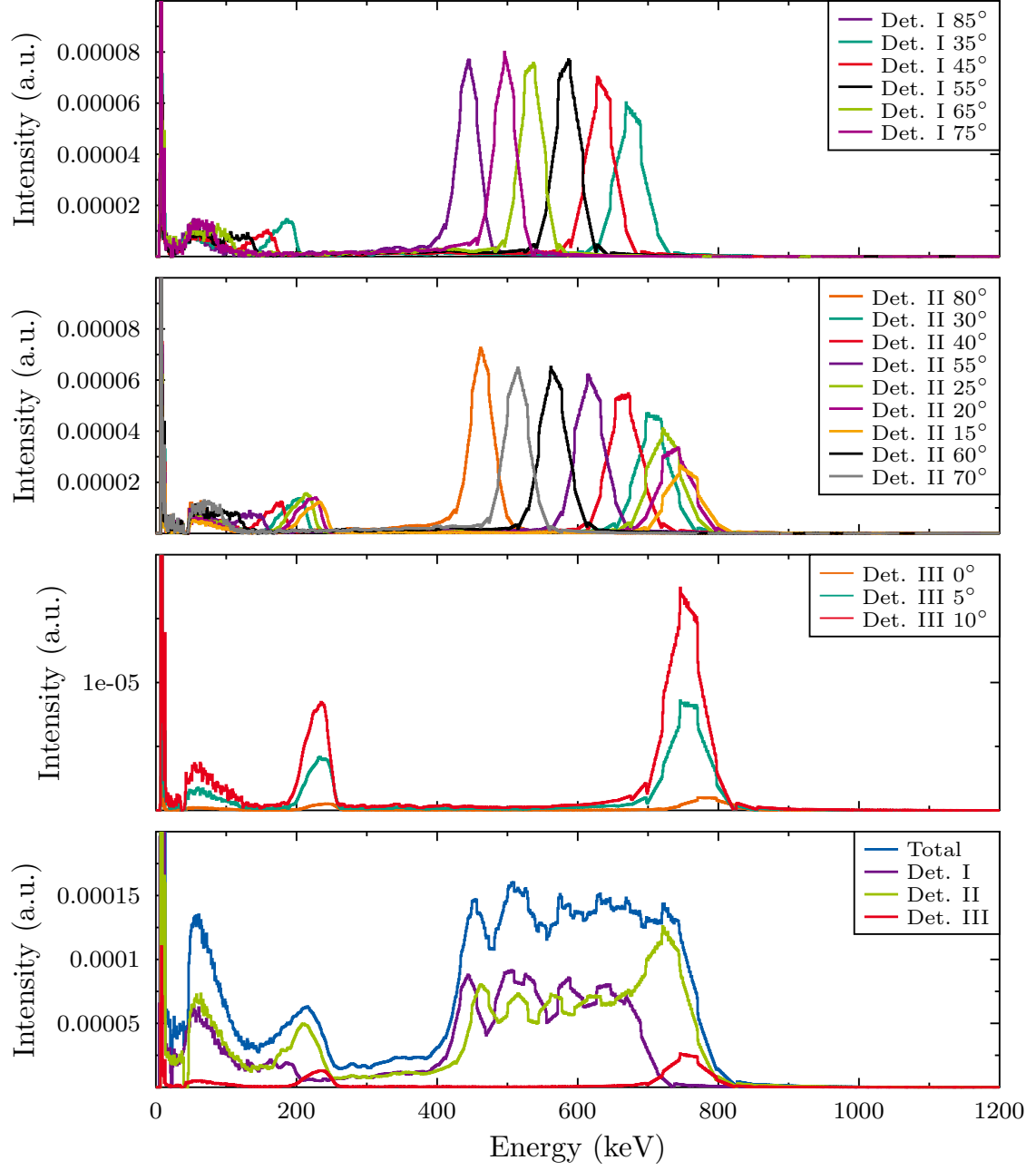


Figure B.9.: Measured neutron spectra for a set proton energy of $E_p = 2500$ keV

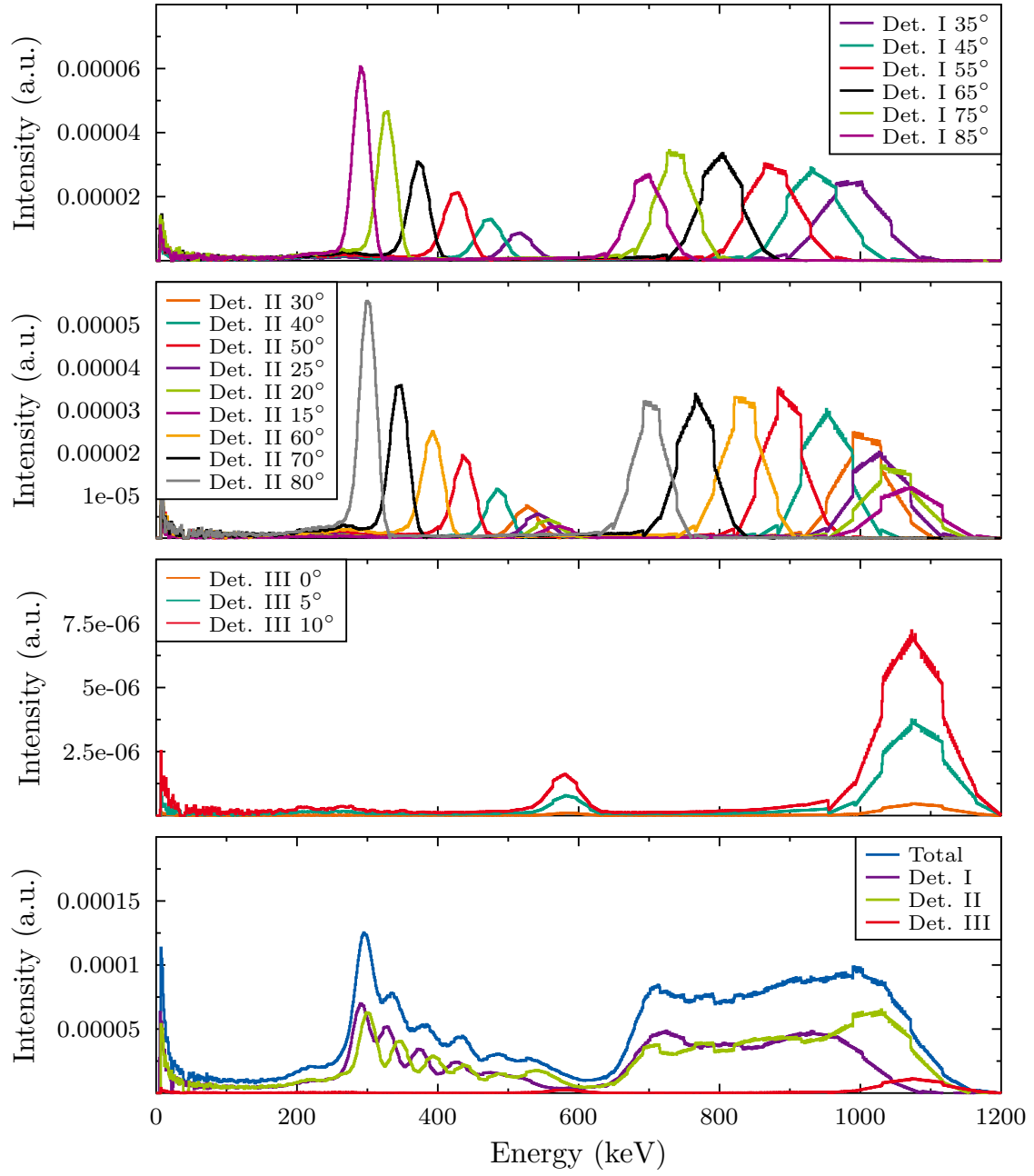


Figure B.10.: Measured neutron spectra for a set proton energy of $E_p = 2800$ keV

C. Appendix - Neutron activation of Gallium

In this chapter all the intermediate steps and values are presented used for the calculation of the cross sections ratios for the neutron activation campaign of gallium. For each activation the determined counts by γ -spectroscopy, the simulation, waiting time, dead time and beam correction factors, as well as the number of produced nuclei are presented.

Isotope	γ -energy (keV)	Reference
^{210}Pb	46.53	[64]
^{57}Co	122.06	[11]
^{57}Co	133.46	
^{133}Ba	80.99	[40]
^{133}Ba	276.40	
^{133}Ba	302.85	
^{133}Ba	356.01	
^{137m}Ba (product of ^{137}Cs)	661.66	[15]
^{54}Mn	834.85	[29]
^{22}Na	1274.54	[7]
^{60}Co	1173.23	[14]
^{60}Co	1332.49	

Table C.1.: Calibration sources used for the detector calibrations. All sources were distributed and calibrated by the Physikalisch-Technische Bundesanstalt (PTB), Braunschweig, Germany.

Sample	Isotopic ratio (%)	Mass (g)	$N_{\text{sample}}/10^{21}$
$^{\text{nat}}\text{Ga}$ I	^{69}Ga : 60.1	0.89506(15)	4.646 ± 0.02 %
	^{71}Ga : 39.9		3.085 ± 0.02 %
$^{\text{nat}}\text{Ga}$ II	^{69}Ga : 60.1	0.97681(15)	5.080 ± 0.02 %
	^{71}Ga : 39.9		3.366 ± 0.02 %
^{69}Ga	^{69}Ga : 99.48	0.94129(15)	8.180 ± 0.02 %
	^{71}Ga : 0.52		-
^{71}Ga	^{69}Ga : 99.8	0.93036(15)	-
	^{71}Ga : 0.2		8.393 ± 0.02 %

Table C.2.: Properties of the activated samples. The isotopic ratio for the enriched ^{69}Ga sample was taken from the Isoflex USA Certificate of analysis No. 5958 and for the enriched ^{71}Ga from Certificate of analysis No. 6803.

Activation I

Decay of	γ -energy (keV)	Counts A	f_{sim} A	Counts B	f_{sim} B
Sample natGa I					
^{70}Ga	176.115 (13)	1534 (71)	$0.0000458 \pm 5.9\%$	1545 (67)	$0.0000461 \pm 5.9\%$
	1039.513 (10)	735 (30)	$0.0000198 \pm 9.2\%$	624 (36)	$0.0000186 \pm 9.2\%$
^{72}Ga	629.967 (19)	1601 (67)	$0.00115 \pm 5.0\%$	1668 (64)	$0.00115 \pm 5.0\%$
	834.13 (4)	4257 (73)	$0.00324 \pm 5.0\%$	3986 (76)	$0.00325 \pm 5.0\%$
	894.327 (18)	403 (36)	$0.000314 \pm 5.0\%$	445 (38)	$0.000300 \pm 5.0\%$
	1050.794 (17)	218 (27)	$0.000202 \pm 5.0\%$	219 (26)	$0.000193 \pm 5.0\%$
Sample ^{69}Ga activation 1					
^{70}Ga	176.115 (13)	2981 (85)	$0.0000458 \pm 5.9\%$	2936 (89)	$0.0000461 \pm 5.9\%$
	1039.513 (10)	1127 (45)	$0.0000198 \pm 9.2\%$	1124 (47)	$0.0000186 \pm 9.2\%$
Sample ^{69}Ga activation 2					
^{70}Ga	176.115 (13)	1956 (72)	$0.0000458 \pm 5.9\%$	1824 (84)	$0.0000461 \pm 5.9\%$
	1039.513 (10)	748 (36)	$0.0000198 \pm 9.2\%$	735 (38)	$0.0000186 \pm 9.2\%$
Sample ^{71}Ga					
^{72}Ga	629.967 (19)	6940 (94)	$0.00115 \pm 5.0\%$	6895 (94)	$0.00115 \pm 5.0\%$
	834.13 (4)	17927 (177)	$0.00324 \pm 5.0\%$	17488 (138)	$0.00325 \pm 5.0\%$
	894.327 (18)	1877 (48)	$0.000314 \pm 5.0\%$	1724 (47)	$0.000300 \pm 5.0\%$
	1050.794 (17)	1110 (39)	$0.000202 \pm 5.0\%$	1087 (38)	$0.000193 \pm 5.0\%$

Table C.3.: Counts and simulation correction factor determined after the activation of gallium during activation I

C. Appendix - Neutron activation of Gallium

Decay of	γ -energy (keV)	Counts A	f_{sim} A	Counts B	f_{sim} B
Monitor Au 44					
^{198}Au	411.80205 (17)	6023 (79)	$0.00673 \pm 5.0\%$	5870 (78)	$0.00670 \pm 5.0\%$
Monitor Au IV					
^{198}Au	411.80205 (17)	24787 (160)	$0.00673 \pm 5.0\%$	23680 (157)	$0.00670 \pm 5.0\%$
Monitor Au 38					
^{198}Au	411.80205 (17)	7593 (88)	$0.00673 \pm 5.0\%$	7188 (36)	$0.00670 \pm 5.0\%$
Monitor Au 26					
^{198}Au	411.80205 (17)	27575 (168)	$0.00673 \pm 5.0\%$	27555 (168)	$0.00670 \pm 5.0\%$
Monitor Au 32					
^{198}Au	411.80205 (17)	5072 (72)	$0.00673 \pm 5.0\%$	4883 (71)	$0.00670 \pm 5.0\%$
Monitor Au 33					
^{198}Au	411.80205 (17)	5149 (72)	$0.00673 \pm 5.0\%$	5088 (72)	$0.00670 \pm 5.0\%$
Monitor Au 31					
^{198}Au	411.80205 (17)	7428 (87)	$0.00673 \pm 5.0\%$	7071 (86)	$0.00670 \pm 5.0\%$
Monitor Au 36					
^{198}Au	411.80205 (17)	19646 (143)	$0.00673 \pm 5.0\%$	19303 (144)	$0.00670 \pm 5.0\%$

Table C.4.: Counts and simulation correction factor determined after the activation of gallium during activation I

Sample	Weight (g)	$N_{\text{sample}}/10^{20}$	$t_{1/2}$ of the product
Au 44	0.14829(15)	$4.534 \pm 0.1\%$	2.6941(2) d [39]
Au IV	0.15148(15)	$4.631 \pm 0.1\%$	
Au 38	0.14699(15)	$4.494 \pm 0.1\%$	
Au 26	0.14489(15)	$4.430 \pm 0.1\%$	
Au 32	0.15662(15)	$4.789 \pm 0.1\%$	
Au 33	0.14062(15)	$4.300 \pm 0.1\%$	
Au 31	0.15611(15)	$4.773 \pm 0.1\%$	
Au 36	0.13401(15)	$4.097 \pm 0.1\%$	

Table C.5.: Specification of the used gold monitors during the first activation measurements, Activation I.

Proton energy (keV)	Number of Protons	Li target thickness (μm)
1912 (2)	10^9	22
Li target radius (mm)	Distance to target (mm)	Sample radius (mm)
1.5	4.3/5.3/6.3	10

Table C.6.: PINO simulation input parameters for activation measurement I. The outcome of the simulation was used to determine the spectrum averaged cross sections for the respective gallium isotopes.

Sample		f_b	f_{wm}	f_{dt}
natGa I	^{69}Ga	0.543	$0.673 \pm 0.13\%$	$0.997 \pm 0.01\%$
	^{71}Ga	0.983	$0.035 \pm 0.10\%$	$0.997 \pm 0.01\%$
^{69}Ga act. 1	^{69}Ga	0.564	$0.747 \pm 0.11\%$	$0.996 \pm 0.01\%$
^{69}Ga act. 2	^{69}Ga	0.554	$0.671 \pm 0.13\%$	$0.996 \pm 0.01\%$
^{71}Ga	^{71}Ga	0.955	$0.043 \pm 0.17\%$	$0.997 \pm 0.01\%$
Au 44		0.996	$0.026 \pm 0.11\%$	$0.998 \pm 0.01\%$
Au VI		0.996	$0.117 \pm 0.03\%$	$0.999 \pm 0.01\%$
Au 38		0.996	$0.034 \pm 0.02\%$	$0.999 \pm 0.01\%$
Au 26		0.996	$0.137 \pm 0.01\%$	$0.999 \pm 0.01\%$
Au 32		0.989	$0.011 \pm 0.07\%$	$0.999 \pm 0.01\%$
Au 33		0.989	$0.013 \pm 0.06\%$	$0.999 \pm 0.01\%$
Au 31		0.996	$0.044 \pm 0.06\%$	$0.999 \pm 0.01\%$
Au 36		0.996	$0.143 \pm 0.03\%$	$0.999 \pm 0.01\%$

Table C.7.: Correction factors for the decays during the activation f_b , the decays between the activation end and the start of and during the measurement f_{wm} and the dead time correction f_{dt} obtained during Activation I.

Sample	Isotope	$\langle N_{\text{prod}} \rangle / 10^7$	$u_{\text{stat}}(\%)$	$u_{\text{syst}}(\%)$
natGa I	^{70}Ga	9.348	1.5	5.6
	^{72}Ga	3.811	0.8	5.0
^{69}Ga act. I	^{70}Ga	14.906	1.1	5.4
^{69}Ga act. II		10.902	1.4	5.3
^{71}Ga	^{72}Ga	13.603	0.4	5.1
Au 44	^{198}Au	3.417	0.9	5.0
Au VI		3.100	0.5	5.0
Au 38		3.253	0.8	5.0
Au 26		3.009	0.4	5.0
Au 32		6.662	1.0	5.0
Au 33		5.813	1.0	5.0
Au 31		2.468	0.8	5.0
Au 36		2.043	0.5	5.0

Table C.8.: Shown is the weighted mean between the two detectors and all γ -lines of the produced nuclei during the Activation I. These values were used for further cross section calculation.

Activation II

Sample	Weight (g)	$N_{\text{sample}}/10^{20}$	$t_{1/2}$ of the product
Au 7	0.15581 (15)	$4.764 \pm 0.1\%$	2.6941(2) d [39]
Au 29	0.15105 (15)	$4.619 \pm 0.1\%$	
Au 3	0.16177 (15)	$4.946 \pm 0.1\%$	
Au 25	0.14749 (15)	$4.509 \pm 0.1\%$	

Table C.9.: Specification of the used gold monitors during Activation II.

Decay of	γ -energy (keV)	Counts A	f_{sim} A	Counts B	f_{sim} B
Sample natGa II					
^{72}Ga	629.967 (19)	5392 (91)	$0.000948 \pm 5.0\%$	5569 (91)	$0.000976 \pm 5.0\%$
	834.13 (4)	14638 (123)	$0.00270 \pm 5.0\%$	15441 (130)	$0.00280 \pm 5.0\%$
	894.327 (18)	1367 (46)	$0.000257 \pm 5.0\%$	1489 (49)	$0.000275 \pm 5.0\%$
	1050.794 (17)	833 (37)	$0.000202 \pm 5.0\%$	887 (40)	$0.000193 \pm 5.0\%$
Sample ^{71}Ga					
^{72}Ga	629.967 (19)	63094 (291)	$0.000948 \pm 5.0\%$	65883 (290)	$0.000976 \pm 5.0\%$
	834.13 (4)	173040 (424)	$0.00270 \pm 5.0\%$	178705 (431)	$0.00280 \pm 5.0\%$
	894.327 (18)	16817 (145)	$0.000257 \pm 5.0\%$	17271 (146)	$0.000275 \pm 5.0\%$
	1050.794 (17)	10077 (120)	$0.000202 \pm 5.0\%$	10309 (120)	$0.000193 \pm 5.0\%$

Table C.10.: Counts and simulation correction factor determined after the activation of gallium during activation II

Decay of	γ -energy (keV)	Counts A	f_{sim} A	Counts B	f_{sim} B
Monitor Au 7					
^{198}Au	411.80205 (17)	1813 (43)	$0.00546 \pm 5.0\%$	1743 (43)	$0.00571 \pm 5.0\%$
Monitor Au 29					
htb ^{198}Au	411.80205 (17)	1294 (37)	$0.00546 \pm 5.0\%$	1306 (37)	$0.00571 \pm 5.0\%$
Monitor Au 3					
^{198}Au	411.80205 (17)	3777 (63)	$0.00546 \pm 5.0\%$	3800 (63)	$0.00571 \pm 5.0\%$
Monitor Au 25					
^{198}Au	411.80205 (17)	3564 (62)	$0.00546 \pm 5.0\%$	3714 (63)	$0.00571 \pm 5.0\%$

Table C.11.: Counts and simulation correction factor determined after the activation of gallium during activation II

Sample		f_b	f_{wm}	f_{dt}
natGa II	^{71}Ga	0.953	$0.128 \pm 0.14\%$	$0.999 \pm 0.01\%$
^{71}Ga	^{71}Ga	0.904	$0.622 \pm 0.09\%$	$0.999 \pm 0.01\%$
Au 7		0.989	$0.009 \pm 0.09\%$	$0.999 \pm 0.01\%$
Au 29		0.989	$0.007 \pm 0.12\%$	$0.999 \pm 0.01\%$
Au 3		0.978	$0.012 \pm 0.36\%$	$0.999 \pm 0.01\%$
Au 25		0.978	$0.013 \pm 0.32\%$	$0.999 \pm 0.01\%$

Table C.12.: Correction factors for the decays during the activation f_b , the decays between the activation end and the start of and during the measurement f_{wm} and the dead time correction f_{dt} , obtained during Activation II.

Sample	Isotope	$\langle N_{\text{prod}} \rangle / 10^7$	$u_{\text{stat}}(\%)$	$u_{\text{syst}}(\%)$
natGa II	^{72}Ga	4.539	0.5	5.0
^{71}Ga	^{72}Ga	11.499	0.1	5.0
Au 7	^{198}Au	3.756	1.7	5.0
Au 29		3.453	2.0	5.0
Au 3		5.745	1.1	5.0
Au 25		4.949	1.2	5.0

Table C.13.: Produced nuclei during the Activation II of the natural Gallium sample (natGa II) and the isotopic enriched sample ^{71}Ga . Only the produced nuclei of ^{72}Ga were taken account during this activation due to the previous measurement discrepancies between natural and isopic enriched samples.

Activation III

Sample	Weight (g)	$N_{\text{sample}}/10^{20}$	$t_{1/2}$ of the product
Au 3	0.16177 (15)	$4.946 \pm 0.1\%$	2.6941(2) d [39]
Au 7	0.15581 (15)	$4.764 \pm 0.1\%$	
Au 29	0.15105 (15)	$4.619 \pm 0.1\%$	
Au 22	0.14655 (15)	$4.481 \pm 0.1\%$	
Au 37	0.15766 (15)	$4.820 \pm 0.1\%$	
Au 38	0.14717 (15)	$4.500 \pm 0.1\%$	

Table C.14.: Specification of the used gold monitors.

Sample		f_b	f_{wm}	f_{dt}
natGa II.I	^{71}Ga	0.953	$0.020 \pm 0.2\%$	$0.988 \pm 0.01\%$
^{71}Ga	^{71}Ga	0.953	$0.020 \pm 0.5\%$	$0.980 \pm 0.01\%$
natGa II	^{71}Ga	0.956	0.026 ± 0.5	$\pm 0.01\%$
^{71}Ga	^{71}Ga	0.956	$0.026 \pm 0.5\%$	$\pm 0.01\%$
Au 3		0.989	$0.003 \pm 0.2\%$	$\pm 0.01\%$
Au 7		0.989	$0.003 \pm 0.2\%$	$\pm 0.01\%$
Au 29		0.989	$0.006 \pm 0.1\%$	$\pm 0.01\%$
Au 22		0.990	$0.006 \pm 0.1\%$	$\pm 0.01\%$
Au 37		0.990	$0.005 \pm 0.1\%$	$\pm 0.01\%$
Au 38		0.990	$0.012 \pm 0.1\%$	$\pm 0.01\%$

Table C.15.: Correction factors for the decays during the activation f_b , the decays between the activation end and the start of and during the measurement f_{wm} and the deadtime correction f_{dt}

Decay of	γ -energy (keV)	Counts A	f_{sim} A	Counts B	f_{sim} B
Sample natGa II front					
^{72}Ga	629.967 (19)	3388 (86)	$0.00300 \pm 5.0\%$	3668 (86)	$0.00300 \pm 5.0\%$
	834.13 (4)	9780 (113)	$0.00877 \pm 5.0\%$	10149 (114)	$0.00872 \pm 5.0\%$
	894.327 (18)	961 (48)	$0.000842 \pm 5.0\%$	896 (49)	$0.000828 \pm 5.0\%$
Sample ^{71}Ga back					
^{72}Ga	629.967 (19)	4758 (79)	$0.00300 \pm 5.0\%$	4859 (79)	$0.00300 \pm 5.0\%$
	834.13 (4)	13197 (118)	$0.00877 \pm 5.0\%$	13658 (119)	$0.00872 \pm 5.0\%$
	894.327 (18)	1130 (39)	$0.000842 \pm 5.0\%$	1297 (42)	$0.000828 \pm 5.0\%$
Sample natGa II back					
^{72}Ga	629.967 (19)	11534 (173)	$0.00300 \pm 5.0\%$	12031 (169)	$0.00300 \pm 5.0\%$
	834.13 (4)	32696 (213)	$0.00877 \pm 5.0\%$	32900 (210)	$0.00872 \pm 5.0\%$
	894.327 (18)	2894 (100)	$0.000842 \pm 5.0\%$	2957 (95)	$0.000828 \pm 5.0\%$
Sample ^{71}Ga front					
^{72}Ga	629.967 (19)	30668 (201)	$0.00300 \pm 5.0\%$	32152 (209)	$0.00300 \pm 5.0\%$
	834.13 (4)	85448 (301)	$0.00877 \pm 5.0\%$	91271 (310)	$0.00872 \pm 5.0\%$
	894.327 (18)	8017 (105)	$0.000842 \pm 5.0\%$	8705 (107)	$0.000828 \pm 5.0\%$

Table C.16.: Counts and simulation correction factor determined after the activation of gallium during activation III

Decay of	γ -energy (keV)	Counts A	f_{sim} A	Counts B	f_{sim} B
Monitor Au 3					
^{198}Au	411.80205 (17)	10709 (104)	$0.0185 \pm 5.0\%$	11117 (107)	$0.0185 \pm 5.0\%$
Monitor Au 7					
^{198}Au	411.80205 (17)	11937 (110)	$0.0185 \pm 5.0\%$	12185 (111)	$0.0185 \pm 5.0\%$
Monitor Au 29					
^{198}Au	411.80205 (17)	16434 (129)	$0.0185 \pm 5.0\%$	116874 (131)	$0.0185 \pm 5.0\%$
Monitor Au 22					
^{198}Au	411.80205 (17)	3030 (556)	$0.0185 \pm 5.0\%$	3042 (56)	$0.0185 \pm 5.0\%$
Monitor Au 37					
^{198}Au	411.80205 (17)	2933 (55)	$0.0185 \pm 5.0\%$	2976 (55)	$0.0185 \pm 5.0\%$
Monitor Au 38					
^{198}Au	411.80205 (17)	5541 (76)	$0.0185 \pm 5.0\%$	5751 (77)	$0.0185 \pm 5.0\%$

Table C.17.: Counts and simulation correction factor determined after the activation of gallium during activation III.

Sample	Isotope	$\langle N_{\text{prod}} \rangle / 10^7$	$u_{\text{stat}}(\%)$	$u_{\text{syst}}(\%)$
natGa II.I	^{72}Ga	20.601	0.3	5.0
^{71}Ga I	^{72}Ga	53.085	0.3	5.0
natGa II.II	^{72}Ga	4.545	0.6	5.0
^{71}Ga II	^{72}Ga	6.117	0.5	5.0
Au 7	^{198}Au	19.022	0.6	5.0
Au 3		18.961	0.7	5.0
Au 29		15.784	0.5	5.0
Au 22		2.879	1.3	5.0
Au 37		3.002	1.3	5.0
Au 38		2.640	0.9	5.0

Table C.18.: Produced nuclei during the activation of the natural Gallium sample (natGa II) and the isotopic enriched sample ^{71}Ga . Only the produced nuclei of ^{72}Ga were taken account during this activation due to the previous measurement discrepancies between natural and isopic enriched samples.

Activation IV

Sample	Activation	$\langle N_{\text{prod}} \rangle / 10^7$	$u_{\text{stat}}(\%)$	$u_{\text{syst}}(\%)$
natGa 0.2 mm II 1cm	I	1.794	0.3	5.0
natGa 0.2 mm I 1cm	I	6.622	0.7	5.0
natGa 0.2 mm I 5cm	I	6.125	0.1	5.0
natGa 0.1 mm I 5cm	I	1.390	0.7	5.0
natGa 0.1 mm I 5cm on	I	1.370	0.3	5.0
natGa 0.3 mm I 5cm	I	2.793	0.2	5.0
natGa 0.5 mm I 5cm	I	5.885	0.3	5.0
natGa 0.2 mm II	II	3.821	0.3	5.0
natGa 0.1 mm I	II	2.108	0.3	5.0
natGa 1.0 mm I	I	12.897	0.2	5.0
natGa 1.25 mm I	I	14.763	0.3	5.0
natGa 1.5 mm I	I	23.226	0.2	5.0

Table C.19.: Produced nuclei during the activation of the natural Gallium sample (natGa II) and the isotopic enriched sample ^{71}Ga . Only the produced nuclei of ^{72}Ga were taken account during this activation due to the previous measurement discrepancies between natural and isopic enriched samples.

Sample	Weight (g)	Thickness (mm)	$N_{\text{sample}}/10^{20}$
natGa 0.1 (1)	233.6 (2)	$0.12 \pm 1\%$	8.049 (7)
natGa 0.1 (2)	233.0 (2)	$0.12 \pm 1\%$	8.028 (7)
natGa 0.2 (1)	424.1 (2)	$0.23 \pm 1\%$	14.613 (8)
natGa 0.2 (2)	424.5 (2)	$0.23 \pm 1\%$	14.626 (8)
natGa 0.5 (1)	897.5 (2)	$0.49 \pm 1\%$	30.924 (11)
natGa 1.0 (1)	1932.5 (2)	$1.04 \pm 1\%$	66.585 (19)
natGa 1.25 (1)	2208.3 (2)	$1.19 \pm 1\%$	76.088 (21)
natGa 1.5 (1)	2755.0 (2)	$1.45 \pm 1\%$	94.925 (26)

Table C.20.: Specification of the used gold monitors.

Sample	Weight (g)	$N_{\text{sample}}/10^{20}$	$t_{1/2}$ of the product
Au 3	0.16198 (15)	$4.952 \pm 0.1\%$	2.6941(2) d [39]
Au 7	0.15581 (15)	$4.764 \pm 0.1\%$	
Au V	0.16373 (15)	$5.006 \pm 0.1\%$	
Au VI	0.15148 (15)	$4.631 \pm 0.1\%$	
Au 2	0.15250 (15)	$4.663 \pm 0.1\%$	
Au 25	0.14734 (15)	$4.505 \pm 0.1\%$	
Au 37	0.15761 (15)	$4.819 \pm 0.1\%$	
Au 10	0.15448 (15)	$4.723 \pm 0.1\%$	
Au 24	0.15806 (15)	$4.833 \pm 0.1\%$	
Au 22	0.14650 (15)	$4.479 \pm 0.1\%$	
Au 29	0.15091 (15)	$4.613 \pm 0.1\%$	
Au 38	0.14698 (15)	$4.494 \pm 0.1\%$	
Au 12	0.14914 (15)	$4.560 \pm 0.1\%$	
Au VII	0.16170 (15)	$4.944 \pm 0.1\%$	
Au 33	0.14062 (15)	$4.299 \pm 0.1\%$	
Au 45	0.15798 (15)	$4.830 \pm 0.1\%$	
Au 6	0.15463 (15)	$4.728 \pm 0.1\%$	
Au 39	0.13017 (15)	$3.980 \pm 0.1\%$	
Au IX	0.16275 (15)	$4.976 \pm 0.1\%$	
Au Z	0.14723 (15)	$4.501 \pm 0.1\%$	

Table C.21.: Specification of the used gold monitors.

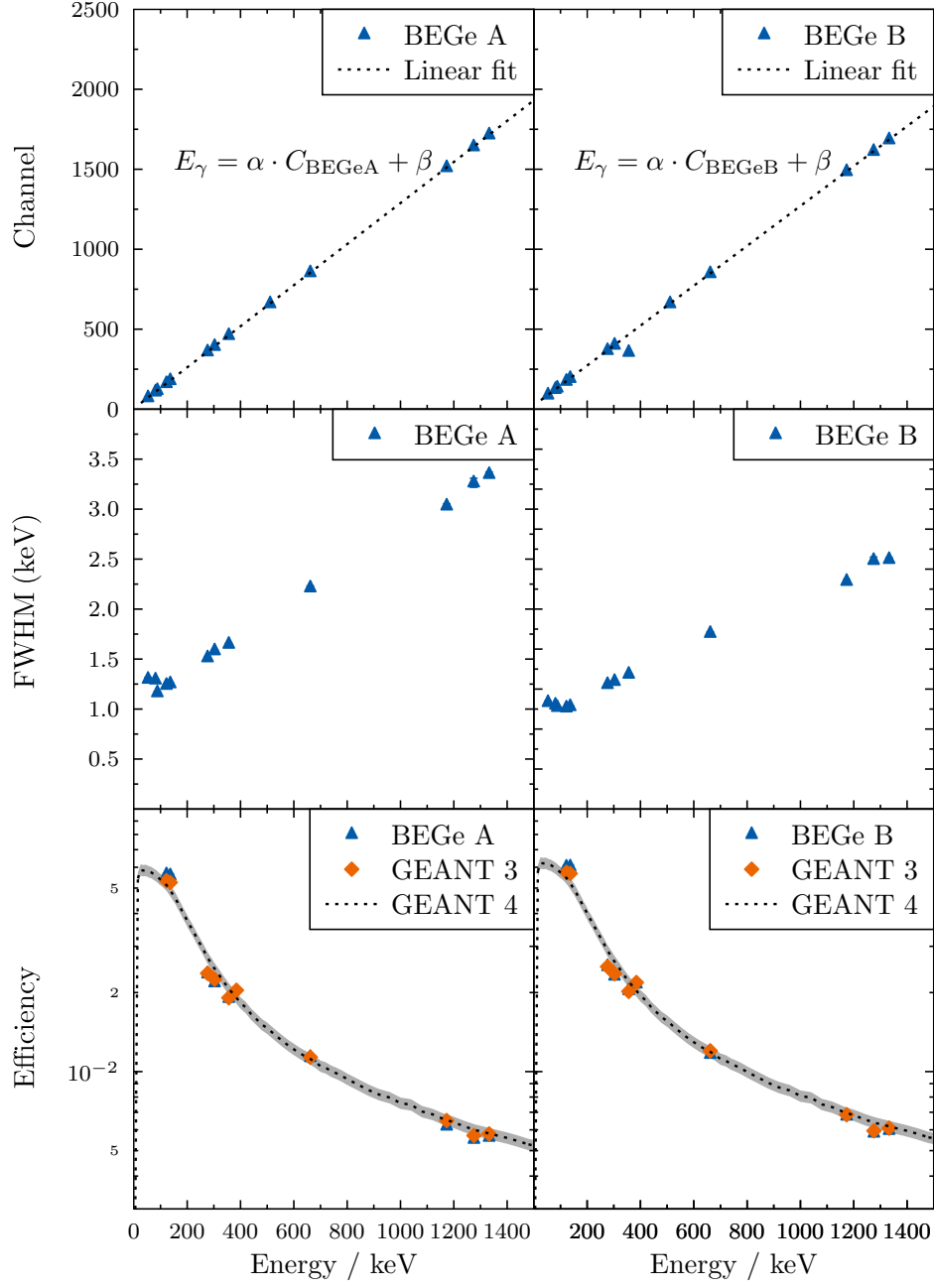


Figure C.1.: Results of the detector calibration for activation IV. From top to bottom: Energy calibration, energy resolution calibration and efficiency measurements.

Decay of	γ -energy (keV)	Counts A	f_{sim} A	Counts B	f_{sim} B
Sample natGa 0.2 mm II					
^{72}Ga	629.967 (19)	19377 (175)	$0.00971 \pm 5.0\%$	23150 (221)	$0.00945 \pm 5.0\%$
	834.13 (4)	66689 (291)	$0.0310 \pm 5.0\%$	73827 (310)	$0.0311 \pm 5.0\%$
	894.327 (18)	5720 (130)	$0.00268 \pm 5.0\%$	6172 (129)	$0.00271 \pm 5.0\%$
Sample natGa 0.2 mm I					
^{72}Ga	629.967 (19)	2288 (76)	$0.00971 \pm 5.0\%$	2393 (76)	$0.00945 \pm 5.0\%$
	834.13 (4)	7148 (98)	$0.0310 \pm 5.0\%$	7645 (100)	$0.0311 \pm 5.0\%$
	894.327 (18)	555 (39)	$0.00268 \pm 5.0\%$	651 (40)	$0.00271 \pm 5.0\%$
Sample natGa 0.2 mm I					
^{72}Ga	629.967 (19)	105631 (357)	$0.00314 \pm 5.0\%$	116031 (408)	$0.00310 \pm 5.0\%$
	834.13 (4)	284681 (635)	$0.00923 \pm 5.0\%$	299977 (785)	$0.00915 \pm 5.0\%$
	894.327 (18)	27998 (188)	$0.000886 \pm 5.0\%$	31488 (215)	$0.000878 \pm 5.0\%$
Sample natGa 0.1 mm I					
^{72}Ga	629.967 (19)	2500 (79)	$0.00314 \pm 5.0\%$	2645 (86)	$0.00310 \pm 5.0\%$
	834.13 (4)	7263 (105)	$0.00923 \pm 5.0\%$	7311 (106)	$0.00915 \pm 5.0\%$
	894.327 (18)	684 (56)	$0.000886 \pm 5.0\%$	802 (59)	$0.000878 \pm 5.0\%$
Sample natGa 0.1 mm I on					
^{72}Ga	629.967 (19)	12177 (129)	$0.00314 \pm 5.0\%$	12472 (132)	$0.00310 \pm 5.0\%$
	834.13 (4)	34935 (192)	$0.00923 \pm 5.0\%$	34533 (190)	$0.00915 \pm 5.0\%$
	894.327 (18)	3217 (65)	$0.000886 \pm 5.0\%$	3323 (67)	$0.000878 \pm 5.0\%$
Sample natGa 0.3 mm I					
^{72}Ga	629.967 (19)	26972 (218)	$0.00314 \pm 5.0\%$	26980 (216)	$0.00310 \pm 5.0\%$
	834.13 (4)	75732 (301)	$0.00923 \pm 5.0\%$	76354 (296)	$0.00915 \pm 5.0\%$
	894.327 (18)	7037 (111)	$0.000886 \pm 5.0\%$	7166 (119)	$0.000878 \pm 5.0\%$
Sample natGa 0.5 mm I					
^{72}Ga	629.967 (19)	18477 (193)	$0.00314 \pm 5.0\%$	19407 (300)	$0.00310 \pm 5.0\%$
	834.13 (4)	50850 (251)	$0.00923 \pm 5.0\%$	52822 (256)	$0.00915 \pm 5.0\%$
	894.327 (18)	4596 (101)	$0.000886 \pm 5.0\%$	4821 (109)	$0.000878 \pm 5.0\%$
Sample natGa 0.2 mm II					
^{72}Ga	629.967 (19)	21732 (206)	$0.00314 \pm 5.0\%$	21726 (194)	$0.00310 \pm 5.0\%$
	834.13 (4)	57800 (264)	$0.00923 \pm 5.0\%$	59608 (267)	$0.00915 \pm 5.0\%$
	894.327 (18)	5990 (122)	$0.000886 \pm 5.0\%$	5665 (107)	$0.000878 \pm 5.0\%$
Sample natGa 0.1 mm I					
^{72}Ga	629.967 (19)	12729 (136)	$0.00314 \pm 5.0\%$	12879 (136)	$0.00310 \pm 5.0\%$
	834.13 (4)	35145 (195)	$0.00923 \pm 5.0\%$	34818 (193)	$0.00915 \pm 5.0\%$
	894.327 (18)	3214 (67)	$0.000886 \pm 5.0\%$	3339 (68)	$0.000878 \pm 5.0\%$
Sample natGa 1.0 mm I					
^{72}Ga	629.967 (19)	87970 (353)	$0.00314 \pm 5.0\%$	81138 (359)	$0.00310 \pm 5.0\%$
	834.13 (4)	238397 (510)	$0.00923 \pm 5.0\%$	242216 (514)	$0.00915 \pm 5.0\%$
	894.327 (18)	22767 (190)	$0.000886 \pm 5.0\%$	23050 (188)	$0.000878 \pm 5.0\%$
Sample natGa 1.25 mm I					
^{72}Ga	629.967 (19)	35386 (242)	$0.00314 \pm 5.0\%$	37942 (249)	$0.00310 \pm 5.0\%$
	834.13 (4)	98318 (337)	$0.00923 \pm 5.0\%$	102509 (345)	$0.00915 \pm 5.0\%$
	894.327 (18)	9377 (131)	$0.000886 \pm 5.0\%$	9876 (135)	$0.000878 \pm 5.0\%$
Sample natGa 1.5 mm I					
^{72}Ga	629.967 (19)	107495 (392)	$0.00314 \pm 5.0\%$	115707 (409)	$0.00310 \pm 5.0\%$
	834.13 (4)	291711 (566)	$0.00923 \pm 5.0\%$	310730 (583)	$0.00915 \pm 5.0\%$
	894.327 (18)	27673 (204)	$0.000886 \pm 5.0\%$	29086 (212)	$0.000878 \pm 5.0\%$

Table C.22.: Counts and simulation correction factor determined after the activation of gallium during activation IV

Decay of	γ -energy (keV)	Counts A	f_{sim} A	Counts B	f_{sim} B
Monitor Au 3 and Au 7					
^{198}Au	411.80205 (17)	18669 (138)	$0.0763 \pm 5.0\%$	20577 (144)	$0.0770 \pm 5.0\%$
		13693 (117)		14956 (123)	
Monitor Au V and Au VI					
^{198}Au	411.80205 (17)	20211 (144)	$0.0195 \pm 5.0\%$	20946 (146)	$0.195 \pm 5.0\%$
		18971 (139)		20290 (144)	
Monitor Au 2 and Au 25					
^{198}Au	411.80205 (17)	52625 (233)	$0.0195 \pm 5.0\%$	55089 (237)	$0.0195 \pm 5.0\%$
		14561 (122)		15207 (125)	
Monitor Au 37 and Au 10					
^{198}Au	411.80205 (17)	17831 (135)	$0.0195 \pm 5.0\%$	19176 (140)	$0.0195 \pm 5.0\%$
		48966 (225)		52110 (231)	
Monitor Au 24 and Au 22					
^{198}Au	411.80205 (17)	14088 (120)	$0.0195 \pm 5.0\%$	14609 (123)	$0.0195 \pm 5.0\%$
		11199 (107)		11861 (111)	
Monitor Au 29 and Au 38					
^{198}Au	411.80205 (17)	19630 (141)	$0.0195 \pm 5.0\%$	20467 (145)	$0.0195 \pm 5.0\%$
		19384 (147)		18670 (139)	
Monitor Au 12 and Au VII					
^{198}Au	411.80205 (17)	18316 (137)	$0.0195 \pm 5.0\%$	18848 (139)	$0.0195 \pm 5.0\%$
		102121 (323)		110815 (338)	
Monitor Au 40 and Au 29.2					
^{198}Au	411.80205 (17)	9837 (100)	$0.0195 \pm 5.0\%$	10225 (102)	$0.0195 \pm 5.0\%$
		86093 (297)		92536 (308)	
Monitor Au 33 and Au 45					
^{198}Au	411.80205 (17)	16422 (130)	$0.0195 \pm 5.0\%$	17636 (134)	$0.0195 \pm 5.0\%$
		55686 (240)		62464 (253)	
Monitor Au 6 and Au 39					
^{198}Au	411.80205 (17)	2879 (54)	$0.0195 \pm 5.0\%$	3166 (56)	$0.0195 \pm 5.0\%$
		18298 (138)		19085 (140)	
Monitor Au IX and Au Z					
^{198}Au	411.80205 (17)	37710 (197)	$0.0195 \pm 5.0\%$	40510 (204)	$0.0195 \pm 5.0\%$
		82613 (292)		86693 (298)	

Table C.23.: Counts and simulation correction factor determined after the activation of gallium during activation IV.

Sample		f_b	f_{wm}	f_{dt}
natGa 0.2 mm II 1cm	^{71}Ga	0.973	$0.129 \pm 0.01\%$	$0.996 \pm 0.01\%$
natGa 0.2 mm I 1cm	^{71}Ga	0.902	$0.004 \pm 0.03\%$	$0.977 \pm 0.01\%$
natGa 0.2 mm I 5cm	^{71}Ga	0.902	$0.593 \pm 0.05\%$	$0.998 \pm 0.01\%$
natGa 0.1 mm I 5cm	^{71}Ga	0.971	$0.060 \pm 0.01\%$	$0.998 \pm 0.01\%$
natGa 0.1 mm I 5cm on	^{71}Ga	0.971	$0.287 \pm 0.01\%$	$0.999 \pm 0.01\%$
natGa 0.3 mm I 5cm	^{71}Ga	0.977	$0.306 \pm 0.03\%$	$0.998 \pm 0.01\%$
natGa 0.5 mm I 5cm	^{71}Ga	0.970	$0.101 \pm 0.01\%$	$0.996 \pm 0.01\%$
natGa 0.2 mm II act 2	^{71}Ga	0.949	$0.180 \pm 0.02\%$	$0.998 \pm 0.01\%$
natGa 0.1 mm I act 2	^{71}Ga	0.978	$0.628 \pm 0.05\%$	$0.999 \pm 0.01\%$
natGa 1.0 mm I	^{71}Ga	0.953	$0.217 \pm 0.02\%$	$0.997 \pm 0.01\%$
natGa 1.25 mm I	^{71}Ga	0.966	$0.078 \pm 0.01\%$	$0.993 \pm 0.01\%$
natGa 1.5 mm I	^{71}Ga	0.970	$0.149 \pm 0.02\%$	$0.993 \pm 0.01\%$

Table C.24.: Correction factors for the decays during the activation f_b , the decays between the activation end and the start of and during the measurement f_{wm} and the deadtime correction f_{dt}

List of Figures

1.1.	Solar abundance distribution taken from Lodders <i>et al.</i> [48]. The given values are normalized to the silicon abundance. Most prominent are the peaks of H and He from the Big Bang nucleosynthesis, C and O from stellar nucleosynthesis, the iron peak and the r- and s-process peaks.	2
1.2.	Schematic of an AGB-star (left) and its different burning phases (right). Based on [58].	5
1.3.	Impact of the cross section uncertainties of the $^{69,71}\text{Ga}(n, \gamma)$ reactions on the abundances of the weak s-process. The simulations were conducted using the online tool NETZ.	7
2.1.	Energy and atomic number dependence of the different interactions of photons with matter. At the continuous lines the cross sections of the two interaction mechanisms next to each other are equal. Data taken from XCOM [8].	12
2.2.	Simplified illustration of a possible γ -ray spectrum in a detector. The Compton continuum and edge, the single- and double-escape (SEP and DEP) lines as well as the full energy peak (FEP) are marked. . .	14
2.3.	Schematic of a scintillation detector for γ -detection.	18
2.4.	Visualization of analog signal processing using a $\text{LaBr}_3\text{:Ce}$ scintillation detector. The output signals, from left to right, show the basic stages of an analog signal processing chain.	19
2.5.	Schematic of a typical activation setup at a low-energy accelerator featuring the $^7\text{Li}(p,n)^7\text{Be}$ reaction as a neutron source at a proton energy of $E_p = 1912 \text{ keV}$. The sample is placed in between gold neutron monitors which will be analyzed by γ -spectroscopy to determine the produced nuclei during the activation.	23
2.6.	Simulated neutron energy spectrum using the PINO tool [57]. The simulated neutron spectrum produced by the $^7\text{Li}(p,n)^7\text{Be}$ reaction, at a proton energy of $E_p = 1912 \pm 2 \text{ keV}$	23

3.1.	Simulation results from PINO for the recreation of a $k_B T = 90$ keV quasi-stellar neutron spectrum using the ${}^7\text{Li}(p,n){}^7\text{Be}$ neutron source.	26
3.2.	Full schatic layout of the PTB Ion Accelerator Facility PIAF. Various different experimental sites are shown. Beamline used for the experimental campaign presented in this thesis is marked in blue. The beam was delivered by the 2 MV tandem accelerator. The proton beam energy was determined using the analyzing magnet. Following, the beam was lead to the neutron production target at the neutron reference field experimental area.	27
3.3.	Schematic of the experimental area for the measurement of the neutron fields. Three detectors are used, which were positioned around the neutron production target at different angles between 0° and 95° . . .	28
3.4.	Part of the scintillation detector assembly: On the left side in figure (a) the Philips XP 2020 PMT ist shown without further wrapping. On the right side in figure (b) the ${}^6\text{Li}$ -glass disk is positioned in the middle of the PTM window. The coupling was ensured by silicon oil.	29
3.5.	Pulse height spectra of the assembled detectors I and II. The spectra show the response for neutrons created by the ${}^7\text{Li}(p,n){}^7\text{Be}$ reaction at a proton energy of $E_p = 1912$ keV.	30
3.6.	Rendered CAD design of the neutron detector holder. The structure was optimized for minimal material to ensure a minimum neutron background.	31
3.7.	${}^6\text{Li}$ -glass detector mounted on the CFRP detector holder an the spectrometer arm at the PIAF facility. A shadow cone was placed in front of the detector for the measurement of scattered neutrons. . . .	32
3.8.	Simplified schematic of the signal processing using a CAEN v1751 digitizer and the DPP-PSD firmware. Based on [66].	33
3.9.	Simplified schematic of the used coincidence logic during the measurement of the neutron fields using the pick up signal as main signal and the signals of the three ${}^6\text{Li}$ -glass detectors. Signals are only recorded if in the set coincidence window.	33
3.10.	Experimental setup: In the center the lithium target cooled by an air jet is visible. On the left edge of the picture two ${}^6\text{Li}$ -glass detectors mounted onto the carbon fiber detector holders can be seen.	36

3.11. Experimental area: Marked in the center is the proton beam line with the lithium target mounted. Surrounding the open pitch to minimize the effects of scattered neutrons. Three static neutron monitors are marked, which are responsible for monitoring the neutron yield during the irradiations.	36
3.12. Time-of-flight spectrum recorded using a BaF ₂ detector at a proton energy of $E_p = 1912(1)$ keV. Only a single peak is visible in the spectrum, the γ -flash.	38
3.13. Measurements for the accelerator time resolution. The blue line denotes the spectra measured using a BaF ₂ detector, while the orange line is the Gaussian fit of the γ -flash. The FWHM denotes the time resolution of the accelerator.	39
3.14. Total time resolution for each ⁶ Li-glass detector during the measurement of the neutron fields at a proton energy of $E_p = 1912$ keV. The blue lines denotes the measurement, the orange line the Gaussian fit of the γ -flash.	40
3.15. Stopping power of protons in lithium. The data presented are taken from the SRIM simulation tool [79].	41
3.16. Long counter readings per charge vs. the total accumulated beam charge on target during the measurements at different proton energies. No significant target degradation during the runs could be observed.	42
3.17. Pulse height spectra for detectors I - III at a selected proton energy of $E_p = 1907$ keV at different angles.	44
3.18. Pulse height spectra for detector I at $E_p = 2100$ keV (left) and $E_p = 2500$ keV (right) at different angles.	45
3.19. ToF spectra measured by detector I at set proton energies of (a) 1907 keV, (b) 2100 keV and (c) 2500 keV.	46
3.20. ToF spectra, corrected for the cable lengths, measured by detector I at set proton energies of (a) 1907 keV, (b) 2100 keV and (c) 2500 keV.	47
3.21. Background corrected ToF spectra measured using detector I at set proton energies of (a) 1907 keV, (b) 2100 keV and (c) 2500 keV.	49
3.22. Energy spectra obtained using detector I at set proton energies of (a) 1907 keV, (b) 2100 keV and (c) 2500 keV.	51
3.23. Rebinned energy spectra using detector I at set proton energies of (a) 1907 keV, (b) 2100 keV and (c) 2500 keV.	52

3.24. Comparison of ToF spectra obtained using detector I and II, measured under the same angle $\varphi = 27^\circ$ at $E_p = 1907$ keV. A slight difference is noticeable due to a different flight path and detector specification. . .	54
3.25. Comparison of ToF spectra obtained using detector II and III, measured under the same angle $\varphi = 15^\circ$ at $E_p = 1907$ keV. The difference a result of the different flight path and detector specification.	54
3.26. Comparison of ToF spectra obtained using detector I and II, measured under the same angle $\varphi = 27^\circ$ at $E_p = 2100$ keV. A slight difference is noticeable due to a different flight path and detector specification. . .	55
3.27. Comparison of ToF spectra obtained using detector II and III, measured under the same angle $\varphi = 15^\circ$ at $E_p = 2100$ keV. A difference is noticeable due to a different flight path and detector specification. . .	55
3.28. Comparison of ToF spectra obtained using detector I and II, measured under the same angle $\varphi = 27^\circ$ at $E_p = 2500$ keV. A slight difference is noticeable due to a different flight path and detector specification. . .	57
3.29. Comparison of ToF spectra obtained using detector II and III, measured under the same angle $\varphi = 15^\circ$ at $E_p = 2500$ keV. A difference is noticeable due to a different flight path and detector specification. . .	57
3.30. Time-of-flight spectra simulated using the PINO tool at proton energies of (a) $E_p = 1907$, (b) $E_p = 2100$ and (c) $E_p = 2500$ keV.	59
3.31. Simulated vs. measured γ -flash for time resolution comparison. From left to right: $E_p = 1907$, 2100 and 2500 keV. Measurements are scaled to fit the simulation.	60
3.32. Simulated detector efficiencies for the used detectors during the experiment. The specifications for the simulation inputs are shown in Table 3.5 and Table 3.6.	62
3.33. Simulated ToF spectra to demonstrate a variation of the proton energy around a set value of (a) $E_p = 1907$, (b) $E_p = 2100$ and (c) $E_p = 2500$ keV. 65	
3.34. Excerpt from the proton energy determination. Spectra obtained by simulation and measurement are compared. For better comparison the measured and simulated spectra were normalized to 1.	66
3.35. Results of the neutron production threshold scan. A proton energy deviation of approximately 2-3 keV is visible. The values for the ${}^7\text{Li}(p,n){}^7\text{Be}$ cross section were taken from [13].	67
3.36. Measured and simulated neutron energy spectra determined using detectors II and III at a proton energy of $E_p = 1884$ keV. Detector I was positioned outside the neutron cone.	70

3.37. Heat maps for comparison between simulation and measurements. Proton energy $E_p = 1884$ keV.	71
3.38. Measured and simulated neutron energy distribution at a proton energy of $E_p = 1894$ keV. A shift of the maximum between simulated and measured spectra of 5 keV towards lower energies is clearly visible.	72
3.39. Heats maps for better comparison between simulation and measure- ments. Proton energy $E_p = 1894$ keV.	73
3.40. Measured and simulated neutron energy distribution for a determined proton energy of $E_p = 1904$ keV. The detector angles are given in Table 3.1. A direct comparison is difficult because of the noise cut off in the measured spectrum at 8 keV.	74
3.41. Heat maps for better comparison between simulation and measure- ments. Proton energy $E_p = 1904$ keV.	75
3.42. Measured vs simulated energy spectra at a measured proton energy of $E_p = 1909$ keV.	76
3.43. Heat maps for better comparison between simulation and measure- ments. Proton energy $E_p = 1909$ keV.	77
3.44. Comparison of the angle-integrated neutron spectra at a selected proton energy of $E_p = 1998$ keV. A clear difference between simulation and measurement is visible in the intermediate energy range and the low energy range of the spectrum.	78
3.45. Heat maps for better comparison between simulation and measure- ments. Proton energy $E_p = 1998$ keV.	79
3.46. Comparison of the angle integrated neutron spectra. As can be seen in the heat maps for this proton energy the match between simulation and measurement is very good except for the high energy flank.	80
3.47. Heat maps for better comparison between simulation and measure- ments. Proton energy $E_p = 2100$ keV.	81
3.48. Comparison of the angle integrated neutron spectra at a selected proton energy of $E_p = 2202$ keV. Despite the problems during the measurement an agreement is visible.	82
3.49. Heat maps for better comparison between simulation and measure- ments. Proton energy $E_p = 2202$ keV.	83
3.50. Angle-integrated neutron spectra for $E_p = 2305$ keV.	84
3.51. Heat maps for better comparison between simulation and measure- ments. Proton energy $E_p = 2305$ keV.	85
3.52. Angle-integrated neutron spectra for $E_p = 2490$ keV.	86

3.53. Heat maps for better comparison between simulation and measurements. Proton energy $E_p = 2490$ keV.	87
3.54. Angle-integrated neutron spectra for $E_p = 2791$ keV.	88
3.55. Heat maps for better comparison between simulation and measurements. Proton energy $E_p = 2791$ keV.	89
4.1. Excerpt from the chart of nuclides in the region of the reactions of interest. The neutron capture reactions are marked with a blue arrow. The subsequent β^- -decay is depicted with a red arrow.	94
4.2. Natural gallium sample glued onto Kapton foil and fenced in by a stainless steel sample ring.	95
4.3. Enriched ^{71}Ga sample glued onto Kapton foil and fenced in by a sample ring.	95
4.4. Schematic of the BEGe detector setup used for γ -spectrometry. The detectors are placed inside copper and lead shielding to lower the ambient background.	97
4.5. Results of the detector calibration for both BEGe detectors. From top to bottom: Energy calibration, resolution calibration and the efficiency measurements.	99
4.6. Neutron flux recorded during the irradiation of the enriched ^{71}Ga sample.	101
4.7. Decay spectrum of the activated natural gallium sample.	102
4.8. Decay spectrum of the activated enriched ^{69}Ga sample.	102
4.9. Decay spectrum of the activated enriched ^{71}Ga sample.	102
4.10. Decay spectrum of one of the activated gold monitors used for neutron flux analysis.	102
4.11. Results of the detector calibration for both BEGe detectors. From top to bottom: Energy calibration, resolution calibration and the efficiency measurements.	106
4.12. Decay spectrum of the activated natural gallium sample.	109
4.13. Decay spectrum of the activated ^{71}Ga enriched sample.	109
4.14. Basic principle of XRF analysis. Based on [69].	110
4.15. Results obtained by μXRF on two gallium samples. Clearly visible are the characteristic X-rays (K_α and K_β) from Gallium. No other significant X-rays are visible ensuring the purity of the samples.	111
4.16. Schematic of the used activation setup for the sample stack activation. No changes at the setup were made. The samples are stacked between gold monitors and placed inside the neutron cone.	113

4.17. Ratio between produced ^{198}Au nuclei and ^{197}Au sample nuclei. The values behave just as expected with a slight decline in ratio.	114
4.18. Cross section ratios for the $^{71}\text{Ga}(n, \gamma)$ reaction. The simulation predicted larger cross section ratios than measured. However, no relation between the measured or simulated cross sections ratios and sample thickness could be observed. The dashed line denotes the weighted mean of the measurement values and the light blue area the uncertainty of the weighted mean.	117
4.19. Cross section ratios determined by neutron capture simulations of ^{69}Ga and ^{71}Ga . No significant dependence of the cross section ratio of either gallium isotope with the sample thickness can be determined up to 1.5 mm. At 2 mm sample thickness the simulated cross section ratios show a sudden increase.	117
6.1. Energiespektren erzeugt aus Flugzeitspektren unter verschiedenen Detektorwinkeln bei $E_p = 2500\text{ keV}$. Aufgrund der problematischen Energieauflösung bei hochenergetischen Neutronen, zeigen sich im rechten Teil der Grafik stufenartige Peaks.	124
6.2. Gezeigt sind die Flugzeitspektren für die verschiedenen Analyse-schritte. Von oben nach unten: Die unkorrigierten, die γ -flash korrigierten und die untergrundbereinigten Flugzeitspektren bei einer eingestellten Protonenergie von $E_p = 2500\text{ keV}$	125
6.3. Vergleich der winkelintegrierten Neutronenspektren bei $E_p = 1897\text{ keV}$.	126
6.4. Vergleich der winkelintegrierten Neutronenspektren bei $E_p = 2800\text{ keV}$.	126
B.1. Measured neutron spectra for a set proton energy of $E_p = 1887\text{ keV}$.	136
B.2. Measured neutron spectra for a set proton energy of $E_p = 1897\text{ keV}$.	137
B.3. Measured neutron spectra for a set proton energy of $E_p = 1907\text{ keV}$.	138
B.4. Measured neutron spectra for a set proton energy of $E_p = 1912\text{ keV}$.	139
B.5. Measured neutron spectra for a set proton energy of $E_p = 2000\text{ keV}$.	140
B.6. Measured neutron spectra for a set proton energy of $E_p = 2100\text{ keV}$.	141
B.7. Measured neutron spectra for a set proton energy of $E_p = 2200\text{ keV}$.	142
B.8. Measured neutron spectra for a set proton energy of $E_p = 2300\text{ keV}$.	143
B.9. Measured neutron spectra for a set proton energy of $E_p = 2500\text{ keV}$.	144
B.10. Measured neutron spectra for a set proton energy of $E_p = 2800\text{ keV}$.	145

C.1. Results of the detector calibration for activation IV. From top to bottom: Energy calibration, energy resolution calibration and efficiency measurements.	157
--	-----

List of Tables

3.1.	Proton energy settings, targets, accelerator frequencies and angle settings for the detectors used during the experimental campaign. . .	37
3.2.	Accelerator time resolutions measured using the BaF ₂ detector. . . .	40
3.3.	Total time resolution of the system determined using ⁶ Li-glass detectors positioned at $\varphi = 0^\circ$	41
3.4.	Used flight path values for the time to energy conversion. The values of the flight path include the target backing thickness, the measured distance between target and detector, and half of the scintillator thickness.	50
3.5.	Specification of the used scintillation glasses. The values are taken from [62].	61
3.6.	Lithium glass specification as input for the GEANT-4 simulations. The presented values are taken from [68].	61
3.7.	Presented are the systematic uncertainties for the detector efficiency. Values taken from [13].	62
3.8.	Determined proton beam energies using PINO. Except for energies higher than 2200 keV, the proton energies deviate between 2 and 3 keV. 64	
4.1.	γ -emission lines of interest during the analysis of the following activation measurements.	94
4.2.	Activated samples and the irradiation times during the activation experiment. The durations for the activations were chosen in reference to the half life of the produced isotopes.	98
4.3.	Final values for the cross section ratios determined for the activation of each gallium sample. For ⁶⁹ Ga the values are in good agreement within the margins of uncertainties. For ⁷¹ Ga there is a large discrepancy. 103	
4.4.	Spectrum averaged gold cross sections for both neutron flux monitors. Values taken from a simulation using the PINO tool using the sample positions during the measurement.	103
4.5.	Determined neutron flux using the gold monitors during the activation. 104	

4.6.	Final results for the spectrum averaged cross sections for each activation and reaction. The values for the reaction $^{69}\text{Ga}(n, \gamma)$ are in good agreement. The values for $^{71}\text{Ga}(n, \gamma)$ show a difference of 32%.	104
4.7.	Activated samples and the activation times for the activation experiment.	105
4.8.	Activated samples and the activation times for the activation experiment.	112
4.9.	Final results of the sample stack activations.	113
4.10.	Ratio of produced ^{198}Au nuclei during the activations as a check of neutron scattering by the gallium samples.	114
4.11.	Results of neutron capture simulations using the sample stack specifications as input. No difference in cross section ratio depending on the sample position in the stack can be seen.	115
4.12.	Samples and the irradiation times.	116
4.13.	Final results for the cross section ratios between ^{71}Ga and ^{197}Au	118
B.1.	Accumulated beam charge on the target during the measurements of the neutron fields at a proton energy of $E_p = 1887 \text{ keV}$	131
B.2.	Accumulated beam charge on the target during the measurements of the neutron fields at a proton energy of $E_p = 1897 \text{ keV}$	131
B.3.	Accumulated beam charge on the target during the measurements of the neutron fields at a proton energy of $E_p = 1907 \text{ keV}$	132
B.4.	Accumulated beam charge on the target during the measurements of the neutron fields at a proton energy of $E_p = 1912 \text{ keV}$	132
B.5.	Accumulated beam charge on the target during the measurements of the neutron fields at a proton energy of $E_p = 2000 \text{ keV}$	133
B.6.	Accumulated beam charge on the target during the measurements of the neutron fields at a proton energy of $E_p = 2100 \text{ keV}$	133
B.7.	$E_p = 2200 \text{ keV}$	133
B.8.	Accumulated beam charge on the target during the measurements of the neutron fields at a proton energy of $E_p = 2300 \text{ keV}$	134
B.9.	Accumulated beam charge on the target during the measurements of the neutron fields at a proton energy of $E_p = 2500 \text{ keV}$	134
B.10.	Accumulated beam charge on the target during the measurements of the neutron fields at a proton energy of $E_p = 2800 \text{ keV}$	134
B.11.	Angular correction factors for the determination of the neutron fields.	135
B.12.	Angular correction factors used for the determination of the neutron fields above proton energies of $E_p = 2000 \text{ keV}$	135

C.1. Calibration sources used for the detector calibrations. All sources were distributed and calibrated by the Physikalisch-Technische Bundesanstalt (PTB), Braunschweig, Germany.	146
C.2. Properties of the activated samples. The isotopic ratio for the enriched ^{69}Ga sample was taken from the Isoflex USA Certificate of analysis No. 5958 and for the enriched ^{71}Ga from Certificate of analysis No. 6803.	146
C.3. Counts and simulation correction factor determined after the activation of gallium during activation I	147
C.4. Counts and simulation correction factor determined after the activation of gallium during activation I	148
C.5. Specification of the used gold monitors during the first activation measurements, Activation I.	148
C.6. PINO simulation input parameters for activation measurement I. The outcome of the simulation was used to determine the spectrum averaged cross sections for the respective gallium isotopes.	149
C.7. Correction factors for the decays during the activation f_b , the decays between the activation end and the start of and during the measurement f_{wm} and the dead time correction f_{dt} obtained during Activation I.	149
C.8. Shown is the weighted mean between the two detectors and all γ -lines of the produced nuclei during the Activation I. These values were used for further cross section calculation.	149
C.9. Specification of the used gold monitors during Activation II.	150
C.10. Counts and simulation correction factor determined after the activation of gallium during activation II	150
C.11. Counts and simulation correction factor determined after the activation of gallium during activation II	151
C.12. Correction factors for the decays during the activation f_b , the decays between the activation end and the start of and during the measurement f_{wm} and the dead time correction f_{dt} , obtained during Activation II.	151
C.13. Produced nuclei during the Activation II of the natural Gallium sample (natGa II) and the isotopic enriched sample ^{71}Ga . Only the produced nuclei of ^{72}Ga were taken account during this activation due to the previous measurement discrepancies between natural and isopic enriched samples.	151

C.14.Specification of the used gold monitors.	152
C.15.Correction factors for the decays during the activation f_b , the decays between the activation end and the start of and during the measurement f_{wm} and the deadtime correction f_{dt}	152
C.16.Counts and simulation correction factor determined after the activation of gallium during activation III	153
C.17.Counts and simulation correction factor determined after the activation of gallium during activation III.	153
C.18.Produced nuclei during the activation of the natural Gallium sample (natGa II) and the isotopic enriched sample ^{71}Ga . Only the produced nuclei of ^{72}Ga were taken account during this activation due to the previous measurement discrepancies between natural and isopic enriched samples.	154
C.19.Produced nuclei during the activation of the natural Gallium sample (natGa II) and the isotopic enriched sample ^{71}Ga . Only the produced nuclei of ^{72}Ga were taken account during this activation due to the previous measurement discrepancies between natural and isopic enriched samples.	155
C.20.Specification of the used gold monitors.	155
C.21.Specification of the used gold monitors.	156
C.22.Counts and simulation correction factor determined after the activation of gallium during activation IV	158
C.23.Counts and simulation correction factor determined after the activation of gallium during activation IV.	159
C.24.Correction factors for the decays during the activation f_b , the decays between the activation end and the start of and during the measurement f_{wm} and the deadtime correction f_{dt}	160

Bibliography

- [1] D. Abriola and A.A. Sonzogni. “Nuclear Data Sheets for $A = 72$ ”. In: *Nuclear Data Sheets* 111.1 (2010), pp. 1–140.
- [2] S. Agostinelli, J. Allison, K. Amako, et al. “Geant4—a simulation toolkit”. In: *Nuclear Instruments and Methods in Physics Research Section A: Accelerators, Spectrometers, Detectors and Associated Equipment* 506.3 (2003), pp. 250–303.
- [3] F. Ajzenberg-Selove. “Energy levels of light nuclei $A = 5$ -10”. In: *Nucl. Phys. A* 490 (1988), pp. 1–225.
- [4] Suha Alzubaidi, Ulrich Bartz, Markus Basten, et al. “The Frankfurt neutron source FRANZ”. In: *The European Physical Journal Plus* 131.5 (2016), p. 124.
- [5] R. P. Anand, M. L. Jhingan, D. Bhattacharya, and E. Kondaiah. “25 keV-neutron capture cross-sections”. In: *Nuovo Cimento A Serie* 50.2 (Mar. 1979), pp. 247–257.
- [6] A Arcones and F-K Thielemann. “Neutrino-driven wind simulations and nucleosynthesis of heavy elements”. In: *Journal of Physics G: Nuclear and Particle Physics* 40.1 (2012), p. 013201.
- [7] M. Shamsuzzoha Basunia. “Nuclear Data Sheets for $A = 22$ ”. In: *Nuclear Data Sheets* 127 (2015), pp. 69–190.
- [8] M.J. Berger, J.H. Hubbel, S.M. Seltzer, J. Chang, J.S. Coursey, R. Sukumar, D.S. Zucker, and K. Olsen. *XCOM: Photon Cross Sections Database, NIST Standard Reference Database 8 (XGAM)*. Online, 25.05.2021. 2010.
- [9] H. A. Bethe and C. L. Critchfield. “The Formation of Deuterons by Proton Combination”. In: *Phys. Rev.* 54 (4 1938), pp. 248–254.
- [10] K. Bethge. *Kernphysik: Eine Einführung*. Springer-Lehrbuch. Springer Berlin Heidelberg, 2013.
- [11] M.R. Bhat. “Nuclear Data Sheets for $A = 57$ ”. In: *Nuclear Data Sheets* 85.3 (1998), pp. 415–536.
- [12] PTB Braunschweig. *Technical Information for Users of the Neutron Reference Fields at the PTB Ion Accelerator Facility PIAF*. Tech. rep.
- [13] D.A. Brown, M.B. Chadwick, R. Capote, et al. “ENDF/B-VIII.0: The 8th Major Release of the Nuclear Reaction Data Library with CIELO-project Cross Sections, New Standards and Thermal Scattering Data”. In: *Nuclear Data Sheets* 148 (2018). Special Issue on Nuclear Reaction Data, pp. 1–142.

- [14] E. Browne and J. K. Tuli. “Nuclear Data Sheets for $A = 60$ ”. In: *Nucl. Data Sheets* 114 (2013), pp. 1849–2022.
- [15] E. Browne and J.K. Tuli. “Nuclear Data Sheets for $A = 137$ ”. In: *Nuclear Data Sheets* 108.10 (2007), pp. 2173–2318.
- [16] Brun, R. and Hagelberg, R. and Hansroul, M. and Lassalle, J.C. *Simulation program for particle physics experiment, GEANT: user guide and reference manual*. CERN. CERN, Geneva, 1978.
- [17] Rene Brun and Fons Rademakers. “ROOT — An object oriented data analysis framework”. In: *Nuclear Instruments and Methods in Physics Research Section A: Accelerators, Spectrometers, Detectors and Associated Equipment* 389.1 (1997). New Computing Techniques in Physics Research V, pp. 81–86.
- [18] Physikalisch-Technische Bundesanstalt. *Technical data 2 MV - Tandetron*. 2022. URL: <https://www.ptb.de/cms/en/ptb/fachabteilungen/abt6/fb-64/641-ion-accelerators/2-mv-tandetron/technical-data-2-mv-tandetron.html> (visited on 03/27/2022).
- [19] E. Margaret Burbidge, G. R. Burbidge, William A. Fowler, and F. Hoyle. “Synthesis of the Elements in Stars”. In: *Rev. Mod. Phys.* 29 (4 1957), pp. 547–650.
- [20] M. Busso, R. Gallino, and G. J. Wasserburg. “Nucleosynthesis in Asymptotic Giant Branch Stars: Relevance for Galactic Enrichment and Solar System Formation”. In: *Annual Review of Astronomy and Astrophysics* 37.1 (1999), pp. 239–309. eprint: <https://doi.org/10.1146/annurev.astro.37.1.239>.
- [21] A. G. W. Cameron. “Nuclear Reactions in Stars and Nucleogenesis”. In: *Publications of the Astronomical Society of the Pacific* 69 (1957), p. 201.
- [22] A G.W. Cameron. “Stellar evolution, nuclear astrophysics, and nucleogenesis. Second edition”. In: (June 1957).
- [23] *Certificate of Analysis No. 5958*. San Francisco, Ca, USA: Isoflex USA, 2016.
- [24] *Certificate of Analysis No. 6803*. San Francisco, Ca, USA: Isoflex USA, 2016.
- [25] M.B. Chadwick, M. Herman, P. Obložinský, et al. “ENDF/B-VII.1 Nuclear Data for Science and Technology: Cross Sections, Covariances, Fission Product Yields and Decay Data”. In: *Nuclear Data Sheets* 112.12 (2011). Special Issue on ENDF/B-VII.1 Library, pp. 2887 –2996.
- [26] A. K. Chaubey and M. L. Sehgal. “Test of Statistical Theory of Nuclear Reactions at 24 keV”. In: *Phys. Rev.* 152 (3 1966), pp. 1055–1061.
- [27] Institute for Nuclear Physics University of Cologne. *Spectra analysing tool TV*. Version 1.9.12-3. Mar. 12, 2009.
- [28] I. Dillmann, R. Plag, F. Käppeler, and T. Rauscher. “KADoNiS v0.3 - The third update of the “Karlsruhe Astrophysical Database of Nucleosynthesis in Stars””. In: *Proceedings of the workshop “EFNUDAT Fast Neutrons - scientific workshop on neutron measurements, theory & applications”*, Geel, Belgium (2009).
- [29] Yang Dong and Huo Junde. “Nuclear Data Sheets for $A = 54$ ”. In: *Nuclear Data Sheets* 121 (Sept. 2014), pp. 1–142.

- [30] A. G. Dovbenko, V. E. Kolesov, V. P. Koroleva, and V. A. Tolstikov. “Cross sections of radiative capture of neutrons in the 10–350 keV energy range”. In: *Soviet Atomic Energy* 27.5 (1969), pp. 1185–1189.
- [31] G. Feinberg, M. Friedman, A. Krása, A. Shor, Y. Eisen, D. Berkovits, D. Cohen, G. Giorginis, T. Hirsh, M. Paul, A. J. M. Plompen, and E. Tsuk. “Quasi-stellar neutrons from the ${}^7\text{Li}(p,n){}^7\text{Be}$ reaction with an energy-broadened proton beam”. In: *Phys. Rev. C* 85 (5 2012), p. 055810.
- [32] C. Freiburghaus, S. Rosswog, and F.-K. Thielemann. “[CLC][ITAL]r[/ITAL][[/CLC]-Process in Neutron Star Mergers”. In: *The Astrophysical Journal* 525.2 (1999), pp. L121–L124.
- [33] Roberto Gallino, Claudio Arlandini, Maurizio Busso, Maria Lugaro, Claudia Travaglio, Oscar Straniero, Alessandro Chieffi, and Marco Limongi. “Evolution and Nucleosynthesis in Low-Mass Asymptotic Giant Branch Stars. II. Neutron Capture and the s -Process”. In: *The Astrophysical Journal* 497.1 (1998), pp. 388–403.
- [34] Gordon R. Gilmore. *Practical Gamma-ray Spectrometry 2nd Edition*. 2nd ed. John Wiley & Sons Ltd., 2008.
- [35] K. Göbel, C. Beinrucker, B. Brückner, et al. “Neutron activation of ${}^{69}\text{Ga}$ and ${}^{71}\text{Ga}$ at $k_B T \approx 25\text{ keV}$ ”. In: *Phys. Rev. C* 103 (2 2021), p. 025802.
- [36] Gürdal, G. and McCutchan, E.A. “Nuclear Data Sheets for $A = 70$ ”. In: *Nuclear Data Sheets* 136 (2016), pp. 1–162.
- [37] M. Heil, R. Detwiler, R. E. Azuma, A. Couture, J. Daly, J. Görres, F. Käppeler, R. Reifarh, P. Tischhauser, C. Ugalde, and M. Wiescher. “The ${}^{13}\text{C}(\alpha, n)$ reaction and its role as a neutron source for the s process”. In: *Phys. Rev. C* 78 (2 2008), p. 025803.
- [38] Andreas Henelius and Jari Torniainen. “MIDAS: Open-source framework for distributed online analysis of data streams”. In: *SoftwareX* 7 (2018), pp. 156–161.
- [39] Xiaolong Huang and Mengxiao Kang. “Nuclear Data Sheets for $A = 198$ ”. In: *Nuclear Data Sheets* 133 (2016), pp. 221–416.
- [40] Yu. Khazov, A. Rodionov, and F.G. Kondev. “Nuclear Data Sheets for $A = 133$ ”. In: *Nuclear Data Sheets* 112.4 (2011), pp. 855–1113.
- [41] Glenn F. Knoll. *Radiation detection and measurement*. 2nd ed. John Wiley & Sons Ltd., 1989.
- [42] V. N. Kononov, I. I. Stavisskii, and V. A. Tolstikov. “Measurement of the radiative capture cross section of 25 keV neutrons.” In: *The Soviet Journal of Atomic Energy* 5(5) (1958), p. 1483.
- [43] Tabea Kuttner. “Stellare Neutroneneinfangsquerschnitte von ${}^{69,71}\text{Ga}$, ${}^{23}\text{Na}$ und ${}^{37}\text{Cl}$ ”. MA thesis. Goethe-University Frankfurt, 2022.
- [44] C. Lederer, F. Käppeler, M. Mosconi, R. Nolte, M. Heil, R. Reifarh, S. Schmidt, I. Dillmann, U. Giesen, A. Mengoni, and A. Wallner. “Definition of a standard neutron field with the ${}^7\text{Li}(p,n){}^7\text{Be}$ reaction”. In: *Phys. Rev. C* 85 (5 2012), p. 055809.
- [45] W. R. Leo. *Techniques for Nuclear and Particle Physics Experiments: A How to Approach*. 2nd ed. Springer Verlag Berlin Heidelberg New York, 1994.

- [46] Geraint F. Lewis, Luke A. Barnes, and Rajesh Kaushik. “Primordial nucleosynthesis in the $R_h = ct$ cosmology: pouring cold water on the simmering Universe”. In: *Monthly Notices of the Royal Astronomical Society* 460.1 (Apr. 2016), pp. 291–296. eprint: <https://academic.oup.com/mnras/article-pdf/460/1/291/8113529/stw1003.pdf>.
- [47] Horst Liskien and Arno Paulsen. “Neutron production cross sections and energies for the reactions ${}^7\text{Li}(p,n){}^7\text{Be}$ and ${}^7\text{Li}(p,n){}^7\text{mBe}$ ”. In: *Atomic Data and Nuclear Data Tables* 15.1 (1975), pp. 57–84.
- [48] Katharina Lodders. “Solar System Abundances and Condensation Temperatures of the Elements”. In: *The Astrophysical Journal* 591.2 (2003), pp. 1220–1247.
- [49] R. L. Macklin, N. H. Lazar, and W. S. Lyon. “Neutron Activation Cross Sections with Sb—Be Neutrons”. In: *Phys. Rev.* 107 (2 1957), pp. 504–508.
- [50] Juris Meija, Tyler Coplen, Michael Berglund, W. Brand, Paul De Bièvre, Manfred Gröning, N. Holden, Johanna Irrgeher, Robert Loss, Thomas Walczyk, and Thomas Prohaska. “Isotopic compositions of the elements 2013 (IUPAC Technical Report)”. In: *Pure and Applied Chemistry* 88 (Jan. 2016), pp. 293–306.
- [51] Dr. Ralf Nolte. personal communication. Sept. 11, 2018.
- [52] N. Otuka, E. Dupont, V. Semkova, et al. “Towards a More Complete and Accurate Experimental Nuclear Reaction Data Library (EXFOR): International Collaboration Between Nuclear Reaction Data Centres (NRDC)”. In: *Nuclear Data Sheets* 120 (2014), pp. 272–276.
- [53] Rebecca Pachua, B. Lalremruata, N. Otuka, L.R. Hlondo, Lalrinmawia Punte, and Hrangming Thanga. “A tool for calculation of ${}^7\text{Li}(p,n){}^7\text{Be}$ neutron source spectra below the three-body break-up reaction threshold”. In: *EPJ Web of Conferences* 146 (Jan. 2017), p. 12016.
- [54] M. Pignatari, R. Gallino, M. Heil, M. Wiescher, F. Käppeler, F. Herwig, and S. Bisterzo. “The Weak s-Process in Massive Stars and its Dependence on the Neutron Capture Cross Sections”. In: *The Astrophysical Journal* 710 (Feb. 2010), pp. 1557–1577.
- [55] B. Povh, K. Rith, C. Scholz, and F. Zetsche. *Teilchen und Kerne*. 8th ed. Springer-Verlag Berlin Heidelberg: Springer-Verlag, May 2008.
- [56] W. Ratynski and F. Käppeler. “Neutron capture cross section of ${}^{197}\text{Au}$: A standard for stellar nucleosynthesis”. In: *Phys. Rev. C* 37 (2 1988), pp. 595–604.
- [57] R. Reifarth, M. Heil, F. Käppeler, and R. Plag. “PINO—a tool for simulating neutron spectra resulting from the ${}^7\text{Li}(p,n)$ reaction”. In: *Nuclear Instruments and Methods in Physics Research Section A: Accelerators, Spectrometers, Detectors and Associated Equipment* 608.1 (2009), pp. 139–143.
- [58] R. Reifarth, C. Lederer, and F. Käppeler. “Neutron reactions in astrophysics”. In: *Journal of Physics G: Nuclear and Particle Physics* 41.5 (2014), p. 053101.
- [59] René Reifarth, Philipp Erbacher, Stefan Fiebiger, et al. “Neutron-induced cross sections”. In: *The European Physical Journal Plus* 133.10 (2018), p. 424.
- [60] Claus E. Rolfs and William S. Rodney. *Cauldrons in the Cosmos*. Chicago and London: University of Chicago Press, 1988.

- [61] S. Röttger, R. Böttger, F. D. Brooks, A. Buffler, J.-P. Meulders, R. Nolte, F. D. Smit, and F. Wissmann. “The PTB neutron reference fields (PIAF)—quasi-monoenergetic neutron reference fields in the energy range from thermal to 200 MeV”. In: *AIP Conference Proceedings* 1175.1 (2009), pp. 375–381. eprint: <https://aip.scitation.org/doi/pdf/10.1063/1.3258255>.
- [62] Scintactor. *Glass scintillators*. Tech. rep. Scintactor - The centre of scintillation, 2020.
- [63] P. A. Seeger, W. A. Fowler, and D. D. Clayton. “Nucleosynthesis of Heavy Elements by Neutron Capture.” In: *The Astrophysical Journal, Supplement* 11 (Feb. 1965), p. 121.
- [64] M. Shamsuzzoha Basunia. “Nuclear Data Sheets for A = 210”. In: *Nuclear Data Sheets* 121 (2014), pp. 561–694.
- [65] Daniel M. Siegel. “GW170817 –the first observed neutron star merger and its kilonova: Implications for the astrophysical site of the r-process”. In: *The European Physical Journal A* 55.11 (2019), p. 203.
- [66] CAEN SpA. *User Manual UM3350 V1751/VX1751*. 16. 2017.
- [67] Mirion Technologies. *Detectors BEGe - Broad Energy Germanium Detectors*. Tech. rep. Mirion Technologies Inc., 2020.
- [68] Glenn C. Tyrrell. “Phosphors and scintillators in radiation imaging detectors”. In: *Nuclear Instruments and Methods in Physics Research Section A: Accelerators, Spectrometers, Detectors and Associated Equipment* 546.1 (2005). Proceedings of the 6th International Workshop on Radiation Imaging Detectors, pp. 180–187.
- [69] R. Van Grieken. *X-ray fluorescence spectrometry and related techniques: an introduction*. Jan. 2013.
- [70] Carl Friedrich Von Weizsäcker. “Über Elementumwandlungen im Innern der Sterne. II”. In: *Physikalische Zeitschrift* 39 (1 1938), pp. 633–645.
- [71] George Wallerstein, Icko Iben, Peter Parker, Ann Merchant Boesgaard, Gerald M. Hale, Arthur E. Champagne, Charles A. Barnes, Franz Käppeler, Verne V. Smith, Robert D. Hoffman, Frank X. Timmes, Chris Sneden, Richard N. Boyd, Bradley S. Meyer, and David L. Lambert. “Synthesis of the elements in stars: forty years of progress”. In: *Rev. Mod. Phys.* 69 (4 1997), pp. 995–1084.
- [72] G. Walter. “Temperatur und Neutronendichte der schwachen Komponente des s-Prozesses”. In: *KfK Bericht* 3706 (1984).
- [73] G. Walter, H. Beer, F. Kaeppler, G. Reffo, and F. Fabbri. “The s-process branching at Se-79”. In: *Astronomy and Astrophysics* 167.1 (Oct. 1986), pp. 186–199.
- [74] Meng Wang, W.J. Huang, F.G. Kondev, G. Audi, and S. Naimi. “The AME 2020 atomic mass evaluation (II). Tables, graphs and references*”. In: *Chinese Physics C* 45.3 (2021), p. 030003.
- [75] M. Weigand, T. A. Bredeweg, A. Couture, et al. “ $^{63}\text{Ni}(n, \gamma)$ cross sections measured with DANCE”. In: *Phys. Rev. C* 92 (4 2015), p. 045810.
- [76] R E White, P H Barker, and D M J Lovelock. “Measurement of Nuclear Reaction Q-values with High Accuracy: $^7\text{Li}(p, n)^7\text{Be}$ ”. In: *Metrologia* 21.4 (1985), pp. 193–199.

- [77] Demtroöder Wolfgang. *Experimentalphysik 4 : Kern-, Teilchen- und Astrophysik*. Springer Berlin Heidelberg, 2014.
- [78] Ashkan Taremi Zadeh. “Charakterisierung eines digitalen Datenerfassungssystems für ein Flugzeitexperiment mit kurzem Flugweg”. MA thesis. Goethe-University Frankfurt, 2017.
- [79] James F. Ziegler, M. D. Ziegler, and J. P. Biersack. “SRIM - The stopping and range of ions in matter (2010)”. In: *Nuclear Instruments and Methods in Physics Research B* 268.11-12 (June 2010), pp. 1818–1823.

Acknowledgement

Am Ende dieser Arbeit möchte ich mich bei allen Menschen bedanken, die mich auf dieser Reise unterstützt, gefördert und auch wieder aufgebaut haben.

Ich danke Prof. Dr. René Reifarh für Alles was er für mich getan hat. Angefangen mit der Aufnahme in die Arbeitsgruppe über die Möglichkeiten nach Berlin an die BAM zu gehen, um andere wissenschaftliche Anlagen kennenzulernen, bis hin zur Betreuung und Unterstützung während meiner Promotion und der gesamten Zeit in der Arbeitsgruppe in Frankfurt. Danke für Deine Unterstützung beim Experiment in Braunschweig, und dass du immer ein offenes Ohr für meine Anliegen hattest!

Ein ganz besonderer Dank geht hier auch an Prof. Dr. Christoph Langer. Christoph du hast mir sehr viel geholfen während deiner Zeit in Frankfurt. Du wusstest immer genau bescheid, wie Du mich weiter pushen kannst.

Auch danke ich Dr. Kathrin Göbel, die sich immer wieder meine Probleme angehört hat und mir geholfen hat diese zu bewältigen. Die ganzen Galliumaktivierungen und die Messungen an der PTB waren nie langweilig. Vielen Dank für das Korrekturlesen und für die vielen Hilfestellungen in ROOT.

Ich danke meinen Freunden und Kollegen: Dr. Philipp Erbacher, Deniz Kurtulgil, Meiko Volknandt, Dr. Stefan Fiebiger, Dr. Mario Weigand, Dr. Tanja Heftrich, Markus Reich, Kirstin Schäfer und der gesamten Astrophysik Arbeitsgruppe. Danke für die lustigen Jahre und dass ihr es mit mir ausgehalten habt. Danke für die Unterstützungen bei Experimenten. Ganz besonders möchte ich an dieser Stelle Dr. Philipp Erbacher, Deniz Kurtulgil und Meiko Volknandt hervorheben. Ohne Euch wäre Vieles nicht möglich gewesen.

Ich danke der Crew von Van-de-Graaff Beschleuniger an der Uni Frankfurt für den guten Strahl während der vielen Aktivierungen. Danke, dass ihr immer versucht habt das Maximum an Strom herauszukitzeln.

Ich danke auch den Personen, die mich an der PTB vor und während der Strahlzeit unterstützt haben. Allen voran Dr. Ralf Nolte. Ich danke Euch, dass die Durchführung

des Experiments ohne große Probleme funktioniert hat. Für die guten Lithium-targets danke ich Michael Thiel. Auch danke ich der Beschleunigermannschaft, die mir immer einen guten Strahl zur Verfügung gestellt hat. Hervorheben möchte ich hierbei Oliver Döhr. Danke für die lustigen Spätschichten.

Weiterhin danke ich Dr. Christian Müntz und Sascha Staubach für die Durchführung der Materialanalyse der Galliumproben. Außerdem der IAP Werkstatt für die hervorragende Arbeit mit meinen Karbondetektorhaltern.

Ich danke meiner Familie, insbesondere meiner Mutter, Rosemarie Brückner, und meinem Bruder, Achim Geyer, ohne die ich es niemals geschafft hätte. Danke für die immerwährende Unterstützung. Auch danke ich Lando durch den ich vieles gelernt habe.

I also thank my second family in Canada, Lou Barnum and Roy Schoenke. The year I spent with you was one of the best of my life. Your enduring support helped to make me a better person.

Curriculum Vitae

Personal information

Name: Benjamin Sebastian Brückner
Date of birth: February 4th, 1990
Place of birth: Frankfurt am Main, Germany
Citizenship: German

Education

since 2018 Research assistant and PhD student
Goethe University Frankfurt

2016-2018 Master student in Physics
Goethe University Frankfurt
Minor: Philosophy and Economics
Masterthesis:
Spectroscopic measurements of pulsed X-ray sources (1.0)
Young scientist award DGZfP 2018
Supervisors: Prof. Dr. René Reifarth,
RD. Dr. Uwe Zscherpel (Bundesanstalt für Materialforschung)
Academic degree: Master of Science (1.3)

2012-2016 Bachelor student in Physics
Goethe University Frankfurt
Minor: Astronomy
Bachelorthesis:
Kernresonanzfluoreszenz an Rubidium-87 (1.1)
Supervisors: Prof. Dr. René Reifarth,
Dr. Jan Glorius, PD. Dr. Kerstin Sonnabend
Academic degree: Bachelor of Science (2.6)

2010-2012	Bachelor student in Mechanical and Process Engineering Technical University Darmstadt
2010	General qualification for university entrance: Abitur (2.2) Otto-Hahn Schule, Frankfurt am Main

